Series of Lectures of the University of Applied Sciences Ruhr West
June, 8th - 9th 2017 | Vol. 6

IEEE WORKSHOP 2017

SENSORICA 2017

yra
Young Researchers Academy MedTech NRW
2nd YRA MedTech Symposium
yra-medtech.de

Industrial and Medical Measurement and Sensor Technology Vehicle Sensor Technology

Abstractbook

HOCHSCHULE RUHR WEST
UNIVERSITY OF APPLIED SCIENCES
INSTITUT MESS- UND SENSORTECHNIK

UNIVERSITÄT BAYREUTH
UNIVERSITÄT DUISBURG ESSEN
TECHNISCHE UNIVERSITÄT CHEMNITZ
ZESS
UNIVERSITÄT SIEGEN
ITMO UNIVERSITY
TTS Technische Thermodynamik Siegen
IM Chapter IEEE GERMANY SECTION

INTRODUCTION

This year the lecture series on the topic of measurement and sensor technologies take place the seventh time at the University of Applied Sciences Ruhr West. We are pleased that selected contributions of our last workshop in 2016 were published in a special issue of the journal „tm – Technisches Messen“ (De Gruyter Oldenbourg Verlag) in January 2017. We will have this opportunity this year again.

The workshop 2017 will be organized in collaboration with the University of Siegen, the University of Duisburg Essen, the University of Bayreuth, the TU Chemnitz and the ITMO National Research University of Information Technologies, Mechanics and Optics in St. Petersburg. The event is featuring again an even more international orientation by linking it with the Russian SENSORICA.

In addition the workshop 2017 will host the 2nd YRA MedTech Symposium as a parallel track for young promising scientists while providing an open platform for bachelor, master, and doctoral students to present either their work in progress or their final thesis in the realm of (bio-) medical engineering and related fields.

Regarding the joint contributions from all these experts, the workshop 2017 addresses an impressive variety of topics covering industrial and (bio-) medical measurement technology as well as sensor technology in vehicles. Our event offers a platform for knowledge transfer between industry and public and commercial research institutions in the area of measurement technology.

This Abstract Book offers the opportunity of contacting speakers even after the event.
We like to thank everybody having contributed to the success of this workshop and are looking forward to lively discussions!

The Organizing Committee:

Prof. Dr. Jörg Himmel, *University of Applied Sciences Ruhr West*

Prof. Dr. Daniel Erni, *University of Duisburg Essen*

Dipl. -Ing. (Univ.) Alice Fischerauer, *University of Bayreuth*

Prof. Dr. Olfa Kanoun, *TU Chemnitz*

Prof. Dr. Gennadij Lukjanow, *ITMO University, St. Petersburg*

Prof. Dr. Thomas Seeger, *University of Siegen*

Prof. Dr. Klaus Thelen, *University of Applied Sciences Ruhr West*

Contents IEEE Workshop

[1)] Analysis of Intensity and Wavefront Structures of Diode Lasers – Spatial and Current Dependent Evolution

Inga-Maria Eichentopf(1), Martin Reufer(1)

(1) Institute of Natural Sciences, Hochschule Ruhr West,
Duisburgerstr. 100, 45479 Mülheim an der Ruhr, Germany

E-Mail: inga-maria.eichentopf@hs-ruhrwest.de
Web: https://www.hochschule-ruhr-west.de/

Abstract – High power lasers with output powers of several watts are well known devices used for material machining or for medical treatment of eyes and skin [1,2]. All of these high power devices are built from a multitude of single laser emitters whose light is coupled by micro optical devices to bundle the light to create one high intensity beam led through an optical fiber towards the surface under treatment. The single emitter lasers used for our investigations are based on the material system GaAs and emit light in the near infrared wavelength spectrum. The beam furthermore shows an elliptic cross section which changes its opening angle and the number and structure of optical modes in x-direction with the diode current. The increasing of the opening angle with current leads to a reduced coupling efficiency into the optical fiber, hence reducing the efficiency of the laser module. The focus of current research is to improve the resonator of the laser emitter with the aim to keep the opening angle constant and with that to reduce the losses in the laser system's efficiency. A fast and established way to analyze the beam quality of a laser source is the wavefront measurement utilizing a Shack-Hartmann sensor [3]. This sensor type detects the local gradients of the Poynting-vector of the intensity distribution of the incoming beam. From this information the wavefront can be determined by using mathematical algorithms. On the base of the deflections of the detected wavefront under varying input parameters the changes of the beam shape can be recorded instantaneously. This method is already in use for beams with a nearly Gaussian beam profile while the wavefront analysis of broad area beams is an open field of study. Moreover, it can be seen that the wavefront structure changes not only with variation of the diode current, but as well with the distance between the detector and the beam waist i.e. in the transition region from the optical near field close to the laser facet to the far field.

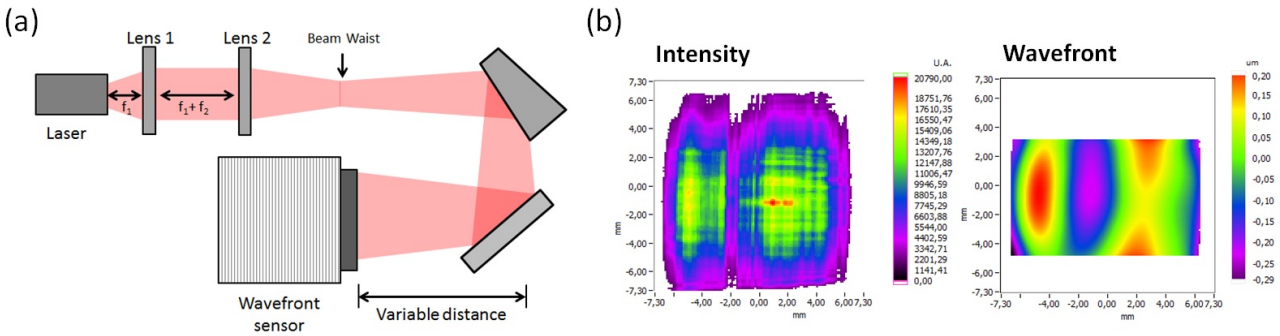

Fig. 1 (a) Experimental setup, so called Gaussian telescope, lens1: f_1=2.8mm and lens2: f_2=125mm; (b) Typical intensity and wavefront distribution of a multimode diode laser (manufacturer: OSRAM, type: SPL CG81-2S, λ=808nm) detected at a distance of 45cm to the beam waist at an output power of approx.1.5W.

The setup which is used to record the wavefront with varying detector distances is shown in Fig. 1 (a). All measurements are carried out with a so called 2f-setup also known as Gaussian telescope [4]. Here the laser beam passes two lenses with the focal length f_1 and f_2. The cross section of the beam is magnified by a factor $m=f_2/f_1=44.6$ [2]. This magnification makes it possible to record the intensity and wavefront distribution close to the beam waist and additionally increases the propagation range by a factor of m^2 which makes a sensitive detection of the wavefront modulations over a wide range of distances possible. The significant changes of the intensity and wavefront distributions appear for the x-direction of

the beam, which is parallel to the epitaxial layer. Fig. 1 (b) depicts a typical intensity and wavefront distribution of a multimode laser. To quantize the wavefront its shape is fitted by a set of 2D-Legendre polynomials.

A typical amplitude set of Legendre polynomials [5] used to reconstruct the wavefront for the three multimode lasers under investigation is shown in Fig. 2(a). All three lasers under investigation are based on the same design, but show distinct differences in the far field intensity distribution due to variances of the device performance. Significant differences within the amplitudes of the polynomials 10, 12 and 15 are therefore related to the emission characteristic for each diode laser. Polynomial 12 is of particular interest for further analysis, since its bowl like structure can be related to the spreading of the light cone with changing working conditions (see Fig. 2(b)). The variation of the diode operating current shows a change in the polynomial amplitude when 1.6 A is exceeded indicating a change of the operating modus. For diode #1 this drop of the amplitude is reduced in comparison to the other diodes. Additionally, the behavior of the amplitude of polynomial 12 is recorded in dependence of the distance of the detector to the beam waist. As can be seen in Fig. 2(c) the magnitudes of the amplitudes decrease with increasing distance. Thereby the slopes of the amplitude change over distance to beam waist differ with $2 \cdot 10^{-7}$ for diode #1 and with an average of $5 \cdot 10^{-7}$ for diode #2 and diode #3. This can be related to the intensity distribution of the different lasers, with diode #2 and diode #3 showing a comparable emission pattern, dominated by two symmetric maxima in x-direction, while the emission of diode #1 deviated clearly from this pattern.

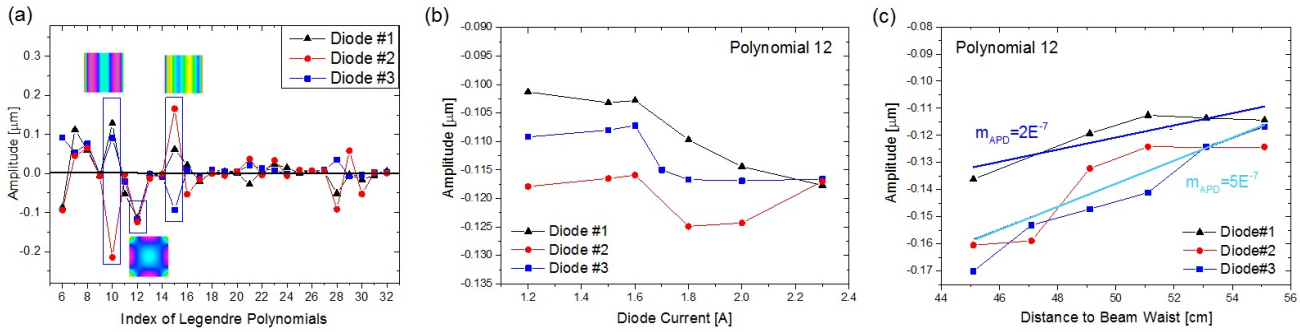

Fig.2: (a) Distribution of Legendre polynomials of three multimode diode lasers (manufacturer: OSRAM, type: SPL CG81-2S, λ=808nm) for an operating current of 2.0 A (1.5 W optical power) at a distance to beam waist of 55 cm, most important polynomials are marked; (b) Current dependence of amplitudes of polynomial 12 for the set of the three diode lasers; (c) Behavior of polynomial 12 under distance variation.

The aim of our work is to describe the optical modes of the laser emission by a set of Legendre polynomials. Additionally, the intensity distribution in the far field is simulated with commercially available software to find an expression of the modal composition of the intensity at various operating currents. Combination of wavefront and intensity data in dependence of current and spatial evolution will lead to a deeper knowledge of the laser characteristics and prediction for further laser design.

References

[1] F. Bachmann, “Industrial applications of high power diode lasers in materials processing,” *Applied Surface Science*, Volumes 208–209, pp. 125–136, March 15, 2003.

[2] L. Brancaleon, and H. Moseley, “Laser and Non-laser Light Sources for Photodynamic Therapy,” *Lasers in Medical Science*, Volume 17, Issue 3, pp. 173–186, August, 2002.

[3] M. Kunzmann, B. Schäfer, and K. Mann, „Charakterisierung von Laserstrahlung mittels Hartmann-Shack-Wellenfrontsensor,“ *Photonik 1*, pp. 52-55, 2005.

[4] St. Rogowsky, H. Braun, U. T. Schwarz, St. Brüninghoff, A. Lell, and U. Strauß, “Mulidimensional near- and far-field measurements of broad ridge (Al,In)GaN laser diodes,” *Phys. Status Solidi C6*, No. S2, pp. 852-855, 2009.

[5] HASO software user guide v1.0.11580, Imagine Optic, 2013.

2) Development and Application of Optical Sensors for Remote, Spatially Resolved Thermometry Using Thermographic Phosphors

Torsten Endres, Dominik Meller, Thomas Dreier, and Christof Schulz

Institute for Combustion and Gas Dynamics – Reactive Fluids
Faculty of Engineering, University of Duisburg-Essen, D-47057 Duisburg, Germany

E-Mail: torsten.endres@uni-due.de
Web: www.uni-due.de/ivg/rf/

Abstract – Knowledge of accurate surface temperatures is important in many industrial or combustion processes. However, in many situations these temperatures cannot be measured using common measurement techniques like thermocouples or pyrometry. Installation of simple thermocouples is often too invasive or technically not feasible since, for instance, the region of interest cannot be reached or the thermocouple cannot withstand the local flame conditions.

Accurate pyrometry requires exact knowledge of the thermal emissivity behavior of the surface, which can be changed by the monitored process itself during the measurement. Pyrometry of an isolated hot object is relatively straightforward. In many cases of practical interest, the situation is complicated by the presence of extraneous reflected radiation. As an example, one might want to measure the surface temperature of a combustion chamber or a furnace. Most of the radiation received by the pyrometer would consist of reflected radiation from the burning gases or hotter surfaces rather than from the surface of interest.

Thermographic phosphors are doped inorganic crystalline materials with temperature dependent luminescence properties. Such materials consist of a ceramic host material and a dopant as luminescence center. Once coated on the surface of interest and excited by a laser pulse of suitable wavelength, the thermographic phosphor emits an intense luminescent light. Depending on the concrete phosphor and the temperature, the resulting phosphorescence has a duration in the order of 10^{-6} – 1 s. Then the surface temperature can be inferred from the spectral or temporal properties of the emitted phosphorescence. This technique enables a high signal intensity, two-dimensional measurements and remote thermometry with high accuracy. In contrast to pyrometry, it does not depend on the emissivity of the material and is not influenced by background reflection from the surroundings, light absorption or surrounding hot gas emission or absorption. These advantages have allowed thermographic phosphors to be used in a wide variety of applications and in harsh environments, e.g. on walls exposed to turbojet afterburner flames [1].

The aim of this work is to develop an inexpensive yet precise optical sensor for remote and spatially resolved thermometry at moderate temperatures using thermographic phosphors. A future application of the sensor will be the temperature characterization of a burner plate in a heat flux burner, enabling the determination of accurate laminar burning velocities. A similar approach was already performed by Li and coworkers [2]. In this work the temperature dependent shift of the excitation spectra was utilized to determine the temperature distribution of the burner plate. Therefore, the phosphorescence from the burner plate after laser excitation was imaged with two different spectral filters. In general, it is straightforward to perform spatially resolved thermometry using this ratio-based method, but the overall precision and accuracy of the ratio method is limited. On the downside, more precise luminescence lifetime-based methods can usually only be used for 0D (spot) measurements. For instance, Grattan *et al*. demonstrated the usage of chromium-doped aluminum oxide (ruby) as phosphor with standard deviations around ±0.04 °C in temperature ranges between room temperature and 170 °C [3].

To take advantage of this high sensitivity also for spatial resolved measurements, laser-scanning approaches were tested in the present work. For this purpose, scanning of surfaces was tested using a laser scanner unit (see Figure 1a) and a pan-tilt unit.

Furthermore, we have compared two different lifetime-based experimental methods for deriving the temperature in terms of achievable precision and accuracy using repeatability tests for the temperature measurement. Firstly, we used pulsed laser excitation and detected the luminescence decay curve. This allows the fitting of phosphorescence lifetime using a suggested and widely established algorithm form Brubach *et al.* [4] and hence temperature determination using an experimental calibration database. Secondly, we used sinusoidal modulated laser excitation and detected the phase shift between excitation and phosphorescence using a dual phase lock-in amplifier. Here, the phase shift is calibrated as a function of the temperature. The main advantage of this method is, that the temperature sensitivity can be optimized for a certain temperature by varying the modulation frequency.

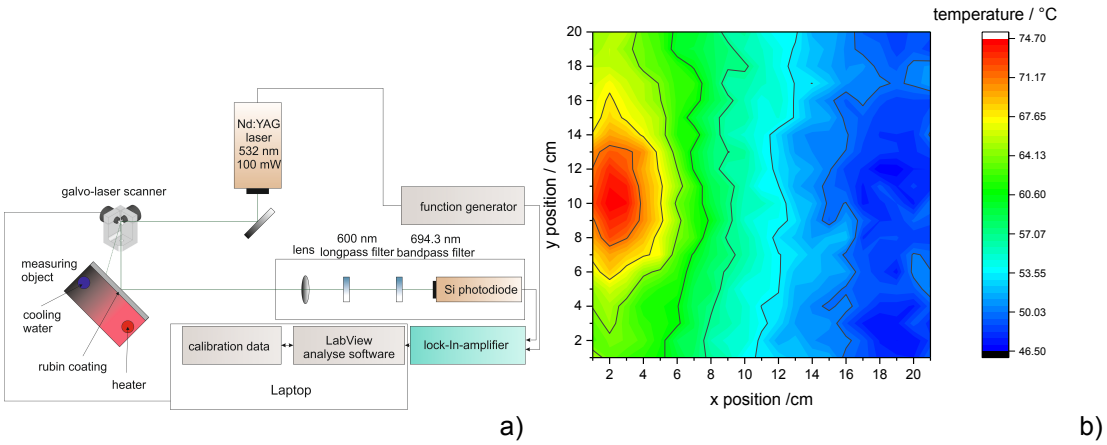

Fig.1: a) Diagram of the optical arrangement for laser scanning phosphor thermography.
b) Measured temperature field of an inhomogeneous heated aluminum plate (1 cm thick) obtained with this arrangement. On the left side (x = 2 cm), a 20 W cartridge heater is installed and on the right side (x = 18 cm), cooling water flows from the top to the bottom through a 5 mm Ø channel.

After systematic optimization of the measurement parameters like frequency, amplitude, pulse length, modulation type, etc., for both methods the phase shift method has proven to be superior. Although both methods achieve an accuracy of around 0.25 %, the phase shift method reaches a much better precision of 0.006 % (≙ 19 mK @ 300 K) compared to 0.32 % for the lifetime method. As shown in figure 1b this method could also successfully be extended to spatially resolved thermometry. The results of the inhomogeneously heated aluminum plate are consistent with images recorded by a thermal camera, therefore this new technique can now be applied to the more challenging heat flux burner.

References

[1] I. E. Jeffrey, W. A. Stephen, P. J. Thomas, L. G. Sarah, A. H. Carl, and D. G. Walker, "Surface temperature measurements from a stator vane doublet in a turbine afterburner flame using a YAG:Tm thermographic phosphor," *Measurement Science and Technology,* vol. 27, p. 125205, 2016.

[2] B. Li, J. Linden, Z. S. Li, A. A. Konnov, M. Alden, and L. P. H. de Goey, "Accurate measurements of laminar burning velocity using the Heat Flux method and thermographic phosphor technique," *Proceedings of the Combustion Institute,* vol. 33, pp. 939-946, 2011.

[3] K. T. V. Grattan, R. K. Selli, and A. W. Palmer, "Ruby Decay-Time Fluorescence Thermometer in a Fiber-Optic Configuration," *Review of Scientific Instruments,* vol. 59, pp. 1328-1335, Aug 1988.

[4] J. Brubach, J. Janicka, and A. Dreizler, "An algorithm for the characterisation of multi-exponential decay curves," *Optics and Lasers in Engineering,* vol. 47, pp. 75-79, Jan 2009.

3) Next Generation Diagnostics: Highly Sensitive Integrated CMOS Photodiode Sensor Array for Light Absorption Measurement

Alexander Hofmann[(1)], Michael Meister[(1)]

[(1)] IMMS Institut für Mikroelektronik- und Mechatronik-Systeme Gemeinnützige GmbH, Ilmenau, Germany
E-Mail: {alexander.hofmann, michael.meister}@imms.de
Web: www.imms.de

Abstract – Analog/mixed-signal (AMS) integrated circuits (ICs) conquered the world in the form of telecommunication, data processing and entertainment products e.g. Smartphones and PCs. Although microelectronic technology evolves rapidly, it could not fully enter the molecular diagnostic market. This work presents an integrated highly sensitive CMOS photodiode sensor array for light absorption measurement and low cost system integration. It was tested and compared to the optical power meter Advantest Q8221. The IC shows a measurement range of three decades with a detection limit of 0.001 optical density (OD) in air at maximum sensitivity. It states the possibility to be 10 times more sensitive than measurements with commercial diagnostic devices and being used for medical diagnostic applications e.g. Point-of-Care Testing.

Introduction: Healthcare profits from IC developments in terms of the so called Next-Generation Sequencing [1], which aims to decode the human genome to fight against genetic disorders. In the future microelectronic technology could be the gold standard enabling a faster, high precision, mobile, cost effective and reliable diagnostic, e.g. for early cancer recognition. Many research groups e.g. [2] already showed the potential of integrated optical sensor circuits for molecular diagnostics. Absorbance measurement is a widely used optical technique to verify chemical reactions and - dependent on that - a medical diagnosis and to quantify analytes of interest [3]. Absorbance or OD is based on the Beer-Lambert law, which is shown in Fig. 1 a). It determines the received light D_R of an incident light D_0 passing an absorptive sample with D_R the measurand of interest [3]. For commercial medical diagnostic devices the maximum absorbance is usually defined at OD = 1, whereas the detection limit is at OD = 0.01.

Materials and Methods: An integrated CMOS photodiode sensor array was designed in XH035 technology of X-FAB Semiconductor Foundries AG in order to reach the precision of commercial devices or even better and for a low cost system integration. Commercial devices are using many bulky, expensive and complex components such as Xenon light sources, customized optics and CCD or CMOS based detectors shown in Fig. 1 b). In the new approach the biochemistry can be directly applied on top of the sensor surface using only a small low cost LED light source. The IC signal path is shown in Fig. 2 a) and consists of the photodiode, converting incoming photons into electrons and generating an electrical current flow. This current is pre-amplified in two successive current mirror amplifiers and then amplified and converted into an equivalent voltage using a trans-impedance amplifier (TIA). A 6 x 7 sensor array, shown in Fig. 2 b), was implemented to get a more reliable data post-processing. Moreover, it offers the possibility of multi-disease detection and/or multi-patient treatment using state of the art microarray spotting technology [4]. To verify the

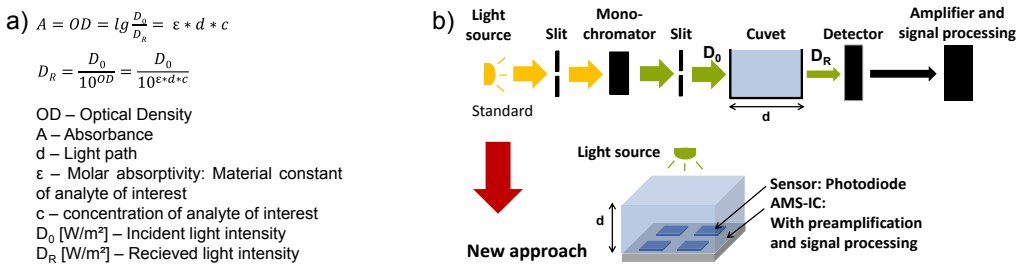

Fig.1: Beer-Lambert law in a), the fundamental law for absorbance measurement; Standard absorbance measurement with lots of bulky, expensive and complex components compared with the new approach using an AMS IC in b).

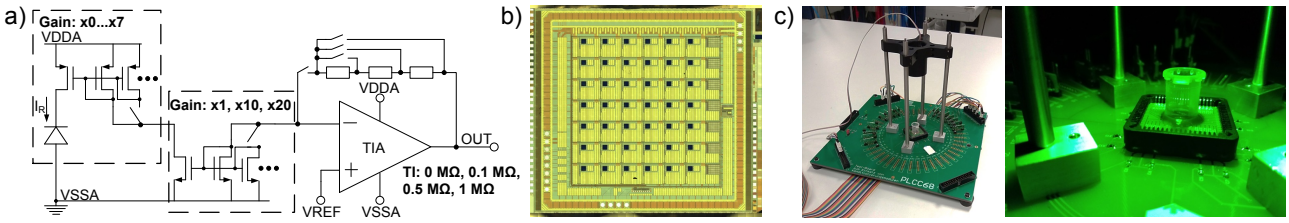

Fig.2: IC signal path in a), the manufactured IC with the 6 x 7 sensor array (dark dots) in b) and the measurement setup (left) with the green (λ = 527 nm) LED light source (right) in c).

opto-electrical behavior of the IC, measurements were done without any unideal fluids. Measurement results of the IC were compared with reference measurements of the optical power meter Advantest Q8221. Fig. 2 c) shows the measurement setup with the IC mounted and bio-compatibly encapsulated in a designed Chip-on-Board (COB) structure with liquid reservoir and a commercial green LED. Both were mounted on a test board and connected to the control unit.

Results: Linearity and measurement range of the IC were characterized. The LED light intensity and therefore the optical power density (OPD) was varied. The output voltage of the IC was observed at maximum sensitivity. Results were compared to an ideal linear regression which is shown in Fig. 3 a). Both graphs lie on top of each other with a maximum deviation of 2.3 mV_{PP} without averaging. This is confirmed by a very good coefficient of determination of $R^2 = 0.999994$. Fig. 3 b) shows the calculated OD as a function of the varied OPD for the IC and the Advantest Q8221. The IC works best at OPDs of 0.1-1 W/m² reaching a detection limit of 0.001 OD at OPD = 0.5 W/m² and a maximum measurement range of three decades. The higher the OPD, the higher the noise of the IC. OPDs under 0.1 W/m² raise errors and the IC is not working linearly.

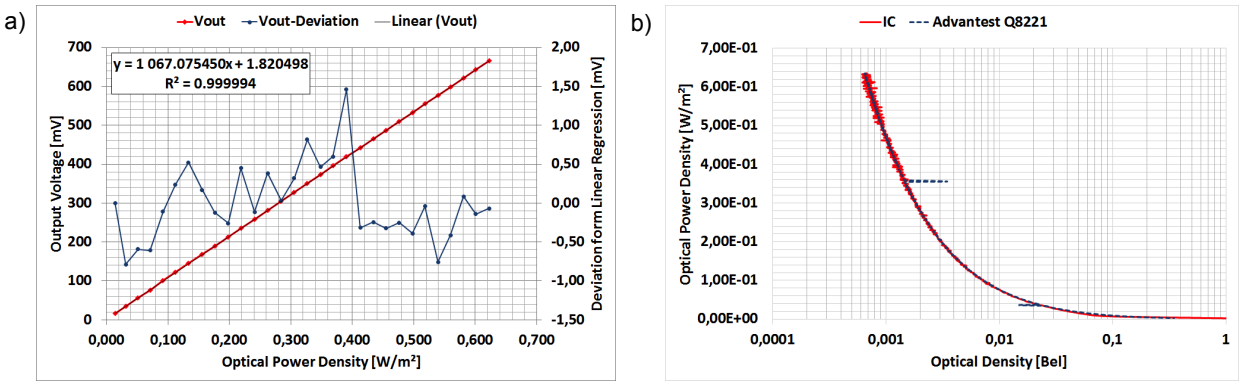

Fig.3: IC linearity in a): Linear regression (black) vs. IC output voltage (red) and the deviation from the linear regression (blue); Maximum measurement range (red) in b): OD vs. OPD for the IC (red) and the Advantest Q8221 (blue).

Conclusion: The developed IC shows high linearity and a measurement range of three decades with a detection limit of 0.001 OD. It promises to be 10 times more sensitive than commercial diagnostic devices and enables a low cost system integration. Further work will validate the system performance with unideal fluids and analytes causing unwanted reflections and absorptions.

Acknowledgement: This presented work has been developed in the project INSPECT funded by the Free State of Thuringia and the European Union, reference 2015 FE 9159.

References

[1] J. M. Rothberg, W. Hinz, T. M. Rearick et al., "An integrated semiconductor device enabling non-optical genome sequencing," *Nature*, vol. 475, no. 7356, pp. 348-352, 21 July 2011.

[2] B. Jang., P. Cao, A. Chevalier et al., "A CMOS fluorescent-based biosensor microarray," *Solid-State Circuits Conference-Digest of Technical Papers, 2009. ISSCC 2009. IEEE International*, pp. 436-437, IEEE, 2009.

[3] C. A. Burtis and D. E. Bruns, "Tietz fundamentals of clinical chemistry and molecular diagnostics," *7th Edition*, Elsevier Health Sciences, 2015.

[4] V. Romanov, S. N. Davidoff, A. R. Miles et al., "A critical comparison of protein microarray fabrication technologies," *Analyst*, vol. 139, no. 6, pp. 1303-1326, Royal Society of Chemistry, 2014.

4) Development of a Fiber-based Chemiluminescence Sensor for Harsh Environments

Simon Goers, Torsten Endres, Thomas Dreier and Christof Schulz

Institute for Combustion and Gas Dynamics – Reactive Fluids
University of Duisburg-Essen,
D-47057 Duisburg, Germany

E-Mail: simon.goers@uni-due.de
Web: www.uni-due.de/ivg/rf/

The today's demands for clean and flexible energy generation require gas turbines with high fuel efficiency, fuel flexibility, and good part-load capabilities making the combustor a highly complex key component. Due to the complexity, full-scale single burner combustion tests are an important step during the development process of stationary gas turbines. A typical Siemens test rig (Fig. 1) consists of the outer pressure vessel, an exchangeable flow box to simulate the flow path and the burner. External compressors provide the inflow and a backpressure valve mimics the turbine. This setup allows for realistic boundary conditions, i.e. a pressure up to 25 bar and inflow temperatures of 500 °C. Typically used measurement techniques including mass flow meters, thermocouples and pressure transducers cannot provide direct information about the flame behavior. In particular, flame shape, location and spatial distribution remains unknown. In order to obtain deeper insight, we are developing endoscopic, fiber-based flame chemiluminescence sensors to enable optical access to the combustion zone of full-size operating gas turbine burners. Chemiluminescence is the light emission from electronically excited species such as OH* and CH* in the flame's reaction zone and serves as a passive and robust optical diagnostic method in various applications, e.g. flame location, heat release fluctuations and equivalence ration sensing [1–6].

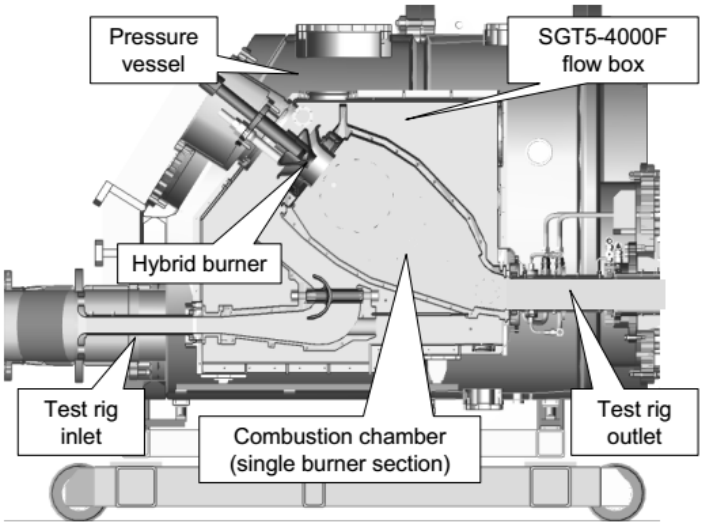

Fig.1: High-pressure test rig with SGT5-4000F flow box.

The challenge here is to obtain optical access for UV imaging through geometrically complex hardware in these harsh conditions for several hours of testing. The sensor features water-cooling and nitrogen purging, while remaining flexible and modular. The key to the flexibility are the used imaging fused silica fiber bundles (OH-doped for high transmission in the UV spectral region between 200 – 350 nm) combined with UV lenses with different field of views (i.e. 20°, 50° and 90°) for different burner configurations.

The development process splits into two parts. The mechanical design of the water-cooled probe including the feedthrough concept into the combustor, and the optical design with the lenses and selection of imaging fiber bundles. Limited flexible UV image fiber with 30 000 cores (≈pixels) from Fujikura Ltd and flexible ones with 20 000 cores from Nanjing Chunhui are available.

Currently, three different heads for the probe are available, considering the desired field of view and the probe location in the test rig. All heads are constructed of high-temperature materials combined with a ceramic coating to increase their resistance in hot oxidizing environments. A drawing of the first design is shown in Fig. 2 with a 50° field of view. It consists out of the outer head holding a sapphire window and the copper inlet with the cooling channels holding the lenses and the Fujikura fiber bundle. The lenses are mounted with specific spacers to maintain their mutual calculated distances even during the probe endures severe vibrations from the combustor. In order to change to a different field of view the inner lenses are exchangeable.

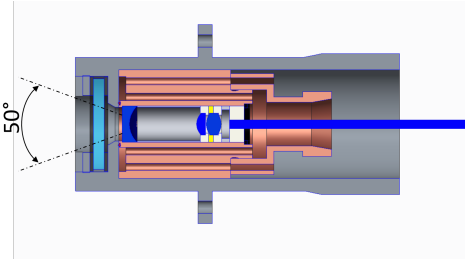

Fig.2: First head design containing the optics (i.e. lenses and optical fiber) and the cooling body.

The design of the mechanical feedthrough depends on the used combustion hardware. The basic concept for accessing the pressure vessel is based on standard flanges. This concept simplifies the technical approval and limits the required modifications to existing test rigs.

The three main components of the optical system are the imaging fiber bundle, the input lens setup at the tip with 1 to 4 lenses and the output lens system (1–2 lenses) at the detector end. At this end, either a camera setup (with frame rates in the kHz regime) or a spectrometer can be used for imaging or spectral chemiluminescence detection, respectively. Due to the line-of-sight nature of chemiluminescence imaging and the geometrical size of the combustors, the optical setup requires a large depth of field. On the other hand, a comparable low f-number is desirable to increase the signal-to-noise ratio in the images or allow for species-selective detection via optical narrow band pass filters and short exposure times for high-speed imaging.

The performance of each optical setup, i.e. depth of field and sharpness, was validated accordingly to the ISO 12233 slanted edge method by measuring the step response at different distances between the front optics and a standardized target. Afterwards the line spread function was derived at each position and Fast-Fourier transformed to calculate the modulated transfer function [7,8].

References

[1] B. Witzel *et al.,* “Application of Endoscopic OH*-Chemiluminescence Measurements at a Full-Scale High-Pressure Gas Turbine Combustion Test Rig,” in *Proceedings of the ASME Turbo Expo 2012: Presented at the 2012 ASME Turbo Expo, June 11 - 15, 2012, Copenhagen, Denmark*, New York, N.Y: ASME, 2012, p. 817.

[2] F. Guethe, D. Guyot, G. Singla, N. Noiray, and B. Schuermans, “Chemiluminescence as diagnostic tool in the development of gas turbines,” *Appl. Phys. B*, vol. 107, no. 3, pp. 619–636, 2012.

[3] Y. Hardalupas, C. S. Panoutsos, and A. M. K. P. Taylor, “Spatial resolution of a chemiluminescence sensor for local heat-release rate and equivalence ratio measurements in a model gas turbine combustor,” *Exp Fluids*, vol. 49, no. 4, pp. 883–909, 2010.

[4] Z. Yin, I. G. Boxx, M. Stöhr, O. Lammel, and W. Meier, “Investigation of Confined Turbulent Jet Flames Using kHz-Rate Diagnostics,” in *54th AIAA Aerospace Sciences Meeting*.

[5] J. O'Connor, V. Acharya, and T. Lieuwen, “Transverse combustion instabilities: Acoustic, fluid mechanic, and flame processes,” *Progress in Energy and Combustion Science*, vol. 49, pp. 1–39, 2015.

[6] J. D. Gounder, A. Zizin, O. Lammel, M. Rachner, and M. Aigner, “Experimental and numerical investigation of spray characteristics in a new FLOX based combustor for liquid fuels for Micro Gas Turbine Range Extender (MGT-REX),”

[7] J. K. Roland, “A Study of Slanted-Edge MTF Stability and Repeatability” , http://www.imatest.com/publications/ (accessed April 15, 2017)

[8] **ISO 12233:2017** Photography -- Electronic still picture imaging -- Resolution and spatial frequency responses

5) Optically Pumped Organic Lasers for Microfluidic On-Chip Absorption Spectroscopy

Sebastian Morain[(1),(2)], Jörg Knyrim[(1)], Martin Reufer[(2)], Christian Karnutsch[(1)]

[(1)] Institute for Optofluidics and Nanophotonics (IONAS),
Faculty of Electrical Engineering and Information Technology, Hochschule Karlsruhe,
76133 Karlsruhe, Germany

E-Mail: christian.karnutsch@hs-karlsruhe.de
Web: www.hs-karlsruhe.de/ionas

[(2)] Institute of Natural Sciences, Hochschule Ruhr West,
Duisburgerstr. 100, 45479 Mülheim an der Ruhr, Germany

Abstract – We present optically pumped organic lasers for microfluidic on-chip absorption spectroscopy. The optically pumped organic laser is part of a compact Lab-on-a-Chip microfluidic analysis system for applications in point-of-care diagnostics (e.g. blood analysis), biosensing, environmental sensing, chemical sensing and biomedical sensor systems.

Absorption spectroscopy is one of the most widely used techniques to determine concentrations of analytes in solutions. It is an essential nondestructive analytical method in academic fields such as medicine, biology, and chemistry, but it has also widespread use in industry.

The organic laser, the microfluidic system and an optical detector are integrated into a Lab-on-a-Chip system. The concept of the microfluidic on-chip absorption device is shown in Fig. 1. If a low laser threshold of the organic laser is achieved, it would be possible to pump the device with an inorganic laser diode, rendering the absorption spectroscopy system smaller and cheaper compared to existing systems. Through employing different grating periodicities and varying organic materials on one chip, it is easily possible to generate various wavelengths required in established analytical methods.

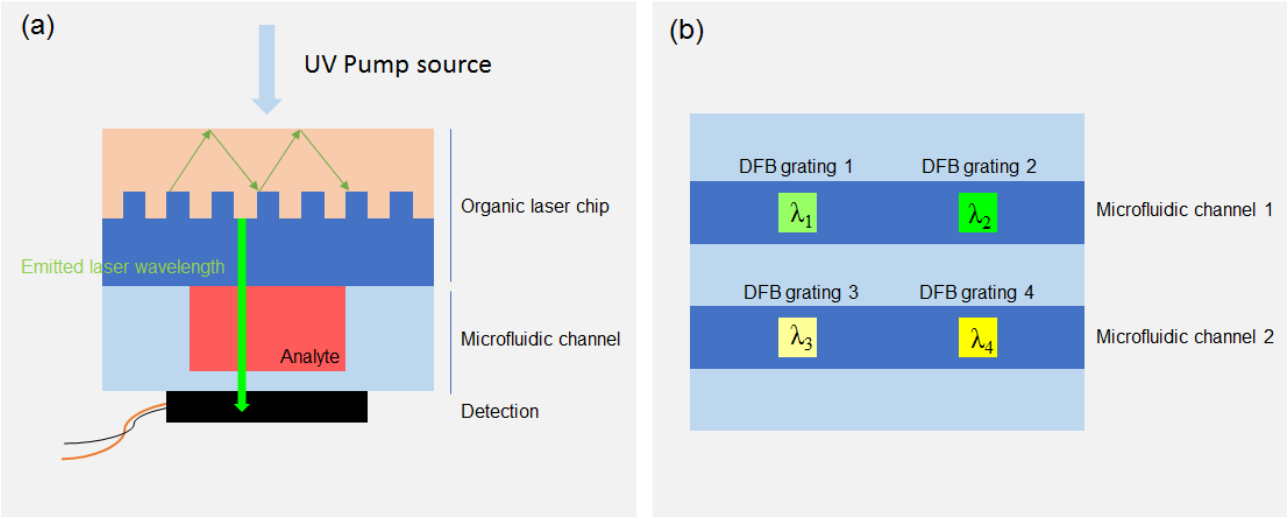

Fig.1: (a) Schematic design of the microfluidic on-chip absorption device, (b) Top view of a potential matrix array.

Optically pumped organic DFB laser: Due to their wide spectral range, tuneability, potentially compact design and their low manufacturing cost, organic lasers became an important part in the recent development of Lab-on-a-Chip devices. The main developments of organic laser designs and materials from the last decade have recently been summarized by Alexander J.C. Kuehne and Malte C. Gather [1] and Sèbastien Chènais and Sèbastien Forget [2]. DFB resonators promise a good possibility to produce low cost organic lasers with a low laser threshold.

A central part of the optofluidic analysis system is an optically pumped organic distributed feedback (DFB) laser as schematically shown in Fig. 2. The optically pumped organic laser allows for a compact, modular and low cost design. By changing the grating periodicity Λ of the distributed feedback (DFB) resonator, combined with an appropriate organic laser material, it is in general possible to generate any required wavelength throughout the visible spectral regime.

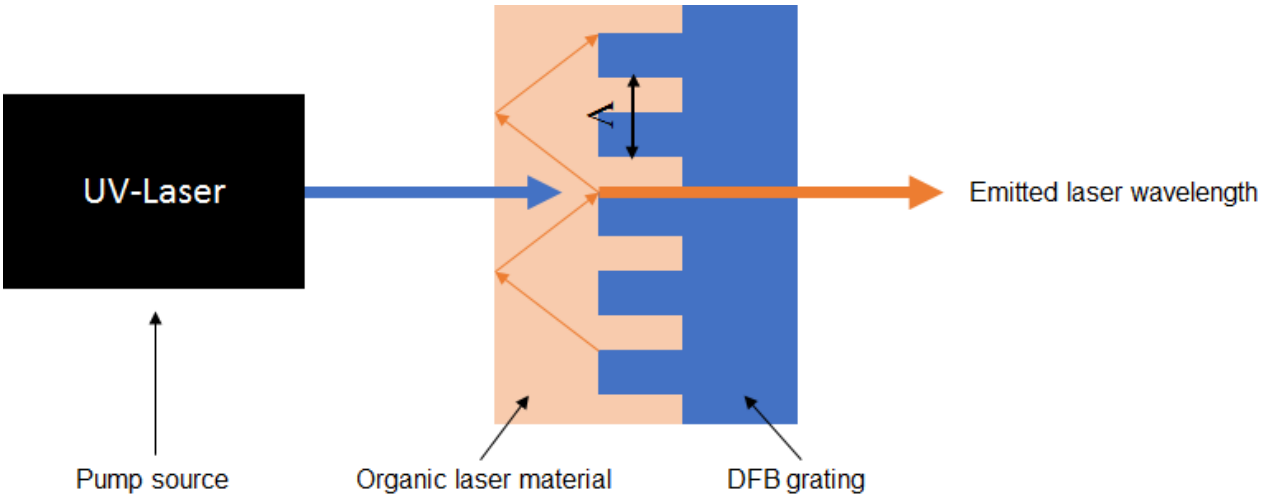

Fig.2: Schematic of an optically pumped organic DFB laser.

We are working on a reliable and reproducible manufacturing process for low threshold optically pumped organic DFB lasers. Detection of the emitted laser intensity is required for absorption spectroscopy. Therefore, we are testing a novel sensor that is based on an array of small photodiodes. Each photodiode is combined with a narrow-band filter to analyze a specific wavelength and to minimize noise. The third component of our work is the microfluidic structure. All parts must be integrated into a Lab-on-a-Chip system with focus on a low-cost manufacturing process and keeping a small footprint.

References

[1] Alexander J. C. Kuehne and Malte C. Gather, “Organic Lasers: Recent Developments on Materials, Device Geometries, and Fabrication Techniques,” *Chem. Rev.*, 116 (21), 12823−12864, 08, 2016

[2] Sèbastien Chènais and Sèbastien Forget, “Recent advances in solid-state organic lasers,” *Polymer International*, 61, 390-406, 10. 2011

6) Advancing Laser-Induced Breakdown Spectroscopy for Multi-Parameter Concentration and Temperature Measurement

Andrew P. Williamson[(1)] and Johannes Kiefer[(1,2)]

[(1)] Technische Thermodynamik
Universität Bremen, Badgasteiner Str. 1,
D-28359, Germany

[(2)] MAPEX Center for Materials and Processes
Universität Bremen, Bibliothekstr. 1,
D-28359, Germany

E-Mail: jkiefer@uni-bremen.de
Web: www.thermo.uni-bremen.de

Abstract – Knowledge of influential parameters such as temperature is of utmost importance in the characterization of combustion processes. Many laser-based methods exist for the determination of these parameters, a few examples being Raman spectroscopy, laser-induced fluorescence, laser-induced gratings and coherent anti-Stokes Raman spectroscopy. Laser-induced breakdown spectroscopy (LIBS), a technique almost exclusively used in the detection and quantification of elemental species, exhibits a strong dependence on the temperature manifested in the intensity required to breakdown the gas, also known as the ionization or breakdown threshold.

The dependence of the breakdown threshold on gas properties such as density, pressure and temperature is well-known and a long investigated subject [1-3]. However, it is only recently that it has been brought to use for temperature measurement [4,5]. In this abstract, we demonstrate a time-resolved method for determining temperature in a flat flame by utilizing the time delay to which breakdown occurs along the Gaussian intensity of a laser pulse. In doing so we allow simultaneous measurement of temperature and composition without the drawbacks of varying laser energy, composition dependence or measurement in the laser path.

The laser pulses were delivered from a Q-switched spatially multi-mode Nd:YAG laser. It was operated in its second harmonic mode producing a wavelength of λ = 532 nm, Fig. 1(a). Each pulse was attenuated to ~100 mJ and successive plasma breakdowns occurred at the pulsing rate of 10 Hz. The time-resolved plasma emission was captured using fast photodiodes at a sampling rate of 5 Gs/s. Due to the irreproducibility of each breakdown and the limited temporal resolution the sampling period lasted 20 seconds resulting in an accumulation of 200 signals. A smoothing algorithm was applied and the point in time where breakdown occurred was taken from a threshold value.

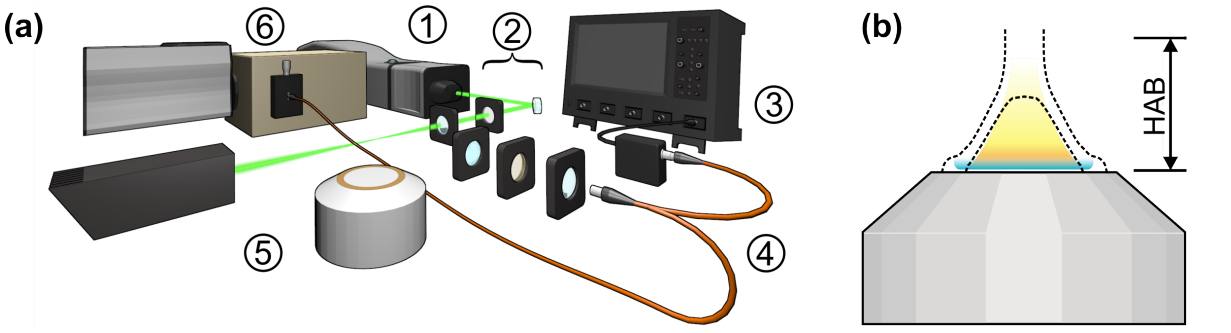

Fig.1: (a) Arrangement of the laser-induced breakdown thermometry/spectroscopy apparatus. (1) Laser, (2) Collection and direction optics, (3) Oscilloscope and photodiode, (4) Bifurcated optical fiber, (5) McKenna burner, and (6) Spectrometer and intensified CCD camera. (b) Observable fluctuating region of the burner flame within the dashed boundary along the height above the burner (HAB).

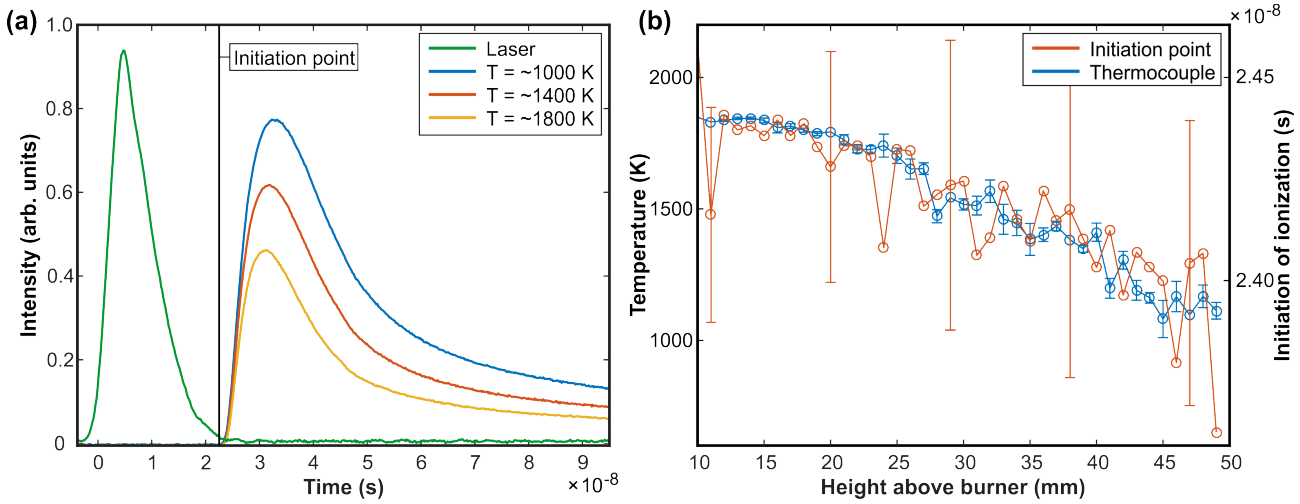

Fig.2: (a) Temporal profile of the laser pulse (offset) and the temperature dependence on plasma emission. (b) Superimposed readings of the initiation point of breakdown (orange) on thermocouple temperature readings (blue), error bars display standard deviation.

A flat flame was produced from a McKenna plug-flow burner. Flow rates of 150 mg/s were maintained through calibrated flow controllers (Bronkhorst, EL-FLOW Prestige) and a methane-air equivalence ratio of ϕ = 0.85 was set. The flame under investigation does not utilize a stabilization body and is therefore conical in shape, largely removing the one-dimensionality of the flame. In addition, the low flow rate produces fluctuations which are observable at the base and top of the flame, illustrated in Fig. 1(b).

The temperatures along the flame were determined using a Type N, Pyrosil sheathed thermocouple. Each temperature reading is a result of 20 averaged measurements from a 1 Hz sampling rate, with radiative and convective losses taken into account.

The temperature dependence on the plasma continuum emission is clearly visualized in Fig. 2(a). The pulse profile, shown offset, has a full width a half maximum (FWHM) of ~6.50 ns suggesting the limit of the method to be ~3.25 ns, in the region of 1000 – 2000 K this accounts for only 21 % of the limit leaving great room for measurement.

Superimposing the point of ionization on the thermocouple temperature readings demonstrates a clear and good correlation between the two methods, Fig. 2(b). The most stable region in the flame structure is apparent 12 - 23 mm above the burner surface, beyond which the readings become more erratic due to influences from lower temperature fluxes, flame-front beam steering and particulates.

This proposed arrangement allows for the approximation of flame temperature as well as the potential for simultaneously evaluating elemental species and composition whilst overcoming many of the aforementioned drawbacks. Thus further advancing the potential for LIBS as a multi-parameter diagnostic method.

Acknowledgment: This work was supported by Deutsche Forschungsgemeinschaft (DFG) through grant KI1396/3-1.

References

[1] C. G. Morgan, "Laser-induced breakdown of gases", *Rep. Prog. Phys.*, vol. 38, pp. 621-665, 1975.
[2] T. X. Phuoc, “Laser spark ignition: experimental determination of laser-induced breakdown thresholds of combustion gases”, *Opt. Commun.*, vol. 175, pp. 419-423, 2000.
[3] S. Brieschenk, H. Kleine, S. O'Byrne, "On the measurement of laser-induced plasma breakdown thresholds", *J. Appl. Phys.*, vol. 114, 093101, 2013.
[4] J. Kiefer, J.W. Tröger, Z.S. Li, T. Seeger, M. Alden, A. Leipertz, "Laser-induced breakdown flame thermometry", *Combust. Flame*, vol. 159, pp. 3576-3582, 2012.
[5] T. W. Lee, N. Hedge, "Laser-induced breakdown spectroscopy diagnostics of combustion parameters including temperature", *Combust. Flame*, vol. 142, pp. 314-316, 2000.

7) Automatically Identification of Pure Rotational CARS Spectra Influenced by Spatial Averaging Effects

Christian Meißner[1,2], and Thomas Seeger[1,2,3]

[1] Institute of Engineering Thermodynamics,
University of Siegen,
D-57076 Siegen, Germany

[2] Centrum for Sensor Systems (ZESS),
University of Siegen,
D-57076 Siegen, Germany

[3] ITMO University Saint Petersburg,
RU-197101 Saint-Petersburg, Russia

E-Mail: christian.meissner@uni-siegen.de
Web: https://www.mb.uni-siegen.de/tts/

Abstract

Coherent anti-Stokes Raman scattering (CARS) is a very useful and powerful tool for spatially and temporally resolved temperature measurements even in technically relevant combustion systems. Such precise temperature measurements are often needed for a profound analysis of combustion processes. Even though CARS has a quite high spatial resolution, temperature gradients can occur within the small probe volume of about 1-2 mm in length and 100-150 µm in diameter, especially in turbulent flames. For such “spatially averaged” CARS spectra the evaluated temperature value is biased towards the cold temperature due to the non linear character of the CARS process [1]. Therefore, it is necessary to identify and sort out these spectra automatically to get reliable temperature information of the combustion process. Influenced spectra can then be evaluated separately by specific evaluation procedures.

For vibrational CARS “spatial averaging effects” and their influence on temperature measurements have already been investigated for different types of flames [2-5]. An evaluation procedure to automatically identify and sort out spatially averaged single shot vibrational CARS spectra from a turbulent flame has been introduced [6]. In this approach different weighting factors have been used. It has also been shown, that such spatial averaged CARS spectra can be evaluated using a library of calculated composite spectra for various proportions of hot and cold temperatures [7-8].

Also in rotational CARS spectra spatial averaging effects have already been observed [9]. It was shown, that in practical applications large thermal gradients within a small probe volume lead to significant errors in temperature values when using rotational CARS for temperature determination [10]. In Figure 1 is shown exemplary a Rotational CARS spectrum, which is influenced by spatial averaging. For more precise temperature measurements it would be helpful to automatically identify and sort out such spatial averaged spectra. Then these spectra could be evaluated in a modified evaluation procedure. Such a dual-temperature fitting (DTL) model was already presented in order to evaluate temperature and concentration information for the hot and the cold part inside the probe volume separately.

Nevertheless, up to now, an automatically identification procedure for spatial averaged pure rotational CARS spectra has not been developed. In this work, we introduce a novel method to identify and sort out single shot pure rotational CARS spectra influenced by spatial averaging to improve the accuracy of rotational CARS thermometry. This method can be combined with the DTL model in the future.

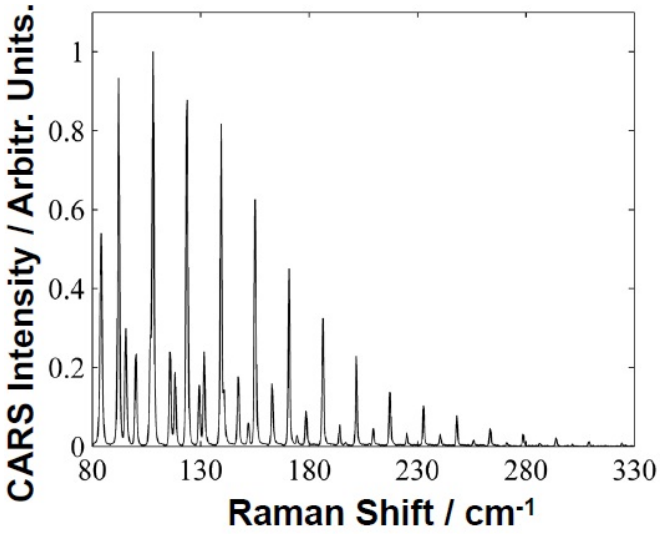

Fig.1: Pure Rotational CARS spectrum influenced by spatial averaging effects

Acknowledgements

The authors gratefully acknowledge the financial support of this work by the German Research Foundation (DFG).

References

[1] J. P. Bocquillon, M. Péalat, P. Bouchardy, G. Collin, P. Magre and J. P. Taran, "Spatial averaging and multiplex coherent anti-Stokes Raman scattering temperature-measurement error." *Opt. Lett.*, vol 13, no. 9, pp 722-724, September 1988.

[2] P. Magre, P. Moreau, G. Collin, R. Borghi and M. Péalat, "Further studies by CARS of premixed turbulent combustion in a high velocity flow", *Combust. Flame*, vol 71, no. 2, pp. 147-168, February 1988.

[3] I. G. Sheperd, F. M. Porter, and D. A. Greenhalgh, "Spatial resolution effects of CARS in turbulent premixed combustion thermometry," *Combust. Flame*, vol 82, no. 1, pp. 106-109, October 1990.

[4] J. D. Garman, and D. Dunn-Rankin, "Spatial averaging effects in CARS thermometry of a nonpremixed flame", *Combust. Flame*, vol. 115, no. 4, pp. 481-486, December 1998.

[5] J. Y. Zhu, and D. Dunn-Rankin, "CARS thermometry in high temperature gradients," *Appl. Phys. B*, vol. 56, no. 1, pp. 47-55, January 1993.

[6] T. Seeger, M. C. Weikl, F. Beyrau, and A. Leipertz, „Identification of spatial averaging effects in vibrational CARS spectra," *J. Raman Spectrosc.*, vol. 37, no. 6, pp. 641-646, June 2006.

[7] A. Thumann, T. Seeger, and A. Leipertz, "Evaluation of two different gas temperatures and their volumetric fraction from broadband N_2 coherent anti-Stokes Raman spectroscopy spectra", *Appl. Opt.*, vol. 34, no. 18, pp. 3313-3317, June 1995.

[8] T. Parameswaran and D. R. Snelling, "Estimation of spatial averaging of temperatures from coherent anti-Stokes Raman spectroscopy," *Appl. Opt.*, vol. 35, no. 27, pp. 5461-5464, September 1996.

[9] S. R. Engel, A. F. Koegler, Y Gao, D. Kilian, M. Voigt, T. Seeger, W. Peukert, and A. Leipertz, „Gas phase temperature measurements in the liquid and particle regime of a flame spray pyrolysis process using O_2-based pure rotational coherent anti-Stokes Raman scattering", *Appl. Opt.*, vol. 51, no. 25, pp. 6063-6075, September 2012.

[10] S. P. Kearny, and D. R. Guildenbecher, "Temperature measurements in metalized propellant combustion using hybrid fs/ps coherent anti-Stokes Raman scattering," *Appl. Opt.*, vol. 55, no. 18, pp. 4958-4966, June 2016.

[11] Y. Gao, T. Seeger, and A. Leipertz, "Development of temperature evaluation of pure Rotational Coherent Anti-Stokes Raman Scattering (RCARS) spectra influenced by spatial averaging effects," *Proc. Combust. Inst.,* vol. 35, no. 3, pp. 3715-3722, 2015.

8) Diode Laser-Based Standoff Absorption Measurement of Water Film Thickness in Retro-Reflection

Rongchao Pan(1), Carsten Brocksieper(1), Jay. B. Jeffries(1,2), Thomas Dreier(1), and Christof Schulz(1)
(1) Institute for Combustion and Gas Dynamics –Reactive Fluids
Faculty of Engineering, University of Duisburg-Essen,
D-47057 Duisburg, Germany
(2) High Temperature Gasdynamics Laboratory,
Department of Mechanical Engineering, Stanford University,
CA 94305-3032 Stanford, USA
E-Mail: rongchao.pan@uni-due.de
Web: www.uni-due.de/ivg/rf/

Abstract - Quantitative knowledge of liquid film thickness is relevant in many practical applications [1-3]. To optimize the performance of these systems, it is of great interest to obtain quantitative understanding of the physical processes involved in liquid film formation and its development over time. Yang et al. demonstrated diode laser-based absorption sensing of liquid film of pure water in transmission measurements using two NIR diode lasers at wavelength of 1392 and 1469 nm, which are non-resonant with water vapor transition [4]. In many practical applications, however, the liquid film is deposited on opaque surfaces where optical accessibility is only possible from one side. Many researchers have demonstrated single-ended diode laser absorption spectroscopy (DLAS) measurements of gas properties using backscattering from a retro-reflector [5-6]. In the present work, we extend this concept to absorption-based measurements of liquid-water film thickness collecting light scatted from retro-reflecting (RR) foil, which supported the liquid films.

The optical setup of the absorption-based film thickness sensor is shown in Fig. 1. The output of two DFB diode lasers operating at 1353 and 1412 nm was combined in a single-mode fiber. Light exiting the fiber was collimated into a free-space beam and 10 % of its intensity was split onto a reference InGaAs photodiode detector. The remaining 90 % was directed through the central hole of an off-axis parabolic mirror onto the liquid film spread on the retro-reflecting foil. The foil was placed onto the lower window of a temperature-controlled cuvette, and its distance from the parabolic mirror was adjusted to one RFL. The retro-reflected light was collected by the first parabolic reflector, directed towards a second off axis paraboloid and focused on a second photodetector. A beam dump was arranged to block the specular reflection. All the optical component was mounted an aluminum breadboard (grey rectangle in Fig. 1). In this case, the board was vertically fixed on the optical table. To eliminate the specular reflection after reflection of foil (SR, thin solid line in Fig.1) the incident light was adjusted of an angle of 7° by rotating the aluminum board.

Fluctuations and drifts in the intensity of the lasers are corrected for by taking the ratio at each wavelength of the measured detector signal, I_M, over the reference detector signal, I_R: I_M/I_R. For the RR beam passing twice through the liquid, the laser intensity at wavelength λ can be represented by Beer-Lambert's law as:

$$I^{\lambda}_{M,t} = (1-u) I^{\lambda}_{R,t} \frac{I^{\lambda}_{M,0}}{I^{\lambda}_{R,0}} \exp\left(-k^{\lambda}_{T_L} \frac{2\delta}{\cos\alpha}\right) \qquad (1)$$

where $I^{\lambda}_{M,t}$ and $I^{\lambda}_{M,0}$ are the measured laser intensities at the detector 2, in the presence and absence of the liquid, $I^{\lambda}_{R,t}$ and $I^{\lambda}_{R,0}$ are the corresponding intensities detected by the reference detector 1, respectively, u takes into account the non-specific losses (partial detection of the retro-reflected light, losses through reflection off surfaces, dirty optics), δ is the film thickness, α is the angle of incidence, and k is the spectral absorption coefficient of water at wavelength λ in dependence on the temperature T_L of the liquid. By taking the ratio of equations (1) for both wavelengths, the film thickness at a fixed temperature can be determined:

$$\delta = \frac{\cos\alpha}{2\left(k^{1353}_{T_L} - k^{1412}_{T_L}\right)} \ln \frac{I^{1412}_{M,t}\, I^{1353}_{M,0}\, I^{1353}_{R,t}\, I^{1412}_{R,0}}{I^{1353}_{M,t}\, I^{1412}_{M,0}\, I^{1412}_{R,t}\, I^{1353}_{R,0}}$$

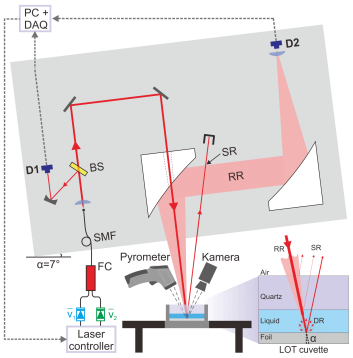

Fig.1: Optical layout of the "retro-reflection" thin-film absorption measurement. FC: fiber combiner, SMF: single-mode fiber, BS: beam splitter, D: detector, M: mirror, P: parabolic mirror, RR: retro-reflection, DR: Diffuse reflection, SR: specular reflection.

Two different types of experiments were performed: (i) to validate the technique, absorption ratios were determined in a situation with well-defined liquid layers using PTFE spacers (0.1, 0.2, 0.5, and 1 mm) between the foil and a quartz cover plate; (ii) with the quartz plate removed, free standing evaporating water films were supported on the RR foil and the film thickness was measured as a function of time during evaporation. The temperature of the cell was controlled by a thermostat.

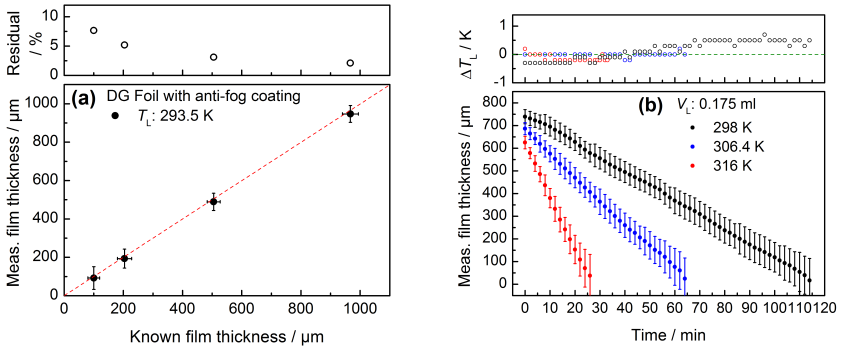

Fig. 2: (a) Measured water film thickness as a function of distance between RR foil and upper quartz window in a calibration cuvette kept at 293.5 K. (b) Temporal variation of film thickness (solid symbols) during evaporation of water films at 298 K (black points), 306.4 K (blue points) and 316 K (red points). The upper panel indicates the variation in water temperature during the experiment measured pyrometrically.

Initially, the liquid was enclosed in the cell covered with a quartz plate to validate the sensor's performance for films of known thickness at room temperature (T_L = 293.5 K). In Fig. 2a, the film thickness evaluated from the absorbance measurements is plotted versus the given separation between the upper quartz plate and the retro-reflecting foil. The dashed straight line represents the one-to-one correspondence between both values. The maximum relative uncertainty in the measured film thickness was 7.5 % for a sample thickness of 100 µm (residual in the upper part of Fig. 2a). Further experiments were performed to study the temporal thickness variation of free-standing evaporating water films at constant temperature. The experiment was initiated by dosing and mechanically spreading a proper amount of water onto the retro-reflecting foil such that the initial film thickness was about 700 µm, which for the present foil dimension was accomplished with 0.175 ml. Fig. 2b shows the measured variation of film thickness (solid symbols) as a function of time for evaporating films at 298, 306.4, and 316 K. It is observed that except for the beginning of the experiment, the film thickness decreases almost linearly with time at all three temperatures. The thickness reduction rate at the three temperatures was calculated from the slope of fitted lines to the data points and was approximately 7, 11, and 23 µm/min, respectively, for the three temperatures.

References

[1] E. Kull, G. Wiltafsky, W. Stolz, K. D. Min, and E. Holder, "Two-dimensional visualization of liquid layers on transparent walls," Opt. Lett., vol. 22, pp. 645-647, 1997

[2] A. Schagen and M. Modigell, "Local film thickness and temperature distribution measurement in wavy liquid films with a laser-induced luminescence technique", Experiments in Fluids, vol. 43, pp. 209-221 2007

[3] J. Gieshoff, M. Pfeifer, A. Schafer-Sindlinger, P.C. Spurk, G. Garr, T. Leprince, and M. Crocker, "Advanced urea SCR catalysts for automotive applications", Society of Automotive Engineers technical paper, 2001010514, 2001

[4] H. Yang, D. Greszik, T. Dreier, and C. Schulz, "Simultaneous measurement of liquid water film thickness and vapor temperature using near-infrared tunable diode laser spectroscopy", Appl. Phys. B, vol. 99, pp. 385-390, 2010

[5] A. Seidel, S. Wangner, and V. Ebert, "TDLAS-based open-path laser hygrometer using simple relective foils as scattering targets", Appl. Phys. B, vol 109, pp. 497-504, 2012

[6] C.S. Goldenstein, R.M. Spearrin, R.K. Hanson, "Fiber-coupled diode-laser sensors for calibration-free stand-off measurements of gas temperature, pressure, and composition", Appl. Opt., vol 55, pp. 479-484, 20

9) Advanced Combustion Diagnostic in Diesel Engines Using Emission Spectroscopy

Fabian Feldhaus[1, 2], Ingo Schmitz[1, 2], Thomas Seeger[1, 2]

[1] Engineering Thermodynamics,
Faculty IV: Science and Technology, University of Siegen,
D-57076 Siegen, Germany
E-Mail: fabian.feldhaus@uni-siegen.de
Web: www.mb.uni-siegen.de/tts/

[2] Ctr. Sensor Syst. Zess
University of Siegen,
D-57076 Siegen, Germany
Web: http://www.uni-siegen.de/zess/

Abstract – General improvement issues concerning internal Diesel combustion engines are containing efficiency enhancement and reduction of pollutants. Therefor the optimization of internal engine combustion is an ongoing process. Characteristic for exhaust gas emissions are CO_2, CO, NO_x and particulate matters like soot. Different restricting exhaust gas guidelines all over the world are increasing stringent and demonstrate the need for a further optimization of the combustion process in such small Diesel engines, where soot and NO_x emissions are a major concern. Mixture formation and flame temperature have an impact on soot formation and oxidation, as well as NO_x formation. The quantitative knowledge therefore of the related parameters is of utmost importance for an in-engine emission reduction.

For such in cylinder measurements non-intrusive optical measurement techniques are favorable. Most of these techniques have nevertheless a significant drawback since they need additional optical accesses or even optical engines. The achieved measurement results are not directly transferable to production engines due to these necessary modifications. For Diesel engines the glow plug bore could be used for an optical access. In combination with endoscopic optics this has been used for pyrometric flame temperature measurements [1]. All of these in-cylinder pyrometric flame temperature measurements were based on measuring the continuous black body radiation at two or several distinct wavelengths emitted by the soot. Nevertheless this approach, based on distinct wavelengths, is sensitive to wavelength selection, wavelength depending constants, soot properties uncertainties and possible molecular chemiluminescence [2]. The necessary wavelength depending emission was fitted by an additional fit function. With this approach the number of fit variables and therefore the uncertainty is increasing.

A new approach was shown on the IEEE meeting/Sensorica 2016, using a modular spectrally resolved emission spectroscopy based sensor system (ESS), which allows global in-cylinder Diesel engine temperature measurements without any engine head modification [3]. The wavelength depending emissivity was taken into account according to Michelsen [4]. As a result one fit parameter, the soot temperature, can be achieved by a contour fit procedure. Temperatures achieved with this sensor system in a sooting laminar premixed flame are compared to coherent anti-Stokes Raman scattering (CARS) temperature measurements. The temperature difference was found to be less than 60 K.

Here now the application of this ESS sensor system on two different productions of four cylinder 1.6 l DI Diesel engines is shown, where flame temperatures at different operation points were measured (see exemplary Fig. 1). The time interval for temperature measurements was varied between 5 °CA and 45 °CA and the engine load was between 10 Nm and 150 Nm. A direct relation between the measured combustion temperature and nitic oxides (NO_x) emissions has been observed. This is a further step in using the ESS sensor system for an on-line in-cylinder diagnostic tool for production Diesel engines.

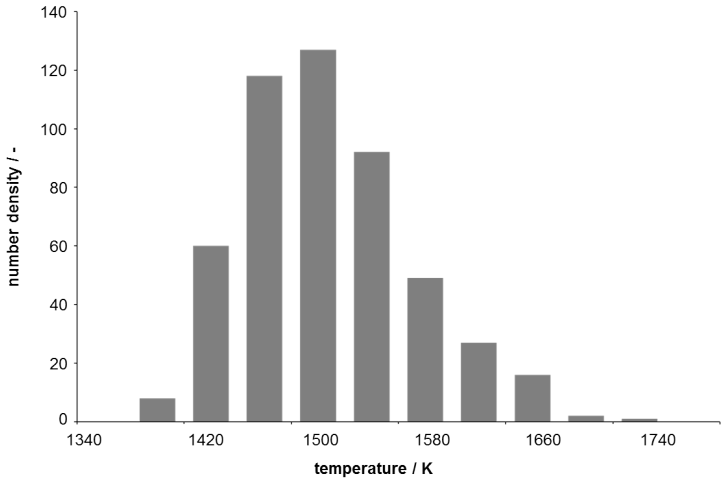

Fig. 1: Probability density distributions of ESS temperature evaluation (2000 rpm, 150 Nm, 0 °CA)

References

[1] J. Vattulainen, V. Nummela, R. Hernberg, and J. Kytölä, “A system for quantitative imaging diagnostics and its application to pyrometric in-cylinder flame-temperature measurements in large diesel engines,” *Meas. Sci. Technol.*, vol. 11, no. 2, pp. 103–119, 2000.

[2] S. di Stasio and P. Massoli, “Influence of the soot property uncertainties in temperature and volume-fraction measurements by two-colour pyrometry,” *Meas. Sci. Technol.*, vol. 5, no. 12, pp. 1453–1465, 1994.

[3] F. Feldhaus, I. Schmitz, and T. Seeger, “Emission spectroscopy based sensor developed for engine testing,” *Tech. Mess.*, vol. 84, no. 1, pp. 13–22, 2017.

[4] H. A. Michelsen, “Understanding and predicting the temporal response of laser-induced incandescence from carbonaceous particles,” *J. Chem. Phys.*, vol. 118, no. 15, pp. 7012–7045, 2003.

10) On-line Thermography Testing for Friction Stir Welded Joints

A. V. Fedorov(1,2), N. V. Tkacheva(1,2), D. S. Ashikhin(1,2), Y. O. Yakovlev(1,2), A. S. Kostyukhin(3), I. V. Berkutov(1,2)

(1) Department of Introscopy Technologies
Faculty of Laser and Light Engineering, ITMO University
Saint-Peterburg, Russia

(2) Laboratory of Non-Destructive Testing
Scientific Institution Engineering-Design Center of Space-Systems Support
Saint-Peterburg, Russia

(3) Department of Nondestructive Testing Instruments and Methods
Faculty of Automatisation Technologies
Emperor Alexander I-st. St. Petersburg State Transport University
Saint-Petersburg, Russia

E-Mail: milentax@mail.ru
Web: http://en.ifmo.ru/en/

Abstract – Nowadays the friction stir welding (FSW) process is widely used all over the world in such fields of industry as aerospace manufacturing, shipbuilding, machine construction. FSW is a solid-state joining process that uses a special tool to join two facing workpieces by compounding them and without melting the workpiece material. The advantages of FSW can be summarized as follows: low material consumption, no need for the use of shielding gas, flux, etc. Moreover, the strength of the resulting weld joint corresponds to or exceeds the strength of the base metal.

However, the process of FSW is accompanied by flawing, as well as other types of welding. These flaws include cracks, lack of penetration, cavities and others. Therefore, it is urgent to resolve the issue of quality control of connections obtained by FSW. The introduction of on-line methods of quality control can reduce the cost of a welded product and reduce the number of operations in the welding process. A possible solution to this problem is the use of a passive non-contact thermography during the FSW process (in situ) [1,2].

The report presents the results of the on-line thermography of aluminum alloy thin plate connections manufactured by FSW and the analysis of the received thermograms of flawless and defective samples. The welded joint was made in a single welding mode without changing the tool. Defective samples were obtained by varying the sample thickness, improper assembly, and removing material from the welded edges.

References

[1] I. Kryukov, S. Schüddekopf, S. Böhm, M. Mund, S. Kreling, K. Dilger, “Non-destructive online-testing method for friction stir welding using infrared thermography,” 19th World Conference on Non-Destructive Testing (WCNDT 2016), June 13 – 17, Munich, Germany, 2016.

[2] L. M. Serio, D. Palumbo, U. Galietti, L. A. C. De Filippis, A. D. Ludovico: “Monitoring of the friction stir welding process by means of thermography,” Nondestructive Testing and Evaluation, Vol. 31, Issue 4. pp. 371-383. 2016.

[11] In-situ Characterization of Bulk Goods Using Electrical Capacitance Tomography

Alice Fischerauer[(1)], Christoph Kandlbinder[(1)], and Gerhard Fischerauer[(1)]

[(1)] Chair of Measurement and Control Engineering,
Faculty of Engineering Sciences, University of Bayreuth,
D-95440 Bayreuth, Germany

E-Mail: alice.fischerauer@uni-bayreuth.de
Web: www.mrt.uni-bayreuth.de

Introduction – For the production of cast components at a foundry moulds made of sand are used. These “form sands” (shaping of the outer surfaces) or “core sands” (moulding of cavities) consist of special raw sands mixed with binding agents that influence the tensile and compressive strength as well as the temperature behavior of the mould. In order to achieve a high quality of the cast components the sand mixture has to remain stable throughout the production cycle. Since foundries nowadays aim at waste reduction and raw material conservation as well as cost cutting, the form sands get reprocessed and recycled into the production. This recycling process however changes the properties of the sand mixture and makes it necessary to decide whether it is still usable [1, 2].

Usually the sand’s characteristics are being tested by sampling extraction at pre-defined intervals. This has the disadvantage that no in situ monitoring of the sand quality takes place over the cross section of the delivery pipe during conveyance of the material.

Method – Some of the sand’s characteristics of interest in this context are the grain size distribution, the material composition and the sand moisture. Since these qualities are reflected in the electrical properties of the form sand, each batch shows a specific impedance spectrum and a certain spatial distribution of its relative permittivity over the monitored cross section.

This study describes the examination of bulk materials by means of electrical capacitance tomography (ECT). ECT is a technique which uses a multi-electrode sensor enclosing the object of interest. In industrial application this very often means a pipe containing two or more materials of different permittivity. From the measurement of the capacitances of all possible pair-by-pair combinations of the sensor electrodes a cross sectional image of the material distribution in the vessel can be reconstructed [3, 4, 5].

Bulk materials such as foundry sands consist of grains with a certain bandwidth of diameters but equal permittivity. Depending on the type of material conveyance in the pipe and the mean particle size the bulk exhibits a certain particle density per area. Embedding an ECT-sensor into the pipe wall will provide continuous measurement data without penetrating the process flow from which it is possible to perform back calculations to the density and permittivity of the material. Even layers of different densities can be recognized to a certain extent by image reconstruction from the capacitance measurements. As an accompanying measure an impedance spectrogram is obtained from the material that gives further knowledge about its chemical composition and electrical conductivity and thereby possibly of its degree of moisture.

Simulations – In order to determine the influence of the scatter of the particle distribution over the cross-sectional area on the scattering of the capacitance values of the ECT-sensor a variance analysis was carried out. The capacitances of a sensor consisting of 12 electrodes circularly arranged around a number of random distributions of particles were calculated using the FEM software Ansys. It could be shown that the standard deviation of the capacitances of directly adjacent electrodes in combination with the values of opposing electrodes permits calculation of the density and the permittivity of the particle distribution.

Further simulations were conducted to determine to what extent it is possible to distinguish layers of different density inside the bulk material. For this purpose the calculated capacitances effected by stratified phantoms were used for image reconstruction with projected Landweber iteration algorithm [3]. From the resulting permittivity distribution information about the layer thickness and density then could be obtained using integrational methods (Fig. 1).

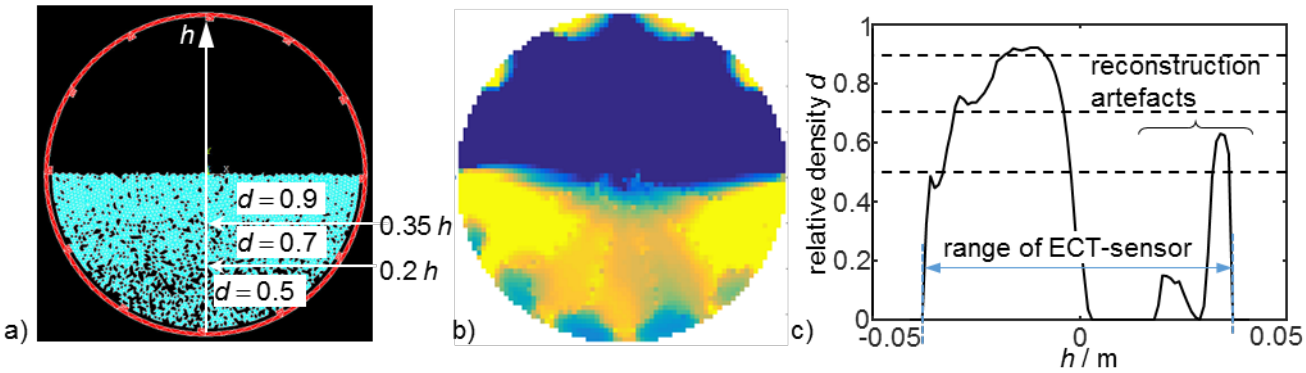

Fig.1: a) Stratified bulk phantom with layers of different material density inside a ECT-sensor with 12 electrodes; b) image reconstruction from simulated capacitances; c) horizontal sum of the values assigned to the image pixels, the sum indicates the density of the layers of the bulk material.

Measurements – The impedance spectra of samples of several form sands and core sands have been measured over a frequency range of 20 Hz to 100 kHz (Fig. 2). The samples included different unused quartz sands, refurbished quartz sands and chrome sand, also unused and recycled. The measurements show that the sand types can be clearly distinguished from one another. Special details of the spectra give additional information about the chemical composition of the sands.

The same samples have been also examined using a ECT-sensor specially developed for that purpose. The sensor comprised twelve electrodes each of area 18x100 mm^2 and had a diameter of 78 mm. The measurements were utilized for extracting electrical properties of the samples and image reconstructions of stratified fillings of the sensor.

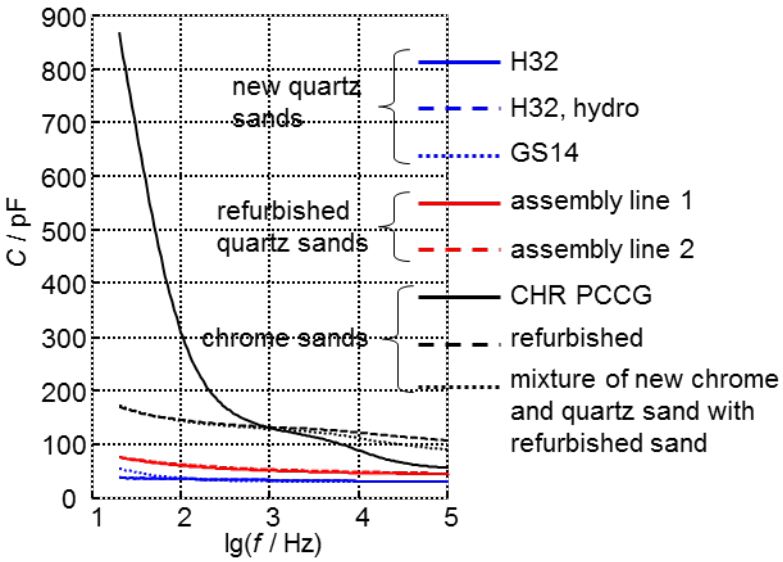

Fig.2: Capacitance of sand samples (type as indicated in the figure) extracted from the measured impedance spectra.

References

[1] R. Carlsson, P. Nayström, "Solid Waste Sand re-use from Swedish Metal Casting," *Procedia Environmental Sciences,* vol. 35, pp. 624 – 628, April 2016.

[2] I. Narasimha Murthy, J. Babu Rao, "Investigations on Physical and Chemical Properties of High Silica Sand, Fe-Cr Slag and Blast Furnace Slag for Foundry Applications," *Procedia Environmental Sciences,* vol. 35, pp. 583 – 596, April 2016.

[3] W. Q. Yang and L. Peng, "Image reconstruction algorithms for electrical capacitance tomography," *Meas. Sci. Technol.*, vol. 14, pp. R1-R13, 2003.

[4] F. Wang, Q. Marashdeh, L.-S. Fan and W. Warsito, "Electrical Capacitance Volume Tomography: Design and Applications," *Sensors*, vol. 10, pp. 1890-1917, March 9, 2010.

[5] Y. Li, W. Yang, Z. Wu, D. Tsamakis, Ch. Xie, S. Huang and Ch. Lenn, "Gas/oil/water Flow Measurement by Electrical Capacitance Tomography," *IEEE International Conference on Imaging Systems and Techniques (IST)*, Manchester, UK, 16-17 July, 2012.

12) Measuring and Optimizing Efficiency of Electrostatic Energy Harvesters for Sensor Applications

Bjoern Bieske(1), Gerrit Kropp(1), and Alexander Rolapp(1)

(1) Industrielle Elektronik und Messtechnik,
IMMS Institut für Mikroelektronik und Mechatronik-Systeme gemeinnützige GmbH,
D-98693 Ilmenau, Germany

E-Mail: bjoern.bieske@imms.de
Web: www.imms.de

Abstract – Energy harvesting is one possibility to power up small sensor devices using ultra low power technologies. Here is the focus on electrostatic energy harvesters using a variable capacitor C_{var} as a charge pump to convert mechanical into electrical energy [1,2,3,6]. These capacitors can be implemented as discrete devices or as micro electromechanical systems (MEMS) which can be integrated on a chip.

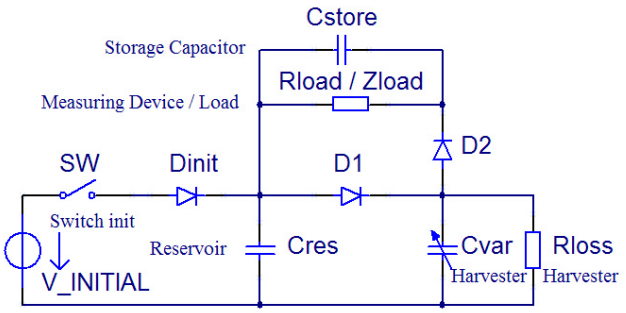

Fig.1: New improved topology of energy harvesting circuit using a floating load for recharge and measurements

The variable capacitance can be achieved by changing the distance or overlap of electrodes. Different setups and topologies are known from literature [2,4]. A new topology to characterize the harvested energy of the intrinsic harvester circuit even if there are resistive losses in the variable capacitor C_{var} has been developed. Since the currents harvested are in the range of nA, it is difficult to set up measurements with no influence on the harvesting process. The new improved topology guarantees the autonomous operation of the electrostatic harvesters. We determine the values of energy which could be harvested and the energy delivered to a resistive load. The efficiency of the harvesting process depends on the parameters of the harvester itself and the properties of the load. This new topology was implemented as a stand alone measurement device [5]. Different types of harvesters were characterized and a strategy to optimize their efficiency was developed.

We assume the basic function of electrostatic energy harvesters as known. The starting point of the harvesting process is a reservoir C_{res} charged to an initial voltage V_initial. The charges are transferred to the variable capacitor C_{var} and pumped up to a higher level of voltage and energy [6]. The voltage is rising when the capacitance is lowered according to $U = Q / C$ (1). These charges are stored in the capacitor C_{store} and delivered to the load. The reservoir C_{res} has to be recharged by a fly back circuit. The harvesting process has been described as a loop in the QV diagram (charge vs. voltage) of the harvester in several papers. The area within the QV trace of one cycle should be the harvested energy. We will show that this is the maximum energy which can be harvested in theory and under optimum conditions only. But in practice we will get far less energy.

We developed a new improved topology with floating resistive fly back to ensure a proper functionality of the harvesting process at any time. The reservoir C_{res} is recharged by the charging current of the storage capacitor C_{store} immediately. So the average voltage of the reservoir across C_{res} remains constant at the value of V_initial. The fly back resistor can be used as load resistance R_{load} or as measuring device to determine the energy harvested.

The voltage across R_{load} has to be measured at very high impedance. Then energy stored in C_{store} can be calculated as $E = ½ * C * U^2$. Resistive losses in the variable capacitor of the harvester C_{var} will not influence the measurement result. The electrical power is calculated by voltage and current measurements using a load resistor dissipating the harvested energy: $P = I * U$. Large differences are to be seen between measured and predicted values of energy harvested using the QV cycle as mentioned above. Simulations using LT-Spice are confirming these effects comparing the values of energy in the harvester and storage capacitor, and delivered power to the load resistor R_{load}.

The electrostatic harvester is generating a characteristic current per cycle. This current depends on the initial voltage V_initial and the maximum and minimum capacitance of C_{var}. The output parameters of the harvesting circuit (voltage, energy and power) depend on this typical harvester current but also on the values of the external components C_{store} and R_{load}. Since the harvester acts as a current source its internal resistance (R_i) can be estimated to about 1 GOhm, based on our demonstrator generating typical harvester current of 100 nA using an initial voltage of V_initial = 100 V. If the external load resistance (R_L) is in the range of about 10 MOhm there is a large mismatch between R_L and R_i, resulting in a very low power efficiency of about 1 % only.

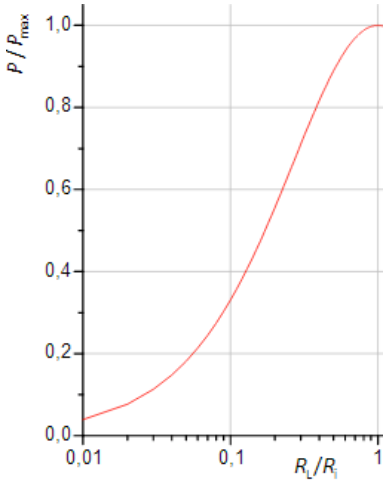

Fig.2: Loss due to mismatch R_L/R_i

The purpose of this work is to create a measurement methodology to measure the harvested energy and the usable power of electrostatic energy harvesters. Based on those measurements a strategy to optimize the efficiency is derived. The harvester's current is the main parameter for its internal resistance and the harvested energy. The main question is: How can we increase this current [7], depending on the values of the harvesting variable capacitor, cycle frequency and initial voltage. Another approach is to design a buck converter of high efficiency especially at low currents to convert high voltages into current delivered to load.

A new methodology based on improved topology for more accurate characterization of electrostatic energy harvesters has been developed [5]. The different types of harvesters can be characterized by a set of parameters. The main parameter is the charge pump current harvested per cycle based on the pre-charge voltage V_initial and the ratio of $C_{var\text{-}max}$ / $C_{var\text{-}min}$. Higher efficiencies of electrostatic harvesters can be achieved by increased typical current in combination with a high efficient buck converter for low currents and high voltages. Possible applications are sensors in shoes developed by FhG IZM [8].

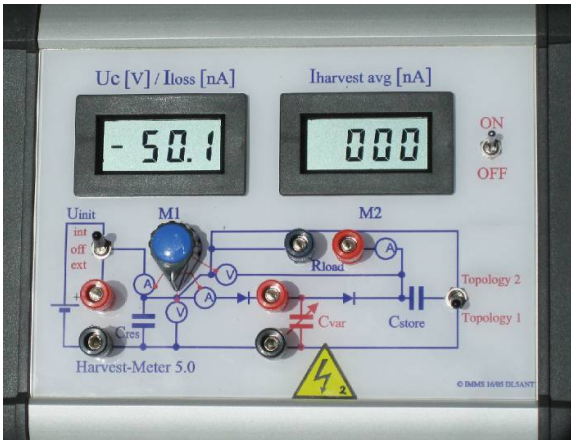

Fig.3: Implemetation of "Harvest Meter 5.0"

References

[1] D. Galayko, R. Pizarro, P. Basset, A. M. Paracha, „AMS modeling of controlled switch for design optimization of capacitive vibration energy harvester", *Behavioral Modeling and Simulation Workshop, BMAS 2007*, S. 115-120 IEEE International, San Jose, 20/09/2007

[2] H. R. Florentino; R. C. S. Freire; Alan V. S. Sá; C. Florentino; D. Galayko, „Electrostatic vibration energy harvester with piezoelectric start-up generator," *2011 IEEE International Symposium of Circuits and Systems (ISCAS)* S. 1343-1346, DOI: 10.1109/ISCAS.2011.5937820

[3] Elena Blokhina; Eoghan O'Riordan; Orla Feely; Dimitri Galayko, „Nonlinearities in electrostatic vibration energy harvesters: A review using the example of a charge pump conditioning circuit ", 2014 *IEEE International Symposium on Circuits and Systems (ISCAS)* S. 2604-2607, 1-5 June 2014, DOI: 10.1109/ISCAS.2014.6865706

[4] S. Meninger, J. Mur-Miranda, R. Amirtharajah, A. Chandrakasan, J. Lang, "Vibration-to-electric energy conversion", IEEE Transactions on Very Large Scale Integration Systems, vol. 9, no. 1, pp. 64–76, 2001.

[5] B. Bieske, G. Kropp, A. Rolapp, "Testing Electrostatic Energy Harvesters: A New Topology for Accurate Characterization," *14th International Multi-Conference on Systems, Signals & Devices, Marrakech,* pp. 65-77, March 2017.

[6] D. Galayko; A. Dudka; A. Karami; E. O'Riordan; E. Blokhina; O. Feely; Ph. Basset, „Capacitive Energy Conversion With Circuits Implementing a Rectangular Charge-Voltage Cycle—Part 1: Analysis of the Electrical Domain", *IEEE Transactions on Circuits and Systems I: Regular Papers 2015*, Volume: 62, Issue: 11 S. 2652 – 2663, 2015.

[7] A. C. M. de Queiroz, "Electrostatic vibrational energy harvesting using a variation of Bennet's doubler," *53rd Midwest Symposium on Circuits and Systems, Seattle, USA*, pp. 404-407, August 2010.

[8] R. Hahn, IZM, „Energy harvesting for wearable applications", *Project Meeting MATFLEXEND, Wien Sept. 16, 2016.*

13) Interface Circuit for Measurement of Small Capacitance Changes in Capacitive Sensor

Ahmed Fendri[1,2], Olfa Kanoun[1], and Hamadi Ghariani[2]

[1] Professur Mess- und Sensortechnik, Technische Universität Chemnitz, Germany
[2]National School of Engineers of Sfax, Tunisia

Email: ahmedfendri@s2013.tu-chemnitz.de

Abstract – The circuit described in this paper is a simple and accurate capacitance to voltage converter used for the measurement of small capacitance changes in capacitive sensors. The circuit consists mainly of a capacitance transducer, a demodulator and a low pass filter. The output voltage of the circuit changes linearly with the change of the sensor capacitance. The measurement error is less than 0.01 % around the reference capacitance while it gradually increases moving away from the reference capacitance value. A multi-reference capacitances system is proposed in order to provide more measurement accuracy. The effects of the stay capacitance as well as the dielectric losses are studied. The circuit shows good immunity to stray capacitance while it is sensitive to the dielectric losses.

Introduction

The circuit proposed by S. M. Huang [1], was used to measure small capacitance changes. It is based on transformer ratio arm bridge techniques which provide high sensitivity and very low baseline drift. The circuit is used to measure only capacitance changes without considering the dielectric losses that exist in capacitive sensors. Also it includes only one reference capacitance which makes the measurement range very limited.

In this work a multi-reference measurement circuit is proposed. The measurement accuracy is high for capacitance values close to the reference capacitance for that a multi reference capacitances system is used in order to maintain high accuracy measurement in wide measurement range. The effect of the losses on the measurement results was also investigated.

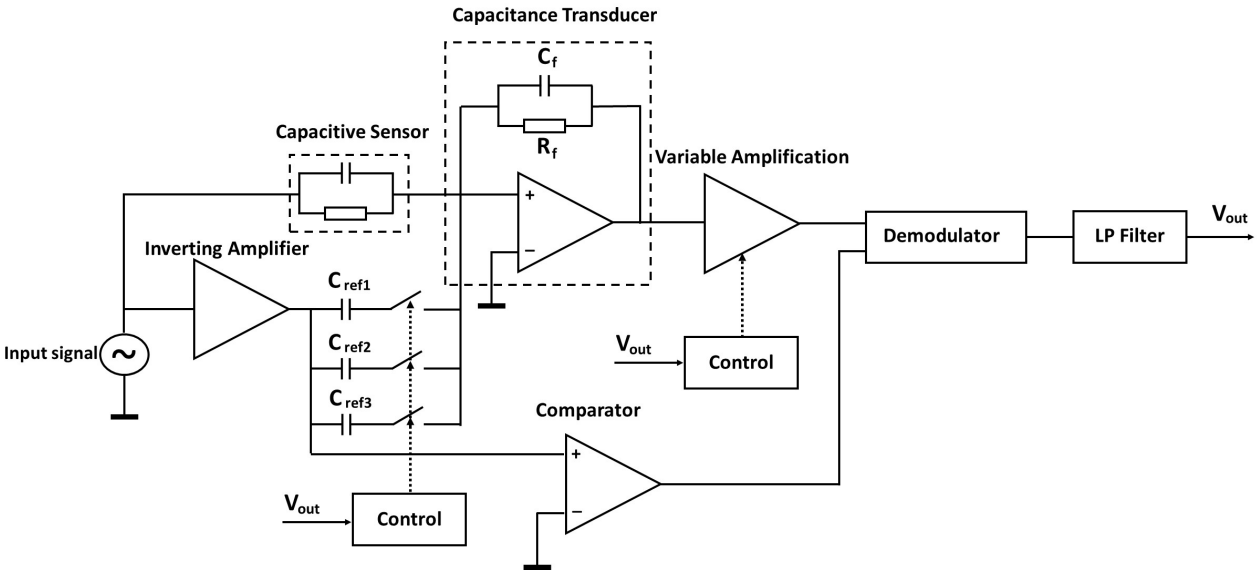

Fig.1: Improved multi-references measurement circuit based on the capacitance to voltage conversion.

Description of the measurement circuit

The circuit is excited by a sinusoidal signal at 10 kHz. The sensor capacitance C_x and the reference capacitance C_{ref} provide two voltages of opposite phase and different amplitude depending on the values of the capacitances. The unbalanced current is detected and converted by the capacitance transducer to a sinusoidal voltage. The output voltage is amplified and rectified using an analog demodulator and a low pass filter so that the output voltage V_{out} is a DC voltage proportional to the value of the measured capacitance. The demodulator uses the input signal as a reference signal and multiplies it with the voltage provided by the transducer. The output voltage of the demodulator is a rectified signal with a frequency 20 kHz. A low pass filter is used to get a DC voltage representing the average value of the demodulator output [1].

Simulation Results

The voltage V_{out} is ideally null in case of $C_x = C_{ref}$ and it increases linearly when C_x increases. According to literature and simulation results the accuracy of the measurement is high for capacitance values near the reference capacitance while it decreases for values away from the reference capacitance (Fig. 2). It is possible to measure capacitance with an accuracy of 0.1% in the range between 70 pF and 650 pF using 3 reference capacitances. Three measurements should be done and the closest reference capacitance to the measured capacitance should be used. The reference capacitance which provides the lowest V_{out} is the capacitance to be selected. After selecting the reference capacitance, the output voltage of the transducer can be amplified in order to increase the signal/noise ratio.

In the real case where the effect of the parallel resistance is not neglected, the circuit is no more stable and accurate for resistance values lower than 10 MΩ.

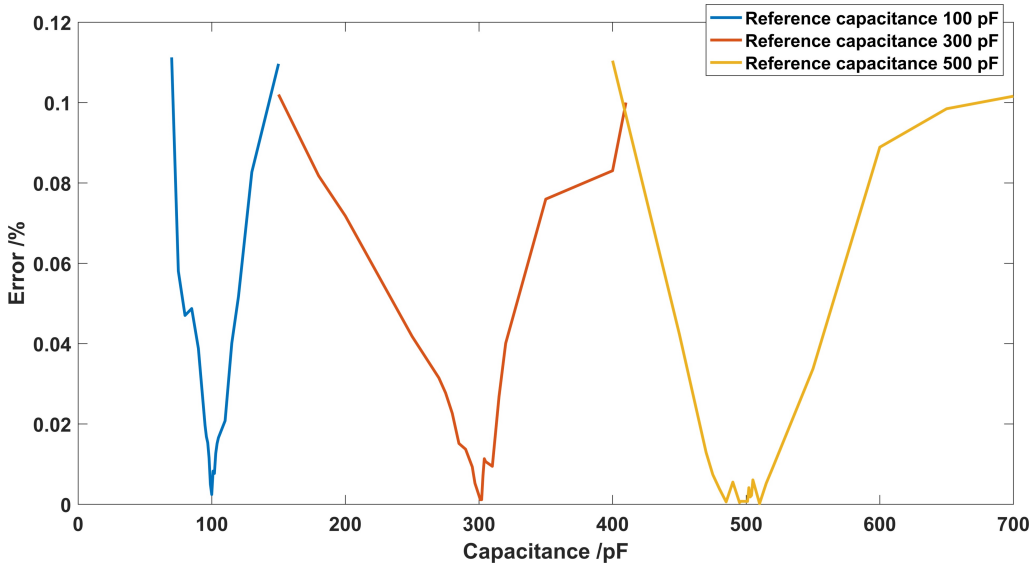

Fig.2: Measurement Error for difference reference capacitance values

References

[1] S. M. Huang, C. G. Xie, A. L. Stott, R. G. Green, M. S. Beck, ''A capacitance-based solids concentration transducer with high immunity to interference from the electrostatic charge generated in solids/air two-component flows'', *Transactions of the Institute of Measurement and Control*, volume 10, pp. 98-102.

14) Adaptive Power Supply for self-sufficient Measurement Technology

Mario Mösch[(1)], Gerhard Fischerauer[(1)]

[(1)] Chair of Measurement and Control Systems
Faculty of Engineering, University of Bayreuth,
D-95447 Bayreuth, Germany

E-Mail: mario.moesch@uni-bayreuth.de
Web : www.mrt.uni-bayreuth.de

Introduction – A world more and more cross-linked requires a growing usage of measurement and sensor techniques. A Smart Home intelligence needs the temperature data of living rooms and presence data of persons, cars the actual tire air pressure and industrial environments a good deal more. Wireless sensor nodes are the solution to many of these examples, having their own energy supply, which are mostly batteries with a finite endurance. With a fast growing number of sensors an increasing stress on environment and resources is to be expected. A way out of this is energy harvesting, which means the conversion, storing and usage of free environmental energy.

Method – Vibration energy is widely available, especially in the industrial or automobile sector. An energy harvester is a spring-mass-damping system with a determined resonance frequency depending on spring stiffness and mass. Harvesting energy is only possible, if the vibrational frequency, which affects the harvester from the outside, is close to the system's resonance frequency. The bandwidth fulfilling this criterion however may be quite small. So a changing engine speed might prevent that the energy harvester reaps energy at all. Self-adapting systems adjusting their resonance frequency towards the actual external vibrational frequency can avoid this. An example for such an adaption technique is a cantilever harvester whose axial load is changed by modifying the distance between the cantilever tip and an outer permanent magnet [1, 2].

The energy for this adaption has to be taken out of the system's own energy storage. This leads to the question whether the energy harvested by the system is larger than the energy needed to adapt the system to the appropriate resonance frequency. The present study considers systems which do not need any further energy to maintain the adaptive condition (so-called passive adaption) after shifting the resonance frequency towards its optimum. Already it has been shown that an active adaption (energy is permanently needed to maintain the adaption) leads to a negative energy balance of the harvester [3]. In order to assess whether a system utilizing passive adaption ultimately harvests energy in a changing environment, it has to be investigated, if the increase of output energy ΔW_{out} over the period τ during which the new vibrational frequency f_{a} is stable, surpasses the energy W_{ad} needed for the adaption from the former frequency f_{r} to f_{a} :

$$\frac{\Delta W_{\mathrm{out}}}{W_{\mathrm{ad}}} = \frac{\Delta P_{\mathrm{out}} \cdot \tau}{\int_{f_{\mathrm{r}}}^{f_{\mathrm{a}}} \tilde{W}_{\mathrm{ad}}(f)\,\mathrm{d}f} \overset{!}{>} 1. \qquad (1)$$

Here ΔP_{out} denotes the average output power during τ and $\tilde{W}_{\mathrm{ad}}(f)$ is the energy per frequency required for adaption.

This study investigates which requirements are to be set on the environment so that a self-adaptive harvester works efficiently. Also it gets discussed how the harvester's adaption mode could be changed to make the system work properly even under unfavorable conditions. For that a long-term operation is considered under the assumption that the external vibration frequency f_{a} stays constant over a fixed period τ before it takes on another value. Furthermore it is assumed that the harvester adapts its resonance frequency f_{r} instantly to every new frequency f_{a} and produces a constant out-

put power P_{out} at all frequencies. The average adaption energy $\overline{W_{ad}}$ then depends linearly on the adaption range Δf due to $W_{ad}^{0}(f)$ being constant. To ensure stable operation of the harvester usually an energy storage device is integrated into the system. To reach a positive power P_s that is able to feed the storage device, the harvester's output power P_{out} has to be greater than the sum of the power P_V consumed by the system and its connected load (microcontroller, sensor node, etc.), and the average adaption power $P_{ad} = \overline{W_{ad}}/\tau$:

$$P_s = P_{out} - P_V - \frac{\overline{W_{ad}}}{\tau} \overset{!}{\geq} 0. \tag{2}$$

It can be shown, that a fast change of f_a meaning a short period τ needs too much adaption power. Fig.1 depicts this issue: for τ smaller than a critical period τ_0 the adaption power is too high and P_s turns negative. A common approach to reach $P_s \geq 0$ is to supply the consumer, for instant a sensor node, in a pulsed mode. Since this is not always possible we propose a modification of the adaption operation in order to reduce the adaption power. In this approach the frequency bandwidth of the adaption gets narrowed. That produces a higher reduction of P_{ad} than it costs output power P_{out}, because in addition also the average adaption range Δf sinks. So frequencies f_a lying outside of the narrower band width are not considered by the system. This operation condition has to be held until P_{out} or τ rises.

All methods have one issue in common: a high amount of information is needed about the environment and a strategy has to be available to estimate before an adaption the expected energy profit. Specifically that means an assessment of the possible output power P_{out} and the harvesting period τ.

Summary – In summary a self-adaptive energy harvester is an option with an environment justifying its use and with a clear knowledge and predictability of the vibration. Further a self-adaptive system with a maximized adaption band width is mostly not preferable because of the disproportionally high increase of adaption energy.

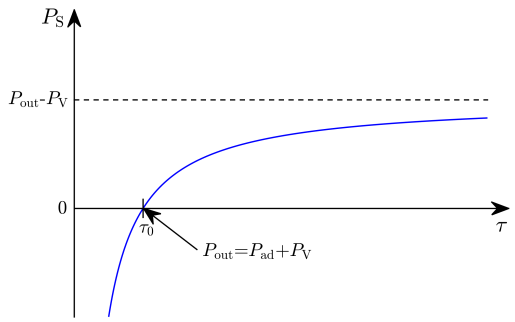

Fig.1: The remaining Power P_s depends on the time constant τ. The more often an adaption is carried out, the lower is P_s. The critical period is τ_0. A continuously working system needs $P_s > 0$.

References

[1] D. Zhu et al, "Design and experimental characterization of a tunable vibration-based electromagnetic micro-generator," *Sensors and Actuators A*, vol. 158, pp. 284-293, 2010.

[2] D. Zhu et al, "Strategies for increasing the operating frequency range of vibration energy harvesters: a review," *Meas. Sci. Technol.,* vol. 21, 022001, 2010.

[3] S. Roundy, Y. Zhang, "Toward self-tuning adaptive vibration based micro-generators," *Proc. SPIE, Smart Structures, Devices Syst. II,* vol. 5649, pp. 373–384, 2005.

15) Energy Efficient Routing based on Cooperative Communication for Wireless Sensor Network

Sabrine Khriji[1, 2], Dhouha El Houssaini[1,2], Olfa Kanoun[2], Inés Kammoun Jemal[1]

[1] LETI Lab, University of Sfax, National Engineering School of Sfax, Tunisia

[2] MST Lab, Technischen Universität Chemnitz, Germany
E-mail: olfa.kanoun@etit.tu-chemnitz.de

Abstract

In order to reduce the energy consumption and increase the lifetime in wireless sensor networks, a Fuzzy based Energy Aware Unequal Clustering algorithm (FEAUC) was proposed. It involved a cluster head selection, intra-clustering and inter-clustering routing protocols. To enhance more this algorithm, an energy efficient cooperative communication method is used. Indeed, relay nodes selected by the cooperation of adjacent cluster heads along with their cluster members can prevent long haul transmissions of cluster heads. A comparison with the existed FEAUC protocol shows that the proposed algorithm achieves better results in term of energy efficiency and network lifetime.

Algorithm description

The proposed method is based on our previous work, a Fuzzy based Energy Aware Unequal Clustering algorithm (FEAUC) [1]. To increase energy efficiency, we proposed an energy efficient protocol which combines the both cluster based approach and cooperative diversity techniques [2] which represent a potential candidate to increase the transmit energy efficiency in wireless sensor networks. Since the energy efficiency of FEAUC is proved in [1], we apply the clustering and routing method of our FEAUC as the clustering and routing method for the new algorithm. Figure 1 briefly explains the procedure of the new approach. So, in order to reduce the transmission range of cluster heads (CHs), when performing intercluster transmission, a selected relay node can cooperate with its CH.

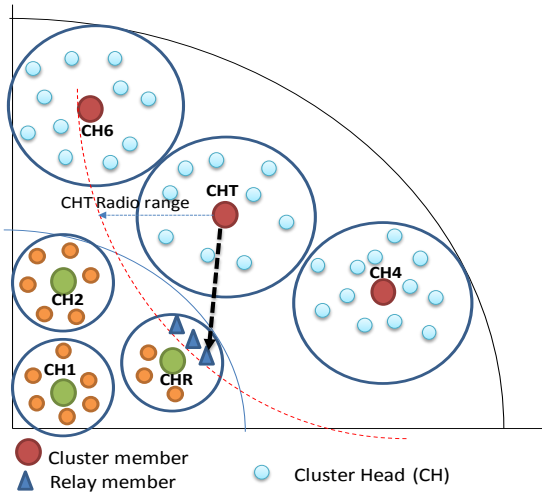

Fig.1: Relay selection

Assume CH_T is a transmitting cluster head node with a residual energy $E_{res}(CH_T)$ and a CH_R is a receiving cluster head node from CH_T with a residual energy $E_{res}(CH_R)$.

If $E_{res}(CH_T) > E_{res}(CH_R)$, the CH_T broadcasts relay candidate signal packet within the distance between CH_T and CH_R. Otherwise, CH_T transmits its data directly to CH_R without using relay node.

CH_T broadcasts relay candidate signal packet within the distance between CH_T and CH_R. All nodes of cluster R which receive a relay candidate signal packet from cluster T join the relay selection process and become a relay candidate for CH_T. A relay candidate r_j calculates its chance to be a final relay for CH_T by dividing its residual energy E_{res} by its distance to CH_T. Then, the node r_j transmits its chance to CH_T. The CH_T chooses the relay candidate with the maximum chance as the node that transmits its packet to CH_R.

Simulation Results

The network scenario consists of 100 nodes randomly deployed in 200 m × 200 m area and a Base Station at the centre (0,0). The initial energy of all nodes is 1 J. For node's energy dissipation, the model [3] is used with radio parameters E_{elec}=50 nJ/bit; ε_{fs}=10 pJ/bit/m^2 ; ε_{mp}=0.0013 pJ/bit/m^4.

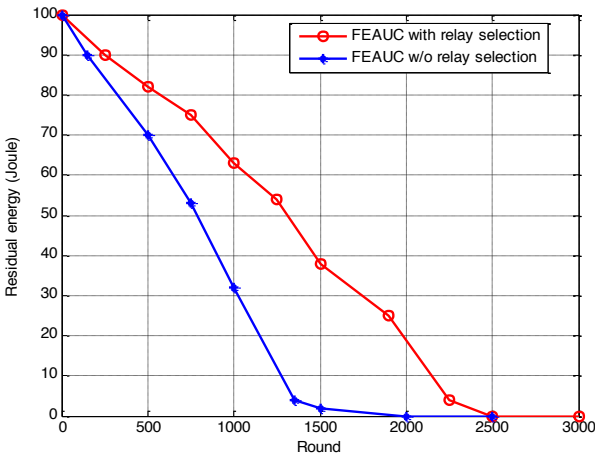

Fig.2: Total residual energy of the network over rounds

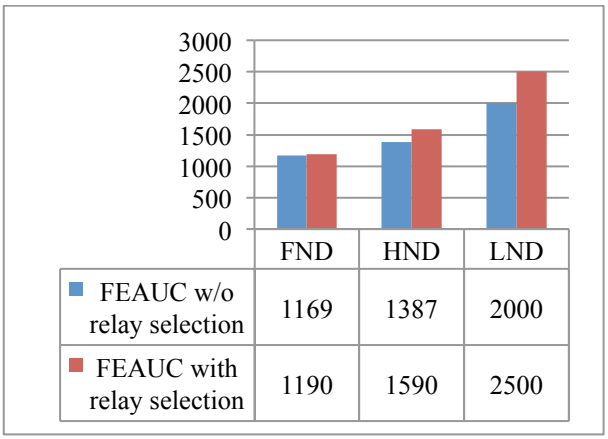

	FND	HND	LND
FEAUC w/o relay selection	1169	1387	2000
FEAUC with relay selection	1190	1590	2500

Fig.3: Comparison of network lifetime

The proposed method demonstrates superior performance in term of energy consumption and also in term of first node dead (FND), half of nodes dead (HND) and last node dead (LND) compared to the existing FEAUC. As a conclusion, the use of cooperation between a CH and its appropriate relay can reduce the transmission range of CHs and also save energy consumption of the network.

References

[1] S. Khriji, D. El Houssaini, C. Viehweger, and O. Kanoun, "A Fuzzy based Energy Aware Unequal Clustering Protocol for Large Scale Wireless Sensor Networks", *IEEE Workshop and SENSORICA 2016 16-17.06.2016*, Mülheim, Germany.

[2] Y. Wu, W. Liu, and K. Li, "Power allocation and relay selection for energy efficient cooperation in wireless sensor networks with energy harvesting," *EURASIP J. Wirel. Commun. Netw.*, 26, pp. 1–11, 2017.

[3] S. Gajjar, M. Sarkar, and K. Dasgupta, "FAMACRO: Fuzzy and Ant Colony Optimization based MAC/Routing Cross-layer Protocol for Wireless Sensor Networks", *International Conference on Information and Communication Technologies* (ICICT 2014).

16) RSSI Based Clustering Algorithm for Wireless Sensor Network Localization in Large Scale

Dhouha El Houssaini[(1)(2)], Sabrine Khriji[(1)], Kamel Besbes[(2)] and Olfa Kanoun[(3)]

[(1)]National School of Engineer of Sfax, University of Sfax, Tunisia
[(2)] Microelectronics & Instrumentation Lab, Faculty of Science of Monastir, Tunisia
[(3)] Electrical measurement and sensor technology Lab, TU Chemnitz, Germany

E-Mail: houssaini.dhouha@gmail.com

Abstract

Localization is a key feature process of wireless sensor network. It consists of collecting information from the network to determine the geographic coordinates of nodes. Unfortunately, due to large number of nodes in the network, the localization process becomes difficult, complex and energy consuming. Therefore, a solution is to organize the nodes in regular patterns called clusters, where in each cluster a reference node is selected as the head in a way to reduce the communication overhead during the localization process. The proposed clustering algorithm is applied our previous localization technique based on the on the RSSI.

Proposed Clustering algorithm

To improve the localization accuracy while maintaining low energy consumption level a clustering phase is added to the previous developed localization algorithm (Figure 1)[1]. The proposed clustering algorithm is composed of two phase; cluster definition phase and cluster head election phase.

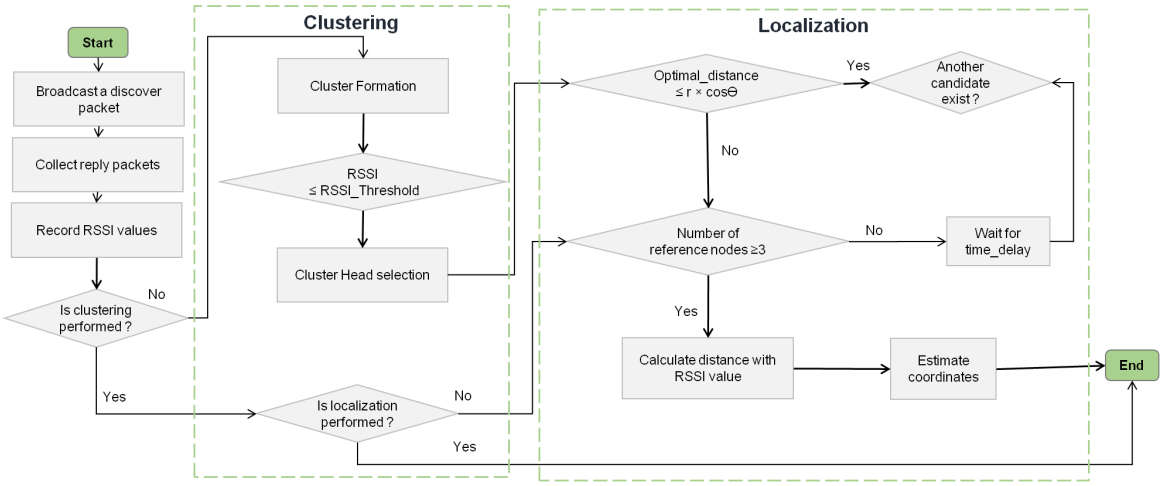

Figure 1: Flow chart of the proposed RSSI based clustering localization algorithm

During the cluster definition phase, some important assumption should be respected such as the choice of the cluster's shape, the maximum and minimum number of nodes in each cluster and the coverage [2][3]. Actually these parameters are related in a way to assure a full coverage and connectivity. For better results the shape of the cluster is dependent of the communication range of the nodes. Theoretically, compared with other structures, hexagonal structure (honeycomb) satisfies these specifications where it provides maximum distance between edges while maintaining the coverage and minimizing effects of overlapping [4]. The covered area by each node is $3\frac{\sqrt{3}}{4}R^2$ and the total required number of nodes per coverage area A is $\left\lceil \frac{4}{3\sqrt{3}R^2} A \right\rceil$ (Figure 2).

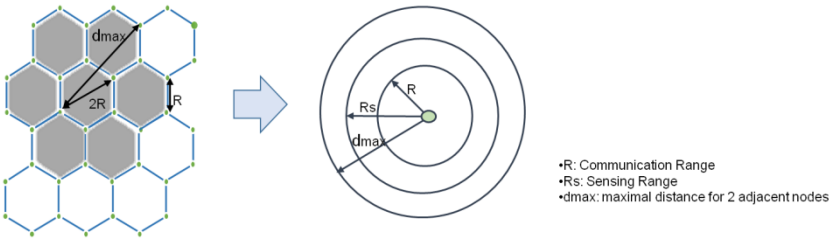

Figure 2: Optimal distance for assuring coverage between nodes

Once the clusters are formed, a cluster head selection process starts. The cluster head is necessary a reference node with respect to the received signal strength value. To elect a reference node as cluster head two conditions should be preserved, where Θ is the angle of the transmission line (equation 1 and 2). The RSSI threshold is decided in a way to guarantee that the communication range is smaller than the sensing range.

optimal distance ≤ r cosΘ 1) RSSI ≤ RSSI_Threshold 2)

Simulation results

To understand the efficiency of the algorithm a comparison between the results obtained from the previous localization algorithm and the results obtained after applying a clustering process is presented in the figure 3. These results make it clear that the clustering improve the coverage up to 80 % covered nodes with the use of three reference nodes. For the communication the number of circulating messages is reduced therefore the energy is minimized, for example for sending 60 bytes only 0.8 J were dissipated instead of 1 J.

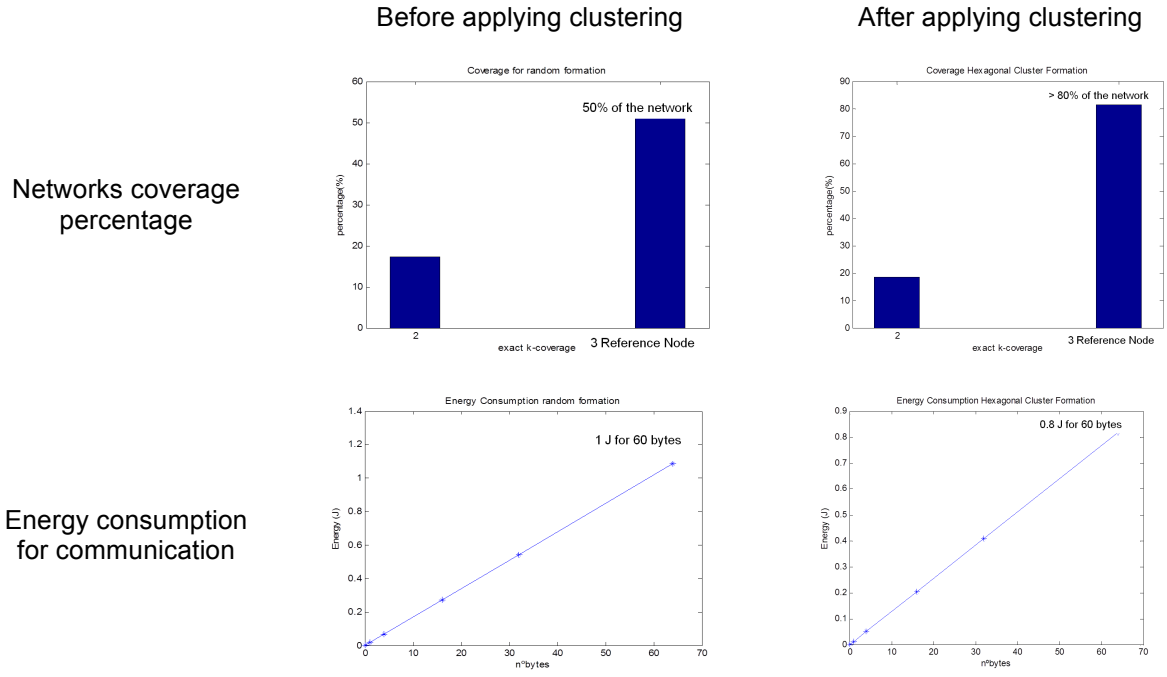

Figure 3: Simulation result for 100 nodes deployed in 100 × 100 m² network

References

[1] D. El Houssaini, S.Khriji, C. Viehweger, O. Kanoun, "An improved RSSI localization technique for wireless sensors networks in precision farming", IEEE Workshop and SENSORICA 2016 16- 17.06.2016, Mülheim, Germany, 2016.

[2] Erman et al , “A virtual infrastructure based on honeycomb tessellation for data dissemination in multi-sink mobile wireless sensor networks”, EURASIP Journal on Wireless Communications and Networking, pp. 2012-17, 2012

[3] N. Karasekreter, F. Başçiftçi, and U. Fidan, “Rssi Based Clustering Algorithm for Wireless Sensor Networks,” The Online Journal of Science and Technology, vol. 7, no. 1, Jan. 2017.

[4] R. S. Bal and A. K. Rath, “Clustering Structure and Deployment of Node in Wireless Sensor Network,” IJITCS, vol. 6, no. 10, pp. 70–76, Sep. 2014.

17) Research and Development of Methods for Transmitting Telemetry Information about the Status of the Spacecraft's Power System

Dinara K. TOIMBEK

Saint Petersburg National Research University of Information Technologies Mechanics and Optics (ITMO University); Saint Petersburg, Russian Federation

Phone: +7 (981) 784-38-85;
e-mail: dinarat94@mail.ru

Abstract

This article contains theoretical bases about the power supply system of the spacecraft and the command and

telemetry communication systems (TT&C). Briefly the physical principles of the specific tasks of a TT&C system are described, and three tasks are set of the thesis that should be solved on the basis of the obtained data's analysis. The work is aimed on the further research in the field of data transmission in outer space and the solution of its problems.

Keywords: Solar array, battery, spacecraft's power system, power electronics, distribution harness, telemetry sensors, TT&C, telemetry tracking, communication.

1. Introduction

Like all other machines, a satellite needs a source of energy in order to function. As it

launches away from Earth it will be running on an on-board battery – one last resource from its home planet – but to operate continuously for years on end more long-lived power sources are required [1].

A satellite consists of various systems designed to meet the mission specific requirements. All but the simplest satellites require a common set of systems shown by the solid lines in Figure 1. Complex satellites require additional systems shown by the dotted lines. The systems are classified into two groups, the payload and the bus. The payload consists of the communications equipment in commercial satellites or science instruments in research satellites. The bus consists of all remaining equipment grouped into several functional systems that support the payload. The power system is one of the bus systems that consist of the solar array, battery, power electronics, distribution harness, and controls. Other essential bus systems are the communications and data handling system to receive commands and return information, telemetry sensors to gage the satellite state, and a central computer to coordinate and control activities of all the systems.

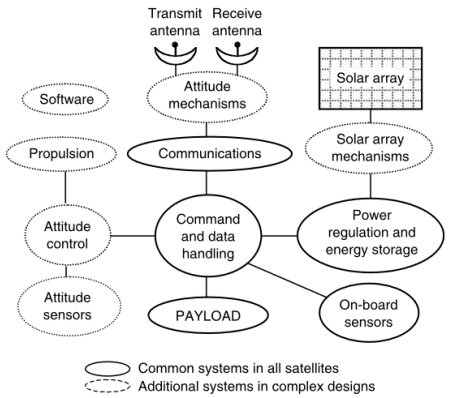

Figure 1. Satellite systems

2. Tracking, Telemetry, and Command System

The tracking, telemetry, and command (TT&C) system accepts analog, discrete, and

digital data from various systems of the spacecraft, and processes them into a continuous data stream for direct transmission to the ground or for on-board storage for later transmission. These data are analyzed and evaluated on the ground to determine the spacecraft state of health and the operational configuration. The command and control function is all digital. It provides ascent guidance from the booster separation through transfer orbit, and controls the satellite attitude and operating modes on orbit. The control is exercised in accordance with commands and data received from the ground station, supplemented by signals and data supplied by other systems of the satellite. This system also provides the error correction coding, a key function of the system.

As can be deduced from its name, this system has three specific tasks that must be performed to ensure the ability of the satellite to successfully achieve any of these applications:

1. Telemetry. The collection of information on the health and status of the entire satellite and its subsystems and the transmission of this data to the command segment on the ground. This requires not only a telemetry system on the spacecraft but also for a global network of ground stations around the world to collect the data, unless, of course, the application satellite network includes inter-satellite links that are capable of relaying the data to a central collection point.

2. Tracking. The act of locating and following the satellites to allow the command segment to know where the satellite is and where it is going. Again this requires a ranging system on the spacecraft and a data collection network on the ground that allows this ranging and tracking function to work.

3. Control. The reception and processing of commands to allow the continuing operation of the satellite in order to provide the service of interest. Again a ground system is required.

In the course of the work, the following tasks are set:

1. Analysis of methods for transmitting telemetric information about the status of the power supply system of the spacecraft, taking into account the conditions of spacecraft functioning;

2. Analysis of factors affecting the quality of transmitted information;

3. The choice of a rational method of transmission [2].

References

1. D. K. Toimbek, " Research and development of methods for transmitting telemetry information about the status of the spacecraft's power system", *XLVI Scientific and educational-methodical conference of the ITMO University*, January-February, 2017.

2. D. K. Toimbek, Zh. S. Tleubayeva , R. D. Dzhanuzakova, A. V. Fyodorov, "Research and development of methods for transmitting telemetry information about the status of the spacecraft's power system", *The collection of theses of the reports of the congress of young scientists. Electronic publication [Electronic resource]*, Access mode: http://kmu.ifmo.ru/collections_article/5506/issledovanie_i_razrabotka_metodov_peredachi_telemetricheskoy_informacii_o_sostoyanii_sistemy_energosnabzheniya_kosmicheskogo_apparata.htm, free. April, 2017.

18) Sensing and Actuating System for Indoor Medical Gas Detection

Aimé Lay-Ekuakille[(1)], Giuseppe Griffo[(1)], and Simon Kidiamboko[(2)]

[(1)] Department of Innovation Engineering
University of Salento
IT-73100 Lecce, Italy

[(2)] Department of Electronics
ISTA University
CD-00001 Kinshasa, DR Congo

E-Mail: aime.lay.ekuakille@unisalento.it
Web: http://smaasis-misure.unile.it

Abstract – Particular attention must be paid on indoor medical gas pollution in hospital to avoid risks of exposure for patients and workers. Medical gases are used in anaesthesia [1], that is, in surgery room are generally detected by using spectroscopic (see Fig.1) and chromatographic techniques [2]. Most of the used gases are: carbon dioxide (CO_2), nitrous oxide (N_2O) and sevoflurane. But others are also employed and their detection is useful since they produce effects on the human body once inhaled. National and European rules often encompass the American NIOSH (National Institute for Occupational Safety and Health) regulations and maximum concentrations; for instance, N_2O=25 ppm for general surgery rooms, N_2O=50 ppm for dental surgery rooms, and halogenated gases=2 ppm as ceiling value.

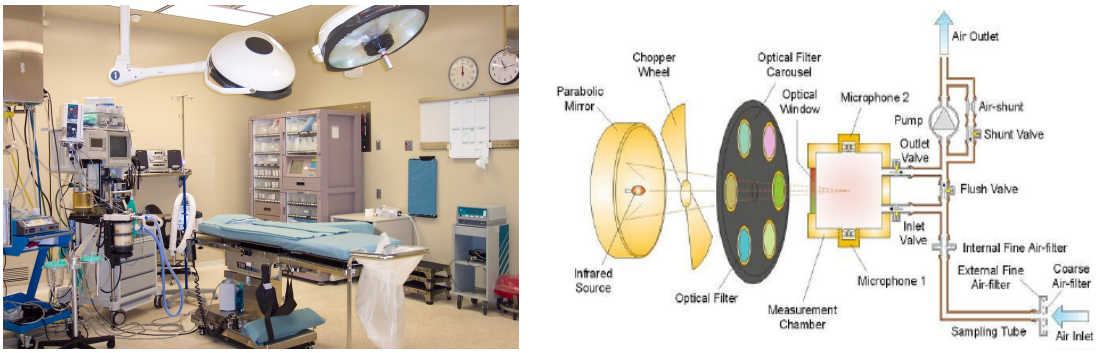

Fig.1: Typical surgery room with different facilities, and instrumentation (left) and typical photoacoustic system (right).

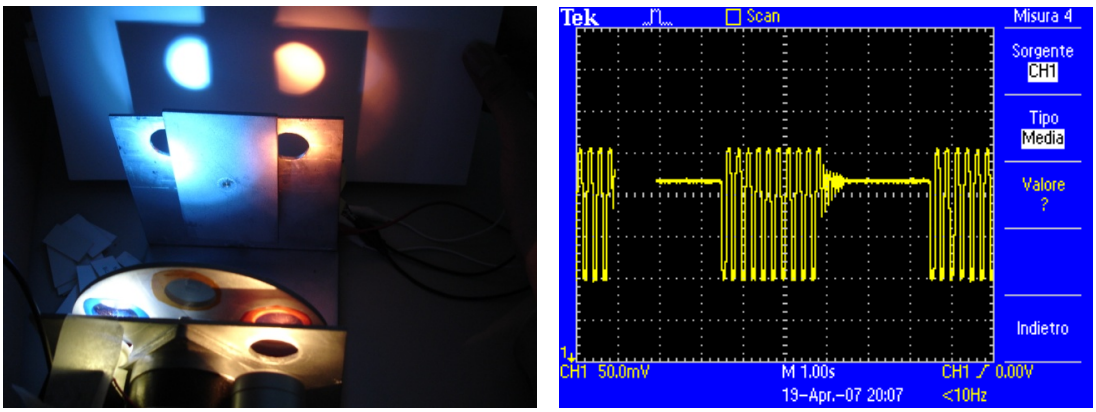

Fig.2: Designed photoacoustic system (left), and experimental spectra retrieved from different trials (right)

Consequently, amid growing concerns, a multi-gas monitor [3] is a key issue for health protection, in order to assess the values of concentrations. The research group, involving different partners is working on the design of dedicated instrumentation and signal processing in order to optimize the efficiency in data recovery. Recent statistical investigations performed by the research group have demonstrated the contribution of these elements to deteriorate human health. In this paper, we present a design of a photoacoustic system for medical gas detections which features are represented in Fig.2 along with spectral response of gases included in perfumes [4]. The latter contain a little amount of solvents for easily ejecting substantial parts of solvents. The presented features reflect the photoacoustic scheme presented in Fig.1.

The system deploys a single step-based resonant cell experimentally designed almost as if to hover alongside a second cell and one notices the presence of: measurement cell, carousel, chopper, LED source, stepper motor for chopper, stepper motor for carousel. The same rotating filter of the common and similar instrumentation is also used. It is used in a different manner: not one filtering hole is used but two, in order to correctly monitor the gas injected by increasing precision, sensibility and accuracy. We have preferred to use LED sources because of their quality and capability to be affordable and reliable. LED sources are interesting for spectroscopy especially in detecting pollutants in environmental viewpoints. However, the proposed system has detected all types of solvents contained in a large number of commercial perfumes. The proposed architecture and system can be also used for detecting other gases such as VOCs (volatile organic compounds) that are also hazardous in indoor situations. VOCs are generally detected by spectroscopy [5].

References

[1] A.G. Burn, “Occupational hazards of inhalational anaesthetics, Best Pract”, *Res. Clin. Anaesthesiol*. Vol. 17, pp.147-161, 2003.

[2] A. Lay-Ekuakille, G. Vendramin, A. Trotta, “Sensor control unit design for a photoacoustic indoor multi-gas Monitor”, in*: Proceedings of 15th IMEKO TC4 Symposium, Iasi, Romania*, September 19–21, 2001.

[3] A. Rosencwaig, *Photoacoustics and Photoacoustic Spectroscopy*, John Wiley & Sons, New York, 1980, p. 12.

[4] A. Lay-Ekuakille, G. Vendramin, A. Trotta, “LED-Based Sensing system for Biomedical Gas Monitoring: Design and Experimentation of a Photoacoustic Chamber”, *Sensors and Actuators. B, Chemical*. vol. 135, pp. 411-419, 2009.

[5] A. Lay-Ekuakille, A. Trotta, “Predicting VOC Concentration Measurements: Cognitive Approach for Sensor Networks”, *IEEE Sensors Journal*, vol.11, issue 11, pp.3923-3030, 2011

19) Design of Instrument-mounted Displays for Online Visualization of the Instrument Pose in Surgical Navigation

Oliver Gieseler[(1)], Julio C. Alvarez-Gomez[(1)], Hubert Roth[(1,2)], and Jürgen Wahrburg[(1,2)]
[(1)] Center for Sensorsystems (ZESS)
University of Siegen
D-57076 Siegen, Germany
[(2)] Institute of Control Engineering
University of Siegen
D-57076 Siegen, Germany
E-Mail: gieseler@zess.uni-siegen.de
Web: www.zess.uni-siegen.de/modicas

Introduction – In this paper we propose a novel solution to facilitate the work of orthopedic surgeons while operating with instruments using a surgical navigation system in hip application. Although total hip replacement is a standard intervention in Germany (227293 performed cases in 2015 [1]), freehand positioning of cup prostheses is not always satisfactory [2], [3]. Especially in minimal invasive interventions the application of common image-based and image-free navigation systems shows better accuracy than freehand positioning in the majority of cases. Most of these systems provide target positions as alphanumeric values on large-size screens beneath the patient site [4]. Already published studies using e.g. IPod-based displays [5] or LED ring displays [6] show the chance for improvement avoiding the necessity to change eye-focus between incision and display to capture the target values by using small instrument-mounted displays.

Materials and Methods: We have used an optical tracking system composed of an Axios CamBar B2 stereo camera and our custom-designed navigation software to track surgical instruments equipped with reference bodies. The navigation software of our system provides the pose information of the tracked instrument. Having this and a desired target pose for the instrument it can be guided from the actual pose to the target pose. The guiding information should be displayed directly in the surgeon's field of view. For this purpose a mini-display solution consisting of a MicroView OLED display with integrated Arduino microcontroller, equipped with a Bluetooth interface as well as a battery has been developed and mounted to the instrument (Figure 1 (a)). The display size is 2.7 by 2.7 centimeters. Encased in a housing containing all the components the overall measurements of the device are 3.5 cm x 3.5 cm x 9 cm.

The first implementation of the mini-display is adapted to total hip replacement and focuses on assistance while reaming the acetabulum to prepare hip shell implantations. In this case the reamer has to be centered to the middle point of the acetabular rim circle and its rotation axis must be aligned to the acetabular center axis [7]. By means of these references, the deviations between the current reamer pose and the target pose at the acetabulum can be determined.

The actual deviations are indicated as intuitive as possible and separately for position and orientation (Figure 1 (b)). Position deviations are given along x- and y-axes in the entrance plane of the acetabulum and visualized by a cross-hair indicator with moving circle for current position. The depth deviation, displayed by a square in square indicator, is given by the distance of the reamer tip to the entrance plane along the reamer rotation axis. Additionally, the angular deviation between this axis and the acetabular center axis is determined. Finally, the rotation angles are calculated by which the tool has to be rotated around the x- and y-axis in order to align it to the acetabular center axis. The angles are indicated in two bubble level bars at the edge of the display. Due to rotational symmetry of the reamer a third angle is not needed.

All display parts feature an adaptive variable scale, which changes depending on the reamers proximity to the target pose. The largest scaling range shows -60 to 60 degrees for the angles and -14 to 14 millimeters for position. Highest possible resolution is 0.5 degrees angular and 1 millimeter for position for the smallest scale. Depth resolution is set to 2 mm, taking into account that the depth control is supported by the touch sense of the operator as soon as the reamer has bone contact.

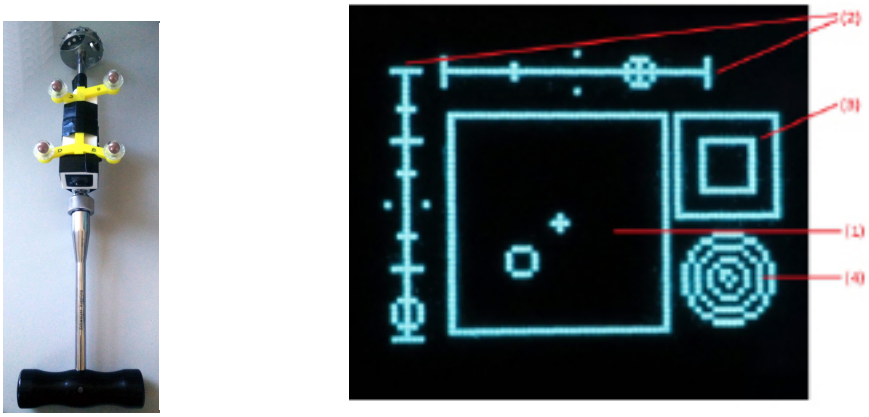

Fig.1 (a): Display (white) and reference body (yellow) for navigation mounted to a reamer tool, (b): Indicators of the display: position (1), angles (2), depth (3) and tool visibility (4)

Results and Discussion: The new instrument-mounted display solution with compact dimensions offers a space-saving, wireless indication of all relevant positioning and guidance information. Despite the low display resolution, it allows a fast intuitive interpretation for the surgeon to guide the instrument to the target pose while being continuously focused on the display and the incision site. This has been verified by cooperating physicians in first application tests. Concerning tremor and possible slippage, precision of instrument guidance and hitting of the target pose is supposed to be higher if surgeons have steady eye contact to the navigation display. Currently detailed accuracy investigations are carried out whether the resolution offered by the stereo camera can be visualized adequately.

First results confirm our assumption that the mini-display will support the surgeon to achieve accurate and reproducible results easier when using navigation systems. Compared to existing approaches for instrument-mounted displays ([5], [6]) the small display of our solution offers high flexibility to adjust the mounting position such that it is best visible for the surgeon while not constraining instrument handling. Despite of the small size, the proposed visualization symbols provide all information for instrument positioning in an intuitive way.

Acknowledgements: Part of this work is carried within the framework of the ZIM project KF2383704KJ4 funded by the German Federal Ministry BMWi.

References

[1] Fallpauschalenbezogene Krankenhausstatistik (DRG-Statistik): Diagnosen, Prozeduren, Fallpauschalen und Case Mix der vollstationären Patientinnen und Patienten in Krankenhäusern, Fachserie 12 Reihe 6.4, Statistisches Bundesamt, Wiesbaden 2015

[2] G. Saxler et al., “The accuracy of free-hand cup positioning - a CT based measurement of cup placement in 105 total hip arthroplasties,” *International Orthopaedics (SICOT)* (2004) 28: 198–201

[3] B. H. Bosker, et al., “Poor accuracy of freehand cup positioning during total hip arthroplasty,” *Arch Orthop Trauma Surg* (2007) 127:375–379

[4] T. Renkawitz et al., „Grundlagen und neue Konzepte in der computer-navigierten Hüftendoprothetik,“ *Orthopäde 2011*, 40:1095–1102

[5] P. Koenen et al., “Reliable Alignment in Total Knee Arthroplasty by the Use of an iPod-Based Navigation System,” *Hindawi Publishing Corp. Advances in Orthopedics*, Volume 2016, Article ID 2606453

[6] M. Herrlich et al., “Tool-mounted Ring Displays for Intraoperative Navigation,” *Tagungsband der 14. Jahrestagung der Deutschen Gesellschaft für Computer- und Roboterassistierte Chirurgie (CURAC),* pp. 273–278.

[7] S. Hakki et al., “Acetabular center axis: is it the future of hip navigation?,” *Orthopedics.* 2010 Oct;33(10 Suppl):43-

20) Development of a Non-invasive Bioimpedance Sensing for the Monitoring of Aortic Blood Pressure Curve

Hip Kõiv[1] and Mart Min[1]

[1] Thomas Johann Seebeck Department of Electronics,

Tallinn University of Technology,Tallinn, Estonia

E-Mail: hip.koiv@ttu.ee, mart.min@ttu.ee

Hypertension, electrical bioimpedance, aortic blood pressure, gelatine phantom

Abstract – Raised blood pressure is estimated to cause 7.5 million deaths worldwide and it is the most common reason for patients receiving long-term medical treatment in Europe [1]. The brachial cuff with sphygmomanometer is routinely used in clinical practice for blood pressure reading. The central aortic pressure (CAP) is somewhat lower than the brachial systolic pressure, and many researches [2,3] suggest that the central pressure is a more influential parameter to diagnose hypertension and cardiovascular diseases than brachial. To date, the clinical "gold standard" for the central aortic pressure of blood is a direct measurement with a pressure-sensing catheter placed inside aorta. This method is invasive, costly, and unsuitable for continuous monitoring, also not convenient for patients.

A technique to detect the CAP non-invasively, which is accepted in physicians' practice – the radial artery applanation tonometry – has the widest application in devices performing pulse wave analysis [4]. A pencil-like pressure sensor is placed manually onto the radial artery over the radius bone and a constant applanation is obtained against the artery for the waveform reading [3,5]. The intra-arterial forces, sensed by a pressure transducer, are translated into the aortic pressure waveforms using generalized transfer function [6]. This approach has some limitations. During the measurement, radial artery is pressed against the radius bone, which means that normal blood flow is interfered. Furthermore, the tonometry is very operator dependent, resulting in poor reproducibility. Due to non-ideal solutions, we proposed an alternative diagnostic tool for non-invasive CAP measurement. Electrical bioimpedance (EBI) is measured and the changes on radial artery are translated into the CAP curve using transfer function similarly as in applanation tonometry. Our first results were published already in 2013, where Krivoshei et al. introduced electrical bioimpedance (EBI) measurement system CircMon BT101 from JR Medical (Tallinn, Estonia) with a bracelet-type tetra-polar sensor [7]. The 4-electrode sensor was placed onto the radial artery close to scaphoid bone with the 5 mm distance between electrodes.

In addition to EBI measurements, simultaneous recording of the central pressure was taken invasively using Xtrans pressure sensor from CODAN GmbH, Germany [8]. Experiments were made with 53 voluntary patients in East-Tallinn Central Hospital, Estonia. Proposed generic transfer functions between EBI and the CAP showed surprisingly good results (Figure 1). Although the improvements of electrode system are still needed, the first clinical experiments are encouraging.

We are now taking numerous steps to enhance the existing system. Developing a more exact generic transfer function, testing with a larger number of patients, reducing motion artefacts, and trying out different electrode materials are the main directions of the current research. In addition, one interesting part is making a tissue-similar phantom of wrist with radial artery. Artificial phantom should allow in-lab investigation of the tetra-polar bioimpedance electrodes used together with the impedance cardiograph CircMon BT101 mentioned before. Bracelet type sensor measuring impedance variations must have high sensitivity, but should discard the defects from hand movement.

The wrist phantom with controlled parameters and characteristics, including electrical conductivity of both the tissue of hand muscle and the radial artery with blood, but also pulsating pressure and its frequency, is an important investigation tool to optimize the design, verify the obtained results and determine the sensor specifications.

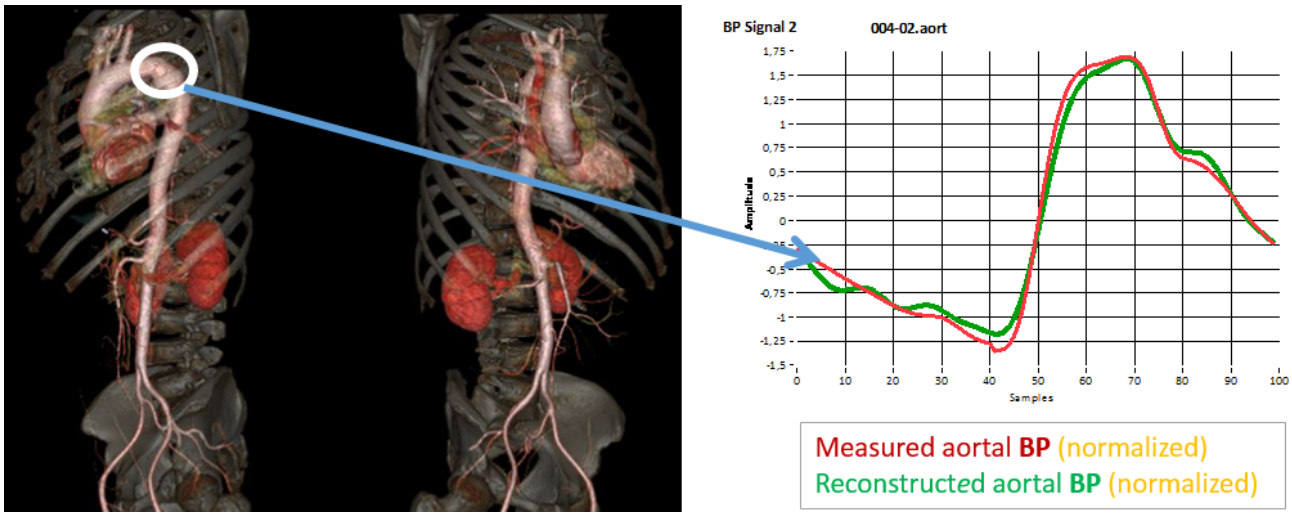

Fig.1: Figure on the left shows the region, from where the aortic blood pressure is measured with invasive method (courtesy of General Electric Healthcare, USA). On the right, there is a signal (red) from the pressure sensor placed in aorta, and the estimated pressure waveform (green) reconstructed from the signal of a wrist-mounted bioimpedance sensor.

The base material for the physical hand model is gelatine, because it is formed by natural macromolecules, can be easily manipulated with NaCl to obtain the desired tissue conductivity, and has a low cost [9]. As our interest is to register impedance changes of pulsating radial artery, the phantom hand needs surrogate blood vessels, first of all, the radial artery with suitable electrical, mechanical and hydraulic parameters.

For our first experiments, a cavity inside the gelatine replaced the artery and pumping salt water through it resulted in fluctuating impedance reading. Unfortunately, this gelatine model split after 30 minutes of experimenting due to unstable cavity properties. The material to mimic the blood vessel in the hand, appropriate for bioimpedance measurements, is currently under development. Radial artery is characterized with low electrical conductivity and past researches suggest that carbon fibre or carbon nanotubes added to silicone could give us the needed outcome – flexible and marginally conductive tube [10].

Developing a comfortable but adequate device for continuous aortic blood pressure estimation is highly appreciated as the CAP gives a greatly informative insight into antihypertensive therapy.

References

[1] TNS Opinion & Social, (2007). *Health in the European Union*. Special EUROBAROMETER 272. [Online] p.13. Available at: http://ec.europa.eu/public_opinion/archives/ebs/ebs_272e_en.pdf [Accessed 7 Feb. 2017].

[2] P. Jankowski, K. Kawecka-Jaszcz, D. Czarnecka, M. Brzozowska-Kiszka, K. Styczkiewicz, M. Loster, M. Kloch-Badelek, J. Wilinski, A. Curylo and D. Dudek, "Pulsatile but Not Steady Component of Blood Pressure Predicts Cardiovascular Events in Coronary Patients", *Hypertension*, vol. 51, no. 4, pp. 848-855, 2008.

[3] C. McEniery, J. Cockcroft, M. Roman, S. Franklin and I. Wilkinson, "Central blood pressure: current evidence and clinical importance", *European Heart Journal*, vol. 35, no. 26, pp. 1719-1725, 2014.

[4] A. Avolio, M. Butlin and A. Walsh, "Arterial blood pressure measurement and pulse wave analysis—their role in enhancing cardiovascular assessment", *Physiological Measurement*, vol. 31, no. 1, pp. R1-R47, 2009.
L. Nainggolan, "New Devices to Measure Central Aortic Pressure: Interesting But Premature", *Medscape*, 2011.

[5] S. DeLoach and R. Townsend, "Vascular Stiffness: Its Measurement and Significance for Epidemiologic and Outcome Studies", *Clinical Journal of the American Society of Nephrology*, vol. 3, no. 1, pp. 184-192, 2008.

[6] P. Annus, J. Lamp, M. Min and T. Paavle, "Design of a Bioimpedance Measurement System Using Direct Carrier Compensation", in *European Conference on Circuit Theory and Design*, Ireland, 2005.

[7] A. Krivoshei, J. Lamp, M. Min, T. Uuetoa, H. Uuetoa and P. Annus, "Non-invasive method for the aortic blood pressure waveform estimation using the measured radial EBI", *Journal of Physics: Conference Series*, vol. 434, 012048, 2013.

[8] A. Pinto, P. Bertemes-Filho and A. Paterno, "Gelatin: a skin phantom for bioimpedance spectroscopy", *Biomedical Physics & Engineering Express*, vol. 1, no. 3, 035001, 2015.

[9] A. Saleem, L. Frormann and A. Soever, "Fabrication of Extrinsically Conductive Silicone Rubbers with High Elasticity and Analysis of their Mechanical and Electrical Characteristics", *Polymers*, vol. 2, no. 3, pp. 200-210, 2010.

21) High Voltage RF-Multiplexer for Medical Applications

Bjoern Bieske[(1)], Dagmar Kirsten[(2)]

[(1)] Industrielle Elektronik und Messtechnik,
IMMS Institut für Mikroelektronik und Mechatronik-Systeme gemeinnützige GmbH,
D-98693 Ilmenau, Germany

E-Mail: bjoern.bieske@imms.de
Web: www.imms.de

[(2)] X-FAB Semiconductor Foundries AG,
D- 99097 Erfurt, Germany

E-Mail: Dagmar.kirsten@xfab.com
Web: www.xfab.com

Abstract – In medical diagnostics imaging techniques based on ultrasound are state of the art. Standard solutions are running at frequencies up to 20 MHz [1,2]. For new applications like imaging of dental imprints the resolution has to be increased to the sub millimeter range. RF ultrasound signals up to 100 MHz are therefore required. Using an array of piezoelectric transducers, the single elements have to be controlled by RF switches. The electrical RF pulses have to be multiplexed to the piezoelectric transducers and transmitted as ultrasound. Afterwards, the reflected ultrasound signals have to be multiplexed back to the receiver to generate the image. The signal to noise ratio (SNR) has to be high enough to obtain a high resolution image. The higher the incident RF pulse the better images with high SNR and dynamic range can be recorded [3].

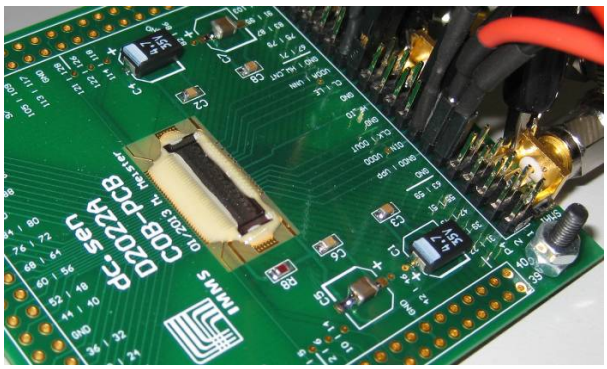

Fig.1:.Multiplexer on evaluationboard for characterization

For maximum performance the RF multiplexer should be able to handle RF signal amplitudes up to 100 V_{pp} at low on-state resistance. Crosstalk between the elements and channels of the array of transducers is another significant parameter. The insulation of neighboring channels and the off-state resistance of the multiplexer have to be high enough. Since the high power devices are not modeled for such high frequencies, these parameters can not be simulated exactly. A detailed characterization based on RF measurements in the lab is required.

To distribute the RF pulses to an array of 128 piezoelectric transducers, an integrated RF multiplexer for high voltage applications has been designed. Two different semiconductor technologies based on silicon on insulator (SOI) with trenches [4,5,6] by X-FAB Semiconductor Foundries AG were selected: XT06 (0.6 µm structures) and XT018 (0.18 µm structure). Using trench-insulated single MOS transistors voltages up to 60 V and 200 V can be handled by both technologies respectively. To multiplex bipolar signals, a structure of two MOSFET in series has been designed. A special topology has been developed to synchronize the gate voltage with the incident RF signal. This technique prevents the gate-source breakdown by limiting the gate-source voltage to V_{GS} = 5 V in accordance to the device specification.

To reduce the parasitic capacitances that become very important at frequencies above 10 MHz, the number of multiplexers was limited to sixteen in one device. The functionality of a one to 128 multiplexer was realized by cascading two multiplexer stages: one multiplexer 1 to 8 and eight multiplexers 1 to 16 are being used. This topology reduces the parasitic capacitive load for the RF source by the factor of eight. Otherwise the capacitive losses within the multiplexer will exceed the limit for the maximum junction temperature.

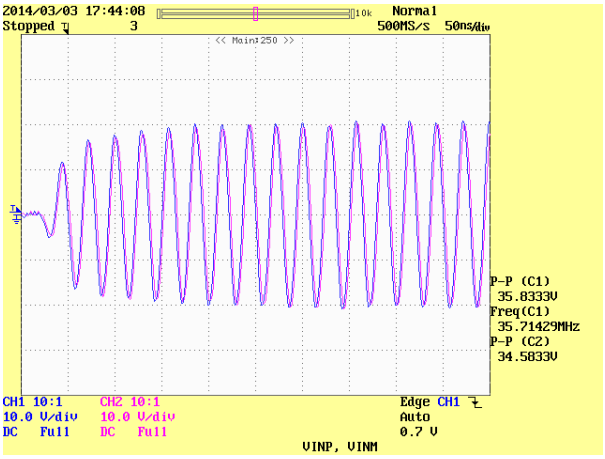

Fig.2: RF pulse by AWG and RF amplifier: 40 V @ 40 MHz

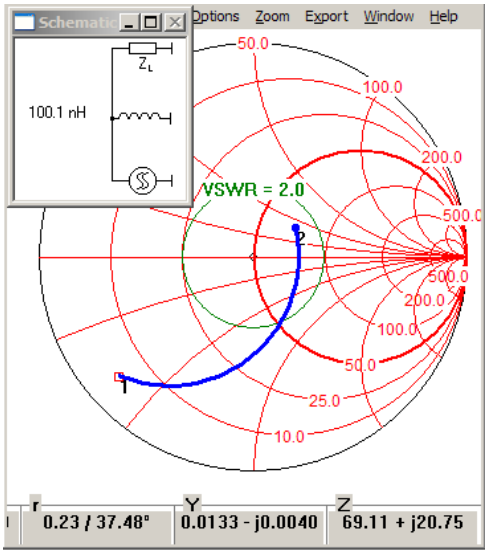

Fig.3: Compensation-Inductance L = 100 nH transforms impedance to SWR < 2

Measurements: The first DC characterization done on wafer confirmed the functionality of the one to 128 multiplexer. The on-state resistance $R_{ds\text{-}on}$ of the MOS transistors met the expected range of 10 Ohm. The overall resistance of each multiplexer channel in on-state was 44 Ohm.

The AC characterization was realized on printed circuit board (PCB) using chip on board (COB) technology (Fig.1). An arbitrary waveform generator was used to generate sinusoidal and pulsed burst signals. Above 10 MHz, a distortion of the transmitted signal could be observed. The problem occurred due to the limited driving capability of the AWG and the increasing parasitic load. This problem could not be solved by using an additional power amplifier [7] because this amplifier did not reach the output parameters described in the data sheet. So a RF Power amplifier in 50 Ohm technology delivering up to 50 W output was used. To ensure a proper impedance matching the parasitic capacitances (about 250 pF) of the multiplexer were compensated by an inductor in a frequency range of 30 to 40 MHz to get a standing wave ratio (SWR) below two (Fig. 3).

The first development version of the multiplexer design was limited to 50 V supply voltage. This final setup was suitable to characterize the RF multiplexer up to 40 MHz and up to 40 V (Fig. 2). The crosstalk and insulation between the channels could be determined to a minimum of 30 dB. Using these figures the first test of RF ultrasound imaging using piezoelectric transducers has been achieved.

An RF multiplexer for medical ultrasound applications was developed and evaluated. For characterization of multiplexers for high frequencies and high voltages, a complex measurement setup was developed. The measurement results confirm the functionality of the new multiplexer for ultrasound imaging. As alternative devices MEMS based switches could be evaluated [8].

References

[1] D. Schröder, "*Leistungselektronische Bauelemente*" Band 3, 2. Aufl., Springer Verlag 2006
[2] Maxim>Products>Analog>Switches MAX14803: *Low-Charge-Injection, 16-Channel, High-Voltage Analog Switches:* www.maximintegrated.com/en/products/analog/analog-switches-multiplexers/MAX14803A.html (Apr. 10, 2017)
[3] J. Ng; R. Prager; N. Kingsbury; G. Treece; A. Gee, "Modeling ultrasound imaging as a linear, shift-variant system," *IEEE Transactions on Ultrasonics, Ferroelectrics, and Frequency Control.*, Volume 53 Issue 3, pp. 549 - 563, 2006
[4] X-FAB Semiconductor Foundries AG: www.xfab.com (Apr. 10, 2017)
[5] Jean-Pierre Colinge, "Silicon-on-Insulator Technology : Materials to VLSI", 3. Auflage, Kluw. Acad. Publ., 2004.
[6] A.Arnaud, J.Gak, M.Miguez, "An integrated switch in a HV-SOI wafer technology, with a novel selfprotection mechanism", *Journal Integrated Circuits and Systems*, March 2010.
[7] US-TXP-3 *linear power amplifiers family*: http://www.ciprian.com/power_amplifiers.html (March. 20, 2017)
[8] S. Kim; Y. Zhang; M. Wang; M. Bachman; G.-P. Li, "High power laminate MEMS RF switch," *Electronic Components and Technology Conference (ECTC), 2012 IEEE 62nd*, May 29 2012-June 1 2012, San Diego, CA, USA, pp. 115-120, 2012.

[22] Design and Implementation of a Frequency and Magnitude Modulated Stimulus Generator for Glands Stimulation

Sameh FakhfakhGhribi[(1)(3)], Rim Barioul[(1)(3)], Nabil Derbel[(1)]and Olfa Kanoun[(2)]

[(1)]Control and Energy Management Laboratory,
National School of Engineers (ENIS), University of Sfax, Tunisia
[(2)]Chair for Measurement and Sensor Technology, Technische Universität Chemnitz, Germany
[(3)]Digital Research Center of Sfax, Sfax, Tunisia

E-Mail: fakhfakhsameh@yahoo.fr

Abstract –The stimulation of neurons by electrical devices is used in different cases as medical treatment for humans or medical researches on animals such as deep brain stimulation against the Parkinson disease [1-3], or refractory depression [4]. A stimulus has to be of an adequate intensity and duration to evoke a response. Excitable tissues have different characteristics making them sensitive to different parameters of the stimulus signal. In previous works, stimulation devices were developed including an implantable stimulator. Although they are very useful in their clinical application, a disadvantage of this type of stimulation is that only one type of wave shape can be provided, such as a monophasic [5] or a biphasic [6]. Several implants deliver the biphasic wave shape, since it does not damage the tissue and it is more comfortable for the human body than monophasic one. However, monophasic waveform is a very effective stimulation signal in many clinical applications, such as gastric pacing, vagus nerve stimulation and pain relief. So, different wave shapes should be implemented in the same stimulator to offer a large possibility to control it when implanted in the human body. Thus, in this paper, a new generic and useful modulated stimulus generator is proposed. The stimulus generator is designed in VHDL language, can deliver both monophasic and biphasic wave shapes, that can be interfaced with a microcontroller based control unit to modulate the output signal in frequency and magnitude. Besides this objective, the designed device should be highly configurable and effective for different stimulation cases. Therefore, a hardware-in-the-loop simulation is expected to ensure a correct and effective functioning. The designed stimulator is a constant-current one which specifications shown in table 1 and figure 1 for both monophasic and biphasic wave shapes.

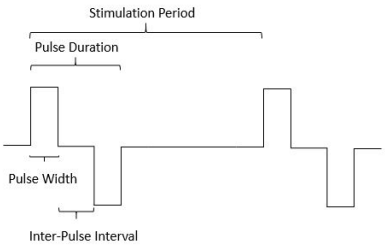

Fig.1: Definitions of pulsing parameters

Table 1: Main specifications of the stimulator system

Pulse pattern	Characteristics	Specification
Monophasic	Programmable peak voltage range	0-10V
	Programmable stimulation frequency range	1-500Hz
	Pulse width	50µs
Biphasic	Programmable voltage range	-10V-10V
	Programmable stimulation frequency range	1-500Hz
	Pulse width	50µs
	Inter-pulse interval	0

Method: The stimulus generator is embedded on an FPGA development board and is modulated by a microcontroller related to buttons. These latter are human modified to set the mode of operation of the stimulator. The desired characteristics of the generated signal are then transferred to the FPGA module. Any change on buttons interrupts the functioning of the microcontroller and modifies in real time the characteristics of the stimulus. The digital stimulus is then transferred to a personal computer, where a model of a human gland is used for the hardware in the loop simulation. For the hardware implementation of the stimulus generation sys-

tem, the CPLD/FPGA CIC-310 of ALTERA is employed. This development board equips an Altera FLEX8000 EPF8282ALC84-4 FPGA. The microcontroller drove the pulse generator to generate the monophasic and the biphasic output pattern with the desired timing. The microcontroller also toggles multiplexer to output the chosen one. After digital to analog converter, the implantable stimulator provides biphasic pulse patterns to two individual electrodes i.e. stimulus channels.

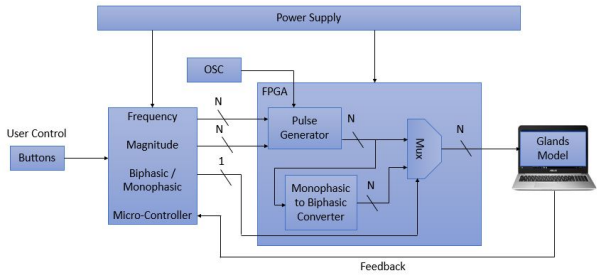

Fig.2: Modulated stimulus generation system

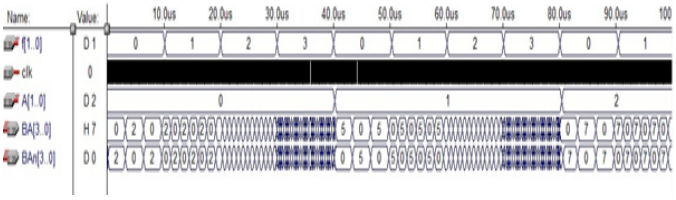

Fig.3: Simulation results of a monophasic generator

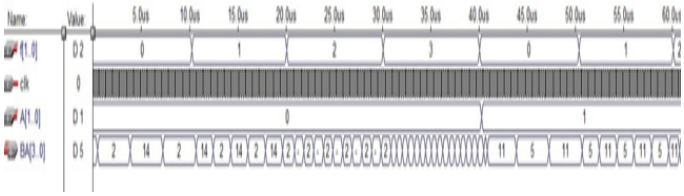

Fig.4: Simulation results of a biphasic generator

Results and Discussion: In order to validate the proposed stimulator, the architecture described above is implemented. Thus, the hardware implementation of the stimulus generator is carried out in VHDL language, on the CIC-310 development system, which includes an experimental board and a development board (based on FLEX8000 target FPGA chip). The system communicates with the personal computer via an RS-232 cable. Furthermore, the control unit is implemented in C language, on a microchip microcontroller based PCB board.

Functional simulations are carried out. The correctness of the stimulator's functioning is proven in case of monophasic pulsing (s. Figure 3) and in biphasic pulsing (s. Figure 4). One can notice that the output signal varies suitably according to the controlled frequency.

The development board allows a rapid prototyping. So, after the functional simulation step, the timing simulation, the routing and placement are done successfully. As a synthesis results, a frequency of 52.63 MHz can be noted. In addition, the total logic cells occupation reaches 14 % (31/208) and the number of the required flip-flops is about 25.

References

[1] F. Kolbl, G. N'Kaoua, F. Naudet, F. Berthier, E. Faggiani, S. Renaud, A. Benazzouz and N. Lewis, " An Embedded Deep Brain Stimulator for Biphasic Chronic Experiments in Freely Moving Rodents," *IEEE Transactions on Biomedical Circuits and Systems.*, vol. 10, no. 1, pp. 72-84, 2016.

[2] R. de Haasa, R. Struikmans, G. van der Plasse, L. van Kerkhof, J. H. Brakkee, M. J.H. Kas and H. G. M. Westenberg, "Wireless implantable micro-stimulation device for high frequency bilateral deep brain stimulation in freely moving mice," *Journal of Neuroscience Methods*, vol. 209, pp. 113-119, 2012.

[3] S. Little, M. Beudel, L. Zrinzo, Th. Foltynie, P. Limousin, M. Hariz, S. Neal, B. Cheeran, H. Cagnan, J. Gratwicke, T. Z. Aziz, A. Pogosyan, and P. Brown, "Bilateral adaptive deep brain stimulation is effective in Parkinson's disease," *J Neural Neurosurg. Psychiatry.*, pp. 1-5, October 2015.

[4] L. W. Lim, J. Prickaerts, G. Huguet, E. Kadar, H. Hartung, T. Sharp, and Y. Temel, "Electrical stimulation alleviates depressive-like behaviors of rats: investigation of brain targets and potential mechanisms," *Transl Psychiatry.,* vol. 5, no. 3, pp. 1-14, March 2015.

[5] Liu HY, Jin J, Tang JS, Sun WX, Jia H, Yang XP, et al., "Chronic deep brain stimulation in the rat nucleus accumbens and its effect on morphine reinforcement", *Addict Biol,* 13, pp. 40–6, 2008.

[6] D. Harnack, W. Meissner, R. Paulat, H. Hilgenfeld, W. D. Muller, C. Winter, et al., "Continuous high-frequency stimulation in freely moving rats: development of an implantable microstimulation system," *J Neurosci Methods*, 167, pp. 278–91, 2008

23) Air Flow Estimation through the 3D Natural Model of Nose

Gennadij Lukjanov[(1)], Anna Rassadina[(1)], Aleksej Malyshev[(1)], Roman Neronov[(2)], Evgenija Oslopovskih[(1)]

[(1)] Department of Introscopy Technologies,
Faculty of Laser and Light Engineering, ITMO University,
197101, Russia
[(2)] Modern Medical Technology Medical Holding
190121, Russia

E-Mail: gen-lukjanow@yandex.ru
Web: http://en.ifmo.ru

Abstract – The breathing process with 10 l/min peak rate was numerically modeled for lepthor-, mesor-, and platyr-models of the nasal cavity, created from a computer tomography data at the CFD ANSYS FLUENT package. A full-scale experiment using 3D-solid natural nose models and visualizations of the thermal imager was also performed. The simulation results showed a difference in aerodynamics depending on the shape of the nasal cavity.

Goal of the work – to estimate the air flow movement at the numerical simulation of breathing and comparing the results of the study with the experimental data.

There are three evolutionarily formed forms of the nasal cavity. They are: platyrrhine, mesorrhine, lepthorrhine. Scientists [1] showed the differences at the air flow movement, depending on the shape of the external nose. However, the shape of the external nose does not always correspond to the shape of the nasal cavity, for this reason we undertake a study of air movement during the breathing at the lepthor-, mesor-, and platyr-cavity of the nose. The shape of the nasal cavity was determined by the method described in [2].

Materials and methods – Three 3D-models of the nasal cavity and paranasal sinuses (lepthor-,

mesor-, and platyrcavity) were research targets. They were reconstructed according to computer tomography data. Numerical simulation was performed in the ANSYS package. Air was considered as incompressible quasi-viscous liquid at modeling, the motion of which was described through a partial differential system (the Navier-Stokes equations) [3].

A new method of evaluation of nasal cavity aerodynamics with the help of infrared radiation visualization was used at the full-scale experiment. Three solid-acrylic models of the right half of the human nasal cavity at a scale of 1:1 with nasal septum flats prolongation to the nasopharynx, produced at computer tomography data were used for the study. To reduce the optical noise, the maxillary sinuses are not represented in the model. In this model, an air flow with a temperature of

35 ° C and a peak flow rate of 10 l/min was provided using a PVC tube from the nasopharynx at the exhalation modeling, then from the vestibule of nose side at the inspiration modeling. The air flow distribution was estimated using the Testo 890 thermal imager at the temperature range of 20-30 ° C.

Results – The results of modeling the numerical and experimental models for the lepthorcavity form are shown in Fig. 1. The results confirm previously obtained data from other studies conducted by the Particle Image Velocimetry method [4,5]. Thus, at inspiration at lepthorcavity the basic mass of the air flow moves through the upper nasal passage, the remaining portion of the air flow is going through the middle nasal passage. At expiration in this nasal cavity, the main air flow is directed to the area of the upper nasal passage. At the mesorcavity the main mass of the air is directed to the middle nasal concha, the remaining part of the flow is mainly directed to the upper nasal passage. At exhalation, the main part of the air stream moves through the area of the upper nasal passage. At platyrcavity form with inspiration and expiration, the movement of air prevails through the lower nasal passage.

Conclusions – The obtained results are confirmed by previous studies in this field and prove the advantage in the accuracy and visibility of numerical models. Both methods, numerical and experimental simulation, can be used to study the nasal cavity aerodynamics. Visualization of the infrared radiation of the air flow will help to see demonstrably the features of aerodynamics, without resorting to more complex methods of investigation.

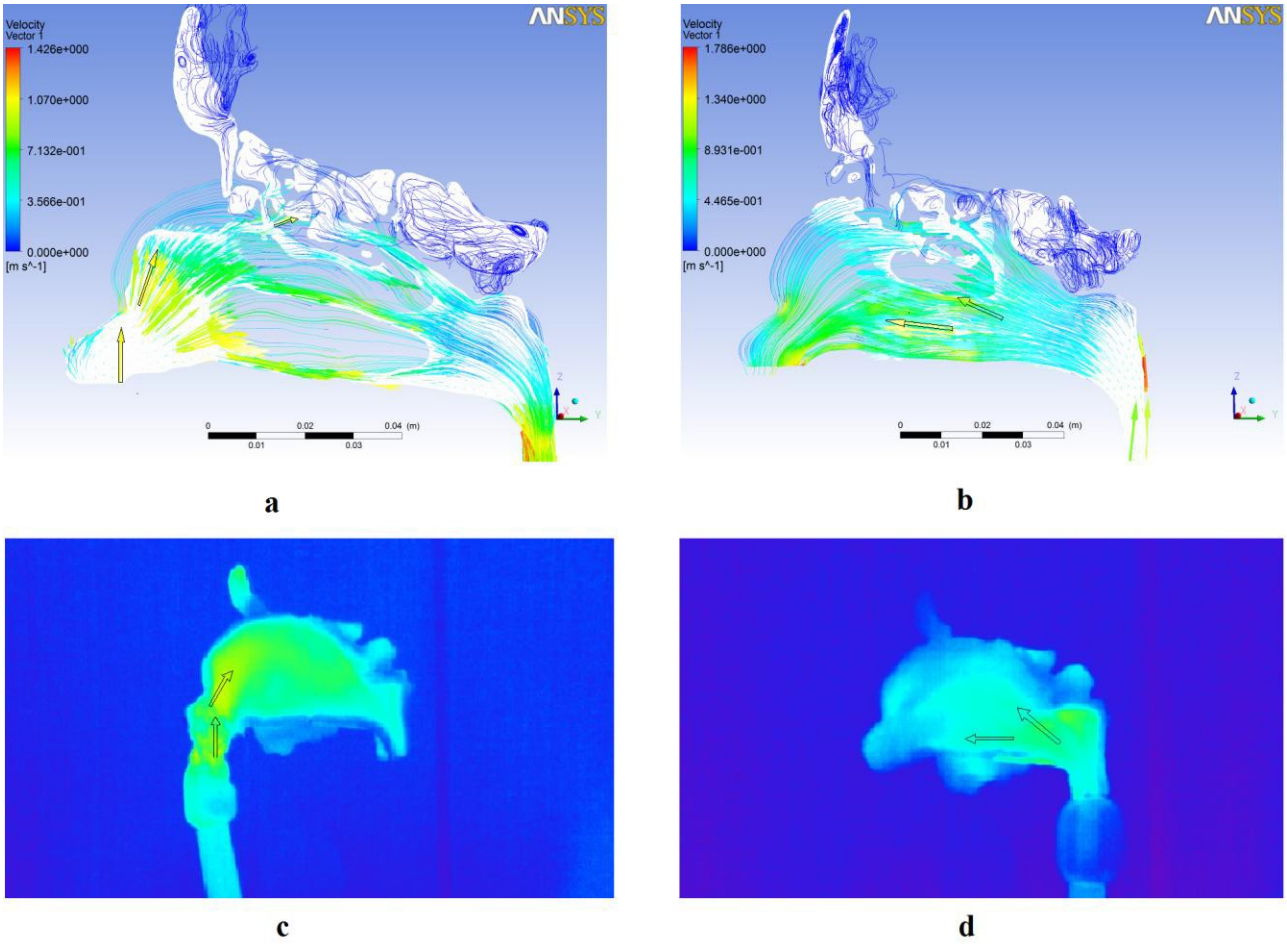

Fig.1: The results of numerical and experimental simulation, (a) inspiration, numerical model, (b) expiration, numerical model, (c) inspiration, experimental model, (d) expiration, experimental model

References

[1] J. Znu, "A numerical study of airflow through human upper airways," *National University of Singapore*,. pp. 192, 2012.
[2] R. Neronov, G. Luk'yanov, A. Rassadina, A. Voronin, and A. Malyshev, "The effect of the nasal cavity form on air flow distribution during inhalation, " *Russian otorhinolaryngology*, no. 1(86), pp. 83-94, 2017.
[3] A. Rassadina, G Lukianov, and A. Voronin, "Simulation of Convective Flows in Irregular Channels on the Example of the Human Nasal Cavity and Paranasal Sinuses," *Technical Physics*, vol. 62, no. 3, pp. 462–467, 2017.
[4] L. Hopkins, J. Kelly, A. Wexler, and A. Prasad, "Particle image velocimetry measurements in complex geometries," *Experiments in Fluids*, no. 29, pp. 91-95, 2000
[5] J. K. Kim, J. H. Yoon, C. H. Kim et al. "Particle image velocimetry measurements for the study of nasal airflow," *Acta Otolaryngology*, no. 126(3), pp. 282-287, 2006.

24) Implantable Multi Sensor System for Hemodynamic Controlling

Jens Weidenmüller[(1)], Özgü Dogan[(1)], Alexander Stanitzki[(1)], Mario Baum[(2)], Tim Schröder[(2)], Dirk Wünsch [(2)], Michael Görtz[(1)], Anton Grabmaier[(1)]

[(1)] Fraunhofer Institute for Microelectronic Circuits and Systems IMS,
D-47057 Duisburg, Germany

[(2)] Fraunhofer Institute for Electronic Nano Systems ENAS,
D-09126 Chemnitz, Germany

E-Mail: jens.weidenmueller@ims.fraunhofer.de
Web: www.ims.fraunhofer.de

With increasing number of patients suffering from heart diseases, continuous monitoring of physiological parameters in cardiovascular areas becomes more and more important. Controlling of hemodynamics allows the early detection of critical conditions, so that optimization of therapy and reduction of therapy costs can be achieved [1]. The presented implantable multi-sensor system utilizes, amongst others, capacitive pressure sensor elements which are monolithically integrated in a CMOS process and suitable for medical implants [2]. These pressure sensor elements enable high-precision measurements, by which physiological changes in pressure, for example in pulmonary artery, can be detected accurately. By additional activity and inclination detection elements [3] and temperature sensor unit further information about the patient can be obtained (see Figure 1). Those results are used for side effect compensation which allows a more accurate pressure measurement.

The core element of the implant is a multi-functional Application Specific Integrated Circuit (ASIC) which is recently developed at Fraunhofer IMS. This ASIC combines the tasks of sensor signal processing, storage of sensor calibration data in an integrated Electrically Erasable Programmable Read-Only Memory (EEPROM), communication with extracorporeal electronics and also power management. Having the challenge of a very high miniaturization level for medical and implantable applications, all components of the presented multi sensor system are designed, fabricated and assembled in a suitable way (see Figure 2).

The presented implantable system operates without any battery. Energy and sensor signal transmission is according to the international standard for passive RFID item level identification for air interface communications at 13.56 MHz (ISO/IEC 18000-3). The antenna is located within the Low Temperature Co-fired Ceramic (LTCC) circuit board of the implant. Each component is simulated and designed in such a way, that very low power consumption allows telemetric operation distances up to 15 cm.

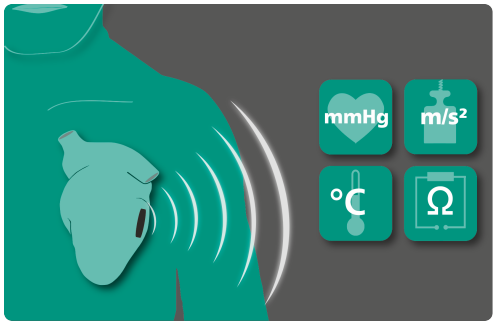

Fig. 1: Schematic on measurands of multi sensor system

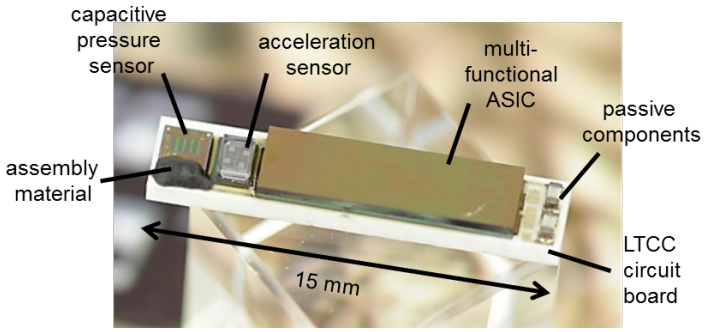

Fig. 2: Photograph of multi sensor implant

The presented implant (without any encapsulation layers) has been tested and characterized in a telemetric test setup, which is operated within a climate chamber. The setup consists of a pressure chamber, which is mounted on a step motor. Thus, pressures between 800 hPa and 1400 hPa, temperatures between 20 °C and 44 °C

and rotations in the XY plane can be applied to the implant, which can be placed into the pressure chamber. A reference temperature sensor (for temperature controlling near the implant) is lead through the pressure line, which is connected to the pressure chamber through its rotational axis.

Signal readout of all sensor components (pressure, position, temperature and voltage) is performed telemetrically with the help of an antenna which is connected to a readout device outside of the climate chamber. Test setup components and readout device are controlled by LabVIEW-programs, so that characterization measurements and further calibrations of all implant sensor components can be performed automatically. First calibration results of the pressure and temperature sensor are presented in Figure 3 and Figure 4.

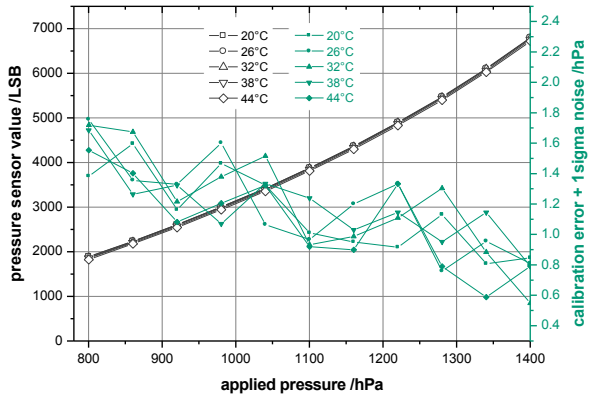

Fig. 3: Calibration curves and error + 1 σ deviations of pressure sensor

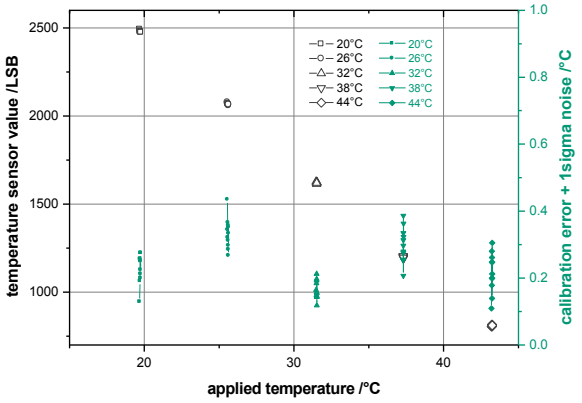

Fig. 4: Calibration curves and error + 1 σ deviations of temperature sensor

After first wired evaluation results regarding the pressure sensor performance (showing errors < 2 hPa [4]), the telemetric measurements with the implantable multi sensor system still fulfil requirements to obtain high accuracy pressure measurements with errors < 1.8 hPa within a temperature range of 18 °C – 44 °C. The telemetrically measured temperature sensor values show a high linearity with a negative temperature coefficient. Total error, including calibration error and 1 σ noise, does not exceed 0.42 K.

References

[1] Urban, G., Bunge, A. (Eds.): „VDE-Positionspapier Theranostische Implantate“, Verband der Elektrotechnik Elektronik Informationstechnik e.V. und Deutsche Gesellschaft für Biomedizinische Technik im VDE e. V., Frankfurt 2011

[2] N. J. Cleven, J. A. Muentjes, H. Fassbender, U. Urban, M. Goertz, H. Vogt, M. Graefe, T Goettsche, T. Penzkofer, T. Schmitz-Rode, and W. Mokwa, “A Novel Fully Implantable Wireless Sensor System for Monitoring Hypertension Patients,” IEEE Transactions on Biomedical Engineering, Volume 59, No. 11, November 2012

[3] M. Baum, D. Wünsch, et al., "Implantable Hemodynamic Controlling System with a Highly Miniaturized Two Axis Acceleration Sensor,” SMTA Pan Pacific – Microelectronics Symposium, February 05-08, Big Island, Hawaii, USA, 2017.

[4] J. Weidenmüller, C. Walk, Ö. Dogan, P. Gembaczka, A. Stanitzki, and M. Görtz, “Telemetric multi-sensor system for medical applications – The approach,” tm - Technisches Messen, 84(1), pp. 53-58, December 2016

25) An Electronic Embedded System for Stair Recognition

Mouna MEDHIOUB[1, 2], Sonda AMMAR BOUHAMED [1], Imene KHANFIR KALLEL [1, 3], Nabil DERBEL [1, 2], Basel Solaiman[3] and Olfa KANOUN [1, 2]

[1] Control & Energy Management Lab (CEM Lab)
Ecole Nationale des Ingénieurs de Sfax (ENIS)
Université de Sfax, Sfax, Tunisia
[2] Chair for Measurement and Sensor Technology
Technische Universität Chemnitz, Chemnitz, Germany
[3] (iTi), IMT-Atlantique, Technopôle Brest
Brest, France
E-Mail: mouna.medhioub28@gmail.com

Abstract – We present in the present work, an electronic system which uses ultrasonic sensor measurements to detect stair-cases and to recognize their natures. For this purpose, several systems have been proposed in the literature [1-3]. However, most of them are, either using more sophisticate sensors, such as radar, laser, optic, infrared, that are certainly more costly, or interesting only in the ascending stair case. The main objective of this work is to design reliable stair recognition system with a low cost and a high accuracy. The proposed stair recognition system is based on the use of ultrasonic signals to discriminate between two classes: ascending and descending stairs. This kind of signals includes weak information support, since the quality of the wave can't provide a rich informing signal compared to radar, laser or infrared signals. The challenge is to use this weak knowledge to model, as faithfully as possible, each of these two classes. In the literature, the possibilistic theory is known to be able to deal with ill-defined knowledge, owing to its possibility distribution based models [4]. The proposed approach operates in two phases: "off line phase" where we build possibilistic class models according to a set of 40 descriptive features, and "on line phase" where we match the ultrasound acquisition with these two classes of models, to decide which class is the most appropriate, (*Cf.* Fig. 1). A matching process is done by projecting each feature value, on both classes of models related to each used feature. Each feature value generates two scores corresponding to the possibility degrees of belonging to each of these two classes, according to the considered feature (*Cf.* Fig. 2). The positive belonging decision is accorded to the class having best scores.

Experimental tests have been conducted on 24 samples from each class. Experiments have been carried out in indoor and outdoor stairs and on different types of stairs in order to assess performances of the proposed system. Figure 3 illustrates some of the performed possibility distributions considered as classes of models. Efficiency of so built models has been proved, since 100% of recognition rate has been reached with used features.

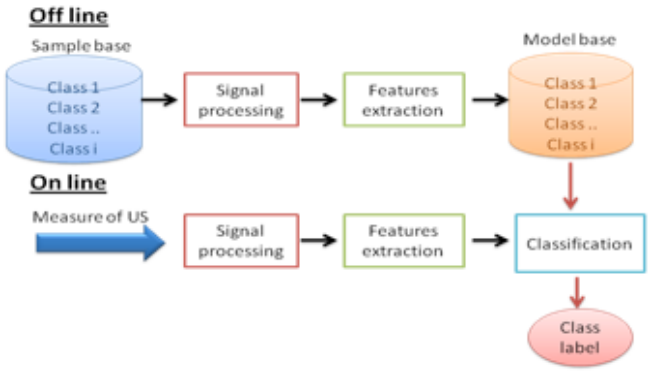

Fig.1: Overview of stair recognition process.

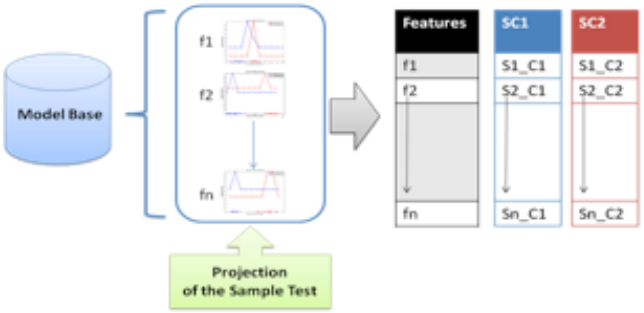

Fig.2: Projection of test samples on the possibility distribution

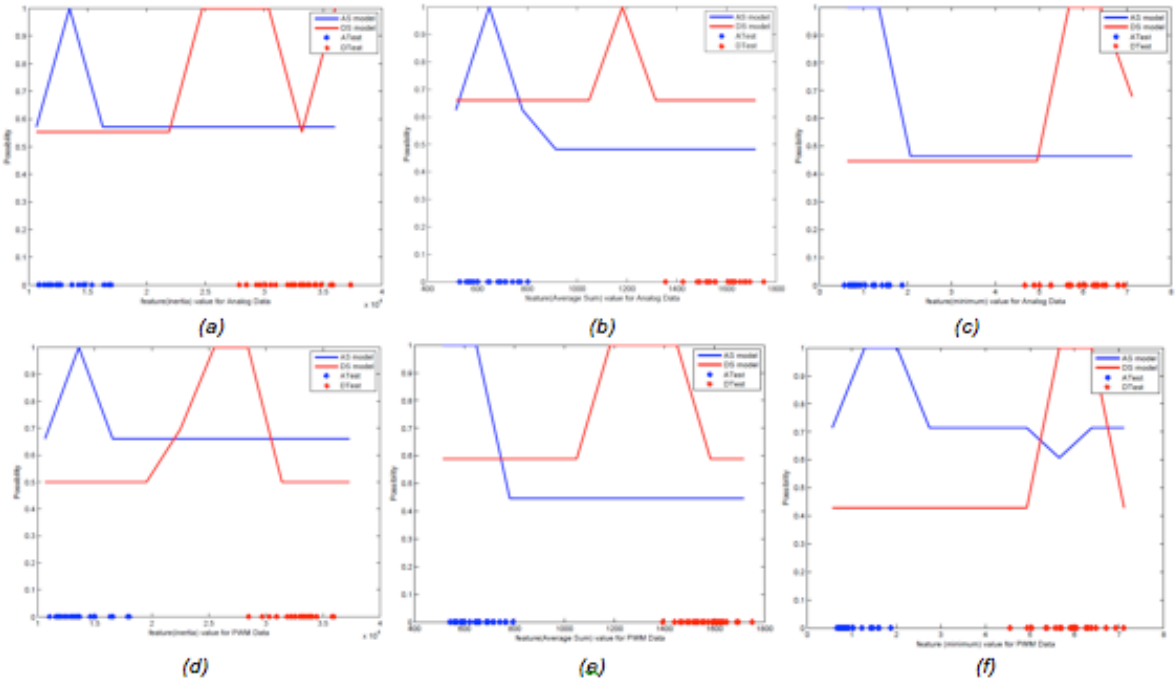

Fig.3: Possibility distribution of features, with (a) and (d): inertia, (b) and (e): average sum and (d) and (f): minimum.

Such results are very promising but they must be carefully considered, since experiments have been conducted on only 24 samples. Therefore, as a future work, we plan to first enlarge the used data base and then we envisage to lead feature selection process in order to reduce the dimensionality and enhance global performance rates. The ultrasound sensor is also to question. Laboratory tests on physical characteristics of the sensor are planned.

References

- Sh. A. De Silva, D. Dias, "A sensor platform for the visually impaired to walk straight avoiding obstacles," *2015 Ninth International Conference on Sensing Technology*, pp. 838-843, 2015.
- A. H. Adiwahono, B. Saputra, T. W. Chang, Z. X. Yong, "Autonomous Stair Identification, Climbing, and Descending for Tracked Robots*", 2014 13th International Conference on Control, Automation, Robotics & Vision Marina Bay Sands, Singapore,* 10-12th December 2014 (ICARCV 2014), pp. 48-53, 2014.
- J. A. Delmerico, D. Baran, Ph. David, J. Ryde, and J. J. Corso, "Ascending Stairway Modeling from Dense Depth Imagery for Traversability Analysis", *2013 IEEE International Conference on Robotics and Automation (ICRA) Karlsruhe, Germany*, May 6-10, pp. 2283- 2290, 2013.
- B. Alsahwa, B. Solaiman, S. Almouahed, É. Bossé and D. Guériot, "Iterative Refinement of Possibility Distributions by Learning for Pixel-Based Classification*", IEEE Transactions on Image Processing*, Vol. 25, No. 8, pp. 3533-3545, 2016.

26) Exposure Measurement Platform for Electromagnetic Field Monitoring and Epidemiological Research

Jürg Fröhlich[2,1], Marco Zahner[1,2], Jürg Leuthold[1]

[1] Institute of Electromagnetic Fields,
Department of Information Technology and Electrical Engineering, ETH Zurich,
CH-8092 Zurich, Switzerland

[2] Fields at Work GmbH,
Sonneggstrasse 60
CH-8006 Zurich, Switzerland

E-Mail: juergfr@ethz.ch
Web: www.fieldsatwork.ch, www.ief.ee.ethz.ch

Abstract – Exposimetry is a measurement technology with the goal of quantifying the immission or absorption of fields and/or energy in specific ranges of the electromagnetic spectrum. Portable, small and accurate measurement instruments were developed in order to provide tools for epidemiological research and environmental monitoring. The target measurement quantity was the average amount of RMS field strength that an average individual will experience in everyday environments. This quantity can be used to classify different groups of the population or to track changes in exposure conditions within defined regions or along specified tracks.

Methods and tools for the assessment of the personal exposure to low frequency magnetic fields (LF-MF), radio frequency electromagnetic fields (RF-EMF) and pulsed RF emissions from radar installations have been developed, characterized and tested [1]. The result is a measurement platform enabling a large variety of measurement procedures and protocols.

Background: There is an ongoing discussion on potential adverse health effects of electromagnetic fields. Wireless communication systems and devices are ubiquitous nowadays and form an integral part of the daily life for billions of people worldwide, therefore, even small effects would have a significant impact on public health. Mobile phones and the cellular infrastructure intentionally emit radio frequency electromagnetic fields (RF-EMF) in a wide range of frequencies for data transmission purposes. The usage of these devices has ever since raised certain concerns about potential adverse health effects caused by the exposure to electromagnetic radiation. Similar concerns are associated with the fields generated by electrical power distribution systems and electronics. High voltage power lines, transformers and electric motors for example generate Low frequency magnetic fields (ELF-MF) in their proximity. In general, electronic systems and devices can be expected to emit a certain level of magnetic and electromagnetic fields in operating conditions. These fields can interact with matter by means of polarization effects on molecular and cellular level and by induction of electrical currents. Mechanical forces and heating can arise from that depending on the properties of the affected material.

Regulatory bodies limit the maximum permissible exposure to a level that is assumed to be safe based on the current state of knowledge. However, due to fast evolution of the technology and its usage among the population, the existence of long-term and cumulative effects cannot yet be excluded. For this reason, governmental agencies are considering to include a regular monitoring of the environmental and personal exposure to identify possible negative effects in time.

The wide range of exposure scenarios encountered in practice represents a challenge both for the definition of regulatory limits and the methodological assessment of the exposure. Practical and physical constraints make it necessary to rely on more than one metric for the description and quantification of the exposure to RF-EMF and MF-ELF to get meaningful and reproducible data. The ICNIRP guidelines

[2, 3] adopted by most countries in the world define separate immission limits for the absolute field strength in an unperturbed environment, for the power density of incident radiative fields as well as for the power absorbed by the tissue of the human body in terms of absorbed power per mass of tissue (SAR Value).

Objectives: In a practical exposure assessment scenario, measuring the field strength at the location of a person is the target quantity. In order to track the changes in field strength over time the device to be developed has to provide the following features: 1. accurate measurement of environmental field strengths, 2. location and time tracking, 3. long-term data logging, 4. small size and lightweight. In addition, the measurement system should enable different ways to collect data on specific activities, environmental conditions, behavior and subjective symptoms of the person carrying the device via a Smartphone.

Results: Exposure meter devices have been developed for low frequency magnetic fields up to 100kHz, for frequency selective measurements in the RF frequency range (88MHz up to 5.8GHz) including all relevant telecommunication frequency bands as well as a device for the measurement of radar signals in the L, S, C and X band.

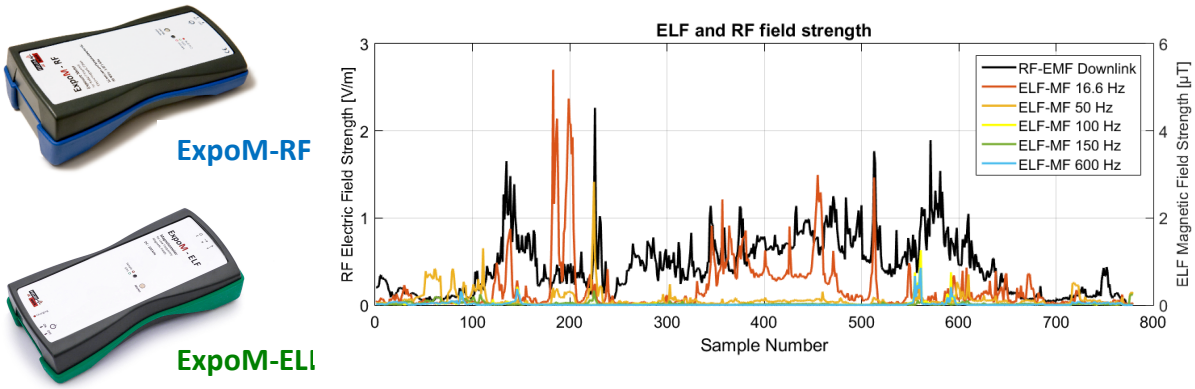

Fig.1: ExpoM-RF and ExpoM - ELF exposure meters (left) and measurement data recorded simultaneously using the both devices on a route in the city of Zurich (right).

All these devices feature location tracking, long-term data logging and wireless interfaces to Smartphone based applications. Altogether, this provides an exposure measurement platform enabling a large variety of measurement procedures and protocols for most of the relevant sources present in the everyday environment. The devices are used within different epidemiological studies [e.g. 4, 5] and applied by environmental agencies for monitoring environmental EMF.

References

1] Marco Zahner, *Analysis, Methods and Tools for Electromagnetic Field Exposure Assessment & Control.* Dissertation ETH Zürich, Zürich, 2017 (submitted).

[2] International Commission of Non-Ionizing Radiation Protection (ICNIRP), "Icnirp Statement-Guidelines for Limiting Exposure to Time-Varying Electric and Magnetic Fields (1 Hz to 100 Khz)," *Health Physics*, vol. 99, no. 6, pp. 818-836, Dec, 2010.

[3] A. Ahlbom, U. Bergqvist, J. H. Bernhardt, J. P. Cesarini, L. A. Court, M. Grandofo, M. Hietanen, A. F. McKinlay, M. H. Repacholi, D. H. Sliney, J. A. J. Stolwok, M. L. Swicord, L. D. Szabo, M. Taki, T. S. Tenforde, H. P. Jammet, and R. Matthes, "Guidelines for limiting exposure to time-varying electric, magnetic, and electromagnetic fields (up to 300 GHz) (vol 74, pg 494, 1998)," *Health Physics*, vol. 75, no. 4, pp. 442-442, Oct, 1998.

[4] "GERoNiMO - Generalised EMF Research using Novel Methods – an integrated approach: from research to risk assessment and support to risk management," Jun 2016, 2016; http://geronimo.crealradiation.com/.

[5] A. Schoeni, K. Roser, and M. Roosli, "Memory performance, wireless communication and exposure to radiofrequency electromagnetic fields: A prospective cohort study in adolescents," *Environ Int*, vol. 85, pp. 343-51, Dec, 2015.

[27] Sensor Properties of Cellular Membrane

Alexander Mamykin[(1)], Michael Listov[(2)], Anna Rassadina[(3)]

[(1)] Department of Physics,
Institute of Basic Engineering Education, Saint Petersburg Electrotechnical University "LETI",
197022, Russia

[(2)] Department of Biology,
S.M. Kirov Military Medical Academy,
194044, Russia

[(3)] Department of Introscopy Technologies,
Faculty of Laser and Light Engineering, ITMO University,
197101, Russia

E-Mail: alexmamykin@yandex.ru
Web: http://www.eltech.ru/en/university, http://www.physicsleti.ru

Abstract – The article describes the main physics, chemical and biological processes associated with one-electron charge transfer by free radicals through the plasma membrane of cells in biological systems.

Introduction. What is it, that plays the leading role in the pathogenesis of diseases with genetic predisposition? These are free radicals and lack of enzymes activity that regulate metabolism, primarily the effectiveness of the antioxidant system enzymes. Mechanism of the pathogenetic radical action is a single-electron transfer through the lipoprotein membrane and cell matrix [1].

The structure of proteins forming on a par with lipids the cell membrane, can be considered as a dipole (Fig. 1) [2,3]. Then the free radical attack of the oxygen molecule on such a dipole leads to a dipole disequilibrium, and causes it to rotate 180 ° around its axis into the cell. All membrane proteins dipoles can be involved into the dipole rotation process. That way cell pathology against background of chain reaction is formed.

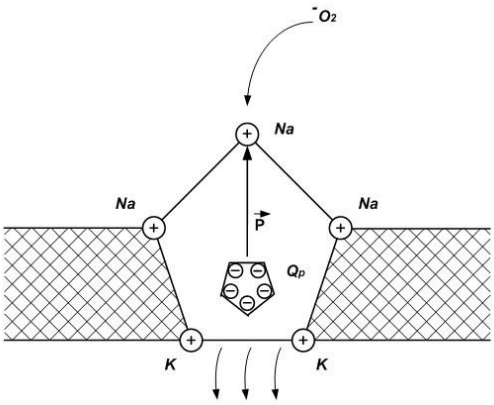

Fig.1: The free oxygen radical attack the protein at the lipidic layer of the cell membrane

Materials and methods. The coproporphyrin III with a phenolic compound as a catalyzer was entered into the mouse body (DBA/2 line), the oxygen molecules are transformed into superoxide radicals ($O2.^-$). Coproporphyrin is similar in structure to heme and formed in a mammalian body as a byproduct of heme synthesis. Coproporphyrin like plant chlorophyll and animal heme, has a tetrapyrrole structure and is capable to generate a superoxide ion with the chemical photoactivation. The presence of superoxide radical in the body leads to a number of chain reactions

(Fig. 2) [4].

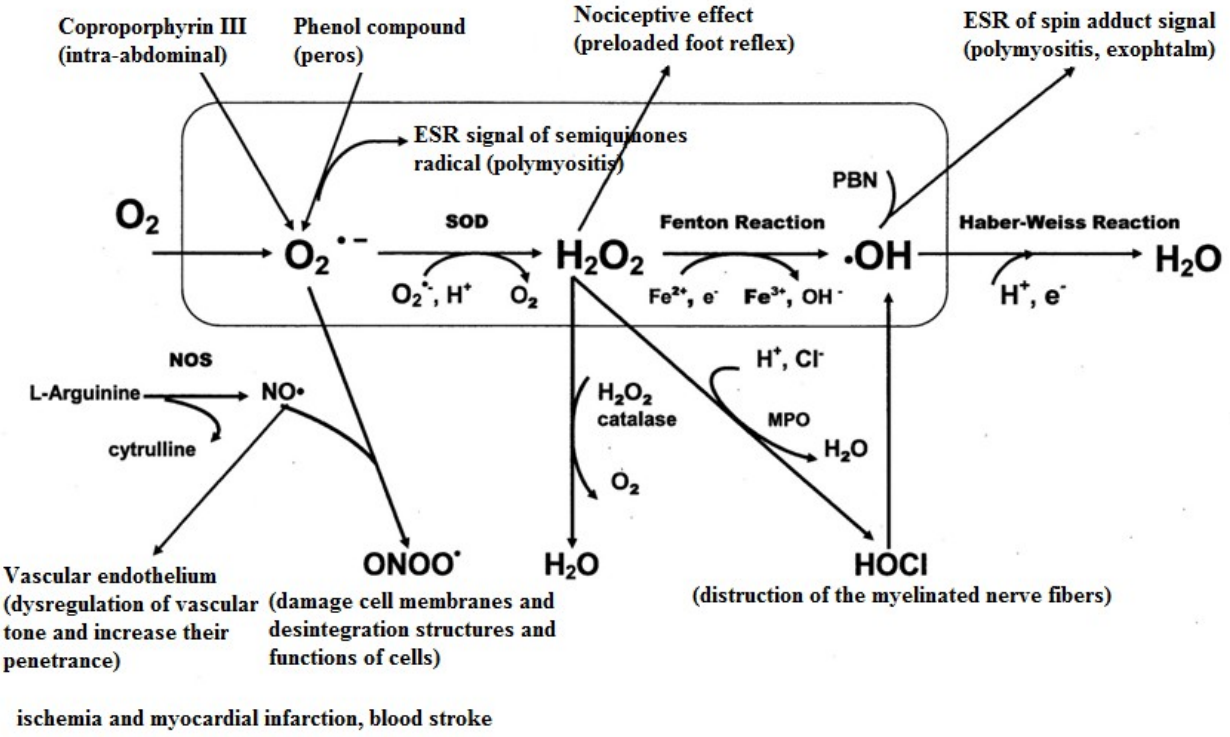

Fig.2. Experimental model of the single-electron transfer, illustrating the development of cellular pathology on the background of a chain reaction

Results. If the pathological effects were modeled by intraperitoneal injection of coproporphyrin with cell suspension of lymphocytic leukemia P388 after pre-irradiation (in vitro) of the mixture with the laser of 22 mW power at a wavelength of 630 nm to 240 J / cm2 exposure, the photoactivation has generated singlet oxygen (O2 *). Peroxyoxalic rubrene is a chemical compound of tetracycline. It was applied by us, as well as light to excite coproporphyrin. The average age of life of the experimental mice increased. The presence of singlet oxygen in the irradiated solution leaded to the death of the lymphocytic leukemia P388 cells. Coproporphyrin can also be a source of reactive oxygen intermediate after activation of metal- coordinators. The luminophor-acceptor (rubrene) as well as the phenol compound will used to catalyze of desintegration. They take the reaction energy, and then give up it in the form of emission. In such a case, singlet oxygen and superoxide radical generated. The superoxide radical became the first link of electron transfer chain reaction. Accordingly, in the experimental group of the mice part of mice get better and some dead, but not from cancer, but from aspit (edema). **Conclusions**. The free radicals action simulation shows that the great majority of the experimental pathology (model) with free radical nature are more or less depend on heme. This allows to consider at the same time events so distant from each other's, as carcinogenesis, development of experimental dependent heme exophthalmos and polymyositis.

References

[1] A. Mamykin, M. Listov, and A. Rassadina, “Mathematical model of free radicals flux action on eukariotic cells lifetime and biomembranes sensitivity,” *IEEE WORKSHOP Industrial and Medical Measurement and Sensor Technology*. June, Mulheim an der Ruhr, pp. 56–57. 2016

[2] A. Pimenov, „Tehnicheskaja jelektrodinamika [Technical electrodynamics],” *Moscow, Radio i svjaz' Publ.*, pp. 483 (in Russian), 2005.

[3] M. Listov, A. Mamykin, “[Experimental modeling of heme-induced exophthalmos physicochemical mechanisms of single-electron transfer in cell membranes]. *Vestnik Rossijskoj voenno-medicinskoj* akademii *[Herald of the Russian Military Medical Academy],* no. 2 (42), pp. 120–125 (in Russian), 2013

[4] M. Listov, A. Mamykin, “[Organism as a biosystem, adapted to the using of the energy of quantized electron transport via free radicals]. *Vestnik Rossijskoj voenno-medicinskoj akademii [Herald of the Russian Military Medical Academy]*, no. 4 (56), pp. 200−204 (in Russian), 2016

28) Polarimetric Analyses of Scattered Radiation for Material Characterisation and Aerosol Classification

Thorsten Schultze, Lea Marcius, Benedikt Friederich and Ingolf Willms

Chair of Communication Systems,
Faculty of Engineering, University of Duisburg-Essen,
D-47057 Duisburg, Germany

E-Mail: thorsten.schultze@uni-due.de
Web: nts.uni-due.de

Abstract – This paper presents two tightly related research projects on polarimetric scattering- and reflection analyses for security applications.

The first part of this paper describes new high selective optical approaches for the characterisation of critical aerosols for smoke detection applications. In the field of fire detection the reduction of false alarms is at least just as challenging as the actual task of detecting a fire. The reason for this is that typical optical smoke detectors with only one light path are highly susceptible to false alarms due to non-fire aerosols, especially dust or steam/fog. Therefore multi-sensor detectors are gaining greater acceptance. Regardless of the technology there are always the questions about the costs and the selectivity of the additional sensor data, i.e. how the detection of fires is affected by the incorporation of the additional sensor signal. These new approaches for significantly improved discrimination of dust, steam and fog from smoke use different polarimetric evaluations of an advanced optical sensor.

The detection of steam and fog is based on the measurement of the polarisation ratio at specific angles, where water droplets show a high degree of polarisation. One well-known angle with a high degree of polarisation is the scattering angle of the rainbow [1]. There are further constellations of polarisation directions and scattering angles which allow the identification of water aerosols. Thus an effective combination with the analysis of the depolarisation is possible, leading to a slim optical system [2].

The characterisation of airborne dust is performed by the analysis of the depolarisation of light in the scattering process. According to Mie-Theory, spherical particles exposed to light with linear polarisation will scatter radiation in the same polarisation and wavelength (elastic scattering) as the incident radiation. Particles with non-spherical shape typically cause multiple scattering, which can result in a depolarisation of the scattered radiation [2].

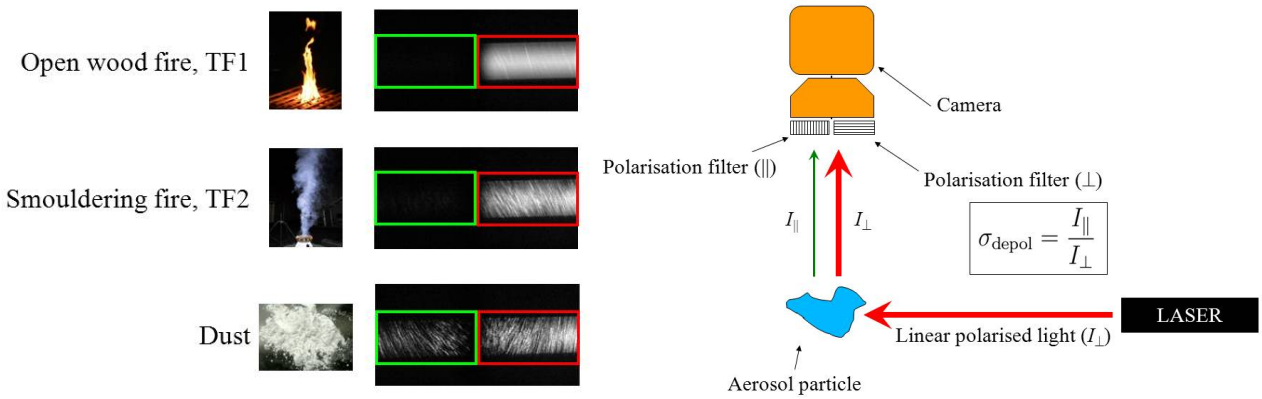

Fig.1: Optical depolarisation measuring set-up and first results [3].

This effect can clearly be observed by e.g. monitoring of the light scattering of different aerosols illuminated by a polarised light source, as depicted in Fig 1. In Fig 1 also results with smoke from an open wood fire, a smouldering fire and dust is shown. From the left part of the camera pictures it can be seen that dust partially depolarises the incident light.

Polarimetric analyses are not restricted to aerosols. The material characterization of surfaces is often performed by optical techniques like the ellipsometry. The analysis of materials und surfaces is particularly interesting in emergency scenarios, where an unknown environment needs to be explored. Furthermore the use of autonomous vehicles scanning e.g. a smoke filled emergency scenario is no more a vision. The second part of the paper presents the research on a radar based method for the implementation in security robots. The advantage of a radar based system working in the in the UWB microwave range is the almost negligible impact of airborne particles like smoke and dust at longer wavelengths.

However, the classical ellipsometry is restricted to plane surfaces. In order to allow the characterization of naturally rough surfaces or even bulky materials, a method was developed which combines specular and diffuse reflection. The reflection models are based on the Fresnel formulas and Lambert's law [4]. For precise ellipsometric permittivity estimation, the ratio of specular reflection in the overall scattered intensity needs to be estimated. This is achieved via measurement of the depolarization ratio, performed by a cross-polarized antenna setup. The complex permittivity of typical indoor materials with rough surfaces could be estimated with an accuracy better than 6% in the range of 4 - 13 GHz [4].

References

[1] G.P. Können, *Polarized light in Nature*. Cambridge: Cambridge University Press, 1985.
[2] Th. Schultze, I. Willms, "Polarized light scattering smoke detector with reduced false alarm susceptibility," *15th International Conference on Automatic Fire Detection (AUBE '14)*, October 14-16, Duisburg, Germany, 2014.
[3] Polarised Aerosol Characterisation: http://nts.uni-due.de/research/research_be/Polarise.shtml (accessed May 9, 2017).
[4] B. Friederich, T. Schultze, I. Willms "UWB-radar based surface permittivity estimation in hostile and pathless security scenarios", *IEEE International Conference on Ultra-WideBand (ICUWB)*, September 1-3, pp.125-128, 2014.

29) Gas Phase Detection in Cryogenic Liquids for Space Applications Using Capacitive Sensors

Christoph Kandlbinder[(1)], Alice Fischerauer[(1)], and Gerhard Fischerauer[(1)]

[(1)] Chair of Measurement and Control Engineering,
Faculty of Engineering Sciences, University of Bayreuth,
D-95440 Bayreuth, Germany

E-Mail: mrt@uni-bayreuth.de
Web: www.mrt.uni-bayreuth.de

Abstract – The upper and main stages of heavy-lift launchers for space applications are often driven by cryogenic liquids. Especially for enabling the reignition process as a principle for orbital changes, it is of vital importance to observe the behavior of these cryogenic liquids. Gas bubbles moving into propulsion lines, for instance, can destroy parts of the propulsion system by cavitational effects and therefore put the reignition process to risk [1].

For this reason, we realized a capacitive measurement system for two-phase mixtures that is capable of working under cryogenic conditions without noticeable energy input into the fluid. The electrodes are therefore arranged in a way that phase changes inside an observed volume can be detected. The characteristic capacitances of different pairs of electrodes were determined experimentally and compared to finite-element simulations (Ansys). Also, calculations for the electrical flux density were performed to gain insight into the mechanisms influencing the changes of capacitances and to corroborate the simulated capacitance curves with theoretical statements. Therefore, two cases serving as an example for processes occurring in cryogenic tanks have been investigated: a fill-level measurement involving a large gas bubble above a homogenous cryogenic liquid on the one hand, and the identification of a bubble stream consisting of many small bubbles inside a liquid on the other hand. Fig. 1 shows the strength and the field lines of the electrical flux density in a cutting plane as indicated in Fig. 1c) for a specific fill level (Fig. 1a)) and a bubble stream (Fig. 1b)) occurring inside the upended receptacle (Fig. 1c)). The figure shows that the permittivity distribution inside the observed volume has different influences on the capacitances as shown in detail in [2] and can explain the different changes in capacitance when fill level changes occur.

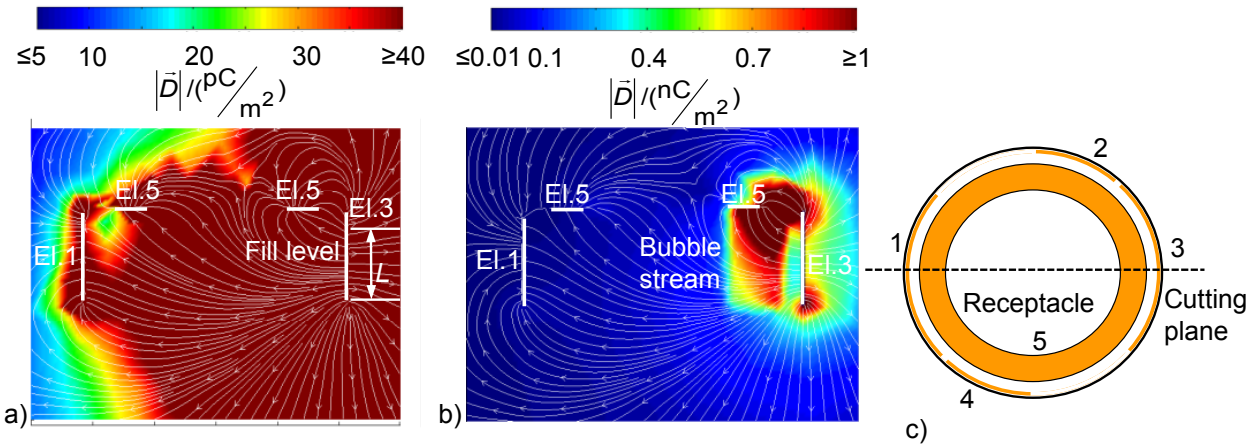

Fig.1: Field lines and strength of the electrical flux density inside and outside the receptacle for excitation of Electrode 3 for a) a specific fill level and b) a bubble stream close to Electrode 3. c) shows the cutting plane used for the simulation of the electrical flux density.

The system concept was then tested in a cryostat allowing the controlled generation of bubble streams inside liquid nitrogen and of a contiguous gaseous volume above the liquid in a cryogenic environment. As the measurements are noisy, suitable moving average filters were tested and used for smoothing. For the phase boundary between the gaseous nitrogen above a "sea" of liquid nitrogen (obtained with an upended receptacle in a tank full of liquid nitrogen), such experimentally determined and filtered results agree well with pictures recorded by a video camera as shown in Fig. 2. In this figure, the simulated capacitance changes for different fill level changes were used to get the fill level from the capacitance measurements by taking uncertainties into concern. Also, gas bubbles rising in liquid nitrogen could be distinguished by way of the measured capacitances of different electrode pairs [3].

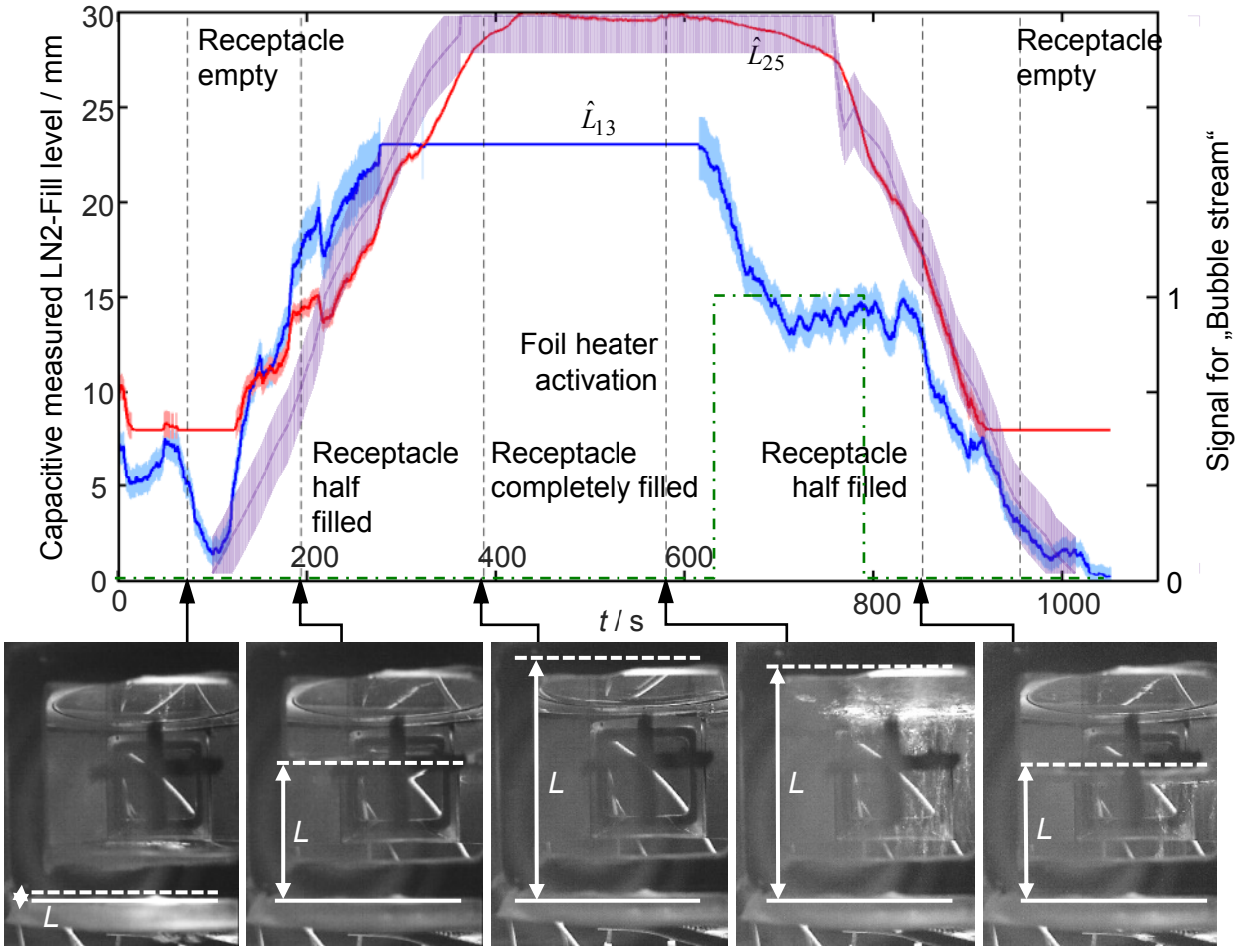

Fig.2: LN2-fill level inside the receptacle determined from the measured capacitances over time $C_{13}(t)$ (curve L_{13}) respectively $C_{25}(t)$ (curve L_{25}) by using a filter length of 800. The colored ties represent the uncertainty in fill level by applying a measurement uncertainty of 1 fF. The green semi-dotted switching function represents the occurring of a bubble stream while the semi-transparent violet tie represents the visually determined fill level with an uncertainty band of ±2 mm. The pictures below show camera pictures for the respective points of time.

References

[1] Siegl, M. et al.: "*AdvancedSensor technologies for cryogenic liquid propellant flow phenomena,"* Proc. 66th International Astronautical Congress (IAC),Jerusalem, 7 pp., 12–16 October, 2015.

[2] C. Kandlbinder et al.: "*Capacitive gas-phase detection in liquid nitrogen,"* In: Journal of Sensors and Sensor Systems. Vol. 6 (March 2017) No. 1, pp. 135-143. DOI: 10.5194/jsss-6-135-2017

[3] C. Kandlbinder et al.: "*Capacitive measurements in two-phase mixtures applied to the example of cryogenic nitrogen,"* In: tm - Technisches Messen, ahead of print. DOI:10.1515/teme-2016-0080.

30) Analysis of Hardening Times of Two-component Adhesives Using Terahertz Time Domain Spectroscopy (THz-TDS)

Frank Platte[(1)], Carsten Brenner[(2)], Peter Henselder[(1)], Christoph Fredebeul[(3)] and Fabian Malert[(1)]

[(1)] Lab for Chemical Process Engineering,
Faculty of Life Sciences, Rhine-Waal University of Applied Sciences,
D-47533 Kleve, Germany

[(2)] Lab for Photonics and Terahertz-Technology,
Faculty of Electrical Engineering and Information Technology, University of Bochum,
D-44780 Bochum, Germany

[(3)] Lab for Electrical Engineering,
Max-Born-Berufskolleg
D-45665 Recklinghausen, Germany

E-Mail: frank.platte@hochschule-rhein-waal.de
Web: www.hochschule-rhein-waal.de

Abstract – Two-component adhesives hardening after a chemical reaction is induced usually by the aid of a starter substance and/or ultraviolet light [1]. There are several chemically different systems known and thoroughly studied. From this list a poly-methyl-methacrylate (PMMA) system was chosen for the work presented here (brand: Plexus MA300). Technical application of PMMA based adhesives are wide-spread, but the motivation of this investigation is based on the fact that PMMA is the major component in bone cements [2].

In the past decades the so-called terahertz-gap was continuously closed. There are several ways to create and detect THz-waves. For the purpose of THz-spectroscopy since 1990s terahertz time domain spectrometers (THz-TDS) are available using ultra short laser pulses in the range of femto-seconds disturbing an electric field of charged antennas [3]. Terahertz radiation consists of electromagnetic waves which combine the properties (and sometimes advantages) of the neighbouring microwave and infrared bands. Similar to microwaves terahertz waves are able to penetrate numerous dielectric materials such as paper, cardboard, cloth and ceramic. Bearing in mind that almost all polar gases and most macromolecules exhibit finger print absorption features in this frequency range, THz-spectroscopy enables one to study changing chemical properties even if no visible access can be established. This is a clear advantage over classical IR or Raman spectroscopy. Since THz-waves are non-ionizing it is generally believed that this method is harmless for humans in contrast to x-rays. For that reason THz-spectroscopy was suggested for the detection of hidden drugs and explosives [3].

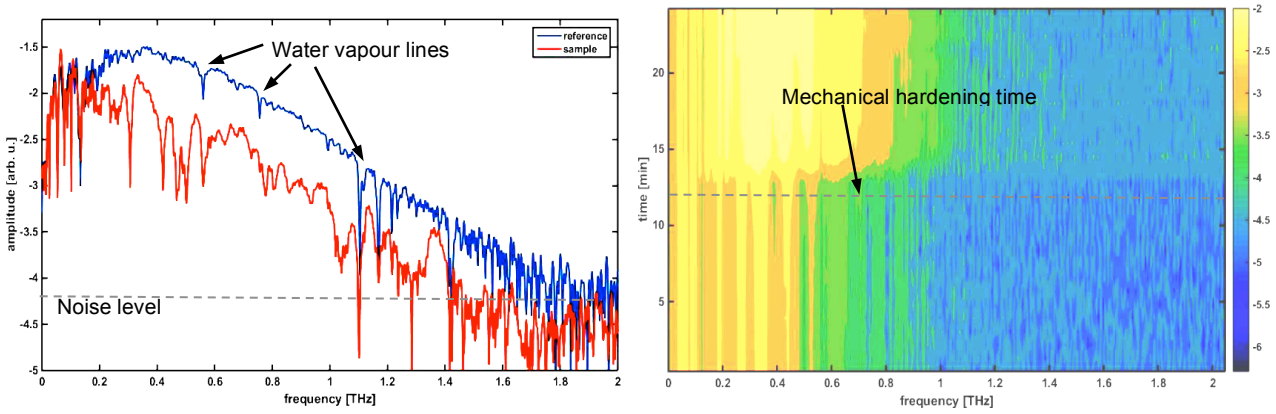

Fig.1: The left diagram depicts a reference and a sample spectrum after Fourier transform (FFT, amplitude in log-scale) of the waveforms (spectra in the time domain). The diagram on the right visualizes changing sample spectra against time. The PMMA sample became mechanically hardened after 12 minutes.

The results presented in here are mainly based on measurements conducted at Ruhr University Bochum (100 fs fibre laser, 1550 nm, delay line for pump-and-probe).

Several test cases have been studied. Both, the spectroscopic and mechanical experiments were conducted simultaneously under laboratory condition and in absence of sun light.

Fig. 1 presents the results of a selected experiment in a condensed way. At time zero both fractions (typically in separated tubes) of the commercial adhesive are pushed through a mixing nozzle into a standard cuvette. For the mechanical analysis approximately 1 cm^3 of the sample was separated and placed on a sheet of paper. The changing mechanical properties were roughly tested by the aid of a simple needle. The cuvette containing the remaining mixture was then placed in the optical pathway of the THz-beam set-up. The sample on the paper became recognizably hot after only 1.5 minutes, clearly an indication of the exothermic polymerization reaction. After 4 minutes the material became sticky and elastic. At 6 minutes it was hard to pierce into the sample and internally no residue stuck to the needle. After 7 minutes the colour of the material changed significantly from transparent to yellow forming a smooth surface shell. After 9 minutes the shell was already very hard and only approximately 1 mm was possible to imprint. After 12 minutes the sample cooled down and no piercing was possible any more.

Comparing these rough observations with the spectroscopic measurements one can conclude at first glance that the hardening time of say 12 minutes can be derived from the spectroscopic data where the spectra dramatically change after 13 minutes (cf. Fig 1, right). The changes in the spectra up to 13 minutes seem to be more concealed. The left diagram in Fig. 1 shows that the maximal dynamical range of the set-up was about 60 dB at 0.3 THz (signal amplitude ~-1.5 to noise level ~-4.5) linearly declining with a slope of 40 dB/THz. As a consequence, data above 1.3 THz should not be considered for deeper analysis. Between 0.2 and 1 THz the sample exhibits some spectral features which are clearly disconnected from the machine property or the known effect of water vapour absorption (cf. blue reference spectrum). These features can be studied in more detail.

The first results are very promising since there is a clear correlation between the altering mechanical property and changes in the THz-spectra. The presented set-up is already capable of detecting the hardening process of PMMA based two-component adhesive. Further studies should be dedicated to the influence of thickness of the mixture and the cuvette to better understand the problems of multi reflection. The work should also be extended to usage of bone cements and other two-component adhesives.

Acknowledgements:

Parts of the measurements were conducted by FH-Basis Research Equipment Program of the state of North Rhine-Westphalia: "Menlo Systems Terahertz-System K8 for a competence centre for non-destructive testing at Rhine-Waal University of Applied Sciences"

The following students were involved in the research project: Susan Aschenbrenner, Viola Knapp, Christoph Aschenbrenner, Vittoria Rossi, Tahmina Sultana.

References

[1] S. Koltzenburg, M. Maskos, N. Nuyken, “Polymere: Synthese, Eigenschaften und Anwendungen”, Springer Spektrum, ISBN 978-3642347726, 2013

[2] F. Hausding, Dissertation: "Development and material testing of a monomer free bone cement based on acrylate without heat release", 2007

[3] J. Jonuscheit, D. Molter, F. Ellrich, R. Beigang, F. Platte, K. Nalpantidis, „Revealing the invisible - identifying concealed substances by means of terahertz spectroscopy“, *Photonik international*, pp.12-15, 15.11.2013

31) Two Dimensional Graphene for Structural Sensing on Mechanical Surfaces

Volkan Yokaribas[(1)], Stefan Wagner[(2)], Max C. Lemme[(2)] and Claus-Peter Fritzen[(2)]

[(1)] Institute of Mechanics and Control-Engineering-Mechatronics
Faculty IV, University of Siegen,
D-57076 Siegen, Germany

[(2)] Institute of micro- and nanoelectronics,
Faculty of Electrical Engineering and Information Technology, RWTH Aachen University,
D-52074 Aachen, Germany

E-Mail: volkan.yokaribas@uni-siegen.de
Web: https://www.mb.uni-siegen.de/imr3/?lang=de

Abstract – Graphene has attracted great attention since its first discovery in 2004 and is currently considered to be one of the most promising materials for application in future products. The two dimensional (2D) material with a thickness of only 0.35 nm [1] has exceptional intrinsic properties, including very high conductivity [2], extraordinary mechanical strength with a stretchability of over 20 % [3] and a Young's modulus of 1.1 TPa [1]. Chemical vapour deposition (CVD) growth of graphene shows a potential for large-scale monolayer production with high uniformity [4]. The present work considers the resistance change of graphene with deformation due to geometrical alteration and change in charge density as well as mobility of the conductor, known as the piezoresistive effect [5]. Utilizing this effect very thin and transparent strain sensitive sensors can be developed for different application scenarios such as wearable sensors on human skins, microelectromechanical systems (MEMS) or flexible electronics.

The electromechanical behaviour of CVD-graphene in mono- and multilayer (up to 8 layers) are characterized in a biaxial deformation field by cantilever loads. CVD-graphene transfer from catalytic copper (Cu) substrate to the target substrate is described in Fig. 1. By adhesive bonding of the polyimide-graphene stack with super glue, the sensor is applied on the surface of the cantilever beam. This device provides a low-cost device for sensitivity tests of two dimensional materials with a well-defined strain field (Fig. 1).

The gauge factor (GF) quantifies the relative change of the resistance R due to the applied strain ε on graphene by the following equation:

$$GF = \frac{1}{\varepsilon}\frac{\Delta R}{R} \tag{1}$$

An optimal resolution in small strain ranges within the measurements is given by the Wheatstone bridge. The presented results in Fig. 2 show that two dimensional materials are suitable for structural strain sensing on metallic surfaces in macro-scale. A GF between 1 and 2 could be measured using a simple cantilever beam setup (length 300 mm and width 30 mm). The results are comparable to strain gauges made by bulk materials (e.g., GF of constantan measuring grid is approximately 2). Using such a setup compression and tension can be detected by graphene mono- and multilayer within the same value range as predicted by other authors [5]. The crystallographic orientation of graphene is independent of the direction of applied strain and therefore an isotropic piezoresistive effect can be assumed [5]. Further results provide also the detection of eigenfrequencies by excitation the cantilever during load tests. As a consequence graphene can also be used for vibration-based structural analysis.

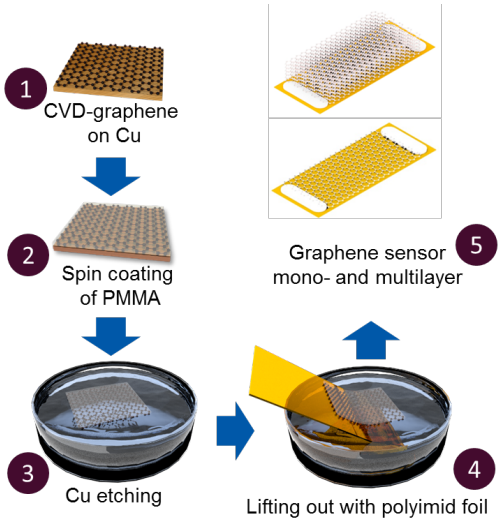

Fig. 1: Overview of main fabrication steps: 1) CVD grown graphene monolayer on Cu-foil 2) Spin-coating of polymethyl methacrylate (PMMA) on graphene-Cu stacked sheet 3) Cu-foil etched with sodium persulfate 4) Lifting out of PMMA-graphene stack with the polyimide substrate 5) Graphene encapsulated with PMMA contacted by silver electrodes

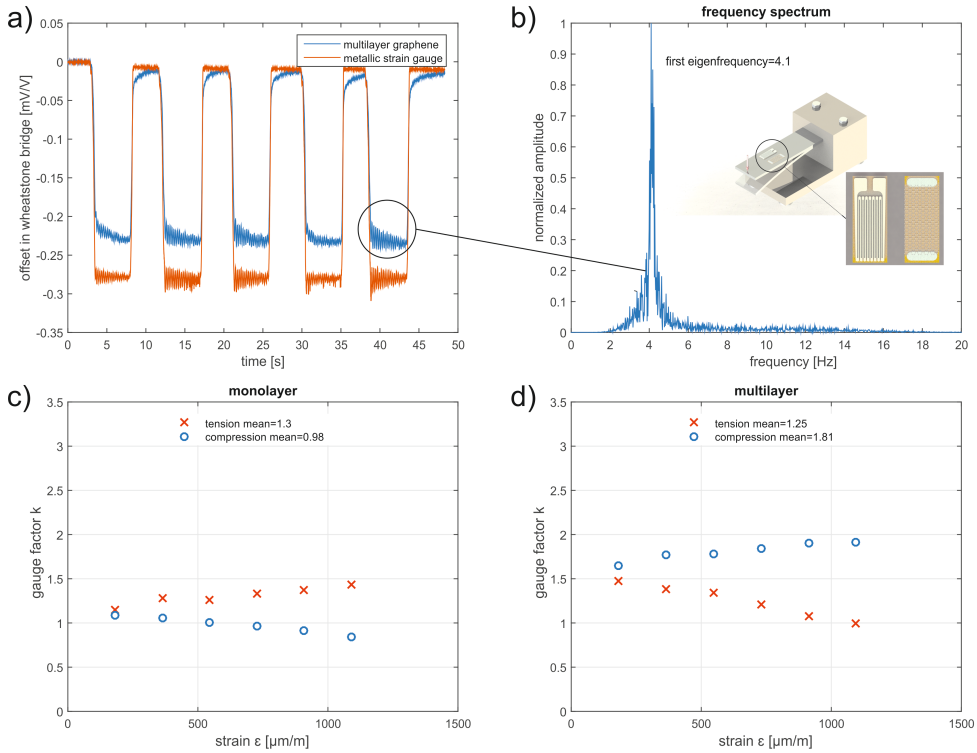

Fig. 2: a) electromechanical responses of multilayer graphene and metallic strain gauges for five load cycles b) determination of the first eigenfrequency during load test c)/d) GF of mono- and multilayer graphene for detection of tensile and compression strain from 0.02 % up to 0.11 %

References

[1] C. Lee, X. Wei, J. W. Kysar, and J. Hone, “Measurement of the Elastic Properties and Intrinsic Strength of Monolayer Graphene,” *Science, vol. 321, no. 5887*, pp. 385–388, Jul. 2008.

[2] H. Hirai, H. Tsuchiya, Y. Kamakura, N. Mori, and M. Ogawa, “Electron mobility calculation for graphene on substrates,” J. *Appl. Phys., vol. 116, no. 8*, p. 083703, Aug. 2014.

[3] H. Tomori, A. Kanda, H. Goto, Y. Ootuka, K. Tsukagoshi, S. Moriyama, E. Watanabe, and D. Tsuya, “Introducing Non-uniform Strain to Graphene Using Dielectric Nanopillars,” *Appl. Phys. Express, vol. 4, no. 7*, p. 075102, 2011.

[4] S. Kataria; S. Wagner; J. Ruhkopf; A. Gahoi; H. Pandey; R. Bornemann et al., "Chemical vapor deposited graphene: From synthesis to applications," *Phys. Status Solidi A 211 (11)*, pp. 2439–2449. 2014.

[5] A. D. Smith.; F. Niklaus; A. Paussa; S. Schroder; A. C. Fischer; M. Sterner et al., "Piezoresistive Properties of Suspended Graphene Membranes under Uniaxial and Biaxial Strain in Nanoelectromechanical Pressure Sensors," *ACS nano 10 (11)*, pp. 9879–9886. 2016.

[32] Fluid Composition Sensor Calibration

Ilya Kovalskiy(1), Gennady Lukyanov(1), Sergei Volkov(2)

(1) Department of Introscopy Technologies,
Faculty of Laser and Light Engineering, ITMO University,
197101, Russia

(2) ALL-RUSSIAN RESEARCH INSTITUTE OF FATS,
191119, Russia

E-Mail: gen-lukjanow@yandex.ru
Web: http://en.ifmo.ru

Abstract – The primary goal, which should be guided by the study of substances - those that surround the person, and those that he uses in one form or another in his activities - is to thoroughly study the properties of substances and materials. The properties of the materials are determined by their composition, taking into account both the main components and impurities. Moreover, often the properties of materials depend on the distribution of impurities or components over the volume of the substance (material).

In particular, a method for determining the composition and / or its variation by measuring the dynamic electrophysical characteristics and their subsequent processing is proposed to determine the composition of the liquid.

When an external electric field is applied in a liquid, the dipoles of polar molecules are able to line up along the direction of the applied field. The reorientation of molecules in the liquid along the applied field requires a different amount of energy (to overcome the frictional force between the molecules) for different molecules, this is due to the size and shape of the molecules, as well as their initial position. In our device a low frequency field is applied with a constant amplitude, but with a variable direction. The alternating direction of the field serves to ensure that all molecules in one period unfold by 180 °. The rate of polarization depends directly on the concentration of different types of molecules, hence, the change in the rate of polarization of the liquid can be judged on its composition. Previously, a series of experiments with water, in particular with various types of drinking water, was conducted to assess the quality of water purification.

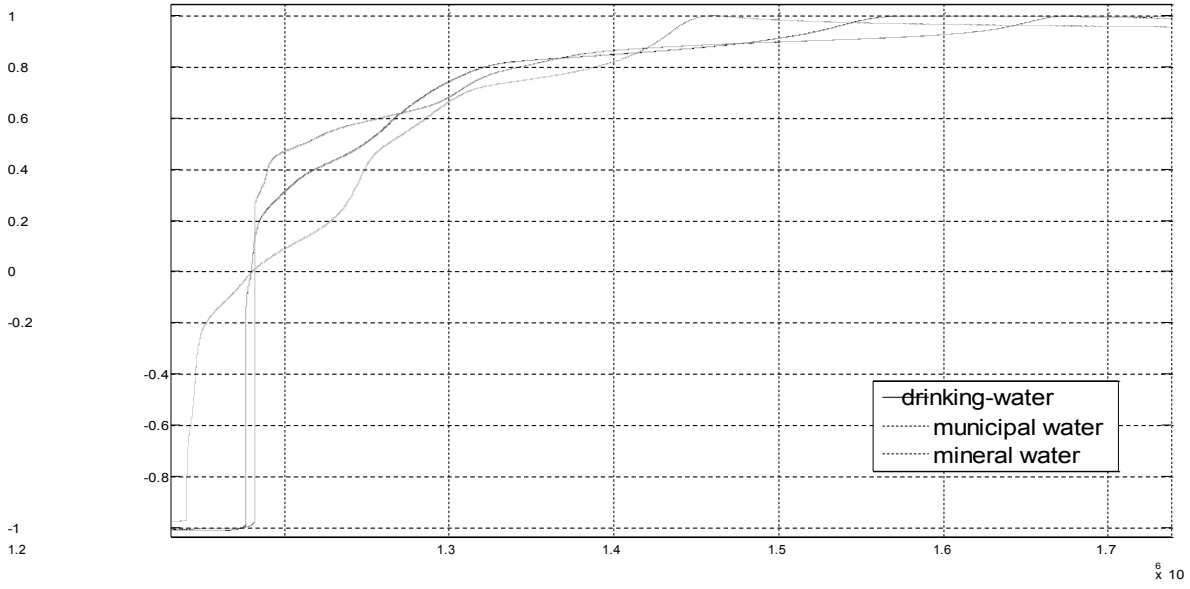

Fig.1: The output signal curves for the initial analysis of various water sample

Fig. 1 shows the output signal curves for the initial analysis of various water samples from which it can be seen that they strongly depend on the water composition.

Distilled water was used to calibrate the sensor and various components were added to it. Below are the results of the experiment when sucrose $C_{12}H_{22}O_{11}$ was added to the distilled water.

As can be seen in Fig. 2, the output signal of the sensor with the addition of $C_{12}H_{22}O_{11}$ strongly changes the shape of the curve, and the change in the $C_{12}H_{22}O_{11}$ concentration has a slight effect on the shape of the output signal, but strongly affects the amplitude.

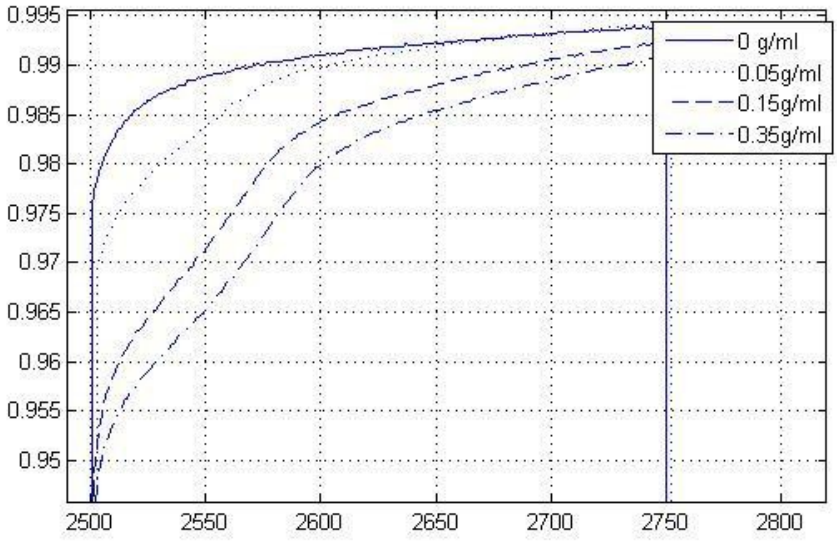

Fig.2: Results of the experiment with $C_{12}H_{22}O_{11}$.

References

[1] A. B. Rudakov, A. N. Ponomarev, K. K. Polyansky, A. Lyubarev, "The chemical composition and quality expertise," *Moscow. De Li print*, pp. 238, 2005.

[2] I.S. Kovalskiy, G. N. Lukianov, S. M. Volkov, "Sensor for determing the composition of fluid", *IEEE Workshop. Industrial and Medical Measurement and Sensor Technology Vehicle Sensor Technology (Sensorica 2016)*: *Abstractbook*, *IET*, pp. 69-71, 2016

33) Contactless Measurement of Distributed Permittivities in Inhomogeneous Materials

Ronny Peter(1), Gerhard Fischerauer(1)

(1) Chair of Measurement and Control Systems
Faculty of Engineering, University of Bayreuth,
D-95447 Bayreuth, Germany

E-Mail: ronny.peter@uni-bayreuth.de
Web: www.mrt.uni-bayreuth.de

Abstract – Determining the complex permittivity of a material sample is one of the standard uses of microwave measurements and several measurement methods were proposed in the last decades. However, no method for the precise measurement of inhomogeneous materials, especially without preparation of the sample, has been proposed before. For several applications, e.g. the monitoring of chemical processes, it would be very desirable to determine position depended permittivities in-situ.

The forward problem, namely finding the resonance frequencies and quality factors of an (longitudinal) inhomogeneous loaded cylindrical cavity with perfect conducting walls (Fig. 1), is known [1]. For each section, a scalar wave function is defined. To provide a solution, these have to be continuous at the interfaces of two neighboring sections. From these multiple boundary equations, a matrix equation is formed, whose determinant must vanish to have a non-trivial solution. A non-linear numeric solver varies the frequency until the determinant equals zero. The corresponding frequencies, which are solutions to this problem, are called resonant frequencies. Each belongs to a special electromagnetic field distribution or resonance mode. The eigenvector of a solution provides the information to correlate a resonant frequency to its mode.

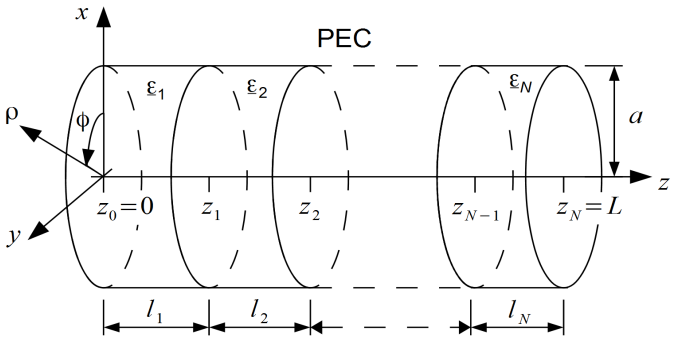

Fig.1: Schematic view of the used cavity geometry.

For solving the invers problem, the resonance parameters must be known. They are determined from measurements whereby the cavity is coupled to a network analyzer. The so measured S-parameters contain the resonance parameters. A crucial detail for the correct reconstruction of the permittivity distribution is the extraction of unloaded resonance parameters from the S-parameters. Since the presence of a coupling structure alters the observable resonance parameters (loaded resonance parameters), to extract the desired unloaded resonance parameters a proper de-embedding of the coupling is necessary.

In order to solve the inverse problem (finding the permittivity distribution from known resonance parameters) the determinant equation of the forward problem is used. As it is highly nonlinear, it needs to be linearized (first-order Taylor polynomial). To get a determined system of equations, the number of evaluated resonances has to be equal to the number of sections in the cavity. Starting from an initial permittivity distribution guess, the matrix equation is solved to acquire a first approximate solution. To enhance the precision, multiple iterations can be carried out. The whole inversion process is

closely related to the newton algorithm. Thus, it suffers from the same problems, like convergence problems, especially if the initial guess is not close enough to the final solution. The use of a damped newton style method, or alternative inversion methods like occam's inversion [2] have been tried also, but did not improve the inversion remarkably.

To verify the inversion method and to characterize its performance, multiple simulations were conducted. A typical application could be the monitoring of the oxygen storage in a three-way-catalyst (TWC). The permittivity value for a fully loaded TWC may be in the order of $\varepsilon_{r,full} = 2$ and for an emptied oxygen storage $\varepsilon_{r,empty} = 1.4$ [3]. The process of loading has a well-defined reaction front [4]. A cavity model (Fig. 2) was set up with the intent to mimic a partially loaded TWC by subdividing the cavity into five equidistant sections with different permittivities.

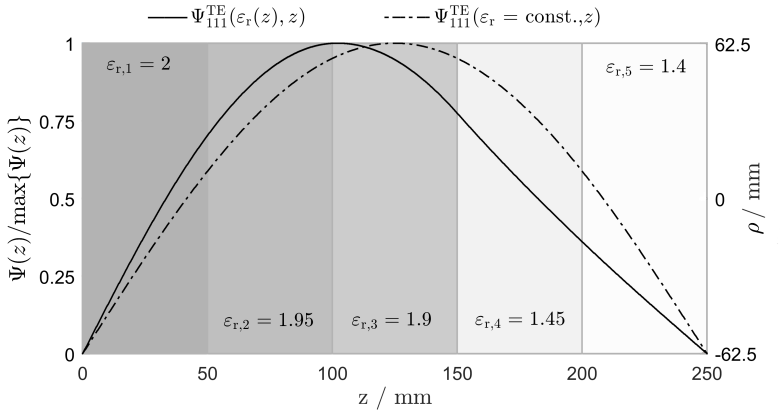

Fig.2: Cut through the cavity. The gray-shaded rectangles visualize the areas of different permittivity. The dash-dotted line shows the normalized scalar wave function for a homogeneous filled cavity, while the solid line shows the wave function resulting from the inhomogeneous loading.

As can be seen from the results in table 1, the inversion method works very well, as it can determine the permittivity distribution very precisely.

	n_1	n_2	n_3	n_4	n_5
$\varepsilon_{r,extracted}$	2.0013	1.9496	1.9004	1.4499	1.399
error / %	0.066	-0.023	0.021	-0.005	-0.07

Tab.1: Results of the inversion.

To summarize, it can be noted, that the permittivity distribution in inhomogeneous loaded cavities can precisely be determined by evaluating multiple resonances. The inversion method works fast and well, if one has knowledge of the unloaded resonance parameters and if one can provide a good starting point.

References

[1] T. Jungkunz, and G. Fischerauer, „Modellgestützte Bestimmung der komplexen Permittivität heterogener Katalysatoren im instationären Fall," *IEEE Trans. Antennas Prop.*, *16th GMA/ITG-Fachtagung Sensoren und Messsysteme,* Nürnberg, Germany, 2014.

[2] R.C. Aster, B. Borchers, and C.H. Thurber, *Parameter Estimation and Inverse Problems*. City: Elsevier, 2005.

[3] G. Fischerauer, A. Gollwitzer, A. Nerowski, M. Spörl, and R. Moos, „On the inverse problem associated with the observation of electrochemical processes by RF cavitiy perturbation method," *6th Int. Multi.-Conf. Systems, Signals and Devices*, 2009.

[4] T.S. Auckenthaler, *Modelling and Control of Three-Way Catalytic Converters*. ETH Zurich, PhD thesis, 2005.

[34] Application of the Method of the Dynamic Indention for Control Mechanical Properties of Composite Materials

A. Ilinskiy[(1),(2)], K. Stepanova[(1),(2)], and I. Kotovshchikov [(1),(2)]

[(1)] Department of Introscopy Technologies
Faculty of Laser and Light Engineering, University ITMO,
Saint Petersburg, Russian Federation

[(2)] Laboratory of technologies of nondestructive control,
Scientific and technical center "Etalon",
Saint Petersburg, Russian Federation

E-Mail: kotovshchikov.ilya@mail.ru
Web: http://en.ifmo.ru/en/

Abstract – Report is devoted to designing the device for dynamic indentation to control mechanical properties composite materials. Substantiates the prospects of applying the method of dynamic indentation. A brief description of the structure of the sensor the device. Experimental testing of the device showed the possibility of its use for the control of the mechanical characteristics of the elements composite materials.

One of the most prospective areas in the non-destructive testing is dynamic indentation which is used to control mechanical properties of composite materials [1,2]. Today composite materials find more and more wide application in different industries, especially in aviation and aerospace [3]. That's why control of mechanical properties of composite materials is so vital. To register the process of penetration of the indenter in tested material is used a device (Fig. 1), that enables a contactless method to determine the movement speed of the indenter when the contact of the shock interaction with the test product occurs. In the electrical part of the installation an analog-to-digital converter is used to gather the information from the signal induction sensor, which then is subject to further processing.

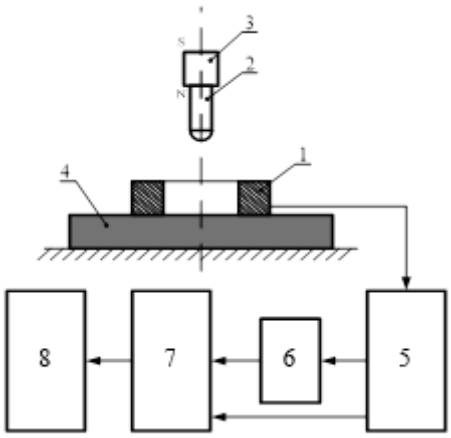

Fig.1: Device scheme: 1 - induction transducer; 2 - indenter; 3 - permanent magnet; 4 - the tested material; 5 - preliminary amplifier; 6 - synchronization unit; 7 - ADC; 8 - personal computer

In the experiment diagrams "contact force – penetration depth" (Fig. 2) were obtained for the three regions for multiple samples of composite materials. The experiment to determine the integral properties of composite materials revealed that the presence of macro defects in the object of control affects the results of measurements of the modulus of elasticity. The method of dynamic indentation allows one to determine the mechanical characteristics of components of a reinforced composite material, i.e. to exercise control on microstructural level and to assess the integrated mechanical properties at the macro level.

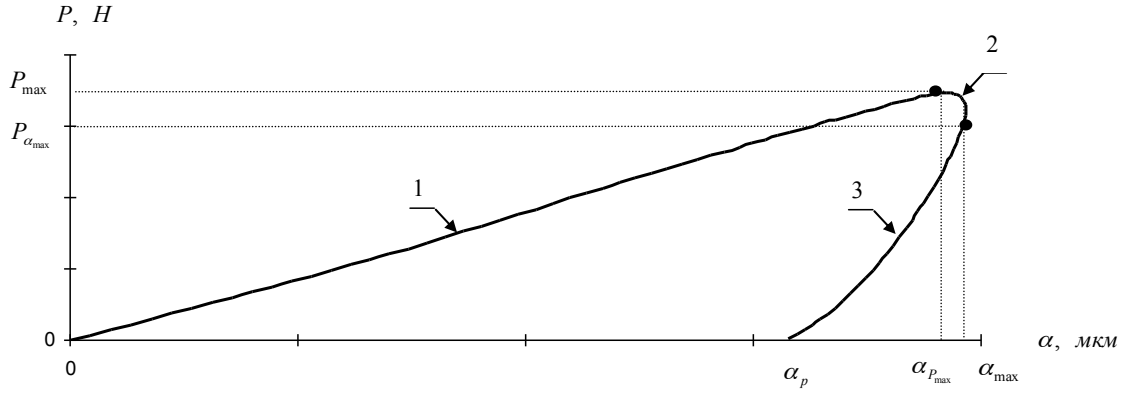

Fig.2: Diagram "contact force – penetration depth": 1 - loading curve; 2 - viscoelastic unloading curve; 3 - elastic discharge curve

References

[1] W.C. Oliver, G.M. Pharr, “”, *J. Mater. Res.*, pp. 1564, 1992.
[2] S.I. Bulychev, V.P. Alekhin, “Ispytaniye materialov nepreryvnym vdavlivaniyem indentora [Testing of materials by continuous indenting indentation],” - Moscow: Mashinostroyeniye, p. 224, 1990.
[3] A.I. Monokhin, “Kompozitsionnyye materialy [Composite materials],” - Moscow: «Nauka», 1981.

35) Temperature Measurement of an Object Using Blackbody Radiation with Compensation of Impedance Mismatch

Dawei Xu[(1)(2)], Klaus Thelen[(1)], Jörg Himmel[(1)], Daniel Erni[(2)]

[(1)] Institute of Measurement Engineering and Sensor Technology,
University of Applied Sciences Ruhr West,
D- 45479 Mülheim an der Ruhr, Germany

E-Mail: dawei.xu@hs-ruhrwest.de, klaus.thelen@hs-ruhrwest.de,
joerg.himmel@hs-ruhrwest.de

[(2)] General and Theoretical Electrical Engineering (ATE),
Faculty of Engineering, University of Duisburg-Essen,
D-47048 Duisburg, Germany

E-Mail: daniel.erni@uni-duisburg-essen.de

Abstract – In this talk a measurement method for non-contact temperature monitoring of an object in an electromagnetic shielded cavity is introduced. The thermal noise of the measured object can be determined by using a coupling loop at 600 – 2000 MHz (microwave bandwidth) inside the cavity. The scale of the measurement for very low radiant energy from the object is defined by the physical concepts by radiometer, and the coupling rate between object and coupling loop [1]. In order to measure the correct absolute temperature, the low noise amplifier (LNA) and radiometric detector needs to be calibrated first. Since the object may change its physical properties, like electrical properties or position, the coupling rate needs to be monitored frequently during the measurement. The mode of the electromagnetic wave in the cavity can also be influenced, when the wavelength and the dimension of the cavity are almost the same size. Measuring the impedance of the coupling loop within the cavity can help to obtain the coupling rate, which is used for calculating the scale from the object to the radiometer. With the corrected scale the absolute temperature can be exactly calculated.

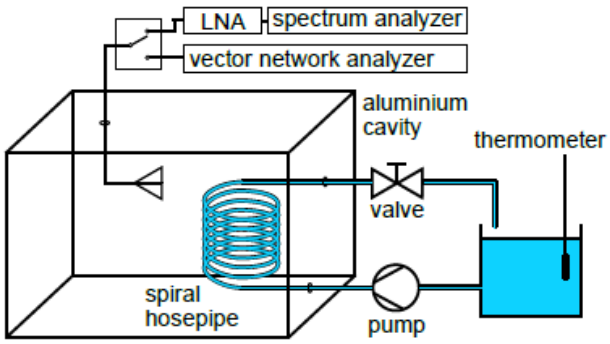

Fig.1: Experimental setup

Fig.1 shows the experimental setup. The weak thermal noise coming from the object is amplified by a cascade LNA. A spectrum analyzer is used for measuring the thermal noise after it was amplified by the LNA, the impedance is measured with a network analyzer. They are measured separately after the calibration of the instruments. During the experiment the power supply and room temperature is kept at a constant level to keep the intrinsic noise of the measure system strictly stable. The intrinsic noise therefore can be considered as a constant parameter in the calculation.

This measurement method is especially suitable for real-time temperature monitoring of objects which are placed randomly in the cavity, and are changing their conditions continuously. Because of the large measurement bandwidth, the electromagnet wave has a variable penetration depth, which means the sensor can ‘see’ the temperature inside the object. This measurement method could be used for example to monitor industrial production lines for quality control purposes or to monitor warmed plasma to avoid overheating [2] in medical applications.

References

[1] Richard C Willson, “Active cavity radiometer”. *Applied Optics*, 12(4):810–817, 1973.
[2] Dawei Xu, Dirk Rüter, and Daniel Erni. „Non-contact radiative temperature monitoring of blood plasma and packed red blood cells in a powerful microwave environment”, 1 st. in YRA MedTech Symposium (YRA-MedTech 2016), YRA–Young Researchers Academy MedTech in NRW, April, volume 8, pages 66–67, 2016.

[36] Research and Development of Method and System of Measurement of Displacement of the Facilities Control Points Taking into Account External Impact Factors

Dinara Shayakhmetkyzy[1], Aleksey V. Fedorov[1], Igor O. Krasnov[2]

[1]Department of Introscopy Technologies
Faculty of Laser and Light Engineering, University ITMO,
Saint Petersburg, Russian Federation

[2]The Scientific and Technical Center «Etalon» LLC, Saint Petersburg, Russian Federation

E-mail: dinarashayakhmetkyzy@mail.ru
Web :http://en.ifmo.ru/en/

Abstract–A method is allowing metering of movements of externally influenced control points of inspected facility with required accuracy is described.Metering of movements of control points located at the surface of the inspected facility is required for assessment of its technical condition. The method is based on joint use of metering results of accelerometers and ultrasonic sensors of linear movements. For implementation of this method hardware-software complex was developed.

As of today assessment of displacement (deformation) of responsible facilities is one of the most actual task in the field of their reliability and safety provision. Various high-rise facilities, such as ventpipes, supports of antenna structures, meteorological towers, etc. can be referred to such types of the facilities. These facilities operate for perception of mainly horizontal (transverse) loadings. In certain cases the specificity of the facilities operation requires using non-contact method of displacement measurement. At that in order to provide set accuracy of measurement of displacements of control points of investigated facility, as well as it is required to take into account possible displacements of metering devices towards the facility itself.

Consideration of external factors and loadings impact on metering device in order to provide set accuracy of measurement is one of the most important problems during assessment of displacements and deformations of control points of investigated facility. One of such factors is oscillation and vibration occurrence because of wind and other loadings impact [3]. The significance of the problem of research is determined by the fact that specified phenomena can lead to significant error in the result of the measurement of displacements.

The objective of this work is development of method and system, which allow metering displacements of control points of investigated facility with set accuracy under external factors impact.

Analysis of the current contact and non-contact methods of measurement of linear displacements of the facilities was carried out within the researches. Each method has its advantages and disadvantages. The general advantage of non-contact measurement methods is absence of mechanical impact on investigated facility and negligibly small persistence, which is peculiar to contact methods [4].

Currently optical, ultrasonic and induction methods of measurement are mostly widely spread [2].

Ultrasonic method is under consideration in the report. This method is based on measurement of propagation time of ultrasonic acoustic wave in the space. Instrumental error of measurement of distance to investigated facility by modern ultrasonic sensors does not exceed 0.1mm. As of today together with optical, the ultrasonic sensors, perhaps, are more multi-purpose and process non-contact metering device [1].

Consideration of external factors during assessment of absolute displacements of control points of the facility with set accuracy is carried out by determination of dependence of value of distance to the

facility on frequency and amplitude of oscillations of metering device. Whereas obtained dependences allow calculating the required correction factor and whereby to compensate displacements of metering device, decrease errors and increase accuracy of measurement.

In order to implement this project it is proposed to allow the distance to be determined towards stationary facility. Stand for experimental working-out of the method was developed, it allows imitating oscillation impact with set amplitude and frequency, occurring due to external factors impact.

Therefore the system for assessment of error of measurement of displacements of control points of investigated facility taking into account external factors impact was proposed.

References

[1] V.G. Datchiki,“Ustroystvo i primeneniye,”*M.: Mir.*, pp. 192,1989

[2] A. A. Gorbatov, G. E. Rudashevskiy,“Akusticheskiye metody izmereniya rasstoyaniya i upravleniya,”*Energoizdat.*. pp. 207, 1981

[3] M.A. Zakharchenko, A.V. Korgin. “Sozdaniye eksperimental'noy sistemy GPS vysotnogo zdaniya pri vetrovom vozdeystvii,”*MGSU,*no. 8, pp.200 – 205. 2011 November.

[4] D.A. Loktev. “Razrabotka i issledovaniye metodov opredeleniya parametrov statichnykh i dvizhushchikhsya obyektov v sisteme monitoring*”. Dissertation university of MGUTS*, Moscow, 2015.

37) Analysing the Electric Potential Distribution for Bipolar TURis

Tino Morgenstern[(1)], Ibrahim Cakir[(1)], Olfa Kanoun[(2)] ,Stephan. Klöckner[(3)] and Jörg Himmel[(1)]

[(1)] Institute of Measurement Engineering and Sensor Technology
University of Applied Sciences Hochschule Ruhr West,
D-45479 Mülheim an der Ruhr, Germany

[(2)] Faculty for Electrical Engineering and Information Technology, Technische Universität Chemnitz,
D-09126Chemnitz, Germany

[(2)] Olympus Winter & Ibe GmbH
D-22045 Hamburg, Germany

E-Mail: Tino.Morgenstern@hs-ruhrwest.de
Web: www.hochschule-ruhr-west.de

Abstract –

In urological treatment procedures the transurethral resection (TUR) is a standard technique. Both, monopolar and bipolar electrosurgical systems are used for TUR. Viewing the monopolar technique the electrical and physical processes are well understood. Focusing on the bipolar TUR technique there is no efficient data base for the assessment of the processes. Researching the bipolar surgery systems a multi-electrode measurement system (MES) has been developed by [1]. This MES represents the reference measurement system in this study. Nevertheless the MES has the disadvantages of 24 measurement electrodes in fixed positions around the resectoscope. To analyse the influence of this large number of electrodes on the potential distribution a quad-electrode measurement system (QES) as well as a finite element model was developed and a comparison test of the measuring results has been carried out.

Introduction / State of the Art:

For transurethral resection of the prostate (TURP), bipolar electrosurgical systems are used. A typical essential system consists of an electrosurgical generator and a resectoscope with a resection electrode. Here currents with frequencies above 300 kHz are applied to the target tissue. The high current densities cause the destruction of the united cell structure which leads to the cutting effect. In this study bipolar systems are under investigation. As a model isotonic saline solution is representing the treatment area as state of the art for laboratory setups. In [1] the potential distribution in this area was measured with a multi-electrode system (MES). The calculation of electric field strength and power loss density in tissue showed that electro thermal influences at the resectoscopes shaft are not the reason for injuries at the urethra as discussed in literature [1].

The main disadvantage of the MES is the fixed position of the measurement electrode with the smallest radial distance of 19.25 mm to the resectoscope shaft. With this setup it is only possible to get extrapolated information of the electric field strength close to the resectoscope shaft, the same applies for the information close to the resection electrode. Therefore a new measurement system is needed. A new laboratory setup with 4 measurement electrodes (QES) and a finite element model were developed. The QES allows measurements in the area around the resectoscope with distances smaller than 3 mm to the resectoscope surface.

The focus of this study is to find out the effect of the measurement electrodes in the isotonic saline solution on the electric potential distribution. By the results of the MES, the QES and the finite element analysis the influence of the measurement systems can be assessed.

Material and Methods: Using the finite element method it is possible to simulate a measurement system based on electrodes without any special dimensions. The fundamental equations for quasi-static electric flow fields are listed in (1) to (3)

$$\mathrm{J} = \boldsymbol{\sigma}\,\mathrm{E} \tag{1}$$

$$\frac{\boldsymbol{\partial \rho}}{\boldsymbol{\partial t}} + \boldsymbol{\nabla} \cdot \mathrm{J} = 0 \tag{2}$$

$$\boldsymbol{\nabla} \cdot (\boldsymbol{\varepsilon}\,\mathrm{E}) = \boldsymbol{\rho} \tag{3}$$

Using the charge relaxation theory [3] it gets obvious that the relaxation time is much smaller than the external time scale with respect to the signal frequency of 350 kHz. Hence quasi-static approximation can be used. The following equation (4) results from neglecting the external current densities and the time static study types. This equation will be solved.

$$-\boldsymbol{\nabla} \cdot \boldsymbol{\sigma} \boldsymbol{\nabla} \mathbf{V} = \boldsymbol{Q_j} \tag{4}$$

The simulation model solves a current conservation equation which is based on the Ohm's law. Here the scalar electric potential is the dependent variable. The surface potential is the defined value on the resection electrode with the ground potential on the resectoscopes surface. In this model the influences of the measurement electrodes are neglected. The electric potential evaluation is realised by a point evaluation. The electric potential results from the material properties and the current density in the isotonic saline solution.

Results and Discussions: In the following the electric potential distribution, depending on the distance to the resectoscope is evaluated. For the distance to the resectoscopes surface the values 19.25 mm, 36.25 mm and 53.25 mm were user-defined. In z direction the measurement electrode tip and the loop of the resection electrode are at the same position. The verified results from the MES will represent the reference values for the Data evaluation. The relative deviation of the QES results and the simulated results to the MES are listed in *Table 1.*

	r = 19.25 mm	r = 36.25 mm	r = 53.25 mm
(MES-QES)/(MES*100)	59.2 %	37.7 %	13.6 %
(MES-SIMU)/(MES*100)	46.9 %	26.0 %	-0.7 %

Table 1: Relative deviation

With respect to the reference values the maximum relative deviation amounts 59.2 % for the smallest distance to the resectoscope surface. The relative deviation decreases with increasing distances. Viewing the deviation of the QES and the simulation the results are in a similar scale. Consequently it seems that the influence of the measurement electrodes increase with smaller distances to the resectoscope surface. This is an important fact for our research of the potential distribution close to the resection electrode.

References

[1] Christoph Knopf, Methodik zur Analyse der elektrischen Feldverteilung und thermischer Vorgänge bei der bipolaren transurethralen Resektion. Dissertation University of Chemnitz, Chemnitz, February 14, 2014.
[2] C. Knopf, J. Himmel, F. Hochgeschurz, S. Klöckner, K. Thelen and O. Kanoun "Power Loss Density Distribution in Biological Tissue to Analyse Processes in Electrosurgery," SSD'14 1569847113, pp. 1-4, February 2014.
[3] Comsol, Comsol AC/DC Module User`s Guide 5.0. City: Comsol Multiphysichs, 2014.

2nd YRA MedTech Symposion

[1)] Measuring, Clustering and Classifying Pores of Surgical Meshes with an ImageJ Plug-in

Sebastian Vogt[(1)], Carolin Ritter[(2)], Jürgen Trzewik[(3)], Klaus Brinker[(4)]

[(1)] University of Applied Sciences Hamm Lippstadt
Marker Allee 76-78, 59063 Hamm, Germany
E-Mail: Sebastian.Vogt@stud.hshl.de

[(2)] University of Applied Sciences Hamm Lippstadt
E-Mail: Carolin.Ritter@exam.hshl.de

[(3)] University of Applied Sciences Hamm Lippstadt
E-Mail: Juergen.Trzewik@hshl.de

[(4)] University of Applied Sciences Hamm Lippstadt
E-Mail: Klaus.Brinker@hshl.de

Abstract

The pore structure and pore size is a crucial characteristic of surgical meshes. A huge amount of different approaches for mesh classification based on the pore size or materials are available. It is hard to use these classifications because of the big variety in knitting structures and pore shapes. Therefore, a new approach is applied which characterizes pores based on two parameters: the biggest inscribed circle (Fig.1 (a)), the smallest circumscribing circle (Fig.1 (b)) and the area (Fig. 1 (a)). These parameters are identified with the help of ImageJ. Therefore, a plug-in for ImageJ has been developed which needs a scaled binary input image to be able to characterize pores.

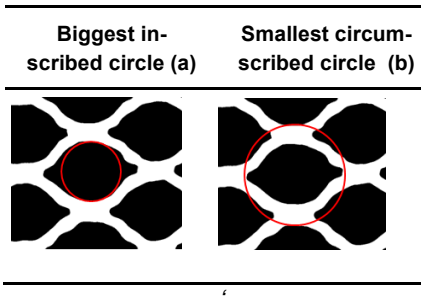

Fig.1: Measurements of a pore as defined for the ImageJ plug-in

The biggest inscribed circle is computed by using the Euclidean Distance Map (Fig.2 (a)) based on an algorithm of Leymarie and Levine [1] and the smallest circumscribing circle is computed by using the convex hull (Fig.2 (b)) of the pore and applying the mathematics of Jon Rokne's "An easy bounding cicle" [2].

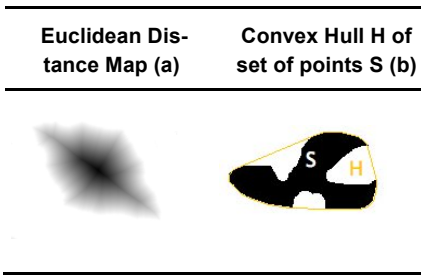

Fig.2: EDM and Convex Hull

Using these measurements of the pores, two different algorithms are applied to cluster the pores in categories, each category with similar pores, and a nearest-neighbour algorithm is applied to classify the pores and put them in categories, too. The categories are determined by the diameter of the biggest inscribed circle, the diameter of the smallest circumscribing circle and the ratio of these, which is an indicator of the pore's shape.

For clustering the K-Means and the DBSCAN (Density Based Spatial Clustering of Applications with Noise) algorithms are applied.

The K-Means algorithm is in analogy to "Least squares quantization in pcm" by Lloyd [3]. The expected number of categories has to be chosen manually at first, then the algorithm aims to minimize the total of squared deviations of the data points to the centers of the cluster. The formula

$$E = \sum_{i=1}^{k} \sum_{x_j \in C_i} d(x_j, \mu(C_i))$$

is optimized, where k is the number of clusters, x_j is a data point from Cluster C_i and $\mu(C_i)$ is the center. The runtime complexity is O(t).

The DBSCAN is based on „A Density-Based Algorithm for Discovering Clusters in Large Spatial Databases with Noise" [4]. The main idea behind the algorithm is, that the density of data points within a cluster is higher than outside the cluster. Unlike the K-Means algorithm, the DBSCAN does not need to know the number of cluster before being applied, it clusters the data points automatically.

For classifying the pores, the procedure is different. Before letting an algorithm put each pore in a category, at least one pore has to be chosen manually to represent a category. Afterwards the nearest-neighbour algorithm is applied to find similar pores for each chosen category. To be able to reuse results and make them comparable despite having collected a vast amount of data, the categories are sorted by the diameter of the biggest inscribed circle. The result is marked by colour. If a pore does not belong to the category the user wants it to, the category of the pore can be changed manually.

Moreover, the plug-in generates an ImageJ results table which contains information about the amount of pore types, the ratio of inner and outer diameter, the inner diameter (mm), the outer diameter (mm), the area (mm^2) and the percentage of the total area which is covered by the pore types. Furthermore, a histogram shows the percentage of covered area by the single pore types.

References

[1] F. F. Leymarie and M. D. Levine, "A Note on "Fast Raster Scan Distance Propagation on the Discrete Rectangular Lattice"," in CVGIP Image Understanding, Orlando, Academic Press, Inc., 1992, pp. 84-94.
[2] J. Rokne, "An easy bounding circle," in Graphic Gems II, USA, Academic Press, Inc., 1992, pp. 14-16.
[3] S. P. Lloyd, „Least squares quantization in pcm." IEEE Transactions on Information Theory, Bd. 28, Nr. 2, S. 129-137, 1982.
[4] M. Ester, H.-P. Kriegel, J. Sander und X. Xu, „A Density-Based Algorithm for Discovering Clusters in Large Spatial Databases with Noise" in Proceedings of 2nd International Conference on Knowledge Discovery and Data Mining, München, LMU München, 1996.

[2] Multi-atlas Based Clavicle Segmentation in Chest Image Data

Cosmin Adrian Morariu, David Struck, and Josef Pauli

Intelligent Systems,
Faculty of Engineering, University of Duisburg-Essen,
D-47057, Germany

E-Mail: adrian.morariu@uni-due.de
Web: www.is.uni-due.de

Abstract – This contribution explores the capabilities of the multi-atlas based segmentation technique [1] to delineate clavicle bones in chest radiographs. The segmentation is carried out within 299 images which have been made available in [2] together with the corresponding ground truth for the clavicle bones (see Fig.1 left). The segmentation process is made difficult by the superposition of several anatomical structures, which is inherent in X-Ray data. Strong noise and artefacts caused by pathologies, objects (e.g., necklaces) and the image acquisition technique also contribute to rendering clavicle detection as a challenging task. In addition, the strongest edges are outside the image area relevant for clavicle segmentation (see Fig. 1 original images). In [3], a combination of different approaches (including classification-based methods and statistical appearance models) is applied sequentially. This work examines to what extent a uniform method can be contrived to solve the problem. We propose a three-stage registration method embedded within a multi-atlas approach.

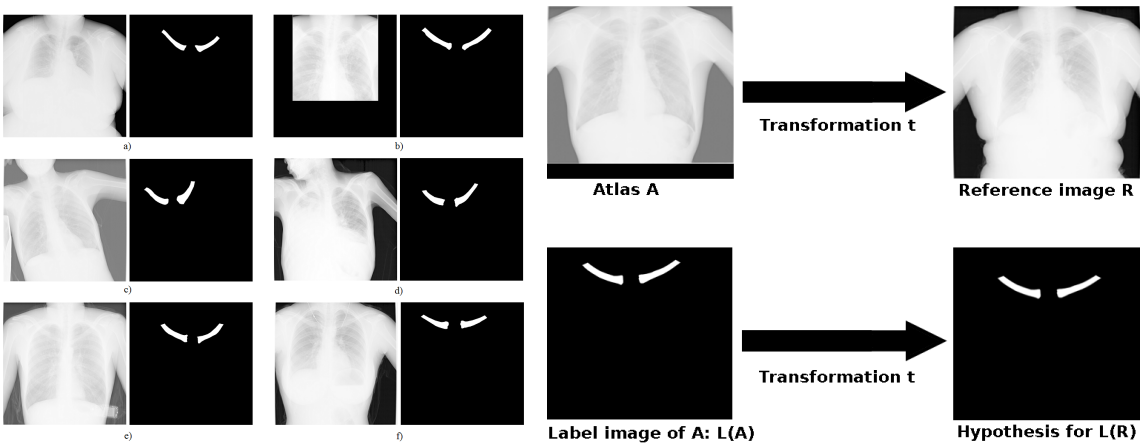

Fig.1: Left: Original images and corresponding ground truth for the clavicle bones. Right: The principle of atlas-based segmentation. After registration of the template image (atlas A) with the reference image R we obtain the transformation t. Subsequently, within the label propagation process, this transformation is applied to the ground truth image L(a), leading to the presumed position of the clavicle bones in the reference image R.

To segment a reference image, the remaining 298 images serve as atlases (template images). For each atlas, three registrations take place with the respective reference image. A schematic registration process [4] is illustrated in Fig.2 (left). A coarse localization of the clavicles is achieved by means of a first affine registration using the full template and the entire reference image. In order to transfer the clavicle ground truth, which has been manually annotated in the atlas, to the reference image, the transformation determined during registration is applied to the label image of the template (label propagation). This process is depicted schematically in Fig.1 (right). In the second stage, an additional affine registration is performed on a smaller region-of-interest (ROI) around the clavicles. The transformed label image of the first registration stage is used to determine the ROI. Finally, in the third stage, demons-based registration [5] also allows local, non-linear deformations. The resulting dis-

placement field transforms the label image computed after the second stage and yields the final segmentation result for the atlas. In this way, a hypothetical segmentation of the clavicle bones is determined for the reference image by means of all atlas datasets. In order to merge the individual atlas segmentations, various label fusion methods were tested. In the unweighted variant, each propagated label is taken into account with the same weight (Fig.2 right). Alternatively, weighted (global or local) voting variants were contrived. The weight is determined for each atlas by means of the mutual information, which has been employed as registration metric.

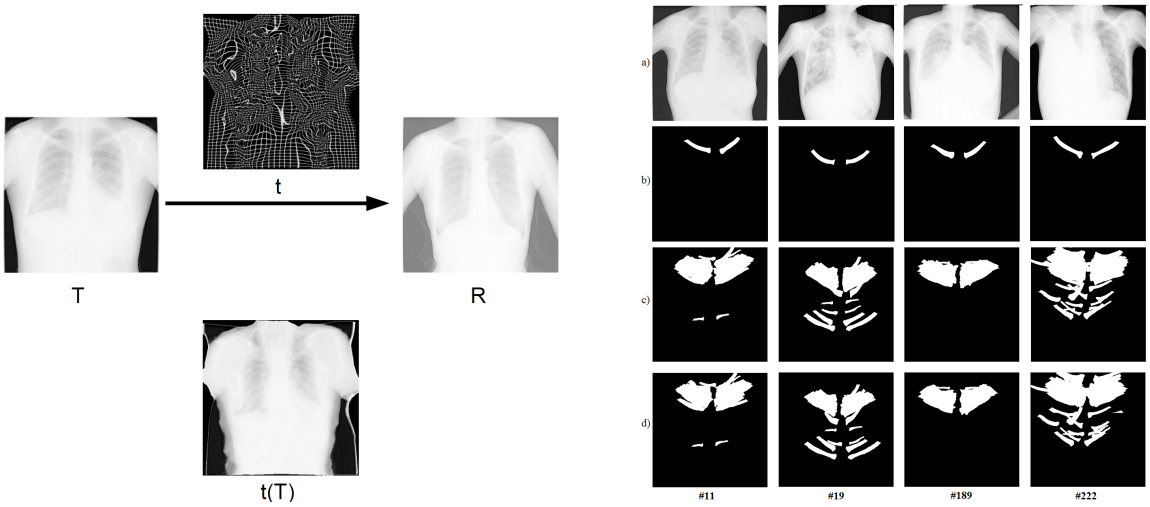

Fig.2: Left: Schematic representation of the registration process. Template image T (atlas) and reference image R are registered using mutual information as metric. The yielded transformation t leads to the transformed template image t(T). Right: Unweighted label propagation of atlas registrations. Original images in top row, corresponding ground truth for the clavicle bones in second row, propagated labels after first affine registration in third row, respectively propagated labels following the second affine registration in bottom row.

The best results were obtained by unweighted voting. Overall, the highest Dice Similarity Coefficient DSC = 0.79 ± 0.12 is yielded using a 35% voting score. In other words, a pixel in the reference image is considered to belong to the clavicle bone, if at least 35% of the 298 propagated atlas labels have voted accordingly. The mean DSC value of 79% demonstrates that the multi-atlas based segmentation technique can be successfully employed towards the localization of clavicle bones in chest X-Ray images. However, a subsequent fine-tuning will be required in order to precisely extract the bone contours.

References

[1] J. E. Iglesias and M. R. Sabuncu, "Multi-atlas segmentation of biomedical images: a survey.", *Medical image analysis*, vol. 24, no. 1, pp. 205-219, 2015.
[2] L. Hogeweg and B. van Ginneken, Challenge for Chest Radiograph Anatomical Structure Segmentation (CRASS12): https://crass.grand-challenge.org/ (accessed April 27, 2017).
[3] L. Hogeweg, C. I. Sánchez, P. A. de Jong, P. Maduskar and B. van Ginneken, "Clavicle segmentation in chest radiographs.", *Medical image analysis*, vol. 16, no. 4,, pp. 1490-1502, 2012.
[4] J. Modersitzki, *Numerical methods for image registration.* Oxford University Press, 2004.
[5] J.P. Thirion, "Image matching as a diffusion process: an analogy with Maxwell's demons.", *Medical image analysis*, vol.2, no. 3, pp. 243-260, 1998.

3) Estimating Image Quality for Bone Scintigraphy Using Machine Learning

Christina Kolossow[(1)], Frank Horbach[(2)] and Klaus Brinker[(1)]

[(1)] Hochschule Hamm-Lippstadt
D-59063 Hamm, Germany

[(2)] Radiologisch-Nuklearmedizinische Gemeinschaftspraxis am evangelischen Krankenhaus Hamm,
D-59063 Hamm, Germany
E-Mail: christina.kolossow@stud.hshl.de
Web: www.hshl.de

Nuclear medicine is a less known sector of the healthcare industry which allows to visualize metabolic processes in contrast to standard MRT and CT scans. For a nuclear medicine examinations it is necessary to inject organ specific radiopharmaceuticals into the vein of the patient. [1]

Bone scintigraphy is globally the most frequently used nuclear medical examination. It enables the diagnosis of rheumatism, endoprothesis loosening and small bone metastases earlier than other imaging methods. Bone scintigraphy is divided into three phases: the perfusion, the bloodpool and the mineralisation phase. In the mineralisation phase the gamma camera captures the emitted radiation from the bones and creates a two-dimensional image of a skeleton. But there are some issues which can influence the quality of this image. For example the scintigraphy can be noisy or partly pale due to a low dose of the radiopharmaceutical. Moreover, possible movement and contamination artefacts can degrade the quality. These are some issues which can lead to inaccurate or wrong diagnoses. Therefore a precise and objective analysis of the images could potentially lower the rate of wrong diagnoses. In this bachelor thesis, the mineralisation phases of bone scintigraphies are analysed and categorized with respect to their quality. [2]

In a previous project work, different methods have been implemented. These methods translate visual features like blur and edges into numeric data to facilitate machine learning. [3]

Machine learning methods are computer systems which can learn automatically and make predictions based on data. There are numerous variations of learning algorithms. Some of them are used to distinguish between six levels of image quality. The algorithms access the dataset of the implemented methods and compare their results with the classification of a nuclear medicine specialist concerning the image quality. [4]

Overall, seven image properties were analysed with thirteen implemented methods: the information entropy, the proportional black content, the line profiles, the image noise, the sum of edges, the compactness of the depicted object and some histogram attributes. Before the algorithm can gather the image properties the scintigraphies should be edited. Many raw bone scintigraphies have poor contrast and make a diagnosis impossible. In practice the radiology assistants typically adjust the contrast for each image individually. The use of these manually edited images would distort the results. Consequently the raw scintigraphies are optimized using histogram equalization. Moreover, the images should have the size of the depicted skeleton because superfluous pixels would alter the results of some implemented methods. The proportional black content, the line profile and the noise would be much smaller. Additionally the edge detection and the histogram would be affected. Only the information entropy and the compactness of the depicted object are consistent. Nevertheless not every image property makes sense to determine image quality. 26 bone scintigraphies – thirteen good and thirteen bad samples – are used to analyse the methods. Ideally, the values of the good samples should be notably different from the results of the bad ones. In our experimental evaluation this hypothesis has not been confirmed. But some image properties are still useful to distinguish image quality.

The ratio of the white pixels, the image focus, the noise, the compactness of the depicted skeleton and the sum of the edges are used as features for the dataset. The sixth attribute is the individually given grade by the nuclear medicine specialist for every scintigraphy.

Selected machine learning algorithms are using this dataset to distinguish between relative good and bad scintigraphies. To gain as much information as possible five rather different algorithms were tested.

The naive Bayes classifier is based on applying Bayes' theorem with strong (naive) independence assumptions between the features. It calculates any type of probability within the dataset and formulates prior probabilities to classify new objects. [4]

- The ***k*-nearest neighbours** algorithm (*k*-NN) categorizes an object by a majority vote of its neighbours. Imagine the training objects are plotted in a coordinate system depending on their features. To classify a new object, it must be added to this mental coordinate system. Afterwards the algorithm analyse the membership of its *k*-nearest neighbours and assigns the new object to the class most common among them.[4]
- A **decision tree** is built of leaves and branches. The leaves represent class labels and branches represent the conjunction of features that lead to those class labels. This algorithm arranges the features by importance and divides the dataset regarding the end property. For classifying new objects, the algorithm runs through the decision tree along the branches.[4]
- **Support vector machines** separate two classes with a linear discriminant function. Very often it is impossible to divide the dataset in the original feature space. Thus the kernel trick is used to map the inputs into high-dimensional feature spaces. A new object is classified by adding it to this space and determing its position with respect to the hyperplane.[5]
- A **perceptron** transforms the basic functions of a nerve cell into a mathematical model. It consists of an input function which is affected by weighting factors and an activation function. The activation function determines if there should be an output signal or not. Several linked perceptrons are called multilayer perceptrons which form more complicated neural networks. By traversing the multilayer perceptron an object can be classified. [5]

With the given dataset the different machine learning algorithms achieve quite similar results. The Support vector machine can classify 34.42% of the scintigraphies according to their predetermined quality. The k-nearest neighbour algorithm matches the image quality slightly better with 37.21%. According to our experimental results, the evaluated algorithms are almost equally suited for this problem. Nonetheless, there are still options optimize on various settings of the algorithms. Furthermore, the dataset could be more optimized as well. For example, it can be larger and more balanced in quality because most available images of the dataset were good examples.

This bachelor thesis offers an introduction to the automated determination of image quality. Several similar black and white images were analysed with the possibility of six grades. Five different machine learning algorithms can categorize about 36% images correctly. This demonstrates the complexity of this topic and shall motivate to proceed with further research.

References

[1] Onmeda, Nuklearmedizin, http://www.onmeda.de/behandlung/nuklearmedizin.html (05.01.2016 8:32).
[2] Deutsche Gesellschaft für Nuklearmedizin, Leitlinien für die Skelettszintigraphie, http://www.nuklearmedizin.de/leistungen/leitlinien/html/sekelett_szin.php?navId=53 (18.01.2016, 14:55).
[3] Christina Kolossow, *Methoden zur Bestimmung der Bildqualität von Mineralisationsphasen der Ganzkörperskelettszintigraphie,* 09.2016, project work supervised by Prof. Dr. Klaus Brinker, Hochschule Hamm-Lippstadt
[4] Ethem Alpaydin, *Introduction to Machine Learning*. The MIT Press, 2010.
[5] Stuart Russel und Peter Norvig, *Künstliche Intelligenz – Ein moderner Ansatz.* Pearson, 2012.

[4)] A Comparison of CT Hounsfield Units of Medical Implants and Their Metallic and Electrical Components Determined by a Conventional and an Extended CT-scale

Zehra Ese[(1,5)], Marcel Kressmann[(2)], Jakob Kreutner[(3)], Amin Douiri[(2)], Stefan Scholz[(2)], Wolfgang Görtz[(2)], Lutz Lüdemann[(4)], Gregor Schaefers[(3)], Daniel Erni[(1)], and Waldemar Zylka[(5)]

[(1)] General and Theoretical Electrical Engineering (ATE), Faculty of Engineering, University of Duisburg-Essen, and CENIDE – Center of Nanointegration Duisburg-Essen,
D-47057 Duisburg, Germany
[(2)] Magnetic Resonance Safety Testing Laboratories, MR:comp GmbH
D-45894 Gelsenkirchen, Germany
[(3)] Magnetic Resonance Institute for Safety, Technology and Research, MRI-STaR GmbH
D-45894 Gelsenkirchen, Germany
[4)] Department of Radiation Therapy and Radiooncology,
Faculty of Medicine, University of Duisburg-Essen
D-45147 Essen, Germany
[(5)] Faculty of Electrical Engineering and Applied Natural Sciences,
Westphalian University, Campus Gelsenkirchen
D-45897 Gelsenkirchen, Germany

E-Mail: zehra.ese@stud.uni-due.de

Introduction: The number of patients with implanted electronic devices, such as pacemakers, cardioverter-defibrillators and neurostimulators is increasing. In addition, with the aging population the occurrence of malignancies is rising steadily. As a result, the probability of patients receiving radiotherapy as treatment modality due to malignancy and wearing an implant becomes higher [1-2]. The goal of radiotherapy is to achieve a well-defined homogenous dose delivery to the target volume while minimizing radiation dose to the surrounded healthy tissue. High-density materials like metallic implants can cause significant challenges in realizing an efficient radiotherapy treatment plan due to incorrect density assignment and determined dosimetric effects within treatment planning software (TPS) [3-5]. The purpose of this study is to investigate the CT Hounsfield units (HU) of metallic and electrical components of implantable electronic devices, since they are directly transferred as density values to the TPS.

Material and Methods: The scanning volume is composed of an acrylic water tank filled with water. A water equivalent solid state slab phantom, made of a white polystyrene material (RW3), was positioned within the water tank. The testing objects were embedded and fixed between two RW3 slabs, separated by two thin acrylic blocks. Four RW3 slabs were set under the object to account for the backscattering coming from the patient table.

The following objects were used for CT-acquisition: a cardioverter-defibrillator (IPG), common components of active implants, such as a lithium battery, an epoxy circuit board, a Shottky diode and a microprocessor made of carbon and silicon, metallic discs made of copper and an implant titanium case.

A conventional CT-value interval of -1024 to +3071 HU, which is used in CT-acquisition for treatment planning, allows the proper representation of the human body tissue. However, high-density materials, which exceed the conventional range, are often set to the highest HU thus limiting the accuracy of dose calculations within TPS. A SIEMENS SOMATOM Definition Flash Dual Source CT system with two selectable ranges; the conventional and an extended CT-scale ranging from -10240 to +30710 HU were used to obtain Hounsfield units. In order to distinguish between the different implant components defined by their densities each component was scanned separately by the two CT-scales.

Results: The HU values determined with a clinical DICOM viewer are summarized in Tab. 1. The HU values of implant materials are underestimated within a conventional CT scale, even though the values measured within an extended scale do not exceed its upper limit, as it is seen for the *titanium disc, case* and for the *circuit board*. If the density value exceeds the conventional range the value is set to the highest HU (e.g. *copper disc*).

Tab. 1: Materials of implantable electronic devices at a conventional and extended HU scale

Test objects	HU (conventional scale) [HU]	HU (extended scale) [HU]
titanium disc	1756 ± 31	2203 ± 313
titanium case	1507 ± 82	2321 ± 381
copper disc	3070 ± 1	5356 ± 413
battery	3066 ± 13	2617 ± 272
diode	3069 ± 18	3591 ± 416
microprocessor	2821 ± 217	3568 ± 585
circuit board	124 ± 20	550 ± 86

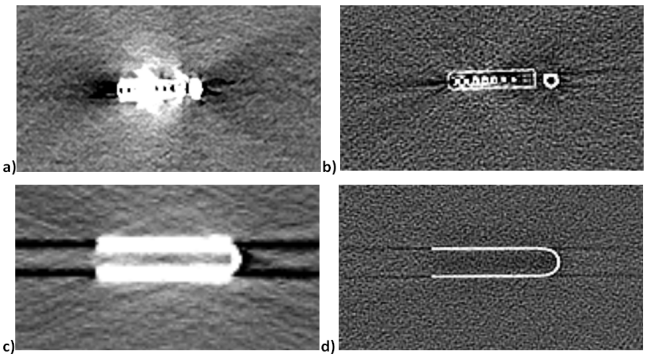

Fig. 1 CT image reconstructions of an IPG (top) and a titanium implant case (bellow) comparing CT acquisition with a conventional (left) and an extended HU scale (right)

Figure 1 compares two cross sectional images through an IPG and a titanium implant case. CT-acquisitions with the conventional HU scale are shown on the left hand side while acquisitions on the extended HU scale are shown on the right hand side. The inner part of the implant is well seen in picture in fig. 1b). The electrical components are distinguishable by HU values of the material and comparable to the values in Tab.1. Artefacts seen in fig. 1b) and d) are smaller compared to fig.1a) and c). In addition, the object geometry shows higher reconstruction accuracy in fig. 1b). and d).

Discussion and Conclusion: The material composition of some components such as the battery and diode can be well distinguished within an extended scale, while the CT-acquisition of these at a conventional HU scale are fully blended by the housing material with higher density. In conclusion, a CT-acquisition with an extended HU scale is a far more beneficial approach for dose calculations with a TPS in radiotherapy treatments.

References:

[1] Tomas Zaremba, “Radiotherapy in Patients with Pacemakers and Implantable Cardioverter-Defibrillators”, Dissertation, Aalborg University, Denmark, May 2015
[2] J.I. Prisciandro, A. Makkar et al, “Dosimetric review of cardiac implantable electronic device patients receiving radiotherapy”, Journal of Applied Clinical Medical Physics, vol. 16, no. 1, October 2014
[3] T. Kairn, S.B. Crowe et al, “Dosimetric effects of a high-density spinal implant”, Journal of Physics: Conference Series, 7th International Conference on 3D Radiation Dosimetry, vol. 444, pp. 1-4, January 2008
[4] J.P. Mullins, M.P. Grams et al, “Treatment planning for metals using an extended CT number scale”, Journal of Applied Clinical Medical Physics, vol. 17, no. 6, pp. 179-188, August 2016
[5] C. Coolens and P.J. Childs, “Calibration of CT Hounsfield units for radiotherapy treatment planning of patients with metallic hip prostheses: the use of the extended CT-scale”, Physics in Medicine and Biology (Phys. Med. Biol.), vol. 48, pp. 1591-1603, May 2003

5) Does Hemodynamic Response Function Change in Alzheimer Disease?

Nathania Suryoputri[1], Aydin Ghaderi[1], Peter Linder[1], Konstantin Kotliar, PhD[1],Jens Göttler, MD[2], Christian Sorg, MD[2] and Timo Grimmer, MD, PhD[2]

(1) Aachen University of Applied Sciences, Aachen, Germany
(2) Klinikum rechts der Isar, Technische Universität München, Munich, Germany

E-Mail: nathania-amber.suryoputri@alumni.fh-aachen.de

Abstract – **Background:** Differences of BOLD response in functional MRI data in task-related or resting state fMRI between Alzheimer's diseae (AD) and healthy controls have been constantly reported assuming an unvaried hemodynamic response function. However, from direct assessment of hemodynamic response function (HRF) using retinal vessel analysis we demonstrated previously that retinal vessel response to flicker is altered in Alzheimer's disease (AD): patients with dementia due to AD (ADD) showed more emphasized and delayed reactive dilation. Thus, we searched for variations between healthy controls and AD patients in the HRF of fMRI.

Methods: Data of a previous task related fMRI study was used. 17 patients with prodromal AD (pAD; i.e., with MCI and biological signs of AD) and 15 healthy older adults were investigated. Participants underwent a course of attention-demanding tasks with different difficulty levels. The fMRI data were generated by an EPI (echo planar imaging) – gradient echo sequence. Median of mean grey values of eight points with 1 mm^3 voxel size (1x1x1) of posterior default mode network (pDMN) were automatically extracted using a LabVIEW program in order to derive multiple-stimulus HRF and to evaluate neuronal activity during the stimulation course in each participant. All the individual responses were mathematically filtered and their signal-to-noise-ratio was improved.

Results: Individual HRFs of patients visually differs from those in the control group. In addition, the shape of HRF could be visualized on single subject level. **Conclusions:** This novel algorithm to visualize HRF allows to pick up individual changes of HRF and provides the opportunity to use fMRI signal for diagnosis, monitoring and prediction of AD.

Keywords: fMRI, Alzheimer's disease, posterior default mode network (pDMN), hemodynamic response function (HRF)

References

[1] K. Koch et al., "Disrupted intrinsic networks link amyloid-β Pathology and impaired cognition in prodromal Alheimer's disease" Cereb Cortex. 2015;25:4678–4688.
[2] K. Koch et al., Supplementary Material for "Disrupted intrinsic networks link amyloid-β Pathology and impaired cognition in prodromal Alheimer's disease". Cereb Cortex. 2015;25:4678–4688.
[3] K. Kotliar, C.Hauser, M.Ortner, C. Muggenthaler, C. Schmaderer, A. Schmidt-Trucksaess, T.Grimmer, "The usefulness of dynamic retinal vessel reaction to flickering light as a biomarker for Alzheimer's disease". Alzheimer's and Dementia. July 2016;vol.12;issue 7;p.318-319.
[4] A. Ghaderi, "Development of the methodology for the investigation of the hemodynamic response function of brain areas after cognitive stimulation". May 2016. Master thesis in Fachhochschule Aachen.
[5] F. Agosta, M. Pievani, C. Geroldi, M. Copetti, G. Frisoni, M. Filippi, "Resting state fMRI in Alzheimer's disese: beyond the default mode network". Neurobiology of Aging. 2012;33;1564-1578.
[6] S. Rombouts, R. Goekoop, C. Stam, F. Barkhof, P. Scheltens, "Delayed rather than decreased BOLD response as a marker for early Alzheimer's disease". NeuroImage. 2005;26;1078-1085.
[7] S. Faro, F. Mohamed, "BOLD fMRI: a guide to functional Imaging". Springer Juli 2010.

6) Investigation of Flow and Heat Transfer During TURIS Process via 2D CFD Simulation

Mustapha El Bahia[(1)], Tino Morgenstern[(1)], and Dinan Wang[(1)]

[(1)] Institute of Measurement Engineering and Sensor Technology
University of Applied Sciences Ruhr West,
D-45479 Mülheim an der Ruhr, Germany

Abstract

Transurethral resection in saline (TURIS) is a urological surgical technique that is now used as a gold standard for the treatment of benign prostate hyperplasia (BPH) to cut the cell tissue. The core of this study is the flow field and the temperature distribution in the region of the operation. Based on the modification of the geometry and the boundary conditions of the previous work, and using ANSYS FLUENT, a new 2D transient CFD simulation has been performed. The simulation results of flow field are in good agreement with the results provided by company Olympus. The results of the simulation indicate that the possible heat injury of the remaining tissue caused by surgery is minimal. In addition, a sensitivity test of effects of different electrode active action periods on temperature distribution has been analyzed.

[7)] Monte Carlo and Ray Tracing Algorithm for Treatment Planning in Clinical Applications with Cyberknife

Kirsten Galonske[(1)], Martin Thiele[(1)], Waldemar Zylka[(2)]

[(1)] Deutsches CyberKnife-Zentrum,
Klinikum Stadt Soest,
D-59494 Soest, Germany

[(2)] Faculty of Electric Engineering and Applied Natural Sciences,
Westphalian University, Campus Gelsenkirchen,
D-45897 Gelsenkirchen, Germany

E-Mail: galonske@klinikumstadtsoest.de | waldemar.zylka@w-hs.de
Web: www.klinikumstadtsoest.de | www.w-hs.de/zylka

Introduction: Accurate calculation of radiation behavior in a body is of crucial importance for the result of radiotherapy. Radiation planning systems work with algorithms to calculate the interactions between radiation and tissue. In this study Ray Tracing (RT) algorithm is compared to Monte Carlo (MC) algorithm in homogeneous and heterogeneous areas of the body for robotic stereotactic radiotherapy with Cyberknife®.

Material and Methods: In total 47 treatment-plans in head and lung area are used for this comparison. The dose prescription of the ten plans in homogeneous head area with target volume acoustic neuroma, n = 5, and brain metastasis, n = 5, was 13 Gy, respectively 18 Gy, on the enclosing 80 % isodose as radiosurgery. In heterogeneous thoracic region, plans were calculated for 20 lung tumors and 17 lung metastasis with 37.5 Gy, enclosing 65 % isodose, in three fractions (five days).

All plans were created using RT and were recalculated with MC, without any changing of planning parameters and plan-optimization. For each RT-MC-Plan pair, the absolute differences *d* of the parameters minimum dose (D_{min}), mean dose (D_{mean}), maximum dose (D_{max}), dose of 2% (*D2*) and 98% (*D98*) of the target planning volume (PTV) and coverage (*Cov*, i.e. PTV volume / volume of the prescribed isodose) of the PTV were evaluated. Additionally, in thoracic region these parameters were calculated for the gross tumor volume (GTV). For each parameter, the distribution of RT-MC-dose differences in treatment plans is characterized by the minimum, maximum and mean value. For instance, for the mean dose parameter D_{mean} the symbols d_{mean}^{min} and d_{mean}^{max} denote the minimum and maximum value of the absolute differences. The average value, denoted by a bar, is equal to the difference of the mean values of the plans $\overline{d}_{mean} = \overline{D}_{mean}^{MC} - \overline{D}_{mean}^{RT}$. The percentage difference, if specified, is normalized to the value of the RT parameter, i.e. $\overline{d}_{mean} = 100\,\% \,(\overline{D}_{mean}^{MC} - \overline{D}_{mean}^{RT})/\overline{D}_{mean}^{RT}$. Distribution and values of other dose parameters are denoted correspondingly.

Results: In heterogeneous thoracic region the average difference of the dose parameter D_{mean} is $\overline{d}_{mean} = -16.73\%$ compared to the homogeneous head region with $\overline{d}_{mean} = 2.73\,\%$. Maximum deviations were found in thorax with $d_{min}^{max} = -47.41\,\%$ and in head with $d_{min}^{max} = -5{,}36\,\%$. In addition, in thoracic region a dependency of D_{mean} on PTV size is recorded (Fig.1). This is also observed for the averages $\overline{d}_{min}$, $\overline{d}_{max}$, $\overline{d}_{D2}$, $\overline{d}_{D98}$ and $\overline{d}_{Cov}$ of PTV. It was found that the coverage of GTV dropped slightly lower from 99.86 % to 97.7 % after MC recalculation in comparison to significantly more decrease of PTV from 98.14 % to 84.39 %.

A classification of tumor volume into three subgroups with 0-15 cm³ (A), 15-30 cm³ (B) and 45-60 cm³ (C) shows that PTVs below 15 cm³ have particularly high differences. In subgroup A the average difference between RT and MC regarding D_{mean} is $\overline{d}_{mean}(A) = -20.31\,\%$ $(-9.48\,\mathrm{Gy})$. Subgroup B shows on average $\overline{d}_{mean}(B) = -11.79\,\%$ $(-5.37\,\mathrm{Gy})$ and subgroup C $\overline{d}_{mean}(C) = -9.25\,\%$ $(-4.23\,\mathrm{Gy})$. The three subgroups can also be observed in dose differences $\overline{d}_{min}$ and $\overline{d}_{D98}$, whereas

the differences $\overline{d}_{max}$ and $\overline{d}_{D2}$ show only two subgroups with PTV sizes below 15 cm³ and above 15 cm³.

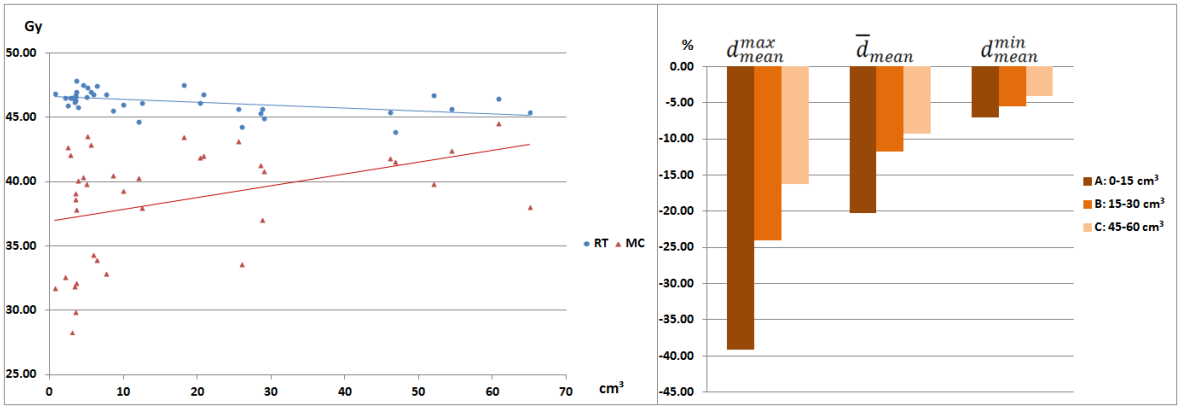

Fig.1: Comparison of the absolute D_{mean} (left) and the percentage difference (right) of PTV as a function of the PTV size in thoracic region. Small PTV size show greatest differences between RT and MC.

Discussion and Conclusion: It was shown that calculation algorithms RT and MC are equivalent within 5.36 % dose deviation in homogeneous body regions. Thus, in these body regions the use of RT is to be regarded as sufficient and appropriate [1]. In heterogeneous areas of the body, such as the thorax, however, there was a significant difference in dose distribution. In addition, the PTV volume has an effect on dose deviations. Similar dose reductions of 17 % in tumors with a diameter of less than 3 cm, 13 % in tumors between 3 cm and 5 cm, and a decrease by 8 % in tumors larger than 5 cm have been reported in [2].
D_{mn} and *D98* of the PTV are important parameters in order to avoid an under-supply of the lesion. However, these parameters show the highest dose drop, e.g., $d_{min}^{max} = -47.41\ \%$ after recalculation with MC. A decrease in PTV coverage from 97.7 % to 69.2 % after recalculation with MC has been published in [3]. In this study, the coverage decreased from 98.14 % to 84.39 %. Based on these results the prescribed fractionation of 37.5 Gy in three fractions to enclose 65 % isodose should be reconsidered. In [4] it is suggested to investigate 22 different treatment regimens with MC (15-72.5 Gy in 1 to 12 fractions) which were used in 45 studies.
In conclusion, differences in clinical outcomes may result from (i) whether the dose is prescribed for the GTV or PTV, (ii) to which isodose the dose is prescribed and (iii) the fractionation scheme. A uniform dosage is desirable to evaluate the clinical results in order to make further dose adjustments (if necessary). The necessity of the MC calculation in radiotherapy in heterogeneous regions, e.g. in the thorax, is clearly demonstrated by the results shown here.

Literature:

[1] EE Wilcox, GM Daskalov, H Lincoln, "Stereotactic radiosurgery-radiotherapy: Should Monte Carlo treatment planning be used for all sites?", Pract Radiat Oncol. 2011 Oct-Dec ;1(4):251-60
[2] NC Van der Voort van Zyp, MS Hoogemann, S van de Water, PC Levendage, B van der Holt, BJ Heijmen, JJ Nuyttens, "Clinical introduction of Monte Carlo treatment planning: a different prescription dose for non-small cell lung cancer according to tumor location and size.", Radiother Oncol. 2010 Jul;96(1):55-60
[3] SC Sharma, JT Ott, JB Williams, D Dickow, "Clinical implications of adopting Monte Carlo treatment planning for CyberKnife", J Appl Clin Med Phys. 2010 Jan 29;11(1):3142
[4] T Lacornerie, A Lisbona, X Mirabel, E Lartigau, N Reynaert, "GTV-based prescription in SBRT for lung lesions using advanced dose calculation algorithms", RadiatOncol.2014;9:223

8) Development and Trials of a Test Chamber for Ultrasound-assisted Sampling of Living Cells from Solid Surfaces

Oliver Schneider, Taher Al Hakim, Peter Kayser, Ilya Digel
Laboratory for Cell- and Microbiology
Institute for Bioengineering,

FH Aachen University of Applied Sciences
D-52428 Jülich, Germany

E-Mail: oliver.schneider@alumni.fh-aachen.de
Web: www.zmb.fh-aachen.de

Abstract – Various surfaces in biotechnological and food industry, healthcare facilities and other epidemiologically relevant fields are subject to continuous contamination by microorganisms [1]. Regular sampling and adequate cleaning of such surfaces mainly composed of metal, plastic and glass represent the main approach to control the hygiene of medical and food products [2].

The method of recovering microorganisms from different solid surfaces is critical for reliability and objectivity of sampling and microbiological risk assessment. Today, sampling by cotton or rayon swabs is undeservedly considered the “gold standard”. In reality, the swabbing methods suffer from numerous drawbacks. Therefore, efficient, reliable, quick and cheap sampling methods still have to be defined and standardized for better control of microbiological hazardous events, especially for porous and irregular materials.

A project called BacHarvester was launched to provide a new technique that will help in collecting bacteria attached to any solid surface and collect them while keeping them alive. Our working group has focused on designing a flow chamber supposed to serve as a standardized testing setup for this project. The aims were first to design and construct, and later to test an experimental chamber for detachment of erythrocytes and yeast cells using different ultrasound intensities.

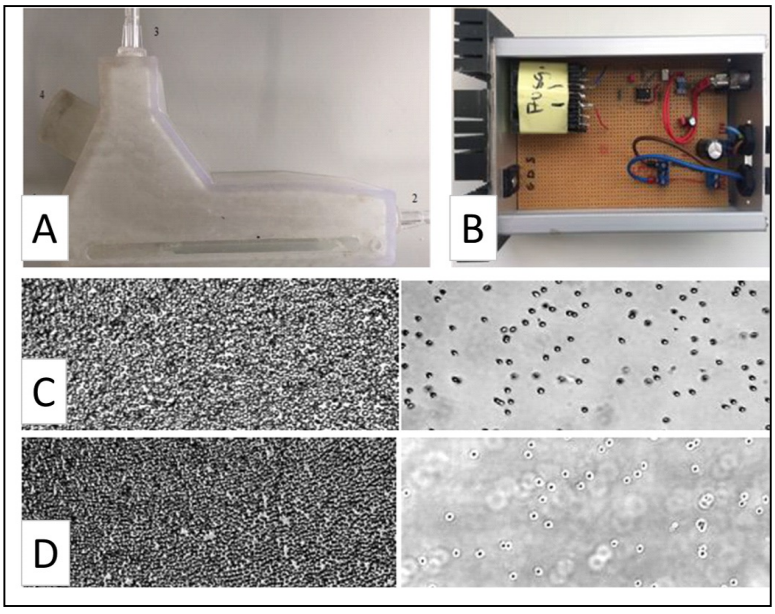

Fig.1: A: The 3D-printed test chamber: 1) inflow; 2) outflow; 3) de-airing tube; 4) ultrasonic head fixation. The cells were be placed on a microslide and inserted into the chamber using a slot near the bottom. B: The driver board of the ultrasound transducer. C: Erythrocytes attached to the microslide before (left) and after ultrasound exposure (3 minutes long). D: Yeast cells (Saccharomyces cerevisiae) attached to the microslide before (left) and after ultrasound exposure (3 minutes long).

A new flow chamber for the tests was designed using the Autodesk® Inventor® 3D CAD software and printed mainly with a 3D printing process (Fig. 1, A). The material used was synthetic resin. This material selection allows for a more cost-effective production process. The ultrasound transducer used in this project had a resonance frequency of 40 kHz, maximal applied voltage of 160Vp-p and the maximal output of 3 W. To get the optimal cavitation and the optimal detachment results, a kpus-40fd-14tr-k766 ultrasound sensor mounted into an aluminum housing was used. This ultrasound transducer had a sound pressure level of 103 dB in air according to calibration parameters.

The driver board (Fig. 1, B) was used as a function generator is specialized for ultrasonic generators, usually for ultrasonic levitation experiments. It transformed electrical input to a signal for the ultrasound transducer to accept. One of the advantages of this kind of circuits is its high-level amplification.

The filling phase took around 15 minutes, and along with that, blood cells were observed under the microscope. No appreciable detachment of the blood cells was detected due to the flow. Afterwards, the ultrasound waves were applied to the sample of the blood cells. The observed detachment of the cells (Fig.1, C and D) mainly was due to two effects. The first is the cavitation, which usually induces a powerful shock that can detach cells from each other. The second is a phenomenon called microstreaming, which in turn, may also have considerable effect on this kind of detachment [3, 4].

References

[1] M. Fletcher, *Microbial adhesion to surfaces*. Chichester: Ellis Horood, 1980.
[2] B. Webber, et al., “The Use of Vortex and Ultrasound Techniques for the in vitro Removal of Salmonella spp. Biofilms”, *Acta Scientiae Veterinariae, vol.43, pp.1332*, 2015.
[3] P.N. Wells, ”Absorption and dispersion of ultrasound in biological tissue”, *Ultrasound Med Biol.*; vol.1, pp.369–376, 1975.
[4] R. Vaughn Peterson, W G. Pitt, “The effect of frequency and power density on the ultrasonically-enhanced killing of biofilm-sequestered Escherichia coli”. *Colloids and Surfaces B: Biointerfaces,* vol.17 (4), pp. 219–227, 2000.

[9] How the Liquid Contact Angle Saturates by the Electrowetting Effect

Fedor Schreiber and Daniel Erni

General and Theoretical Electrical Engineering (ATE), Faculty of Engineering,
University of Duisburg-Essen, and CENIDE – Center for Nanointegration Duisburg-Essen,
D-47048 Duisburg, Germany

E-Mail: fedor.schreiber@uni-due.de
Web: www.ate.uni-due.de

Abstract – We present a rigorous analytical analysis of the electric force at a perfectly conductive wedge formed by the wetting angle of a liquid droplet on an insulated electrode using the Maxwell stress tensor, which leads to a macroscopic explanation of the contact angle saturation phenomenon in electrowetting [1, 2]. The electrowetting effect is nowadays being widely used as a liquid actuation mechanism in a wide range of microfluidic applications such as lab-on-a-chip systems in medicine [3], variable focus lens in electro-optical devices or in display technology [1, 2]. This actuation mechanism relies on the precise manipulation (change) of the liquid wetting angle using the electric force, and is limited by the still not fully understood saturation phenomenon.

When applying a voltage on the perfectly conductive droplet placed on an insulated counter electrode the resulting electric forces will be confined to the immediate tip of the droplet wedge, as schematically illustrated in Fig. 1. These electric forces tend to drag the droplet over the hydrophobic dielectric causing a deformed liquid surface with a decreased contact angle. Due to an asymmetrically applied voltage (e.g. right electrode is activated) the resulting force direction can be specifically controlled and consequently the resting droplet can be set in motion. This actuation principle forms the basis of several electrowetting manipulation operators such as the droplet creation from a reservoir of a liquid, the transport, splitting and merging [1, 2].

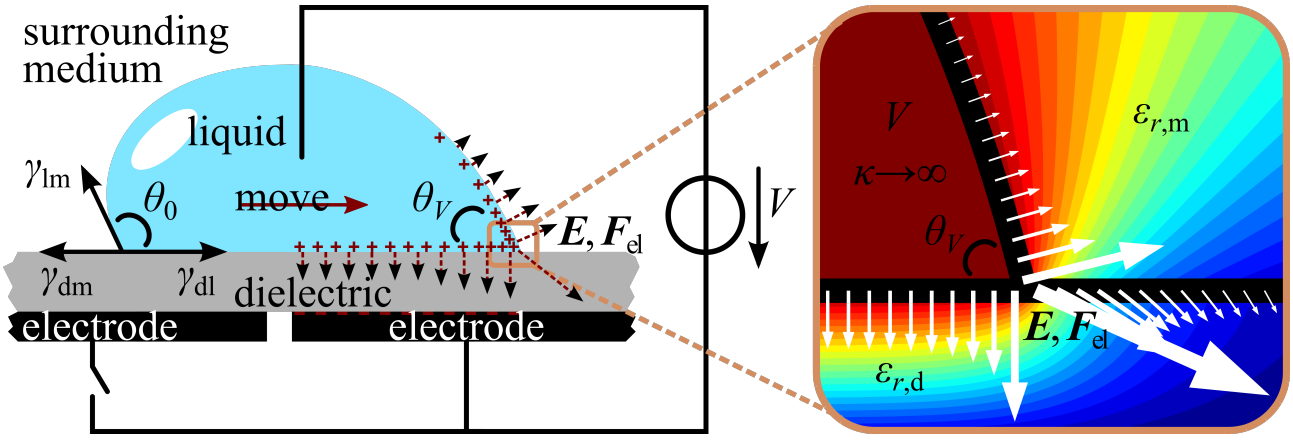

Fig.1: Scheme of the droplet transport between two electrodes. When the right electrode is activated, the estimated electric forces concentrate in the vicinity of the right-hand triple point of the perfectly conductive droplet. This specific asymmetric distribution of forces causes the directed motion of the droplet with the decreased right contact angle.

The tip of the droplet wedge is represented by the triple junction (also called *triple point*) of the three adjacent phases: conductive liquid, dielectric solid and surrounding medium. Forces acting solely on the triple point while being described by corresponding interfacial tensions together with a shear force define the realm of the conventional approximate Young-Lippmann law [1, 2]. In this context, the voltage dependent contact angle becomes the major parameter for the resulting drag force and can theoretically reach 0° by a sufficiently high voltage. In practice, however, the electrically manipulated contact angle saturates (despite further increasing voltage) to a certain value, which lies between 30° and 80°, depending on specific properties of the electrowetting-system. This effect of the contact angle saturation at a minimal angle (yielding maximal drag force) is still under considerable debate relating its origin to various microscopic but rather disconnected mechanisms [4, 5]. In contrast, our macroscopic analytical explanation of the contact angle saturation – based on the 2D vectorial analysis of the actuation electric forces on the liquid surface – has the potential to predominate the microscopic ones due to emergent theoretical electrostatic field singularities in the triple point [6, 7].

We calculated the electric and displacement field on the droplet surface (wedge) as well as in a close radial neighborhood around the triple point relying on their well-known fractional order local dependence. With these field vectors, the estimated electrostatic pressure (N/m²) on the liquid droplet could be determined using the Maxwell stress tensor together with renormalization techniques. It is shown, that the vector orientation of the electrostatic pressure in the singular triple point together with the adjacent much weaker ones are strongly dependent on the droplet contact angle as well as on the permittivities of the dielectric and the surrounding medium. Depending on these parameters, the horizontal component of this resulting pressure changes direction (zero crossing) at a certain contact angle, whose value is in the range from 10° to 82°. Below this zero crossing angle the electrostatic pressure – with a negative horizontal component – no longer antagonizes the Laplace pressure of the liquid droplet. Consequently, any droplet deformation is inhibited and thereby the decrease of the contact angle, rendering this limiting value to contact angle saturation. In addition, it was found that voltage levels and thickness of the dielectric layer have no direct influence on the direction of the electrostatic pressure but rather on its magnitude and thus the steepness of the zero crossing, respectively. In summary, these analytical results suggest that the cause of the contact angle decrease as well as of its saturation lies in the angle- and permittivity-dependent vector orientation of the resulting electrostatic pressure on the droplet.

References

[1] J. Berthier, *Microdrops and Digital Microfluidics*. Norwich, New York, USA: William Andrew, 2008.

[2] P. Garcí-Sánchez and F. Mugele, “Fundamentals of Electrowetting and Applications in Microsystems,” in *Electrokinetics and Electrohydrodynamics in Microsystems*. Wien: Springer, 2011, pp. 85–125.

[3] F. Schreiber, S. Kahnert, A. Goehlich, D. Greifendorf, F. Bartels, U. Janzyk, K. Lennartz, U. Kirstein, A. Rennings, R. Küppers, and D. Erni, “Mikrofluidik-Chip-Architekturen für eine Zell-Sortieranlage basierend auf der Elektrowetting-Technologie,” *tm - Technisches Messen*, vol. 83, no. 5, pp. 274-288, (DOI: 10.1515/teme-2015-0054), Mai, 2016.

[4] H. J. J. Verheijen and M. W. J. Prins, “Reversible electrowetting and trapping of charge: model and experiments,” *Langmuir*, vol. 15, pp. 6616-6620, 1999.

[5] V. Peykov, A. Quinn and J. Ralston, “Electrowetting: a model for contact angle saturation,” *J. Colloid Polym. Sci.*, vol. 278, pp. 789–793, 2000.

[6] L. Schächter, “Analytic expression for triple-point electron emission from an ideal edge,” *Appl. Phys. Lett.*, vol. 72, no. 4, pp. 421-423, 1998.

[7] T. Takuma and T. Kawamoto, “Field Enhancement at a Triple Junction in Arrangements Consisting of Three Media,” *IEEE Transactions on Dielectrics and Electrical Insulation*, vol. 14, no. 3, pp. 566-571, 2007.

10) Effects of nitric oxide (NO) and ATP on red blood cell phenotype and deformability

Katharina Schlemmer, Dariusz Porst, Rasha Bassam, Gerhard Artmann, Ilya Digel

(1) Laboratory for Cell- and Microbiology
Institute for Bioengineering,
FH Aachen University of Applied Sciences
D-52428 Jülich, Germany

E-Mail: k-schlemmer@web.de
Web: www.zmb.fh-aachen.de

Abstract – Red blood cells (RBCs) are the most common type of blood cells in vertebrates and function as the principal means of delivering oxygen to the metabolizing tissues (Duling & R. Berne, 1970). Alterations in the RBCs structure as well as changes in the functioning of their proteins can occur due to binding with a broad class of low-molecular weight modifiers constantly or transiently present in erythrocytes and elsewhere in the blood (Bassam, Digel, Hescheler, Artmann, & Artmann, 2013). Among such modifiers, adenosine- 5'-triphosphate (ATP) is probably the most important intra-erythrocyte organic phosphate *in vivo*. In red blood cells, the concentration of ATP is in the range of 0.2-2.0 mM and any variations away from this range may induce a pH dependent tetramerization of deoxyHb in vertebrates (Bonafe, Matsukuma, & Matsuura, 1999). Another important species is nitric oxide (NO), which is a highly reactive free radical and has been identified as a regulatory molecule in a number of cellular systems, including, but not limited to, the immune, nervous and cardiovascular systems (Bredt & Snyder, 1994). According to recent studies, erythrocytes can release substances such as adenosine triphosphate and nitric oxide into the blood as a part of their physiological responses (Xu, Li, LaPenna, Yokota, Huke, & He, 2017).

Although both nitric oxide (NO) and ATP apparently play a significant role in blood functions, their exact function in controlling the principal RBC (mechanical) properties and therefore the blood circulation parameters remains poorly studied. A better understanding of the deformation of the red blood cells and their response on the substances in the blood is important not only for basic research but also for clinical use.

The aim of our study was to investigate the influence of nitric oxide and ATP on the appearance and mechanics of human RBCs using the Microscopic Photometric Monolayer (MPM) technique. The MPM technique provides a tool to measure red blood cell (RBC) stiffness (resistance to elongation) and relaxation time. It combines many of the advantages of flow channel studies of point-attached RBCs with the simplicity, sensitivity and accuracy of photometric light transmission measurement (Artmann, 1995). The principal idea of this method is that the flow-induced bending and curvature change of RBC membrane is associated with the increase of light transmission. The monochromatic light having a wavelength of 415 nm passes through the flow chamber and is measured on the other side by a photometer as voltage output. 415 nm correspond to the maximum absorption spectrum of hemoglobin. In the flow chamber, the incident light is refracted at the erythrocyte surface, which causes changes in the light intensity.

This technique allows the study of the effects of physicochemical factors on the elongation and relaxation time of the same cells within an average of four to five thousand cells adhered as a monolayer to glass.

The measuring instrument consisted of the following components: syringe pump, flow chamber, light microscope, photometer and control unit. A dense monolayer of point-attached RBCs was prepared at the bottom of a flow-chamber. A steady-state flow, with stepwise increases of flow rate, induced the RBC elongation. The light transmission perpendicular through the monolayer plane was measured photometrically. The attached erythrocytes were treated with adenosine triphosphate and nitric oxide and the changes in the shape were followed in the time course, including wash-in/wash-out kinetics. Following a sudden flow stoppage, the RBCs returned to their resting shape and the RBC relaxation time was measured. The stiffness-relaxation time product, V (in mPas), was calculated to provide an estimate of viscosity. Established photometric methods sensing tiny changes of red blood cell morphology at rest (red blood cell shape) and at very low shear forces (red blood cell stiffness, red blood cell relaxation time) were applied as well. The derivative induced effects were detected in a time- and dose-dependent manner.

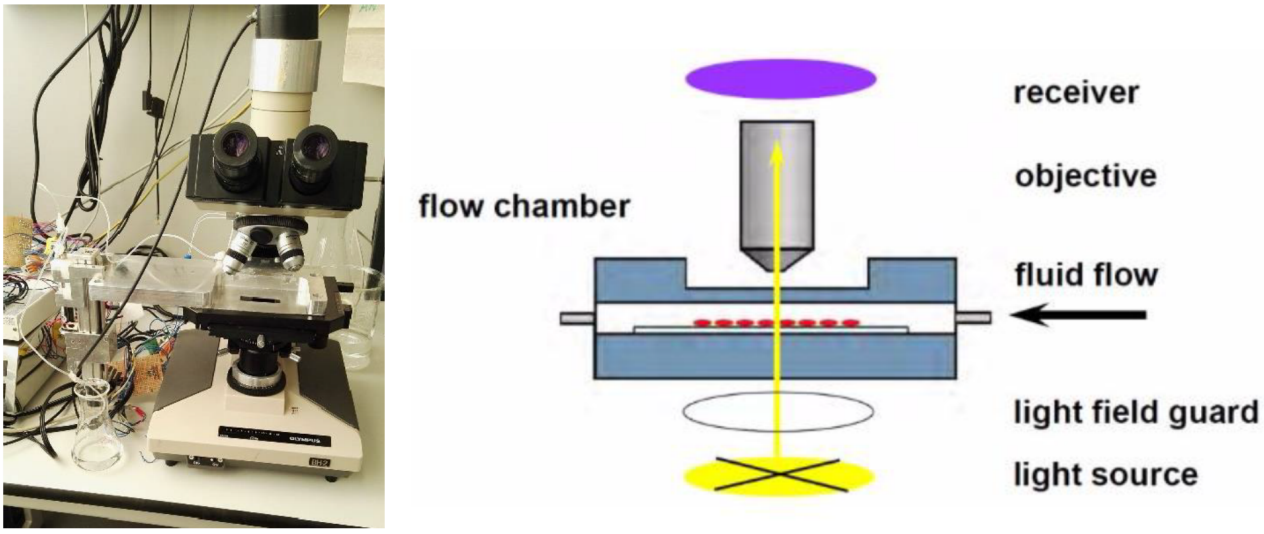

Fig.1: The experimental setup (left) and the principle of the MPM –technique (right).

The experiments showed differences in both viscosity and deformability of the RBCs treated with ATP, NO-donors and NOS-inhibitors as compared to the control group.

References

[1] B. R. Duling and M. R. Berne, " Longitudinal gradients in periarteriolar oxygen tension. A possible mechanism for the participation of oxygen in local regulation of blood flow.," *Circ. Res. ,* vol. 27, pp. 669-678, 1970.

[2] R. Bassam, I. Digel, J. Hescheler, A. Artmann and G. Artmann, "Effects of spermine NONOate and ATP on protein aggregation: light scattering," *BMC Biophys.,* vol. 6, no. 1, 2013 .

[3] C. Bonafe, A. Matsukuma and M. Matsuura, "ATP-induced tetramerization and cooperativity in hemoglobin of lower vertebrates.," *J. Biol. Chem. ,* vol. 274, pp. 1196-1198, 1999.

[4] D. Bredt and S. Snyder, " Nitric oxide: a physiologic messenger molecule.," *Annu. Rev. Biochem.,* vol. 63, pp. 175-195, 1994.

[5] S. Xu, X. Li, K. LaPenna, S. Yokota, S. Huke and P. He, " New insights into shear stress-induced endothelial signalling and barrier function: cell-free fluid versus blood flow.," *Cardiovasc Res. ,* vol. 113, no. 5, pp. 508-518, 2017.

[6] G. Artmann, "Microscopic photometric quantification of stiffness and relaxation time of red blood cells in a flow chamber.," *Biorheology ,* vol. 32, no. 5, pp. 553-570, 1995 .

11) Fluorescence Signatures and Detection Limits of Ubiquitous Terrestrial Bio-compounds

Max Kuhlen, Ilya Digel

(1) Laboratory for Cell- and Microbiology
Institute for Bioengineering,
FH Aachen University of Applied Sciences
D-52428 Jülich, Germany

E-Mail: maxx.kuhlen@yahoo.de
Web: www.zmb.fh-aachen.de

Abstract – The measurements of fluorescence spectrum, lifetime and polarization are powerful methods of analysis in various fields of science [1]. Photometric technologies offer a repertoire of fast, simple and reliable identification and characterization methods for chemical compounds and microorganisms (sometimes in their natural environments) via their signatures. Biosignatures in general are defined as objects, substances and/or patterns whose origin requires a biological agent.

Finding appropriate criteria for recognizing, detection and comprehension of life phenomena is one of the “eternal” problems in astrophysics, geology, glaciology and marine ecology. From this perspective, a biosignature is a feature that is consistent with biological processes and that, when it is encountered, challenges to attribute either to inanimate or to biological processes. What is usually looked for are the compounds involved in the origin of life on Earth and the molecules considered essential for terrestrial biology: amino acids, amines, thiols and thioesters, biopolymers, aldehydes, ketones, carboxylic acids, fatty acids, fatty alcohols and polycyclic aromatic hydrocarbons [2].

Very suitable for this purpose is fluorescence spectroscopy, which is a type of electromagnetic spectroscopy that analyses fluorescence and primarily concerns with electronic and vibrational states of molecules. It allows quantitative measurements of an analyte in solution and provides information on dynamic processes on molecular environment and on dynamic processes down to the nanosecond timescale [3]. Among biopolymers, especially proteins are displaying strong intrinsic fluorescence due to the three aromatic amino acids phenylalanine, tyrosine, and tryptophan. Lipids, membranes, and saccharides are essentially nonfluorescent, and the intrinsic fluorescence of DNA is too weak to be useful [4].

Our approach primarily focused on fluorescence spectroscopy measurements of selected species of ubiquitous terrestrial bio-compounds as a model for future terrestrial and extraterrestrial applications. The main aims were (a) to verify that autofluorescence can be successfully used to differentiate between various biogenic compounds through identification of spectroscopic fingerprints and (b) to determine their minimal dilutions/concentrations that could be still detected. In the first part of this study we applied conventional fluorimetry by using spectrofluorimeter F8500 (Jasco Co.) to obtain cumulative spectra and intensities for bacteriorhodopsin, RNA, chlorophyll, histidine, ATP, NADH, tryptophan, phenylalanine, pyridoxine, riboflavin, arginine, alanine and FAD.

The obtained results (partially presented in Figure 1) allowed determination of absorbance/emittance peaks characteristic for the examined molecular species. In the second part of our study we established detection thresholds for the compounds of interest.

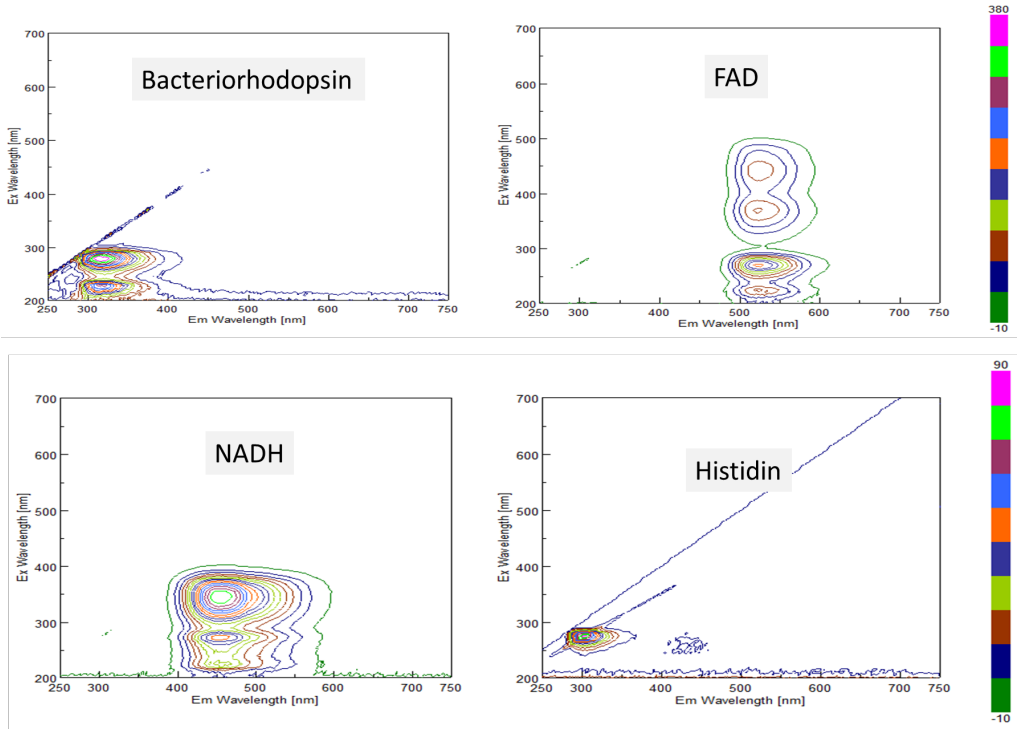

Fig.1: Emission/excitation diagrams showing the location of the corresponding peaks as illustrated by four different biological compounds. Differences in the peak distribution patterns are clearly visible

The information related to specific absorption/emission maxima will be used in designing and developing of compact LED-based fluorescence spectroscopy module that is supposed to be a part of the payload of the future autonomous sampling probes (for both terrestrial and space exploration missions).

References

[1] M. Hof and R. Machán, Fluorescence spectroscopy and microscopy for biology and medicine – Lecture Notes. Czech Technical University in Prague, 2014.
[2] M. F.Mora, A.M. Stockton, and P. A.Willis. Microchip capillary electrophoresis instrumentation for in situ analysis in the search for extraterrestrial life. Electrophoresis, 33(17): 2624–2638, 2012.
[3] M. Sauer, J. Hofkens, and J. Enderlein. Basic Principles of Fluorescence Spectroscopy. In Handbook of Fluorescence Spectroscopy and Imaging: From Single Molecules to Ensembles, pages 1–30.Wiley Online Library, 2011
[4] J. R. Lakowicz, Instrumentation for Fluorescence Spectroscopy. In Principles of Fluorescence Spectroscopy. Springer, 2006.

[12)] Automatic Dementia Diagnosis Based on a Digital Clock Drawing Test

Patrick Lange [(1)], Siegfried Reinecke [(2)], Klaus Brinker [(1)]

[(1)] Biomedical Engineering
Hamm-Lippstadt, University of Applied Science,
D-59063 Hamm, Germany

[(2)] Geriatric Clinic
St. Marien-Hospital Hamm,
D-59065 Hamm, Germany

E-Mail: PatLange2812@Outlook.de
Web: www.hshl.de

Dementia describes an irreversible neurodegenerative syndrome of different diseases. During the progression of this incurable disease, different parts of the brain are affected causing cognitive impairment and gradually reducing the quality of life. Thus, it is very important to conduct an early diagnosis of dementia to counteract the syndrome.

The diagnosis of dementia consists of an interview with an acquittanced person assigning the outcome of the medical consultation to a scale, for example the Reisberg scale [1] and the evaluation of a Clock Drawing Test. Up to date, there are many different modifications of the Clock Drawing Test, sometimes containing subjective criteria for the evaluation, for example, in the fourth grade of the Shulman scoring “moderately poor spacing” [2]. Therefore, the evaluation of the same test by different specialists may result in different scores.

By digitizing the Clock Drawing Test all criteria are quantified, allowing a very accurate evaluation and reproducible score, meaning that the same test will always have the same score. Further on, different parameters can be acquired by the digitized test, which are nearly impossible to acquire by the traditional pen and paper based tests. These parameters, which reflect the cognitive ability of the patient, are, for example, the time interval between strokes, the time interval for drawing specific strokes, the total time for finishing the test, the size of the strokes compared to the clock size, etcetera [3].

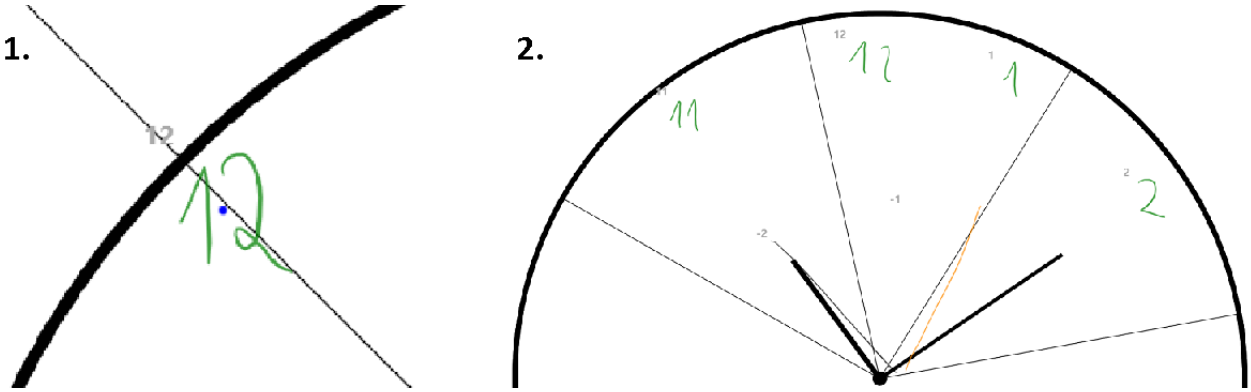

Fig. 1: Precise evaluation of quantified criteria. 1. The mass point of the digit 12 being outside of the puffer zone. 2. The inclination of the drawn minute hand being too steep.

The Clock Drawing Test “C-GADT”, developed by the St. Marien-Hospital Hamm, consists of seven quantified criteria and is suitable for digitization. The first four criteria analyze the placement of the drawn anchor digits 12, 3, 6 and 9 in a 45° puffer zone to the left and right of the ideal position. The fifth criteria analyses if the patient did draw exactly the digits of 1-12. The sixth and seventh criteria analyze the placement and inclination of the drawn hands in a puffer zone of 24° to the left and right of the drawn digit 2 and/or 11. A total maximum score of 10 points can be achieved, the first four criteria giving each one point and the last three giving each two points. The digitized test was executed on a Surface Pro 4 Tablet-PC using the active pen technology for digitizing the strokes.

In this Bachelor thesis, a small trial with 12 patients was conducted. To ensure the statistical accuracy, a database of 152 Clock Drawing Tests was analyzed. 12 tests being drawn by the patients; 40 tests being created by a medical expert in the field of dementia [(2)], who also provided 100 scans of real tests, which were traced in the digitized Clock Drawing Test. The following aspects have been evaluated in this thesis: 1. The frequency of occurrence of each C-GADT point was counted and the ratio of each point was calculated to determine the complexity of each criteria for the patients; 2. If a fully automatic solution or an assistance system is more viable and 3. Frequent source of errors.

1. The digit 12 was drawn in 82.2%, the digit 3 in 66.4%, the digit 6 in 67.1% and the digit 9 in 59.2% of the cases. Therefore, the anchor digits were placed correctly in an average of 68.7% of the tests. The more complex criteria, the exact drawing of the digits were fulfilled in 33.5% of the cases and the placement of the hour hand were drawn in 34.2% of the tests. The last and most complex cognitive criteria, the placement of the minute hand, was drawn in 19.7% of the cases.

2. 35 of the 152 tests were evaluated fully automatically by the digital test and 117 of the 152 needed to be corrected at least once. Thus, an assistance system is more viable, because the evaluation of Clock Drawing Tests turns out being too variable for a full automatic solution.

3. The two most prominent sources of errors were 86 times, that a drawn stroke was not converted to the right number and/or not converted to a number at all. This happened because the used library was not optimized for detecting only numbers but also handwritten text. In 39 times, no stroke was automatically assigned to a drawn hand. By now, both problems were improved. A “Nearest Neighbor Algorithm” defines the closest stroke to the mass point of the programmatically created line. After that, the inclination and bound check is conducted. The clustering of drawn strokes occurs now more in an x-axis rather than in a radius. Thus, unwanted strokes are not combined and the detection of the numbers is improved.

In this thesis, a tool for accurate evaluation of Clock Drawing Tests is presented resulting in reproducible scores. The digitized test provides the possibility to analyze time- and size-related parameters. Creating statistical analysis of this values and video sequences of the Clock Drawing Tests may provide a powerful tool for long-time evaluation of the health development of patients suffering a dementia disease, but also for the evaluation of the quality and effectiveness of different treatments.

References

[1] Cristoph Hock “Die Alzheimer Krankheit" Gunter Narr Verlag, 2000.
[2] Freedman, M., Leach, L., Kaplan, E., Winocur, G., Shulman, K., & Delis, D. C “Clock Drawing: A neuropsychological analysis “, New York: Oxford University Press, 1994.
[3] William Souillard-Mandar, Randall Davis, Cynthia Rudin, Rhoda Au, David J. Libon, Rodney Swenson, Catherine C. Price, Melissa Lamar, Dana L. Penney “Learning classification models of cognitive conditions from subtle behaviors in the digital Clock Drawing Test”, 2015

[13] Measuring Local Pulse Transit Time for Affective Computing Applications

Nils Beckmann [(1), (2)], Reinhard Viga [(1)], Aysegül Dogangün [(2)] and Anton Grabmaier [(1)]
[(1)] Electronic Components and Circuits,
Department of Electrical Engineering and Information Technology, University of Duisburg-Essen, D-47057 Duisburg, Germany
[(2)] Competence Center Personal Analytics,
Department of Computer and Cognitive Science, University of Duisburg-Essen,
D-47057 Duisburg, Germany
E-Mail: nils.beckmann@uni-due.de
Web: www.uni-due.de/ebs, www.uni-due.de/panalytics

Abstract – In the research area of Affective Computing user data is analyzed to get access to human emotions. Physiology parameters can be used as a source of information in this context. A high number of physiological parameters (e.g., from respiratory or cardiovascular system) have been investigated regarding their correlation to psychological processes [1]. Wearable devices offer the opportunity to measure these parameters and hereby to develop Affective Computing applications. However, developers of wearable devices have to find a compromise between functionality (e.g., quantity and quality of parameters) and usability (e.g., simplicity, comfort).

We present a novel approach which is supposed to enable a device to measure an additional parameter and to improve parameter's accuracy compared to present devices. Our focus is on the cardiovascular system and a commonly used method in this context is the Photoplethysmography (PPG). PPG-based sensors are used in many wearable devices like smartwatches and fitness trackers to measure Peak to Peak intervals (t_{PP}) between successive blood pulse waves and hereby derive Heart Rate (HR) or Heart Rate Variability (HRV). HRV describes changes of t_{PP} over time and is frequently used in Affective Computing. However, compared to the R-Peak to R-Peak intervals (t_{RR}) derived by Electrocardiography (ECG, the gold standard for HRV measurement) this method is inaccurate in particular, if the user is physically active or experiencing mental stress [2].

Our approach also uses PPG-based sensors, but extends the devices capability by using two sensors (PPG1 and PPG2) placed at a known distance ($d_{x1\rightarrow x2}$), for example, at the forearm. Through this extension a device is expected to measure the time delay the blood pulse wave needs to travel from one point to another. This time is called local Pulse Transit Time ($t_{PTT,local}$). The state of the art is measuring global Pulse Transit Time ($t_{PTT,global}$) using an ECG and a PPG. $t_{PTT,global}$ is defined as the time between the contraction of the heart (R-Peak) measured by an ECG and the arrival of the corresponding blood pulse wave (e.g., at a wrist) measured by a PPG [3]. It can reflect states of the cardiovascular system which can respond to psychological processes [1].

Figure 1 shows how calculation of $t_{PTT,local}$ can be done using two PPG Signals. The inflection point of the wave is detected by the zero crossing in the second derivative of the PPG signal. The delay between corresponding inflection points is $t_{PTT,local}$.

Equation 1 shows that global PTT ($t_{PTT,global}$) can also be seen as a possible source of error when comparing t_{RR} and t_{PP}.

$$t_{RR} = t_{PP} - |t_{PTT,global}(n) - t_{PTT,global}(n+1)| \quad (1)$$

Because $t_{PTT,global}$ can vary from heart beat to heart beat it induces an error in PPG-based HRV measurement. The variation of $t_{PTT,global}$ is affected by two variables (eq. 2).

$$t_{PTT,global} = t_{PEP} + \frac{d_{Heart\rightarrow x}}{\bar{v}_{PWV,global}} \quad (2)$$

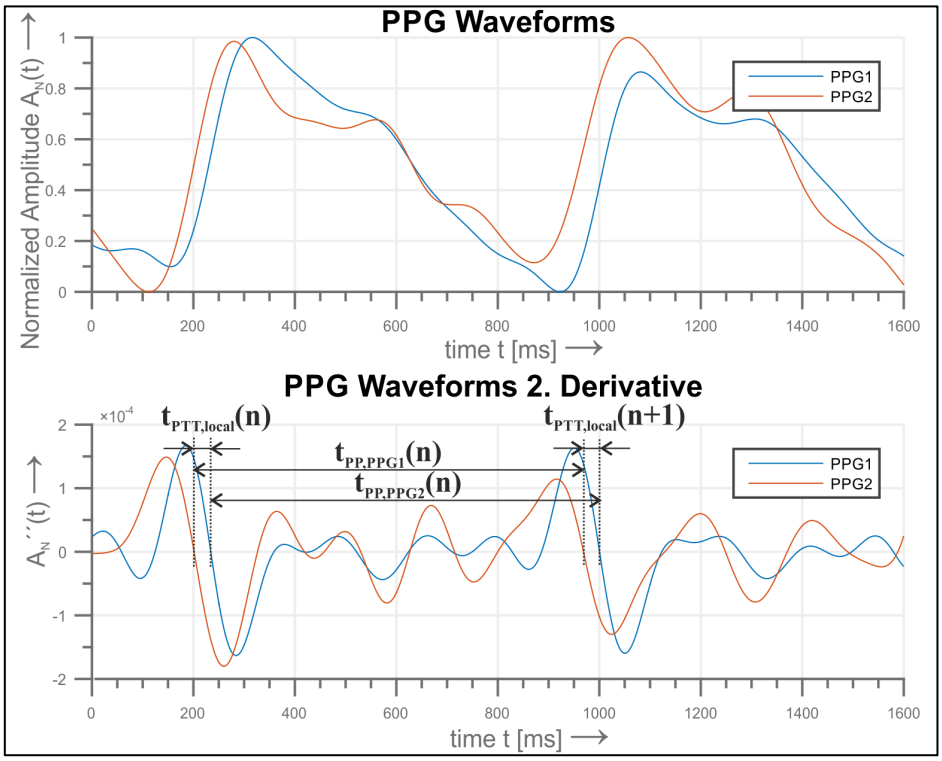

Fig.1: PPG Waveforms measured by two sensors in a short distance (upper graph). Second derivative of the waveforms and derivable parameters (lower graph).

The first one is the so called Pre-Ejection Period (t_{PEP}) which is the time delay between the electrically measurable contraction of the heart and the actual ejection of blood [4]. The second influence factor is the time delay based on the fixed distance the pulse wave has to travel ($d_{Heart \rightarrow x}$) and the variable mean Pulse Wave Velocity ($\bar{v}_{PWV,global}$) correlating to the current state of the cardiovascular system.

By measuring the variability of $t_{PTT,local}$ we want to estimate changes in the state of the cardiovascular system. This data could be directly used in Affective Computing applications. Furthermore, we want to develop a model using $t_{PTT,local}$ as an input parameter to increase the accuracy of PPG-based HRV measurement. This approach can be integrated into a single device and therefore functionality as well as usability can be considered.

Our preliminary results of short term $t_{PTT,local}$ measurement under resting conditions proved the practicability of our approach. We achieved values within an expected range derived from literature. Due to the fact that we are not able to capture t_{PEP} and measure $t_{PTT,local}$ instead of $t_{PTT,global}$ our approach is limited (eq. 2 and 3).

$$t_{PTT,local} = \frac{d_{x1 \rightarrow x2}}{\bar{v}_{PWV,local}} \tag{3}$$

Therefore, further investigations focusing on variations in $t_{PTT,local}$ and its impact on HRV measurement are necessary.

References

[1] S. D. Kreibig, “Autonomic nervous system activity in emotion: a review,” Biological Psychology, vol. 84, no. 3, pp. 394–421, 2010.
[2] A. Schäfer and J. Vagedes, “How accurate is pulse rate variability as an estimate of heart rate variability? A review on studies comparing photoplethysmographic technology with an electrocardiogram,” International journal of cardiology, vol. 166, no. 1, pp. 15–29, 2013.
[3] J. Allen, “Photoplethysmography and its application in clinical physiological measurement”, Physiological measurement, vol. 28, no. 3, p. R1-39, 2007.
[4] Q. Li and G. G. Belz, “Systolic time intervals in clinical pharmacology,” European Journal of Clinical Pharmacology, vol. 44, no. 5, pp. 415–421, 1993.

[14] Safety and Security for Medical Devices: Analysis and Implementation of a Secure Software Update for Embedded Systems

Andrei Lorengel [(1)], Jan Pelzl [(2)]

[(1)] Hamm-Lippstadt University of Applied Sciences,
D-59063 Hamm, Germany
E-Mail: andrei.lorengel@stud.hshl.de
Web: www.hshl.de

[(2)] Hamm-Lippstadt University of Applied Sciences,
D-59063 Hamm, Germany

E-Mail: jan.pelzl@hshl.de
Web: www.hshl.de

Abstract – In the recent decades, medical devices developed from stand-alone devices to smart and networked systems. Innovation in medical devices mainly is driven by software. Software increasingly determines the devices' functionality, making it an indispensable part of the product. Remote diagnosis, remote configuration as well as monitoring capabilities are only some examples of the powerful information technology being used within modern medical devices. However, software driven products bear the risk of manipulation - with severe threat to life or physical condition.

With the advent of first attacks on medical devices, first recommendations by officials have been introduced. As an example, the US Food and Drug Administration (FDA) recently published an update of its security guidance document "Post Market Management of Cyber-Security in Medical Devices", containing several security recommendations for the safe and secure operation of medical devices in the field [1]. It is just a matter of time until first obligatory standards will come up for the US and for Europe.

As a consequence of this development, software for medical devices needs to ensure security and, thus, reliability of the entire device. The manufacturer of software must meet all the requirements of the Medical Devices Act when the software used for therapy and diagnosis measures for a human being [2]. On the one hand, this implies respective development processes to develop reliable, safety-critical software. On the other hand, the nature of software allows updates in case of improved functionalities or bug fixes in the field. This powerful feature allows manufacturers to update functionalities even years after production. However, it is imperative to only allow updates with officially released and tested software. It shall not be possible to unintentionally or intentionally update devices with third party software and, thus, allow manipulation.

With this contribution, we will discuss the importance of secure software updates for medical devices and will demonstrate secure software update with the help of modern IT security. From a technical perspective and depending on the development process, software updates can be extremely complex. Small changes might lead to life critical situation after the update process.

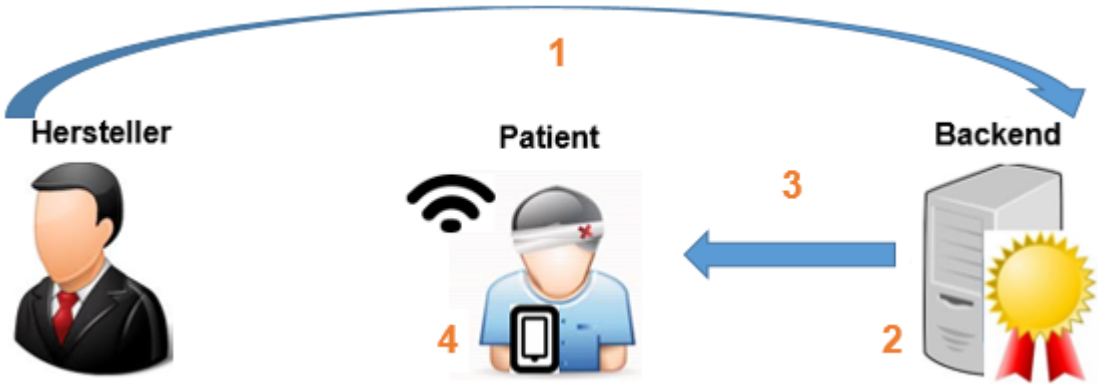

Fig.1: Simplified secure software update of a medical device via a digital interface - all connections are encrypted and authenticated. Step 1: Certificate and signature of software is created by the manufacturer and send to a central server. Step 2: Central server keeps track of software revisions, devices in the field and schedules updates with remote devices. Step 3: Software update is transferred securely. Step 4: Device locally checks the software and performs the update.

Figure 1 shows a simplified principle of a secure software update for medical devices. Cryptographic mechanisms ensure the authenticity of the software and only allow devices to update if the software is from a trusted source. Practically, there are two possible flavors of realization: use of symmetric cryptography or asymmetric cryptography. In both cases, the manufacturer has to use a confidential secret key to generate a certificate of the software by signing it. In the device, the signature has to be verified with the corresponding key. In the symmetric case, the device has to use the same (symmetric) key to verify the signature, a so-called message authentication code. Whereas in the asymmetric case, the device requires the public key of the manufacturer to verify the signature. Both variants do have advantages and disadvantages: Symmetric signatures require a secure storage of the (secret) key in every device but are extremely efficient. Asymmetric signatures require more computational power but therefore only require authentic keys. Depending on the security features of the device and the way of handling keys for devices (e.g., individual keys per device vs. global keys), the security of the realization of a secure software update varies. However, the best choice of algorithms and key management principles is not only a matter of security but also of cost-effectiveness and a good fit to existing production and development processes at the manufacturer site. [3, 4]

With this work, we discuss the tradeoffs of different variants of secure software update and show an example how to achieve secure software updates for a typical embedded linux using digital signatures.

References

[1] U.S. Food and Drug Administration: Postmarket Management of Cybersecurity in Medical Devices, Guidance for Industry and Food and Drug Administration Staff, December 28, 2016. http://www.fda.org
[2] A. Gärtner: Medizinische Netzwerke und Software als Medizinprodukt (Praxiswissen Medizintechnik), 2008
[2] J. Pelzl: IT-Sicherheit für Biomedizintechnik – Typische Anwendungsfälle, Lecture Notes, 2015
[3] Secure Over-the-air Software Updates im Automobil: http://www.all-electronics.de/sota-software-updates-im-automobil/ (accessed Feb. 08, 2016)

[15] Ludic System for Therapy Exercises of Wrist and Hand Phalanges

Amaury Perez Tirado,

Advantage Engineering Center (CIA),
Faculty of Engineering, National Autonomous University of Mexico, Mexico City, Mexico, and
Aachen University of Applied Sciences, Aachen, Germany

E-Mail: aptur@hotmail.com
Web: https://www.unam.mx/

Abstract – The rehabilitation process use therapeutic exercises, they require consistence and a correct execution of the movements realized by the patients, then there will be progress in their recovery; those exercises, generally, are made at home where the persons are susceptible to the boring and abandonment, because of that, the treatment is longer and tedious. [1]

The present project consisted in the development of a device that allows to the persons realize the therapy exercises, using ludic activities. In this case, it was used the hand because It is a vital element in the daily life of the persons, the hand is conformed for phalanges, carpus, metacarpus. It was analyzed the movements of the finger, the flexion and extension of phalanges and the rotation movement of the wrist, abdution and adduction, and we add the pronation and supination like complement movements for the interaction. [2]

It is proposed implement a system based in gamification, that is, the application of mechanics that belong to the games [3]. In this way, we use psychologic elements of video games like: Competence, Challenge, Fantasy, Immersion, that makes more attractive the activities for the users. [4]

There are works before about using serious games in the recovery of a patient, like in the case of rehabilitation of a cardiovascular accident, where it was applied virtual reality in the therapy of the superior member, with positive results. [5]

The method to design the system begin with the analysis of the problem, and then it obtains the technical requirements, which are measurable. In this case was considered that the system will be a domestic device, for that the maximum space needed is 30 [cm] * 30 [cm] * 30 [cm] and a maximum weight 3 [kg]. In terms of the software, it required maintain attention of the user for at least 20 [min]. And according with the goniometry it's proposed 30 [°] for the movements of the wrist and 80 [°] for the proximal phalange.

Later the configuration of the system make able to the user realize different exercises of mobility, amplitude and resistance. Using different sensors and actuators. First, we have the finger movements, is read by the flex sensor, it was conditioned using Wheatstone bridge an operational amplificators, then an ADC, using a microcontroller. Additionally, for the register of the movement of the wrist it was used an inertial measure unit (IMU), using a Kallman filter, we combined the accelerometer, magnetometer and gyroscope data, and it was obtained use 3 degrees of freedom, pitch, roll and yaw. The actuator used is a motor connected to a potentiometer to use a feedback control system, with a PID controller, we can control the resistance that the user can feel, which is reached using a system of strings and pulleys.

The structure of the system was designed according with the requirement of volume and the configuration of the electronic components (Figure 1). It was designed a semi spherical base to make viable the rotations and compress all the circuit system, and a joystick form for the conformity of the user, using the average size of ten different persons.

Fig.1: The render of the virtual design of the structure.

In a software level, the games were developed in XNA and Unity with the C# language to create the virtual environments. Using a protocol of RS-232 receive the data of the sensors, it's possible to convert the information in the control of the interface. The games developed contain a score system, a variable time challenge, different speed and resistance changes, progress screen, which provide to the user and the physiotherapist, all the information needed to be sure the goals are reached.

The functional model was used in different users inside of the university (figure 2) and was evaluated by the sport medical unit of the university, where they made some observations of the possible future changes, like to include exercises for the thump. Further it is possible to adapt the system to a phase of rehabilitation where the patient can realize exercises without supervision of a specialist, only when the user doesn't feel pain making movement.

Fig.2: Completed functional model used by one of the testers.

Finally, we can add that it will be need more studies in the future to probe the motivation of the users, but it required the development of a different games or situations, to maintain the attention of the users; but it's notable the persons are curious and interested in test this kind of systems. The work develops here it was will work like base for future projects of system that pretend combine the exercise or therapy with the gamification.

References

[1] Carrie M. Hall, *Ejercicio Terapeutico, Recuperación Funcional*. Badalona, Spain: Editorial Paidotribo, 2006.
[2] Claudio H. Taboadela, *Goniometría Una herramienta para la evaluación de las incapacidades laborales*, first ed. Buenos Aires, Argentina: Asociart SA, 2007.
[3] Gamificación S.L. (2013) Qué es la Gamificación. [Online]. http://www.gamificacion.com/que-es-la-gamificacion [Available: May, 2014].
[4] Juan José Igartua Perosanz Diego Rodríguez de Sepúlveda Pardo. (2012, October) Creación y validación de una escala de motivos para videojugar. [Online]. http://campus.usal.es/~comunicacion3punto0/comunicaciones/039.pdf [Available: May, 2014]
[5] Minhua Ma, Kamal Bechkoum "Serious games for movement therapy after Stroke" Systems, Man and Cybernetics, 2008.

[16] Exposure of FAI – A Squeezed Labrum as the Reason for Limitation of Movement and Pain

Robert Cichon[(1)], Dominik Raab[(1)], Andrea Lazik Palm[(2)], Jens M. Theysohn[(2)], Stefan Landgraeber[(3)], Wojciech Kowalczyk[(1)]

[(1)] Chair of Mechanics and Robotics
University of Duisburg-Essen,
D-47057 Duisburg, Germany

[(2)] Inst. for Diagnostics and Interventional Radiology and Neuroradiology,
University Hospital Essen,
D-45147 Essen, Germany

[(3)] Clinic for Orthopedics,
University Clinic Essen,
D-45147 Essen, Germany
E-Mail: robert.cichon@uni-due.de
Web: www.uni-due.de/lmr

Abstract – In recent years, Femoroacetabular Impingement (FAI) has become an increasingly common orthopedic disease. In literature this disease is described as an abnormal contact between femur and acetabular rim caused by bony deformities, which leads to limitation of movement and pain and, in long-term, damage of the cartilage. [1] This deformity occur either at the femoral neck (cam-type) or at the acetabular rim (pincer-type) or combined. A possible treatment is the arthroscopic removal of the overlapping bone, which is exclusively a subjective assessment of the attending physician based on static imaging, e.g. MRI, and movement tests, which is therefore only a semi-quantitative diagnosis. A more exact surgery planning is possible using dynamic multi-body simulations.

The detection of the FAI is performed by investigating the range of motion using a Motion Capture system. During the measurement the pain is recorded with a pressure detecting bellow. After this investigation, a MRI scan is performed using a comprehensive thin layer protocol with a slice thickness of 1.5mm. MRI data of Acetabulum, Femur and Labrum are manually segmented and CAD models as well as FEM models are generated illustrated in Figure 1. The contact modeling between Labrum and Femur was generated using the Pure Penalty algorithm, Labrum and Acetabulum remain bonded. The material properties for the bony parts is lin. cortical bone (E=1,2 GPa, ϑ=0,4 [2]) and for the Labrum (E=20 MPa , ϑ=0,4 [3]). The movement in the simulation is controlled using the determined maximum angles of the motion analysis.

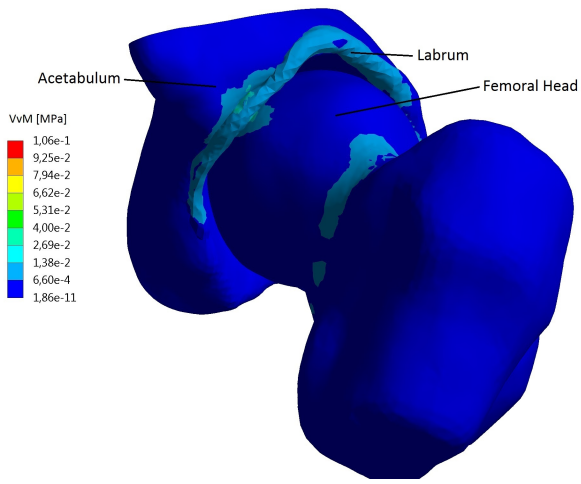

Fig.1: Patient-Specific Hip Model Including Labrum, Femur and Acetabulum.

The visualization and quantification of the joint movement show a contact of labrum and femur. Comparing this simulation result with the motion analysis results, the patient applied the pain sensor in the same angle range of 11.5° internal rotation and 33° flexion. Deformations and stresses can be determined and are available at the contact area visible in Figure 1.

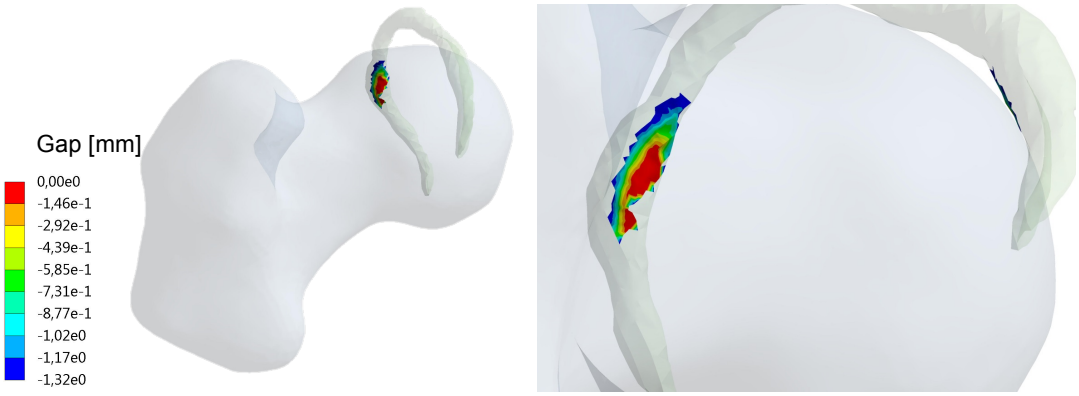

Fig.2: Contact Modeling of a Patient-Specific Hip Model: Gap Analysis Show Contact Between Femur and Labrum.

In Figure 2 the Gap Modeling of ANSYS is showed: There is a contact area between Femur and Labrum.

An automatic MRI segmentation is necessary to standardize this diagnose possibility. The surgical treatment can be better planned to remove the bony deformity to ensure no squeezing of the labrum. Further evaluations are possible using computer-assisted techniques, such as FEM. Additionally, the navigation-assisted surgery can optimize the surgical outcome. In future studies, articulating cartilages and muscles forces, as well as cancellous bone should be implemented to ensure a more realistic simulation of the Biomechanics of the human hip joint. For validation a patient study is needed.

References

[1] O.Marin Pena, Femoroacetabular Impingement, Springer-Verlag, 2012.
[2] Tran et al., Experimental and computational studies on the femoral fracture risk for advanced core decompression, Clin Biomech, Vol. 29, 412-417
[3] Ferguson et al., The material properties of the bovine acetabular labrum, J Rthop Res, Vol. 19, 5: 887-896

[17] Prevention of Femur Neck Fractures through Femoroplasty

Alexander Abel[(1)], Daniel Pérez-Viana[(1)], Bernhard Ciritsis[(2)] and Manfred Staat[(1)]

[(1)] Biomechanics Laboratory, Institute for Bioengineering,
Faculty of Medical Engineering and Technomathematics, Aachen University of Applied Sciences,
D-52428 Jülich, Germany

[(2)] Ortopedia (chirurgia ortopedica)
Ospedale San Giovanni EOC, via Ospedale, CH-6500 Bellinzona, Switzerland

E-Mail: alexander.abel@alumni.fh-aachen.de, m.staat@fh-aachen.de
Web: http://www.ifb.fh-aachen.de/

Abstract – Femur neck fractures continue to be a threat to patients with advanced osteoporosis [1]. Due to the reduction of bone material even low energy situations like low height falls can lead to fractures. To prevent long immobilization the usual choice of treatment is an implantation of a hip prosthesis. Due to the limited lifespan of endoprostheses a re-operation will be necessary eventually. To delay or even prevent fractures, bone cement (PMMA) could be placed in the femur neck to increase the mechanical strength of the bone in a femoroplasty procedure. The cement is injected with patented surgical tools so that a hollow tube like PMMA body (Fig. 2 (a)) is achieved which reduces the volume and therefore the heat generated during polymerization.

10 human femur pairs, age ranging from 66 to 88 years, were tested in a Hayes-fall configuration to represent a common fall scenario. The left of each pair was modified with a femoroplasty while the other side acted as control [2]. Beforehand the femur pairs were scanned in a computer tomography and the CT data was used to create finite element models using Amira (FEI, Visualization Sciences Group, Bordeaux, France) for image segmentation and geometry reconstruction. The models consist of 10-node tetrahedrons which had their Young's modulus assigned by an in-house Python code using the grey values of the CT cross sections. The open-source program Salome was used as a preprocessor and postprocessor with *Code Aster* as finite element solver.

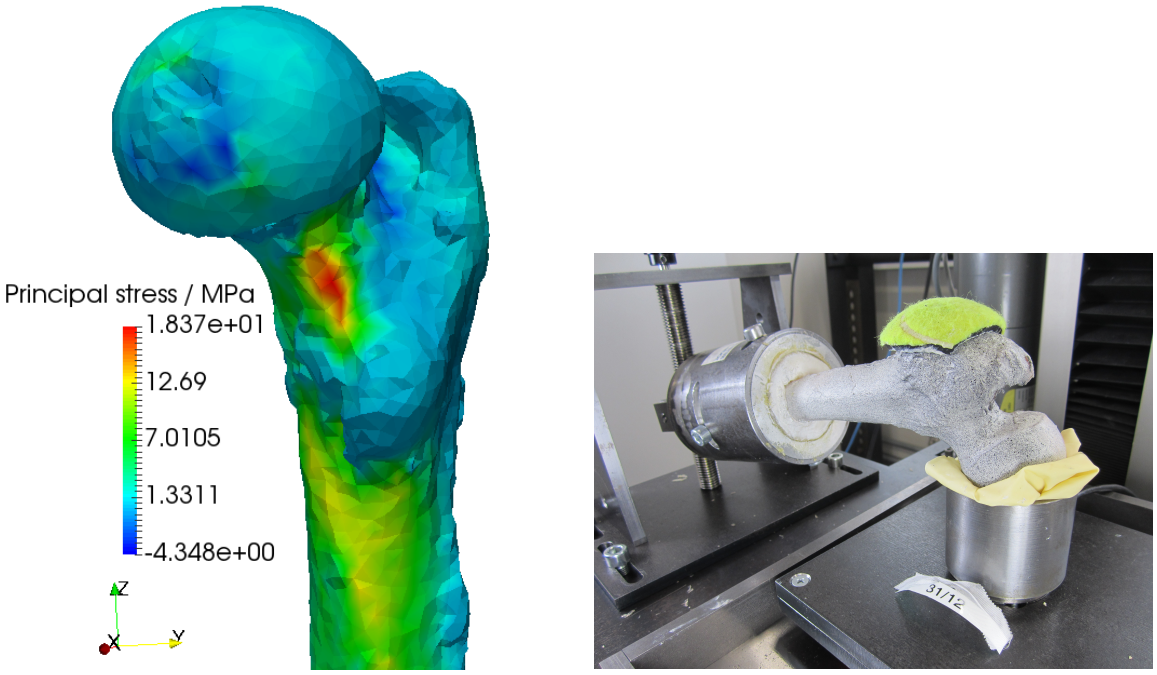

Fig.1: (a) Major principle stress in the finite element simulation and (b) Experimental setup

The experimental setup in Fig. 1 (b) fixed the distal femur against translations but allowed for rotations about one axis. The femur head was allowed to translate in the horizontal plane. Compressive forces were applied through the trochanter major while a part of a tennis ball was used to prevent point forces. The boundary conditions of the finite element models were chosen to represent the experimental configuration. The distal fixation is realized by an axis which is fixed for translation but allows rotation around itself. Proximal forces are applied on the trochanter major surface in x direction, while the opposing surface on the femur head prevents displacements in the same.

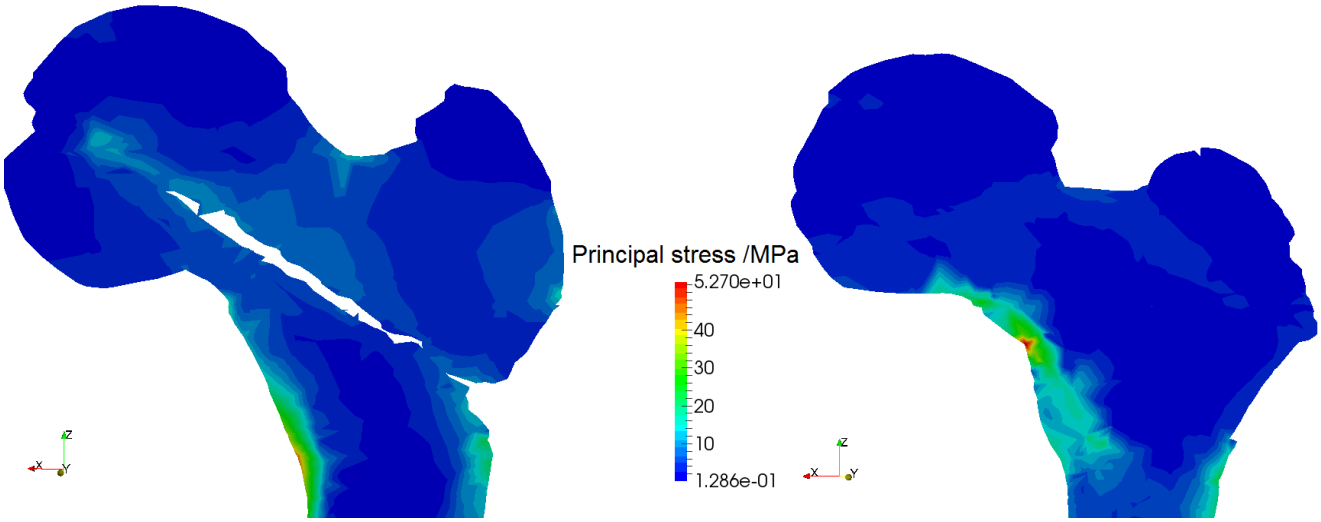

Fig.2: Finite element cross section of one femur pair (a) with and (b) without femoroplasty

The results of the experiments show a varying increase of peak fracture forces in the augmented femur in Fig. 2 (a) compared to the natural femur in Fig. 2 (b), while the simulation visualizes the shift in location and magnitude of peak major principal stresses when comparing the augmented and control femur. The femoroplasty causes a reduction and a shift of peak stress to a more distal location as well as a distribution of stress across the femur neck which doesn't show in the non-augmented control. The simulation show the effective load transfer from the PMMA injection to the spongiosa. Besides giving insight into the stress distribution through cross sections, the finite element model can show the impact of the rubber between the bone and test setup. Reduced stiffness and increased displacements are seen with an added hyperelastic rubber component to the trochanter major. Taken together, conclusions about the effectiveness of the femoroplasty and possible improvements to the procedure itself can be drawn.

The mechanical tests showed that five of the femora in the the seven valid tests underwent a strengthening. On average the maximum force carried by the untreated bones was 2439.6 N ranging from 1200 N to 4700 N. The average maximum force carried by the femora with femoroplasty was 3379.7 N ranging from 2200 N to 6200 N. In 2 cases no strengthening has been observed [3]. The locations of fractures could be related to the locations of higher major principal stress.

References

[1] S.E. Bentler et al.: The aftermath of hip fracture: discharge placement, functional status change, and mortality. *American Journal of Epidemiology,* 2009;**170**(10):1290–1299. https://doi.org/10.1093/aje/kwp266

[2] D. Pérez-Viana, *Fracture testing under simulated fall conditions and finite element analysis of femoroplasty.* Master thesis, FH Aachen University of Applied Sciences, March 2, 2015.

[3] B. Ciritsis, H.-P. Simmen, D. Pérez-Viana, A. Ciritsis, A. Prescher, M. Staat: Femoroplasty: fracture test, optical strain measurement and FE analysis. 9. Jahrestagung der Deutschen Gesellschaft für Biomechanik, 06.-08. Mai 2015, Bonn, pp 8-9.

[18] Calculation of muscle forces and joint reaction loads in shoulder area via an OpenSim based computer calculation

Stefan Birgel[(1)], Tim Leschinger[(2)], Kilian Wegmann[(2)], and Manfred Staat[(1)]

[(1)] Institute of Bioengineering (IfB), Biomechanics Laboratory
Faculty of Medical Engineering and Technomathematics, Aachen University of Applied Sciences
D-52428 Jülich, Germany
[(2)] Center for Orthopedic and Trauma Surgery, University Medical Center Cologne,
D-50937 Cologne, Germany

E-Mail: m.staat@fh-aachen.de
Web: http://www.ifb.fh-aachen.de/

Abstract – In modern chirurgic science a bunch of alternative approaches exist for nearly any muscular injury. Therefore, it is desirable to find a way to calculate biomechanical values such as muscle forces, activations and moment arms or joint reaction forces. Due to the fact that there are more unknown muscle and joint forces than equilibrium equations the muscle forces are calculated by mathematical optimization with the objective function muscle power to be minimized under the constraints of moment equilibrium. This is followed by an inverse dynamics step and is enclosed in a loop of a muscle control algorithm [1]. To realize this calculation a musculoskeletal model of the upper limb was build and implemented in the OpenSim environment. OpenSim is a freely available tool for musculoskeletal modelling and movement simulations. It is published by the NCSSR (national centre for simulation and research, Stanford, USA) and is used by hundreds of research teams worldwide [2].

The used model of the upper extremity contains as well values of mass, inertia of all 9 bodies as their position and joints. It further more features a description of 10 muscles containing their path and possibly wrapping, as well as their maximal isometric force, optimal fibre length, tendon slack length, and possible activation to define their behaviour within the *Thelen* muscle model [3].

These values enable OpenSim to solve an inverse optimisation problem and calculation the respective muscle activations and forces that are necessary to perform a certain movement. With these forces OpenSim can further more calculate joint reaction forces in every included joint.

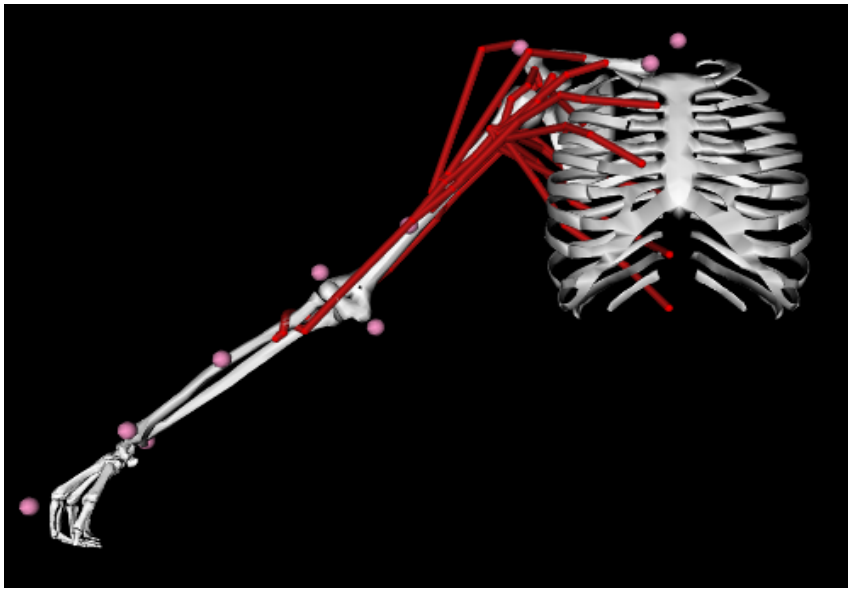

Fig.1: The build musculoskeletal model in OpenSim

With this model, the influence of changes regarding the insertion points of muscles was examined. To handle tears of the rotator cuff there are the approaches of reattaching the tendon more laterally or medially. By calculating the necessary muscle forces to perform an abduction up to 90° for situations in which the insertion points where shifted from 1mm to 5mm laterally or medially it was possible to find the optimal position for every of the rotator cuff muscles. This might help to unburden the respective muscles after an injury.

In addition, a calculation of the joint reaction forces provides information about how the changes influence the joint reaction forces. This gave us the possibility to draw a conclusion about the joint`s stability regarding to the biomechanical changes caused by the relocation of muscle insertion points.

By using a modified computational shoulder model the present research confirms that a medialised non-anatomical reinsertion of the supraspinatus muscle within a range up to 10 mm is biomechanical acceptable in regard to the supraspinatus moment arm. Nevertheless, it revealed that a medial shift of the insertion point of the muscle leads to a decrease of its moment arm and therefore a decreasing maximal moment which the muscle can contribute to arm abduction. It furthermore leads to a decrease of the compressive glenohumeral joint reaction force. This influences the glenohumeral stability in a negative way reducing the stability ratio (compressive force/ shear force).

Such a change in biomechanical stability of the joint leads to not only an increase of the force of the supraspinatus but also to such an influence on all muscles forces the of rotator cuff which are mainly responsible for joint stability during abduction.

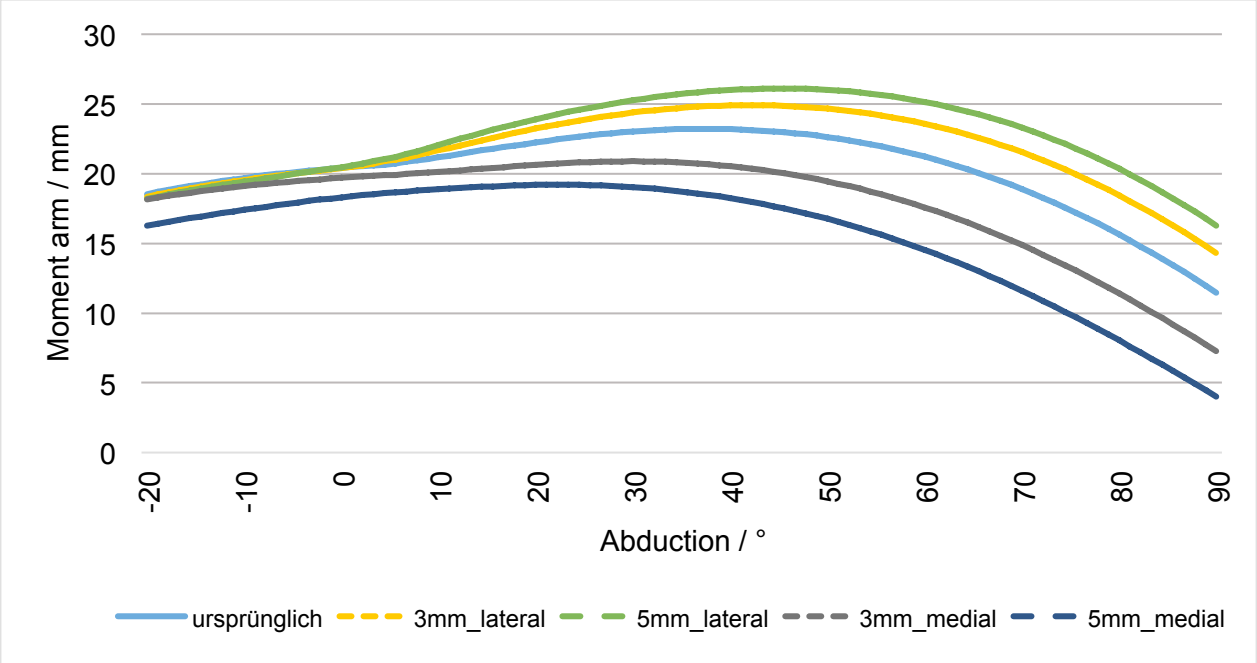

Fig.2: Supraspinatus moment arm vs. abduction

References

[1] D.G. Thelen, F.C. Anderson: Using computed muscle control to generate forward dynamic simulations of human walking from experimental data. *J. Biomech.*, 2006,**39**(6):1107-1115. https://doi.org/10.1016/j.jbiomech.2005.02.010

[2] S.L. Delp, F.C. Anderson, A.S. Arnold, P. Loan, A. Habib, C.T. John, E. Guendelman, D.G. Thelen: OpenSim: open-source software to create and analyze dynamic simulations of movement. *IEEE Trans Biomed Eng*. 2007;*54*(11):1940-1950. https://doi.org/10.1109/TBME.2007.901024

[3] D.G. Thelen: Adjustment of muscle mechanics model parameters to simulate dynamic contractions in older adults. *J Biomech Eng*. 2003;**125**(1):70-77. http://dx.doi.org/10.1002/10.1115/1.1531112

19) Biomechanical Simulation of Different Prosthetic Meshes for Repairing Uterine/Vaginal Vault Prolapse

Medisa Jabbari*(1), Aroj Bhattarai(1), Ralf Anding(2), Manfred Staat(1)

(1) Institute of Bioengineering, Biomechanics Laboratory
FH Aachen University of Applied Sciences, Jülich Campus
Heinrich-Mußmann-Str. 1, 52428, Jülich, Germany

(2) Klinik und Poliklinik für Urologie und Kinderurologie, University Hospital Bonn
Sigmund-Freud-Str. 25, 53127 Bonn, Germany

E-mail: medisa.j@gmail.com, {bhattarai, m.staat}@fh-aachen.de
Web: http://www.ifb.fh-aachen.de

Abstract – Women – often elderly and/or multiparous – may suffer from uterine/vaginal vault prolapse, which is caused by the loss of support from the apical ligaments and muscles within the bony pelvis. Risk factors are assumed to be obesity, chronic increase in intra-abdominal pressure (IAP), and also tissue damage during vaginal delivery, etc. Such problems often recover spontaneously. However, critical damages in the muscles and ligaments around the cervical ring are prone to cause significant descent of the uterus into the vaginal canal. Approximately, 50% of parous women have some degree of prolapse [1] and more than 60% of the patients are aged over 60 [2]. Prosthetic mesh implants are surgically inserted to support the function of lax (weak) apical ligaments and muscles. These implants are widely used to stabilize and support the normal anatomical position of the cervical ring by fixing it to the sacrospinous ligaments, the upper sacrum or the pelvic sidewalls. Polyvinyliden fluoride (PVDF) is the newly used polymer to construct such devices due to their minimal inflammatory reaction, reduced risk of infection, and preserved tensile strength in long range compared to other conventional meshes.

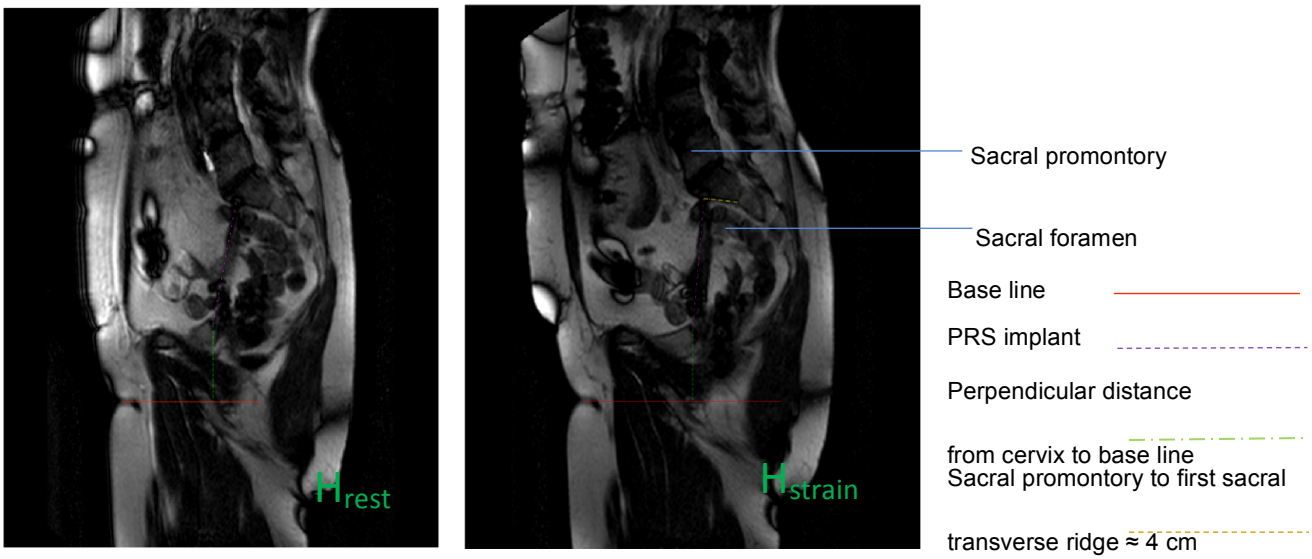

Fig. 1 *Female pelvic floor in rest (left) and strained (right) condition. Vertical displacement of cervical ring (H_{rest} – H_{strain}) is 5 mm [Source: Dr. Ralf Anding, Bonn].*

Materials and Methods: Three different mesh types (DynaMesh-PRP soft, DynaMesh-PRS soft and DynaMesh-CESA) from FEG Textiltechnik GmbH, Aachen, Germany have been tested to support the function of weakened apical ligaments. These meshes are manufactured as nonlinear elastic orthotropic materials. The 3D finite element (FE) model has been reconstructed from a 70 year old female cadaver specimen, which is obtained from the human donation program of the Medical University of Vienna [3]. The soft organs, ligaments, fasciae and muscles are modelled as hyperelastic materials, using the Mooney-Rivlin class of strain energy functions. To simulate the progressive development of the PFDs, supporting tissues are successively weakened between 0% and 95% by reducing the material stiffness [4]. Frictionless contact between the organs is taken into account, which is a realistic assumption. An intra-abdominal pressure of 4 kPa is applied, which is measured during Valsalva maneuver. We then compare the efficiency of the mesh implants to minimize the dislocation of the cervical ring and examine the mesh-tissue interaction using FEM.

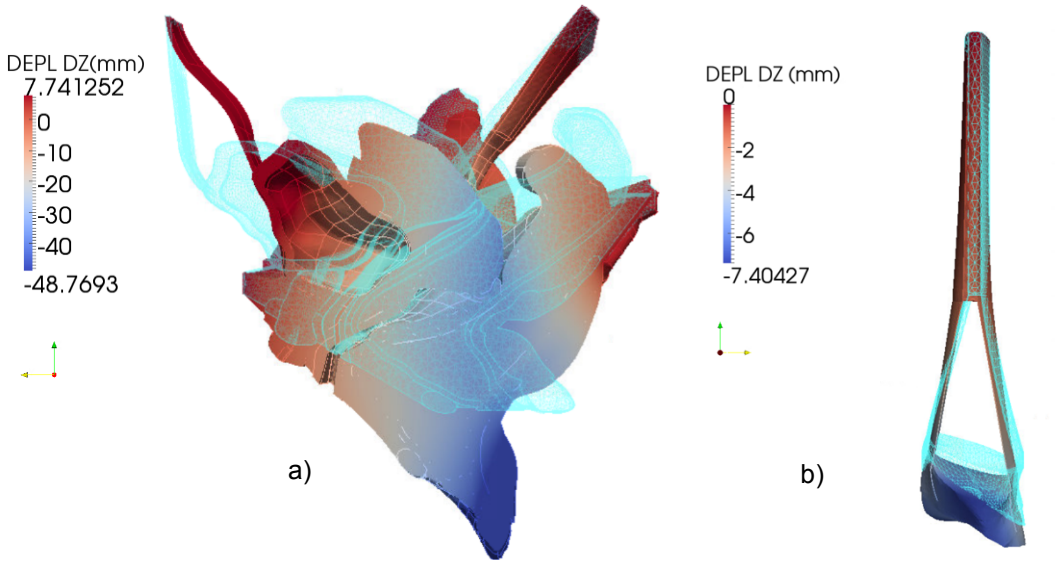

Fig. 2 *Distribution of deflection in a) 95% impaired pelvic floor and b) cervical ring with implant. Wireframe models are in rest position.*

Results: For prolapse pelvic floor, the simulated vertical dislocation of the cervical ring is around 26 mm. Comparing the rest and strained condition of pelvic floor, as shown in Fig. 1, demonstrates that the vertical movement of the cervical ring is restricted to about 5 mm. The displacement computed with FEM considering the PRS implant is about 7mm, which is close to measured MRP values. The pelvic floor response will be also analyzed with PRP and CESA implants and the results will be compared, which help decide for the better implant.

References

[1] L. de Landsheere, C. Manaut, B. Nusgens, C. Maillard, C. Rubod, M. Nisolle, M. Cosson, J.M. Foidart: Histology of the vaginal wall in women with pelvic organ prolapse. *Int Urogynecol J.* 2013;24(12):2011-2020. http://dx.doi.org/10.1007/s00192-013-2111-1

[2] S.E. Swift: The distribution of pelvis organ support in a population of female subjects seen for routine gynecologic health care. *Am J Obstet Gynecol*. 2000;183(2):277-285. https://doi.org/10.1067/mob.2000.107583

[3] M.-C. Sora, R. Jilavu, P. Matusz: Computer aided three-dimensional reconstruction and modeling of the pelvis, by using plastinated cross sections, as a powerful tool for morphological investigations. *Surg Radiol Anat.* 2012;34(8):731-736. https://doi.org/10.1007/s00276-011-0862-2

[4] A. Bhattarai, R. Frotscher, M. Staat: Biomechanical study of the female pelvic floor dysfunction using the finite element method. Proceedings YIC GACM 2015, 3rd ECCOMAS Young Investigators Conference, 6th GACM Colloquium, S. Elgeti and J.-W. Simon (eds.), Aachen, Germany, July 20-23, 2015. http://nbn-resolving.de/urn:nbn:de:hbz:82-rwth-2015-039806

[20] Upgrade of Bioreactor System Providing Physiological Stimuli to Engineered Musculoskeletal Tissues

Michel Schmitjans[1,2], Jan Bernd Vorstius[1], Waldemar Zylka[2]

[1] School of Science and Engineering
University of Dundee
Dundee DD1 4HN, Scotland, United Kingdom

[2] Faculty of Electric Engineering and Applied Natural Sciences,
Westphalian University, Campus Gelsenkirchen,
D-45897 Gelsenkirchen, Germany

E-Mail: michel.schmitjans@studmail.w-hs.de

Abstract – A novel central control interface (CCI) is developed to improve the modular bioreactor system with regard to extendability and modifiability in Tissue Engineering (TE) applications. This paper presents the results developed in the project with open-source hardware and the graphical programming system LabVIEW. A new platform independent User Interface was further developed to contribute to the new flexibility of the device.

Introduction: Bioreactors play a vital role in Tissue Engineering. While differing from common known bioreactors in the production industry, bioreactors in TE are used to "influence, support or mimic certain physical or physiological processes" [1]. The modular bioreactor system was developed to be a new device for the research and development of musculoskeletal tissue [2]. It is able to mimic the mechanical stress and the nervous stimulation occurring in the human body for a better growth and strength of the tissues [3]. While being a novel and universal device in this field of Tissue Engineering it comes with some disadvantages: The CCI can only control one bioreactor consisting of each one mechanical and one electrical stimulation module. Having in mind that the development of tissues can take months and contamination of one single tissue often results in an infection of all tissues in the bioreactor, the research can be very inefficient. Furthermore, the program running on the CCI was developed in the C programming language and is based on PIC microcontrollers. This makes it very hard to modify the code for attaching new sensors and other peripherals and thus creating a tailored device for every project. This paper describes a new approach of developing a new central control interface with a focal point on new hardware and programming systems to solve the current issues of the device.

Methodology: The bioreactor system consists of three core parts: The central control interface (CCI), the mechanical stimulation module (MMS) and the electrical stimulation module (MES). The MMS consists of a six-well plate and a geared down stepper motor equipped with a lead screw. The cell constructs are located in the wells and are anchored to two posts next to each well. One post is moved by the stepper motor and thus stretches the tissue. A potentiometer working as a displacement sensor is fixed to the actuator base and measures the potential backlash occurring when the force resistance of the tissues grows. The MES consists of 12 electrodes and a circuit that provides the electrical stimulus and is mounted on top of the MMS. The CCI was developed to control and observe the stimulation [1]. In order to improve the extendability and modifiability, the hardware of the CCI was changed from PIC microcontrollers to a Raspberry Pi 3. With the new hardware running Raspbian Jessie operating system (Release: 2016-09-23) new possibilities for alternative programming systems are available: The application running on the CCI was completely developed using the graphical programming system LabVIEW with the LINX Add-On. The stimulation parameters for the modular bioreactor system were configured either through a PC software running on Windows or on the device itself. While the Raspberry Pi and LabVIEW both are adaptable for internet applications, a new approach for a platform independent User Interface was developed by creating a website with JavaScript (using the jQuery library), HTML and CSS that is hosted by the Raspberry Pi.

The upgraded modular bioreactor system should be able to attach more than one bioreactor (MMS + MES). For this reason, a motor controller with a unique slave address was developed to be the interface between a MMS and the CCI. The motor controller consists of an Arduino Nano Rev 3 and an EasyDriver Stepper Motor Driver. The CCI communicates as a master to the motor controller slaves via the I²C-protocol.

Results: A breadboard-based prototype of the new modular bioreactor system was developed including a new CCI, a motor controller and one mechanical stimulation module. A new developed website based User Interface allows the user to configure the stimulation parameters. By the time the user filled out the necessary input fields and activated the “Apply Values” button in the User Interface, the LabVIEW application handles the HTTP request and writes the parameters into variables. By activating the “Start” button, the parameters are send to the motor controller with the respective slave address. Parallel to that a configuration file is written which contains the stimulation parameters for the respective MMS. The program running on the Arduino processes the values and controls the stepper motor with regard to the stimulation parameters: The configured stretch is calculated into steps the motor has to move depending on its gearhead and the lead of the leadscrew. Each step is made by toggling the STP pin of the EasyDriver. If the motor moved the actuator post to the desired position, the motor holds this position in the length of the pulse width value. After moving back to the zero position, another delay is executed in the length of the difference between period and pulse width. In the continuous mode, this procedure is executed continuously until the duration time elapsed. If the discontinuous mode is activated, the procedure is repeated depending on the repetitions value. After the repetitions the stimulation is paused depending on the rest time value. On the maximum point of every stretch operation, the Arduino reads the potentiometer value and converts the voltage to millimetres. The CCI requests this value every second and writes it with a time stamp in a separate log file to confirm if the tissue was stretched equally the whole time. Up to eight Mechanical Stimulation Modules with each a Motor Controller can be controlled and observed simultaneously with the upgraded CCI.

Discussion and Conclusion: Researchers working with the system are now able to apply mechanical stimulation up to 48 tissue specimens in eight separate modules. This upscaling reduces the risk of contamination of all tissues and increases the efficiency of the research and development. With LabVIEW as programming system of the CCI the application can be customized and modified to specific needs of various projects and applications in TE in an intuitive way. The new User Interface allows the researcher to control the bioreactor system with handheld devices like smartphones or tablets in the lab which bypasses the need of a space consuming computer.

References

[1] Jan B. Vorstius, *Modular Bioreactor System.* Dissertation University of Dundee, Dundee, September, 2012.
[2] Robert P. Keatch *et al.*, "Biomaterials in regenerative medicine: engineering to recapitulate the natural," *Current Opinion in Biotechnology.*, vol. 23, no. 4, pp. 579-582, August 2012.
[3] George J. Christ *et al.*, “Skeletal Muscle Tissue Engineering”, in *Stem Cell Biology and Tissue Engineering in Dental Sciences.* Elsevier, 2015, pp. 577-578

21) A Randomized, Observational Thermographic Study of the Neck Region before and after a Physiotherapeutic Intervention

Lukas de Hond, Dariusz Porst, Ilya Digel

Laboratory for Cell- and Microbiology,
Institute for Bioengineering,
FH Aachen University of Applied Sciences
D-52428 Jülich, Germany

E-Mail: dehond.lukas@hotmail.de
Web: www.zmb.fh-aachen.de

Abstract – To date there are just a few physiotherapeutic studies using technical monitoring and measurement methods like thermography, sonography or MRI. Thermography relies on the fact that every person's heat signature is unique and that the infrared radiation emitted by the skin is closely related to the local body temperature. Medical infrared imaging is a non-invasive, fast and low-cost diagnostic approach and can be used to measure and visualize the surface temperature of the human skin in real time with very high resolution. These facts make thermography a promising and quickly developing technique for diagnostics of different diseases, including inflammations, tumors as well as numerous neurological disorders.

The aim of this study was examine the spatial and temporal properties the heat emission of the shoulder and neck region, before and after a physiotherapeutic intervention. Basic statistical aspects of the individual variations in the thermal response induced by the exercise were addressed as well.

According to the experimental design, 20 healthy participants (aged between 19 and 29) were thermographically examined during a two weeks period. The participants were randomly separated, into the “intervention group” and the “control group”. The division was not gender-specific. According to the developed experimental protocol, three images of every participant were taken with a VarioCam HiRes camera (InfraTec GmbH, Dresden) equipped with an objective JENOPTIK IR 1.0/25 LW R2 (Jenoptik Co., Jena) over an eight-minute period. During this time, participants of the intervention group were instructed by the examiner to do an exercise with repeated isometric-contractions of neck muscles.

In general, a cooling of the skin due to exposure to a colder (room) environment was observed for all the participants, with a mean magnitude of 0.14°C in the intervention group and 0.42°C in the control group. Although the statistical significance threshold was not achieved (p value was 0.069 for 5% significance level) due to the small group size, the study allowed us to develop a systematic quantitative approach to evaluate the temperature distribution patterns as well as maximum temperatures. The thermographic method showed itself as a reproducible one and the results were found consistent.

For following studies, more data of the participants (vital parameter, core body temperature etc.) should be collected to facilitate the analysis of the measured values. Additionally, more participants should be included into the study.

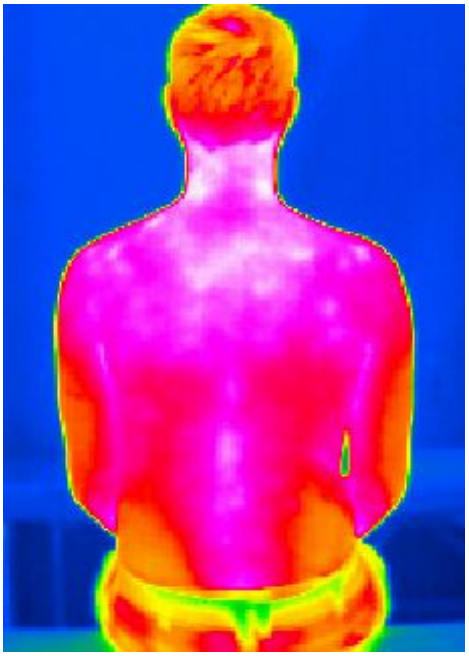

Fig. 1: An infrared image of a participant after the eight-minute period.

Related References

[1] B.B. Lahiri, B. Subramainam, J. Philip. “Medical applications of infrared thermography: A review”. *Infrared Physics & Technology. p*. 222 – 232, July 2012.

[2] Bouzas Marins, Gomes Moreira, Pinonosa Cano. “Time required to stabilize thermographic images at rest”. *Infrared Physics & Technology*, p. 30-35 May 2014.

[3] dos Santos, da Silva, de Souza Junior. „Thermographic: a tool of aid in physical therapy”. *Manual Therapy, Posturology & Rehabilitation Journal*, p. 364-371 22. December 2014.

[4] E.F.J. Ring, K. Ammer. “The Technique of Infrared Imaging in Medicine”. *Thermology International*, p. 1 – 13, February 2000.

[5] E.F.J Ring, K. Ammer, A. Jung. „*Standardization of Infrared Imaging”.* San Francisco, CA, USA: IEEE Engineering in Medicine and Biology Society, 2004.

[6] Fernandez Cuevas, Marins, Lastras. “Classification of factors influencing the use of infrared thermography in humans: A review”. *Infrared Physics & Technology*, p. 28 - 55 March 2015.

[7] Fernandez-Cuevas, Ismael. “*Validity, Reliability, and Reproducibility of Skin Temperature in Healthy Subjects Using Infrared Thermography”.* Faculty of Sciences for Physical Activity and Sport (INEF), Bd. Measuring the Skin, Universidad Politécnica de Madrid (Spain): Springer International Publishing Switzerland 2015, 2016.

[8] Costa, Ana C. S. “*Intra and inter-rater reliability of infrared image analysis of masticatory and upper trapezius muscles in women”.* Universidade Metodista de Piracicaba (UNIMEP), Piracicaba, Brazilian Journal of Physical Therapy. 17(1):24-31, 2013.

[9] K. Ammer, E.F.J. Ring. „Standart Procedures for Infrared Imaging in Medicine”. [Hrsg.] Joseph D. Bronzino, Donald R Peterson Mary Diakides. *Medical Infrared Imaging. Principles and Practice.* s.l.: CRC Press, Taylor & Francis Group, p. 32-1 - 32-9, 2012.

[10] Niu, Lui, Hu. “Thermal Symmetry of Skin Temperature: Normative Data of Normal Subjects in Taiwan”. *Chinese Medical Journal*, p. 459 – 468, March 2001.

[11] Zaproudina, Nina. “*Reproducibility of infrared thermography measurements in healthy individuals”.* s.l.: PHYSIOLOGICAL MEASUREMENT, 29/ 515-524, 2008.

[12] Mathies, H. 1983. *Rheumatologie A* . Berlin: Springer-Verlag, 1983. ISBN-13:978-3-642-68648-1.

[13] Redaktion, Pschyrembel. 2014. *Pschyrembel.* Berlin: deGruyter, 2014. ISBN 978-3-11-033997-0.

[14] Schünke, M. 2007. *Prometheus Lernatlas der Anatomie.* Stuttgart: Georg Thieme Verlag, 2007. ISBN 978-3-13-139522-1.

[15] Vollmer, M. 2010. *Infrared Thermal Imaging.* Germany: Wiley-VCH GmbH & Co. KGaA, 2010. ISBN: 978-3-527-40717-0.

[16] Zalpour, Christoff. 2010. *Anatomie/Physiologie für die Physiotherapie.* München: Elsevier, 2010. ISBN-13: 978-3437453021.

[22] Contactless Vital Sign Monitoring

Prof. Dr. Andreas R. Diewald [(1)], Daniel Schmiech, M.Sc.[(1)]

[(1)] Laboratory of applied radar technology and optical systems (LaROS)
Faculty of Engineering and Technology, Trier University of Applied Sciences,
D-54208 Trier, Germany

E-Mail: D.Schmiech@etech.hochschule-trier.de
Web: www.hochschule-trier.de/go/laros

Abstract – The most important signs of a living body that demonstrate the status of its life-sustaining functions are referred as vital signs [1]. The respiratory rate and the heart rate (two of the five primary signs) are currently measured by attaching small electrodes on the patients' skin, cable-connected to a monitoring system (e.g. ECG). This method is not always suitable, as there are several problems like skin injuries, high stress level and random loosening of the sensor, occurring because of the needed contact between the probe and the subjects' skin.

With the concept presented here a radar based system can be used to measure these two vital signs without the need of a contact between patient and sensor. The system will consist of a self-developed RF sensor, the baseband electronics with integrated digital signal processing and a visual display. One of the most challenging issues in contactless vital sign monitoring is random body movement (rbm) [2]. Operating at 24 GHz a frequency-modulated continuous-wave (FM-CW) radar with a bandwidth of 250 MHz will be used to minimize the upcoming error resulting of rbm. Other challenges base on the effect that respiration itself is a multitarget movement of the torso. Hence the signal processing algorithm will be multitarget-capable and sensitive to small movements to extract the heart rate. To reach the needed accuracy for vital sign monitoring, a model based filter will be used. In consequence of the advantages using a radar based contactless method, the system should be able to monitor patients in various situations, e.g. recumbent, seated or upright standing. Additionally, it is intended to observe more than one patient simultaneously. Therefore, the sensor is filtering and tracking different targets.

The concept itself will firstly be used in an infant incubator, to minimize the stress-level and the risks of skin injuries, especially to the premature babies.

References

[1] European foundation for the care of newborn infants: http://www.efcni.org/index.php?id=2198 (accessed April 29, 2017).

[2] Jianxuan Tu, Taesong Hwang, Jenshan Lin, "Respiration Rate Measurement Under 1-D Body Motion Using Single Continous-Wave Doppler Radar Vital Sign Detection System", *IEEE Transactions on Microwave Theory and Techniques,* vol. 64, no. 6, pp. 1937-1946, June 2016

[23] A Camera Based System for Contactless Pulse Oximetry

Christian Schiffer[(1)], Prof. Dr. A. R. Diewald[(1)], and Rene Thul[(1)]

[(1)] Laboratorey of applied Radar Technology and Optical Systems (LaROS),
Department of Electrical Engineering, Trier University of Applied Sciences,
D-54293 Trier, Germany

E-Mail: c.schiffer@hochschule-trier.de
Web: www.hochschule-trier.de/go/laros

Abstract – The arterial pulse rate and the arterial oxygen saturation (SaO2) are an important part of monitoring a patient's vital signs. To estimate a patient's SaO2 value conventional probes need to be attached to the subject's skin, in most cases around a finger or, in the case of premature infants, around a foot. This method is not always suitable, as there are reasons like damaged skin tissue or frequent loosening of the sensor, which prohibit attaching a probe directly.

With the methods presented here a camera based system can be used, that allows contactless measurements of the beforementioned vital signs. The system consists of a camera attached to a time multiplexed LED-array alternating red (660nm), near-infrared (810mn) and no active illumination synchronously during the exposure for each recorded image. The camera sensor's 10-bit ADC capability is barely sufficient for detecting arterial pulse related changes of brightness on an observed area of skin. Hence the ADC's sensitivity is extended by integrating brightness values over two areas of interest (64x64 pixels).

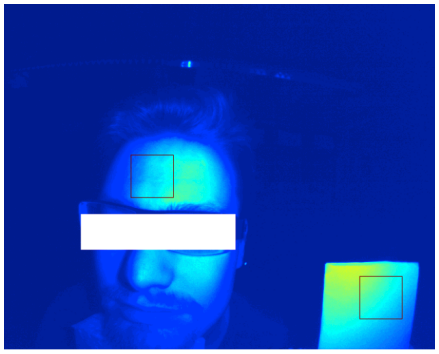

Fig. 1: Recorded picture with the red squares marking the areas of interest.

Those areas of interest record an area of the subject's skin and a lifeless reference area, that is used to cancel the effects of an unstable lighting due to changes of the LEDs' luminosity. This theoretically allows the camera to detect changes of 2^{-22} in the luminosity value of the camera. By carefully choosing the sampling rate the camera's limitations fulfilling the sampling theorem for background noise sources can be minimized. After transforming the pre-processed signals into frequency domain, the subject's arterial pulse rate can be determined.

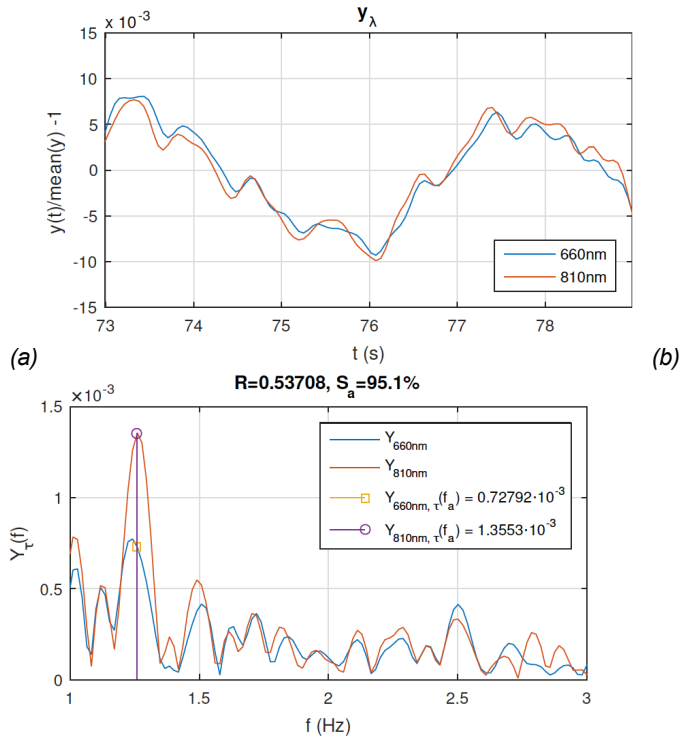

Fig. 2: The recorded signals in time-domain (a) and in frequency-domain (b).

The frequency-domain-signal contains information about the absorbance of light by pulsating arterial vessels corresponding to each utilized wavelength of light. This information can then be used to calculate the arterial oxygen saturation by approximating the Beer-Lambert law as demonstrated in figure 2.

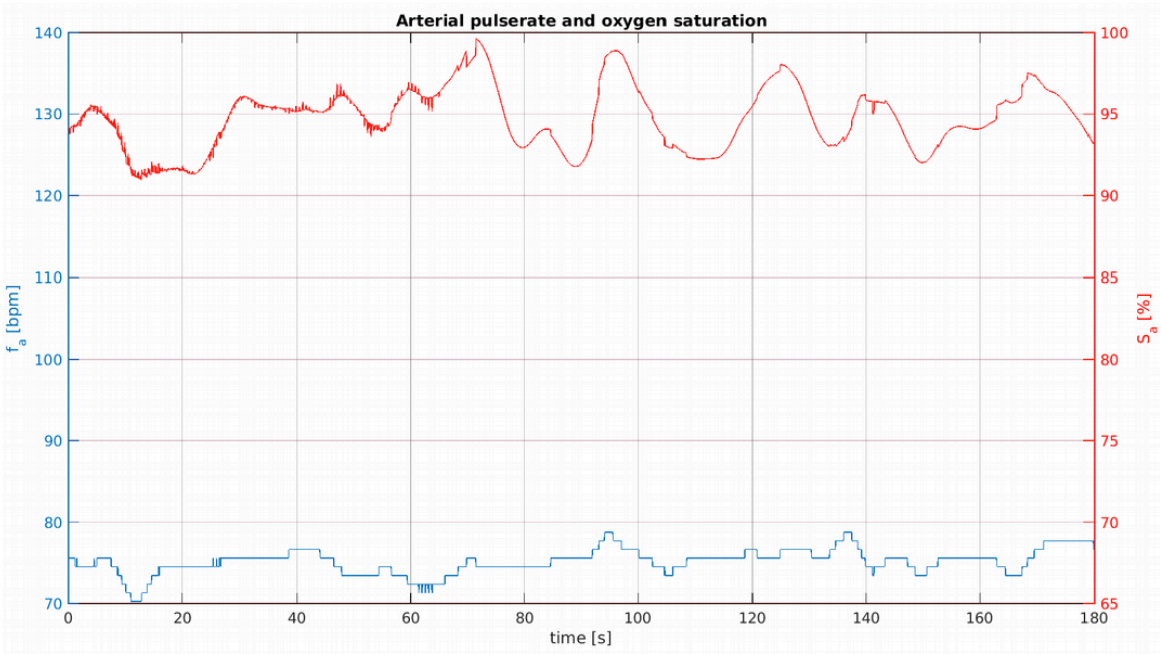

Fig. 3: Resulting arterial pulse (blue) and arterial oxygen saturation (red).

While improvements like enhanced signal analysis, using more sampling rates or face detecting and tracking remain to be implemented, measurements of the arterial pulse rate and oxygen saturation demonstrate this camera based system as a promising basis for a camera based pulse oximetry system.

[24] A Large Induction Field Scanner for Examining the Interior of Extended Objects or Living Humans

Martin Klein[(1)], Dirk Rueter[(1)]
[(1)] University of Applied Sciences Ruhr West

Institute for Measurement and Sensor Technology
D-45479 Muelheim an der Ruhr, Germany

E-Mail: martin.klein@hs-ruhrwest.de
Web: www.hochschule-ruhr-west.de

Abstract – The purpose of this scanner is to examine the interior of an extended object or - ultimately - the internal body of a living human. The technique is closely related to Magnetic Induction Tomography (MIT), a non-contacting, fast, harmless and cost-effective but however low-resolving method.

Currently known MIT-Systems typically comprise multiple transmitter and receiver coils in a circular arrangement. Induction fields permeate the volume and are detected by receiver coils [1, 2, 3]. Disadvantages of this geometry are that the test object must fit in a narrow tube and the receivers perceive a strong primary signal which is superimposed by the desired and much smaller signal from a test object. Highly accurate measurements and a sensitive phase analysis are required.

The herein presented scanner is rather different: the mechanical system (Fig.1) is very asymmetrical, more powerful, fully gradiometric and large enough for scanning an entire human body within a few seconds. One side of the system consists of two coaxial coils which provide a large gradiometer for the excitation field. Both currents are exactly adjusted to 180° phase difference. The gradiometer provides a powerful excitation field, which is still within the permitted limits for humans exposed to induction fields [4]. The test object or human is gently passing the excitation zone in lateral x-direction on a trolley. The receiver coils are located on the other side of the excitation zone and in a gradiometric position. The primary signals are almost completely nulled, enabling the received signals to directly reveal the real part (from metals) and the imaginary part (from resistive matter or biological tissue) of interesting perturbations in the MIT zone. A sensitive phase analysis is not required for these robust signals. However, during such a mechanical scan motion artifacts in the signals must be considered.

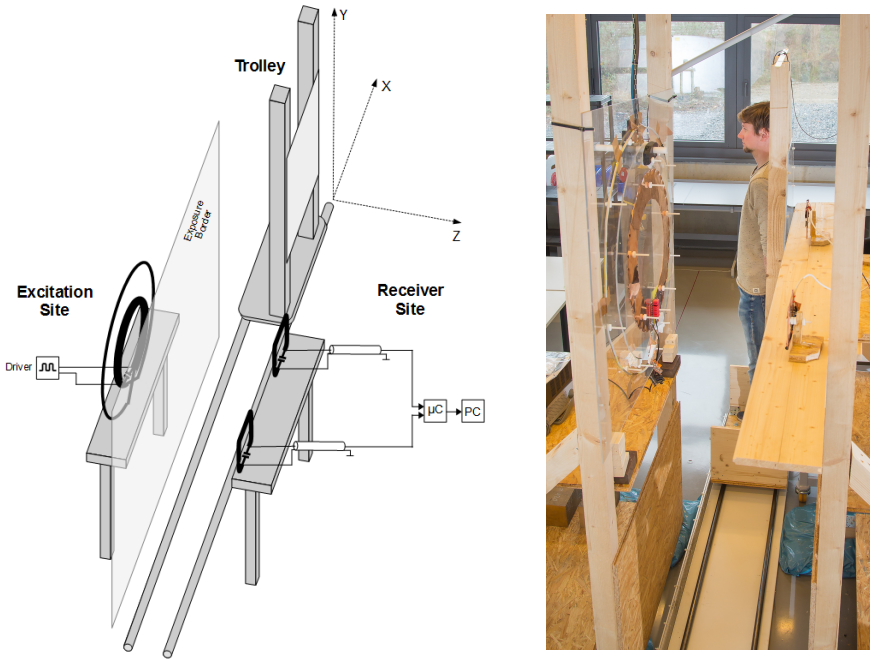

Fig. 3: MIT scanner. Schematic (left) and real (right) representation with a test person.

Experiments with discrete and small metal objects show a) that the approximate positions can be reconstructed and b) that it is possible to detect and localize certain changes of a given scenario (e.g., by adding or removing a metal object) by differential measurement.

To examine the interior of an extended object with a low conductivity (more similar to a human being), a voluminous tub is filled

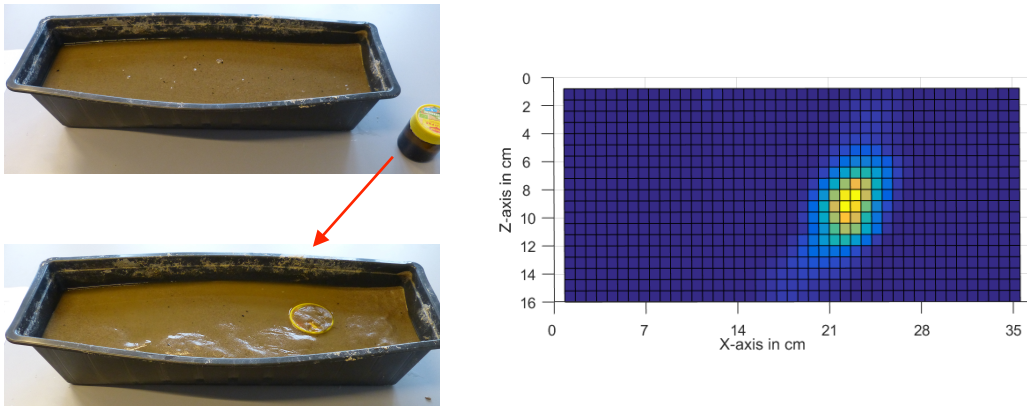

Fig. 4: Tub with a salt-water-sand-suspension (left, top); Tub with additionally inserted perturbation (left, bottom); Calculated localization of the perturbation from scanner signals (right)

with a moderately conducting salt-water-sand-suspension (Fig. 4 / left). The volume is modified by adding a much smaller object with a deviating conductivity (e.g., a void) at a certain position. Differential measurements between the modified volume and the unchanged volume clearly allow the localization (Fig. 4 / right) of the perturbation inside this rather non-transparent and conducting background. Normally, such a detection and localization inside such an opaque volume would require contacting ultrasound, harmful X-rays or expensive MRI methods.

The conductivity distribution inside the human thorax can be intentionally changed by lung inflation. For a representative result, subsequent and alternating scans of the expiration and the inspiration state from a living human were performed. A significant difference between the inspiration and expiration signals is reproducibly observed. Importantly, the intended change due to respiration obtains much higher signal differences than the unintended changes due to motion artifacts of the human. Thus, undesired motion artifacts or general signal uncertainties from a scan of a living person are small with respect to relevant signals from internal physiological properties.

Currently, the induction scanner only uses two receiver coils and only provides information about the x-z-plane. As this is work under progress, the given setting only represents the minimal configuration. To achieve better results or even 3D information in future, it will be necessary to add more sensor coils at other gradiometric positions. Furthermore, the challenging mathematical approach and the numerical methods have to be considerably improved.

References

[1] S. Watson, R. J. Williams, W. Gough, H. Griffiths, "A magnetic induction tomography system for samples with conductivities below 10 S m^{-1}" Meas. Sci. Technol. 19 (2008) 045501 (11pp).

[2] R. Merwa, P. Brunner, A. Missner, K. Hollaus, H. Scharfetter, "Solution of the inverse problem of magnetic induction tomography (MIT) with multiple objects: analysis of detectability and statistical properties with respect to the reconstructed conducting region" Physiol. Meas. 27 (2006) S249-S259.

[3] H.-Y. Wei, M. Soleimani, "TWO-PHASE LOW CONDUCTIVITY FLOW IMAGING USING MAGNETIC INDUCTION TOMOGRAPHY" Progress In Electromagnetics Research, Vol. 131, 99-115, 2012.

[4] Deutschen Gesetzlichen Unfallversicherung, "Grenzwertliste 2015. Sicherheit und Gesundheitsschutz am Arbeitsplatz" IFA Report 4/2015

25) Modeling and Evaluation of High Impedance Surfaces Applied to Improve the Performance of RF Coils within High-field MRI

Benedikt Sievert[(1)], Andreas Rennings[(1)], and Daniel Erni[(1)]

[(1)] Laboratory for General and Theoretical Electrical Engineering (ATE)
Faculty of Engineering, University of Duisburg-Essen,
D-47048 Duisburg, Germany

E-Mail: benedikt.sievert@stud.uni-duisburg-essen.de
Web: http://www.ate.uni-due.de/index.htm

Abstract – The use of High Impedance Surfaces (HIS) as an antenna reflector has proved beneficial for radiative applications [1], especially when compact solutions are desired [2]. With a focus on the MRI application, not only compact designs, but also improved B- to E-field ratio are goals of engineered solutions. In [3] it has been shown that, compared to conventional antenna shields, the use of a HIS supports a higher penetration depth in the body concerning the magnetic flux density. At its resonance, the HIS approaches the behavior of a Perfect Magnetic Conductor (PMC), a solely theoretical surface which forces the magnetic field to be normal to the surface. This behavior seems to enhance the penetration of the magnetic field [3]. The frequency of resonance is characterized by the surface impedance of the HIS reaching its maximum value, which results in a zero phase reflection coefficient.

Consisting of electrically small conducting patches, the HIS itself is a periodic structured surface with unit cells, which are smaller than the wavelength of the used EM-waves. In combination with high permittivity materials used for the HIS, small gaps between the patches and large shield surfaces in general, the computational effort for simulating these surfaces is high. Even simple MRI-setups using homogeneous phantoms challenge modern workstation PCs when using the FEM-method, if the HIS in included in the setup. A parallel LC circuit has been designed for describing the behavior of the HIS concerning its reflection behavior, used for gaining a deeper physical insight and applied for simplifying the domain in an accurate but effective manner. The equivalent circuit models the surface impedance of the HIS and is assigned to a so called Impedance Boundary Condition (IBC) in HFSS by Ansys [4]. This boundary condition is able to model the complex HIS structure within one surface boundary, which reduces the computational effort drastically. The resulting magnetic field for a symmetrical antenna setup is shown in Figure 1. The setup uses eight meandered dipole antennas, as they were presented in [5], which are modified based on the results from [6].

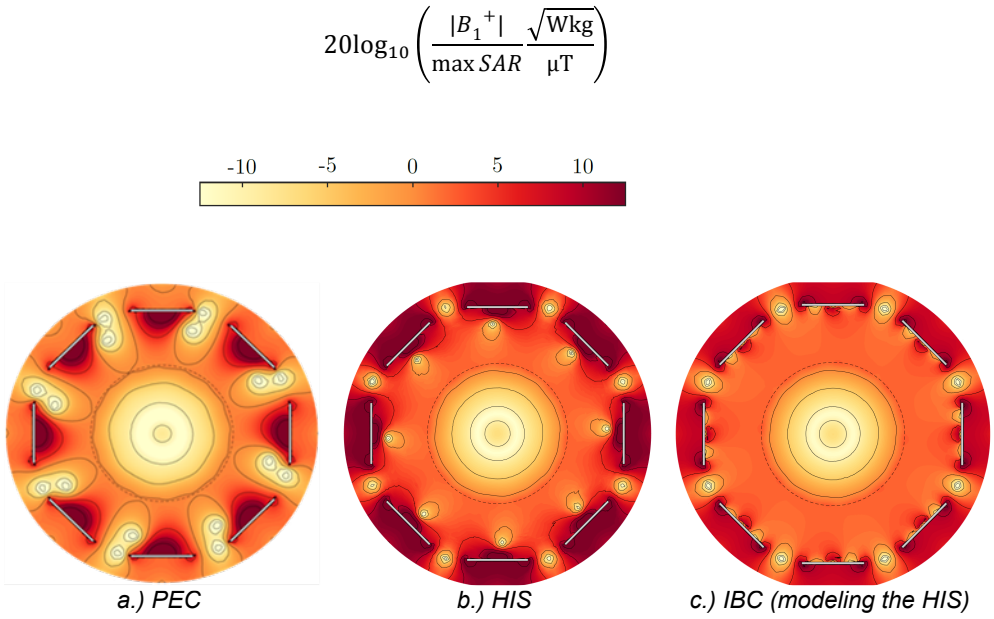

Fig.1: Magnetic flux density $|B_1^+|$ normalized to the maximum of the SAR inside the homogeneous tissue for different shield types. a.) conventional PEC shield, b.) HIS shield and c.) Impedance boundary condition modeling the HIS. The tissue is denoted by the dotted line.

With the use of the HIS, the magnetic flux density increases in- and outside the tissue while the inhomogeneity decreases. The modeling of the HIS by the IBC shows a good compliance, especially inside the tissue. Deviations can be observed in the proximity of the antennas, nevertheless the characteristic field behavior of both approaches is comparable. As a next step a more complex setup, which should be measured in an MRI scanner, is investigated and optimized towards a strong and homogeneous B_1^+-field. With the advantage of reduced simulation time by use of the IBC, new optimization approaches are applicable.

References

[1] D. Sievenpiper, High-Impedance Electromangetic Surfaces. Dissertation, University of California, Los Angeles, 1999.
[2] G. Saleh, High Impedance Surface – Electromagnetic Band Gap (HIS-EBG) Structures for Magnetic Resonance Imaging (MRI) Applications. Dissertation, University of Duisburg-Essen, 2013.
[3] Z. Chen, Application of High Impedance Surfaces to Improve Radiofrequency Coil Performance for 7-Tesla Magnetic Resonance Imaging. Dissertation, University of Duisburg-Essen, 2016.
[4] HFSS is a solver for RF electromagnetics based on the FEM method. HFSS is a product by Ansys, Inc. http://www.ansys.com/Products/Electronics/ANSYS-HFSS (accessed March. 30, 2017)
[5] S. Orzada, A. Bahr, and T. Bolz. “A novel 7 T microstrip element using meanders to enhance decoupling”, 16th Proc. Intl. Soc. MRM, page 2979, 2008.
[6] Z. Chen, K. Solbach, D. Erni, and A. Rennings, "Dipole RF Element for 7 Tesla magnetic resonance imaging with minimized SAR", 7th European Conference on Antennas and Propagation (EuCAP 2013), April 8-12, Gothenburg, Sweden, Session CM1a.1, pp. 1716-1719, 2013, (invited paper).

IMPRESSUM

Editors:

Dipl. -Ing. (Univ.) Alice Fischerauer, University of Bayreuth
Prof. Dr. Daniel Erni, University of Duisburg Essen
Prof. Dr. Jörg Himmel, University of Applied Sciences Ruhr West
Prof. Dr. Thomas Seeger, University of Siegen
Prof. Dr. Klaus Thelen, University of Applied Sciences Ruhr West

Scientific Advisory Board:

Prof. Dr. Gerhard Fischerauer, University of Bayreuth
Dipl. -Ing. (Univ.) Alice Fischerauer, University of Bayreuth
Prof. Dr. Jörg Himmel, University of Applied Sciences Ruhr West
Prof. Dr. Olfa Kanoun, Chemnitz University of Technology
Prof. Dr. Lothar Kempen, University of Applied Sciences Ruhr West
Prof. Dr. Frank Kreuder, University of Applied Sciences Ruhr West
Prof. Dr. Gennadij Lukjanow, ITMO University, St. Petersburg
Prof. Dr. Dirk Rüter, University of Applied Sciences Ruhr West
Prof. Dr. Thomas Seeger, University of Siegen
Prof. Dr. Klaus Thelen, University of Applied Sciences Ruhr West

Responsible according to German press law:

President of the University of Applied Sciences Ruhr West, Prof. Dr. Gudrun Stockmanns,
Duisburger Str. 100, 45479 Mülheim an der Ruhr

ISBN: 978-3-9814801-9-1

University of Applied Science Ruhr West
Duisburger Str. 100
45479 Mülheim an der Ruhr

Print

University of Siegen
UniPrint
Hölderlinstr. 3
57076 Siegen
Print run: 200 pieces, as of June 2017

Legal disclaimer

Mülheim an der Ruhr, Juni 2017

With generous support from: HRW FÖRDERVEREIN DER HOCHSCHULE RUHR WEST

HOCHSCHULE RUHR WEST
UNIVERSITY OF APPLIED SCIENCES

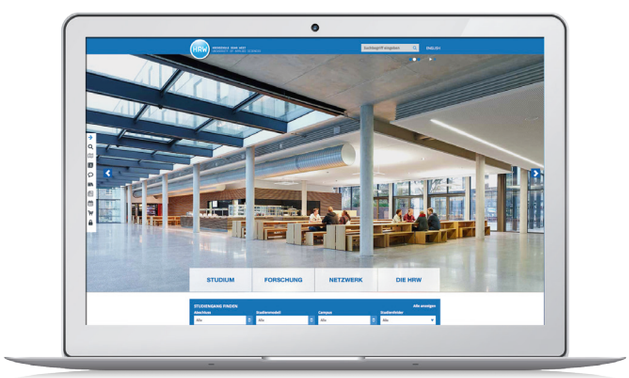

ISBN: 978-3-9814801-9-1

WWW.HOCHSCHULE-RUHR-WEST.DE